OPTIMIZED AND APPLIED DESIGN OF A TUNABLE PROTON POST-ACCELERATION AND FOCUSING DEVICE FOR THE PETAL LASER

CONCEPTION OPTIMISÉE ET APPLIQUÉE D'UN DISPOSITIF ACCORDABLE DE FOCALISATION ET DE POST-ACCELERATION DE PROTON POUR LE LASER PETAL

Par

Clément Lacoste

Thèse présentée pour l'obtention du grade de Philosophiae Doctor (Ph.D.)

en sciences de l'énergie et des matériaux

Jury d'évaluation

Président du jury et examinateur interne	François Légaré Institut national de la recherche scientifique
Examinateur externe	Xavier Davoine Commissariat à l'Énergie Atomique et aux Énergies Alternatives
Rapporteure	Brigitte Cros Laboratoire de physique des gaz et des plasmas
Rapporteure	Michèle Raynaud Laboratoire des Solides Irradiés
Directeur de recherche	Patrizio Antici Institut national de la recherche scientifique
Directeur de recherche	Emmanuel D'humières Université de Bordeaux

THÈSE PRÉSENTÉE
POUR OBTENIR LE GRADE DE

Docteur de l'Institut national de la recherche scientifique et de l'Université de Bordeaux

PROGRAMME : SCIENCES DE L'ÉNERGIE ET DES MATÉRIAUX
ÉCOLE DOCTORALE SCIENCES PHYSIQUES ET DE L'INGÉNIEUR
ASTROPHYSIQUE, PLASMAS, NUCLÉAIRE

Par **Clément LACOSTE**

Optimized and applied design of a tunable proton post-acceleration and focusing device for the PETAL Laser

Sous la direction de : **Emmanuel d'HUMIÈRES and Patrizio ANTICI**

Soutenue le 10 décembre 2025

Membres du jury :

M. François LEGARE	Professeur	INRS-EMT	President of the jury
M. Xavier DAVOINE	Ingénieur de recherche	CEA	Examinateur
Mme. Michèle RAYNAUD	Directrice de Recherche	LSI	Rapporteure
Mme. Brigitte CROS	Directrice de Recherche	LPGP	Rapporteure
M. Emmanuel d'HUMIÈRES	Professeur	Université de Bordeaux	Directeur de thèse
M. Patrizio ANTICI	Professeur	INRS-EMT	Directeur de thèse

Membres invités :

Matthieu BARDON	Ingénieur chercheur	CEA	Co-encadrant
Vladimir TIKHONCHUK	Professeur émérite	Université de Bordeaux	Invité

Science, my boy, is made up of mistakes,
but they are mistakes which it is useful to make,
because they lead little by little to the truth - Jules Verne

La science, mon garçon, est faite d'erreurs,
mais d'erreurs qu'il est bon de commettre,
car elles mènent peu à peu à la vérité - Jules Verne

Résumé :

Le premier tube à ondes progressives (TWT, Traveling Wave Tube) a été conçu en 1947. Le concept du TWT consiste à utiliser un faisceau d'électrons incident pour amplifier l'amplitude d'un champ électromagnétique d'entrée par couplage entre le faisceau et un courant se propageant dans une hélice. L'intérêt croissant pour ce système trouve son origine dans le domaine des dispositifs micro-ondes à haute puissance et haute fréquence, tels que les gyrotrons, les tubes à ondes progressives relativistes ou les lasers à électrons libres.

Les applications du TWT incluent les systèmes de communication par satellite, les contre-mesures électroniques ou les systèmes radar, grâce à une large bande passante instantanée, un gain élevé et un faible poids.

D'autre part, l'accélération d'ions par laser est actuellement l'un des domaines de recherche les plus dynamiques en raison de sa compacité et de ses nombreuses applications, telles que le chauffage isochore, la production d'isotopes ou de neutrons, la radiographie plasma et la fusion nucléaire dans un schéma d'allumage rapide. Parmi tous les mécanismes d'accélération d'ions par laser, le Target Normal Sheath Acceleration (TNSA) fait partie des plus robustes, et repose sur l'interaction d'un faisceau laser de haute intensité avec une cible solide d'épaisseur micrométrique. La pré-impulsion du laser crée un plasma sur la cible, et l'impulsion principale accélère les électrons qui, lorsqu'ils sortent de la cible, génèrent une séparation de charges et un champ électrique statique de plusieurs TV/m. Ce champ accélère les protons, présents à la surface de la cible sous forme d'impuretés hydrogénées, à des énergies allant de quelques MeV à plusieurs dizaines de MeV. Cependant, la divergence angulaire de l'accélération par TNSA qui reste encore trop élevée ($\pm 20°$), et la distribution énergétique des protons qui décroit exponentiellement avec l'énergie, limitent les possibilités d'applications.

Dans ce contexte, l'idée d'implémenter un dispositif (cible hélicoïdale) couplé au TNSA a été proposée pour post-accélérer et focaliser le faisceau de protons. Ce concept consiste à faire propager un courant de décharge, créé lors de l'interaction laser-plasma, dans une hélice. La physique de la propagation du courant dans cette hélice est analogue à celle des systèmes de transmission couplés (comme les TWT). Cependant, compte tenu de l'étendue spectrale de ce courant (impulsion large bande fréquentielle de l'ordre de 10 ps de durée d'impulsion), la dispersion du courant le long de l'hélice est plus importante que dans le cas d'un TWT, ce qui ne permet pas l'obtention d'une post-accélération et d'une focalisation efficace sur toute la longueur de l'hélice, limitant ainsi son champ d'application.

C'est dans ce contexte que ce manuscrit prend place, présentant dans une première partie le modèle analytique développé durant cette thèse ayant pour but de comprendre la physique et d'optimiser les géométries des cibles hélicoïdales. Ensuite, dans une deuxième partie, une expérience sur le laser ALLS, montrant l'impact des cibles hélicoïdales sur les spectres de protons et d'ions carbones, est présentée. Laissant place dans une troisième partie à une étude numérique de l'application des cibles hélicoïdales sur des ions α pour la production de radio-isotopes du scandium pour la médecine.

Mots-clés : Cible hélicoïdale, TNSA, Traveling Wave Tube, accélération de protons, accélération d'ions lourds.

Abstract :

The first Travelling Wave Tube (TWT) was conceived in 1947. The concept of TWT involves utilizing an incident electron beam to amplify the amplitude of an input electromagnetic field through coupling between the beam and a current propagating in a helix. The growing interest of this system takes source with the domain of high power and high frequency microwave devices such as the gyrotrons, the relativistic travelling wave tubes or the free-electron lasers. Applications of TWT include satellite communication systems, and electronic countermeasures or radar systems permitted by a wide instantaneous bandwidth, high gain and light weight.

On the other hand, laser-driven ion acceleration is currently one of the most dynamic research domains due to its conpactness and numerous applications such as isochoric heating, isotope or neutron production, plasma radiography, and nuclear fusion in a fast ignition scheme. Among all laser ion acceleration mechanisms, Target Normal Sheath Acceleration (TNSA) is one of the most robust. It relies on the interaction of a high-intensity laser pulse with a solid target of micrometric thickness. The laser's pre-pulse creates a plasma on the target surface, and the main pulse accelerates electrons that propagate through the target. When these electrons exit the target, they generate a charge separation and a static electric field of several TV/m. This field accelerates protons—present on the target surface as hydrogenated impurities—to energies ranging from a few MeV to several tens of MeV. However, the angular divergence of TNSA acceleration, which remains relatively high (around $\pm 20°$), and the exponential energy distribution of the protons with energy, limit its potential for applications.

In this context, the idea of implementing a device coupled with TNSA has been proposed to post-accelerate and focus the proton beam. This concept, known as the helical coil, consists of guiding a discharge current, generated during the laser-plasma interaction, along a helical coil. The physics of current propagation in this coil is analogous to that of coupled transmission systems, such as traveling-wave tubes (TWTs). However, due to the broadband nature of the current pulse (with a spectral width corresponding to a duration of approximately 10 ps), dispersion along the coil becomes significant, which prevents efficient post-acceleration and focusing over the entire length of the helix, thereby limiting the range of potential applications.

It is within this framework that the present manuscript is situated. The first part presents the analytical model developed during this thesis, aimed to understand the underlying physics and optimizing the geometry of the helical targets. The second part describes an experiment carried out on the ALLS laser facility, highlighting the impact of the helical targets on the spectra of protons and carbon ions. Finally, the third part is devoted to a numerical study of the application of helical targets to α-particles for the production of scandium radioisotopes intended for medical use.

Keywords: Helical coil, TNSA, Traveling Wave Tube, proton acceleration, heavy ions ac-

celeration.

Publications and Conferences

Publications

1. C.L.C. Lacoste, D. Oportus, J. Béard, R. Lelievre, T. Waltenspiel, W. Yao, M. Bardon, F. Condamine, P. Antici, J. Fuchs, and E. D'Humières Detailed Influence of External Magnetic Field on Laser-Plasma Instabilities in Inertial Confinement Fusion Experiments, to be submitted to Physics of Plasmas (PoP)
   DOI : https://doi.org
2. K. Aliane, C. L. C. Lacoste, A. Poyé, Y. Elskens, E. d'Humières, V. T. Tikhonchuk, P. Antici, M. Bardon, A. Selemani, and F. Andre Evaluating self-consistency effects in helical coil post-acceleration using the 1-D multiparticle hamiltonian model DIMOHA, submitted to Physics of Plasmas
   DOI : https://doi.org
3. C.L.C. Lacoste, T. Carrière, H. Larreur, V.T. Tikhonchuk, D. Batani, D. Raffestin, P. Antici, E. D'Humières, P. Nicolaï, and M. Bardon Numerical Study of Enhanced Radioisotope Production from Laser-driven Particles Bunching Using Helical Coil Target with Tube, accepted to Physical Review Accelerator and Beams
   DOI : https://link.aps.org/doi/10.1103/fg53-l53v
4. C.L.C. Lacoste, E. Catrix, S. Vallières, A. Hirsch, T. Guilberteau, M. Lafargue, J. Lopez, I. Manek-Hönninger, V. T. Tikhonchuk, S. Fourmaux, D. Raffestin, E. d'Humières, P. Antici, and M. Bardon Experimental Investigation of the Impact of Helical Coil on Laser-driven Protons and Carbons, Matter and Radiation at Extremes, 10(3)
   DOI : https://doi.org/10.1063/5.0257518
5. Lacoste, C. L. C., Hirsch-Passicos, A., d'Humières, E., Tikhonchuk, V. T., Antici, P., & Bardon, M. (2024). Theoretical model of current propagation in a helical coil with varying geometry and screen tube. Matter and Radiation at Extremes, 9(6).
   DOI : https://doi.org/10.1063/5.0221820
6. Hirsch-Passicos, A., Lacoste, C. L. C., André, F., Elskens, Y., D'Humières, E., Tikhonchuk, V., & Bardon, M. (2024). Helical coil design with controlled dispersion for bunching enhancement of protons generated by the target normal sheath acceleration. Physical Review E, 109(2), 025211.
   DOI : https://doi.org/10.1103/PhysRevE.109.025211

Oral presentations

1. Asia-Pacific Conference on Plasma Physics
   C.L.C. Lacoste, A. Hirsch-Passicos, E. Catrix, T. Carrière, S. Vallières, S. Fourmaux, D. Raffestin, V.T. Tikhonchuk, P. Antici, E. D'Humières et M. Bardon Optimization and application of helical coil target with varying geometry and screen tube
   21 to 26 of september 2025, Fukuoka, (Japan)

2. IRP LUMAQ
   Lacoste, C. L. C., Hirsch-Passicos, A., d'Humières, E., Tikhonchuk, V. T., Antici, P., & Bardon, M. Optimized and applied design of tunable proton focusing and post-acceleration
   December 2024, Bordeaux, (France)

3. GPR LIGHT
   C.L.C. Lacoste, D. Oportus, J. Béard, R. Lelievre, T. Waltenspiel, W. Yao, M. Bardon, F. Condamine, P. Antici, J. Fuchs, and E. D'Humières Theoretical and Experimental Study of the Impact of an External Magnetic-field on Cross Talk and Laser-Plasma Instabilities
   December 2024, Bordeaux, (France)

4. LIGHT GSI
   Lacoste, C. L. C., Hirsch-Passicos, A., d'Humières, E., Tikhonchuk, V. T., Antici, P., & Bardon, M. Optimized and applied design of tunable proton focusing and post-acceleration
   29 of october 2024, Darmstadt, (Germany)

5. AAC physic conference
   Lacoste, C. L. C., Hirsch-Passicos, A., d'Humières, E., Tikhonchuk, V. T., Antici, P., & Bardon, M. Optimized and applied design of tunable proton focusing and post-acceleration
   21 to 26 of July 2024, Naperville, Illinois, (USA)

6. Light Sciences and Technologies - Annual Student Conference
   Lacoste, C. L. C., Hirsch-Passicos, A., d'Humières, E., Tikhonchuk, V. T., Antici, P., & Bardon, M. Optimized and applied design of tunable proton focusing and post-acceleration
   29 of april 2024, Bordeaux, (France)

7. Virtual Symposium -Speech contest "Showcase your research project in 5 minutes"
   Lacoste, C. L. C., Hirsch-Passicos, A., d'Humières, E., Tikhonchuk, V. T., Antici, P., & Bardon, M. Optimized and applied design of tunable proton focusing and post-acceleration
   11 of march 2024, Montréal, (Canada)

8. GPR APPEL
   Lacoste, C. L. C., Hirsch-Passicos, A., d'Humières, E., Tikhonchuk, V. T., Antici, P., & Bardon, M. Optimized and applied design of tunable proton focusing and post-acceleration
   13 to 15 of november 2023, Saclay, (France)

Poster presentations

1. NIF user meeting 2025
   C.L.C. Lacoste, A. Hirsch-Passicos, E. Catrix, T. Carrière, S. Vallières, S. Fourmaux, D. Raffestin, V.T. Tikhonchuk, P. Antici, E. D'Humières et M. Bardon Optimization and application of helical coil target with varying geometry and screen tube
   11 to 13 of February 2025, Livermore, California (USA)

2. AAC physic conference
   C.L.C. Lacoste, D. Oportus, J. Béard, R. Lelievre, T. Waltenspiel, W. Yao, M. Bardon, F. Condamine, P. Antici, J. Fuchs, and E. D'Humières Plasma Instabilities with external magnetic field
   21 to 26 of July 2024, Naperville, Illinois, (USA)

3. PhD day of University of Bordeaux 2024
   C.L.C. Lacoste, E. Catrix, C. Boynukara, S. Fourmaux, A. Hirsch-Passicos, VT. Tikhonchuck, P. Antici, E. d'Humières et , M. Bardon Optimization of the PIXE analysis method with laser-accelerated ions using a helical target and a tube
   2024, Talence (France)

4. PhD day of CEA 2024
   C.L.C. Lacoste, E. Catrix, C. Boynukara, S. Fourmaux, A. Hirsch-Passicos, VT. Tikhonchuck, P. Antici, E. d'Humières et , M. Bardon Optimization of the PIXE analysis method with laser-accelerated ions using a helical target and a tube
   2024, Ile-de-France (France)

5. 49th EPS Plasma Physics Conference
   C.L.C. Lacoste, E. Catrix, C. Boynukara, S. Fourmaux, A. Hirsch-Passicos, VT. Tikhonchuck, P. Antici, E. d'Humières et , M. Bardon Optimization of the PIXE analysis method with laser-accelerated ions using a helical target and a tube
   3 to 7 of July 2023, Bordeaux (France)

6. 11th Laser Plasma Interaction Forum (ILP)
   C.L.C. Lacoste, E. Catrix, C. Boynukara, S. Fourmaux, A. Hirsch-Passicos, VT. Tikhonchuck, P. Antici, E. d'Humières et , M. Bardon Optimization of the PIXE analysis method with laser-accelerated ions using a helical target and a tube
   26 to 31 Mars 2023, Orcières Merlette (France)

Remerciements

Ces remerciements sont autant pour vous que pour moi. Autant pour vous témoigner ma plus grande gratitude que pour me remémorer tout ce que je vous dois. Autant pour vous dire merci que pour inscrire à jamais ma dette. Aussi, il y aura peu de nom, mais j'espère que les concernés se reconnaitront. Ainsi, je n'oublierai personne même si je ne peux remercier tout le monde.

En premier lieu, je voudrais dire merci à mes encadrants de thèse, Matthieu, Emmanuel, Patrizio et Vladimir. Vous avez cru en moi et m'avez fait confiance. On a fait de belles choses ensemble je pense. Merci de m'avoir tant appris, merci pour votre bienveillance, vos encouragements perpétuels et votre soutien, malgré mon caractère, qui est le mien.

La famille, il y a celle du sang et celle que l'on choisit. Il y a ceux que l'on connait depuis l'âge de 2 ans, à tel point qu'on ne les a pas vraiment choisis. Il y a ceux que l'on connait depuis moins, avec qui on partage les doutes, les potins et les bières. Il y a ceux que malheureusement, on voit peu, mais qui restent dans notre esprit comme si on les avait vus hier. Il y a celles qui viennent de nous rejoindre comme Arya ou Marìlia encore trop jeune pour que je leur parle de Maxwell ou de plasma. Et dans tout ça, quelques-uns se démarquent en donnant leur canapé, leur temps et leur bonne humeur. Ou en me martyrisant sur smash de nombreuses heures. Vous êtes des Hommes d'honneur, des samouraïs des temps modernes, aux côtés desquelles je demeure.

Bien sûr, s'il y a une personne qui a chamboulé mon quotidien, c'est bien toi Mélissa. Je ne te remercierai jamais assez pour tout ce que tu m'as apporté. M'extirpant de mes stressantes pensées d'innombrables fois, faisant de ma vie l'anti-thèse d'une routine et me donnant un foyer où me reposer, un air neuf à respirer. Et alors que souvent, je m'absentais, à l'étranger ou dans mon palais, jamais ton soutien ne m'a été retiré. Tu as même accepté de me suivre à vie, écoutant patiemment tous mes discours barbants sur la physique et les galaxies.

Les derniers sont les premiers. Les premiers soutiens émotionnels ... et financiers. Je me rappelle vos encouragements et de votre absence de doute lors de mon redoublement. Vous me faisiez confiance, aucun reproche, comme si vous saviez que 7 ans plus tard j'aurais un doctorat en poche. Si dans cette famille, une devise devait demeurer, elle serait de toujours finir ce qu'on a commencé. On a fini ce manuscrit. Que dans l'éternité résonne ce qui y est écrit : Memento Amoris.

Dans cette famille, il y a aussi mon premier professeur. Le premier à avoir soufflé sur les braises qui demeurent aujourd'hui ma passion. Je veux parler de mon grand-père, m'apprenant la structure du système solaire avec des oranges, des balles de ping-pong et un ballon. Ne négligeons jamais le pouvoir des mots, les siens ont fait naître ma vocation. Quelques discussions,

en observant les étoiles, ont été les balbutiements des équations que je peins aujourd'hui sur ma toile. Cette thèse, je la lui dédis pour que son rôle déterminant, personne n'oublie.

Table des matières

Table des figures

Chapitre 1

Introduction-Français

Sommaire

1.1 Accélération de particules

Les accélérateurs de particules sont des instruments expérimentaux qui permettent d'accélérer des particules chargées, telles que les électrons, les protons et les ions, à des vitesses proches de celle de la lumière. Le principe de base des accélérateurs de particules repose sur l'utilisation de champs électriques pour accélérer des particules chargées, et de champs magnétiques pour les confiner et les orienter dans la direction souhaitée. Des découvertes majeures ont ainsi été réalisées et des applications, notamment en médecine, ont vu le jour, comme le traitement du cancer par exemple où ils sont utilisés pour délivrer des rayonnements à haute énergie avec précision sur des tumeurs, une technique connue sous le nom de radiothérapie. Les accélérateurs servent également à la production de radio-isotopes médicaux pour l'imagerie et le diagnostic, tels que le fluor-18 utilisé dans les tomographies par émission de positons (PET scans).

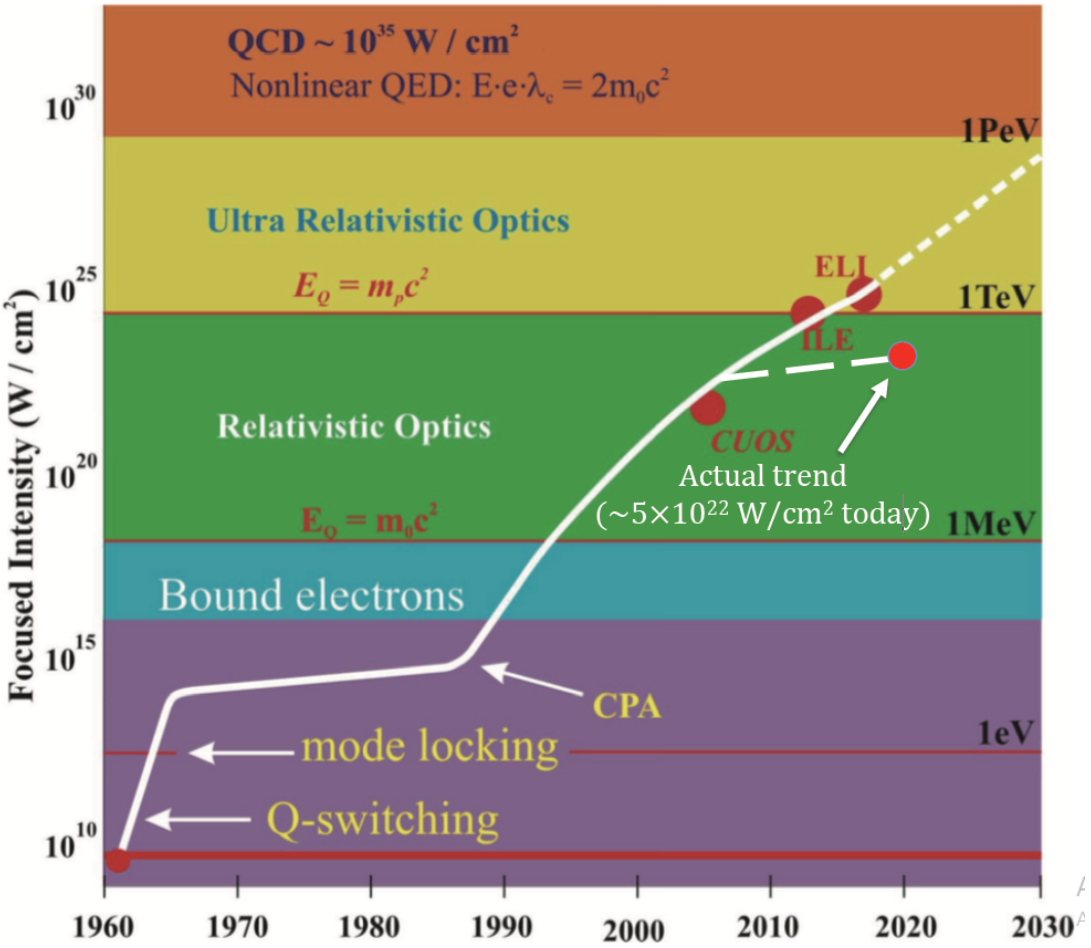

FIGURE 1.1 – L'évolution des intensités laser depuis leur invention en 1960. Cette figure est extraite et adaptée de G. A. Mourou, T. Tajima & S. V. Bulanov, "Optics in the relativistic regime" [1]

D'autre part, les lasers à haute intensité comptent parmi les dispostifs expérimentaux les plus puissants utilisés en physique moderne. Ces lasers peuvent délivrer des niveaux de puissance extrêmement élevés sur de très petites surfaces, permettant d'explorer les processus fondamentaux de la matière et de faciliter une large gamme d'applications, notamment, l'accélération de par-

ticules par laser, comme l'accélération d'électrons par onde de sillage, rendue possible grâce à l'utilisation d'impulsions laser ultra-courtes capables de générer dans le plasma un champ d'accélération extrêmement intense (Laser Wakefield Acceleration, LWFA). Cet objectif est rendu possible grâce à l'amplification par dérive de fréquence [13](*Chirped Pulse Amplification*, CPA, cf. Fig. 1.1), une technique qui a valu à ses inventeurs, G. Mourou et D. Strickland, le prix Nobel de physique en 2018.

Un laser à haute intensité produit un faisceau de lumière avec une densité de puissance suffisamment grande pour provoquer des effets significatifs sur la matière tels que l'ablation ou de l'ionisation de celle-ci. Les principaux paramètres qui déterminent l'intensité d'un laser sont son énergie E, sa durée d'impulsion τ et la surface sur laquelle il est focalisé (tache focale).

La puissance d'un laser peut être exprimée par $P = \frac{E}{\tau}$, où P est la puissance de l'impulsion. Dans les lasers à haute intensité, l'objectif est de concentrer l'énergie sur un temps très court et sur une zone très réduite pour atteindre une intensité extrêmement élevée, pouvant dépasser 10^{18} W/cm^2 et permettant ainsi certains mécanismes d'accélération de particules par laser tels que le LWFA pour les électrons ou le Target Normal Sheath Acceleration (TNSA) pour les ions.

Les lasers à haute intensité utilisent des systèmes à impulsions courtes, où l'énergie est délivrée sur des temps extrêmement courts (allant de la dizaine de femtosecondes à plusieurs nanosecondes). Cela permet d'obtenir une puissance de crête élevée (supérieur au TW), essentielle pour déclencher des effets non linéaires dans la matière, tels que l'ionisation (voir Sec. 3.2).

1.2 Accélération par intéraction laser-plasma

L'une des applications les plus prometteuses des lasers à haute intensité est l'accélération laser-plasma. L'interaction du laser avec le plasma crée des champs électriques intenses capables d'accélérer les particules à des vitesses relativistes sur de très courtes distances.

L'acceleration laser-plasma ouvre la possibilité à des dispositifs compacts et moins couteux, qui pourraient être complémentaires des accélérateurs de particules traditionnels dans de nombreuses applications, comme les traitements médicaux.

Plusieurs mécanismes d'accélération par laser sont cependant à distinguer. Nous nous focalisons ici sur les mécanismes d'accélération d'ions par laser.

1.2.1 Radiation Pressure Acceleration (RPA)

La Radiation Pressure Acceleration (RPA) [14,15] repose sur le transfert direct de la quantité de mouvement du laser vers une cible mince. La pression du laser pousse la cible dans son ensemble, accélérant les électrons qui par séparation de charge accélèrent les ions de manière quasi-monoénergétique. Ce mécanisme promet des rendements extrêmement élevés (plusieurs dixaines de pourcents) et des dispersions d'énergie étroites ($\pm$10 MeV) [16], à condition que l'impulsion laser ait un contraste temporel élevé et que la cible reste intacte pendant l'interaction.

1.2.2 Collisionless Shock Acceleration (CSA)

La Collisionless Shock Acceleration (CSA) [17] est un mécanisme où les ions sont accélérés à l'avant d'un choc électrostatique sans collision, typiquement dans un plasma surdense. Le choc électrostatique est généralement généré par un piston induit par la RPA se propageant dans le plasma surdense. L'onde de choc réfléchit des ions en amont, les accélérant ainsi à des vitesses égales à deux fois celle du choc. Ce processus repose fortement sur un profil de densité bien contrôlé avec des gradients importants et un contraste laser élevé pour assurer une formation stable du choc et une réflexion efficace.

1.2.3 Problèmes du CSA et du RPA

Malgré leurs caractéristiques attrayantes, le CSA et le RPA souffrent de limitations pratiques. Le CSA nécessite une adaptation précise du gradient de densité et est sensible aux effets de pré-impulsions qui peuvent détruire le profil souhaité. Le RPA est extrêmement sensible au contraste laser et à la qualité de la surface de la cible ; toute expansion précoce du plasma ou déformation de la cible peut dégrader significativement la qualité du faisceau d'ions. De plus, ces deux mécanismes fonctionnent généralement dans des conditions expérimentales exigeantes (controle du grandient de densité, du contrast laser, etc), ce qui limite la possibilité de développer des systèmes à fréquence de répétition élevée.

Étant donné ces contraintes, le Target Normal Sheath Acceleration (TNSA) offre une alternative plus robuste et facile à mettre en place.

1.2.4 Target Normal Sheath Acceleration

Le TNSA est l'un des mécanismes les plus étudiés pour l'accélération d'ions par laser. Ce phénomène se produit lorsqu'un laser de haute intensité (10^{18} W/cm^2 à plus de 10^{22} W/cm^2) interagit avec une cible solide. Lors de l'interaction laser-solide, le champ électrique du laser ionise la surface de la cible, créant un nuage dense d'électrons dans une région appelée « gaine » (représentée en bleu en Fig. 1.2). Le processus se déroule comme suit :

- **Interaction laser-plasma** : Lorsque la pré-impulsion du laser interagit avec la surface de la cible, elle crée un plasma dense. L'impulsion principale accélère les électrons dans la cible et vers la face arrière, générant un nuage d'électrons chauds, tandis que les ions plus lourds sont peu affectés.
- **Formation de la gaine** : La sortie des électrons énergétiques de la cible entraîne une séparation de charge entre les électrons et les ions, conduisant à la formation d'un champ électrique intense au niveau de la surface de la cible.
- **Accélération des ions** : Les champs électriques créés par la gaine accélérent les ions dans la direction normale à la cible. Les électrons ayant suffisamment d'énergie (de l'ordre du MeV) peuvent s'échapper du champ électrique.

Récemment, plusieurs travaux ont mis en évidence la capacité des installations laser de haute énergie à produire des faisceaux d'ions de haute qualité. Par exemple, sur les laser PETAL et

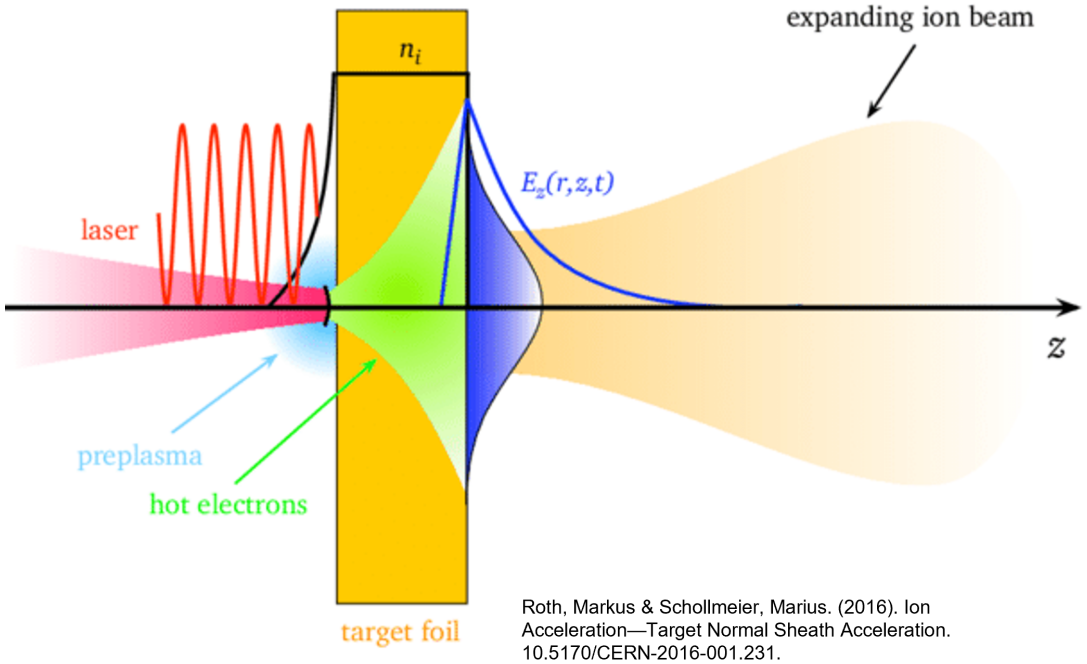

FIGURE 1.2 – Schéma du processus d'accélération par champ de gaine normale à la cible (TNSA). Reproduit de Roth, M., Schollmeier, M. (2013). "Ion acceleration : TNSA. In Laser-Plasma Interactions and Applications" [2]

LFEX, des impulsions de plusieurs centaines de femstoseconde jusqu'à plusieurs picosecondes et de plusieurs centaines de joules jusqu'au kilojoule permettent d'obtenir jusqu'à 10^{13} protons avec une énergie de coupure comprise entre 30 et 50 MeV [18, 19]. À l'inverse, les installations femtosecondes à basse énergie (quelques joules) produisent typiquement 10^{11} protons avec des énergies de coupure de 6 à 7 MeV, mais à des cadences beaucoup plus élevées de l'ordre de 0.5 Hz sur ALLS [20] par exemple. Ainsi, les lasers à haute énergie présentent un fort rendement énergétique mais une faible répétition (quelques tirs par jour), tandis que les systèmes à haute cadence offrent une productivité supérieure pour des applications nécessitant une source stable et répétitive.

L'objectif à long terme de ces recherches est de rendre les sources d'ions laser compétitives avec les accélérateurs conventionnels, notamment pour des applications médicales (thérapie par protons, production de radio-isotopes) grâce à leur compacité, leur coût réduit et leur flexibilité d'utilisation.

1.3 Cible hélicoïdale

Les cibles hélicoïdales ont suscité un intérêt croissant dans le domaine de l'accélération d'ions par laser, en particulier pour la post-accélération et la focalisation des protons. Pour surmonter les limitations du TNSA (énergie de coupure trop faible, grande dispersion angulaire, nombre de protons diminuant exponentiellement avec leur énergie cinétique), il a été proposé de propager les ions à travers une bobine hélicoïdale (HC) connectée électriquement à la cible, comme suggéré par

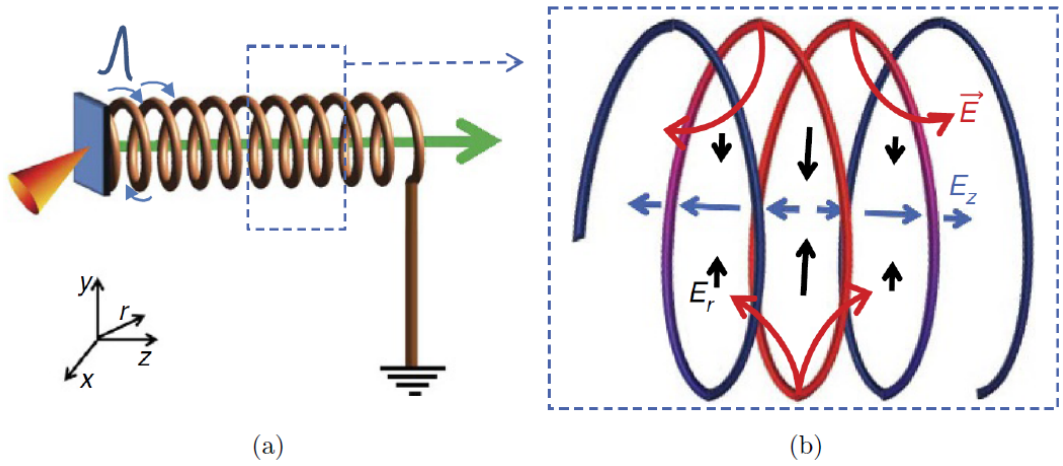

FIGURE 1.3 – Schéma de (a) une cible avec bobine hélicoïdale et (b) les champs électriques générés par la propagation du courant de décharge à l'intérieur de la bobine. Reproduit de S. Kar, H. Ahmed, R. Prasad, et al., « Guided post-acceleration of laser-driven ions by a miniature modular structure », *Nature Communications*, vol. 7, no. 1, pp. 1–7, 2016. [3]

S. Kar et al [3]. En effet, comme expliqué dans la section 2.2.4, lors de l'interaction laser-plasma, les électrons échappés de la gaine vont créer un défaut de charge dans la cible solide, qui se charge alors positivement, et qui, en se neutralisant, va engendrer un courant de décharge [4, 21, 22] qui se propage à travers la bobine, générant un champ électromagnétique capable de post-accélérer et de focaliser le faisceau de protons issu de la TNSA.

1.4 Objectifs de la Recherche et Structure du Manuscrit

Les objectifs de cette thèse sont la modélisation et l'optimisation des cibles hélicoïdales, avec le développement d'un modèle théorique analytique pour les cibles hélicoïdales et l'optimisation de leur géométrie pour obtenir des spectres de protons adaptés à des applications choisies. Dans un second temps, une validation expérimentale a été réalisée avec le laser ALLS (INRS-EMT, Varennes, Canada). Après la validation, nous avons exploré des régimes de puissance laser plus élevés pour étendre l'applicabilité des cibles hélicoïdales aux lasers plus puissants, comme LFEX (Institute of Laser Engineering, Osaka University, Japon), afin d'étudier l'accélération des ions dans les régimes TW (ALLS) et PW (LFEX). La dernière étape a été l'application des cibles hélicoïdales à la production de radioisotopes, le chauffage protonique isochore ou encore la production de neutrons. Durant cette thèse, un modèle analytique, des simulations Particle-in-Cell (PIC) et des expériences ont été réalisés pour fournir une étude complète et robuste.

La thèse est structurée en six chapitres comme suit :

Chapitre 3 : Contexte théorique général

Ce chapitre présente les mécanismes entrant en jeu lors de l'interaction laser-solide, responsable de l'ionisation de la matière. Ensuite, je décris les champs responsables de l'accélération par TNSA ainsi que la charge d'électrons échappés, principale source du courant de décharge récupéré par la cible hélicoïdale. Pour finir, je présente l'analogie des cibles hélicoïdales avec les tubes

à ondes progressives.

Chapitre 4 : Modélisation Théorique de la Propagation d'un Courant dans une Cible Hélicoïdale et avec l'écrantage d'un tube
Ce chapitre détaille le développement d'un modèle théorique analytique pour les cibles hélicoïdales. Le modèle décrit la propagation d'un courant pulsé dans la cible hélicoïdale, en se concentrant sur la génération de champs électriques et l'accélération des ions qui en résulte. Il inclut également l'optimisation, via la variation de la géométrie des cibles hélicoïdales, pour obtenir des spectres de protons spécifiques adaptés à différentes applications.

Chapitre 5 : Étude Expérimentale de l'Impact de la Cible Hélicoïdale sur les Protons et Carbones Accélérés par Laser
Ce chapitre se concentre sur la validation expérimentale des modèles théoriques et des simulations numériques. Une expérience a été réalisée avec des cibles hélicoïdales optimisées pour tester leurs performances dans le régime laser de 150 TW avec le laser ALLS. Les résultats significatifs sur les spectres de protons et de carbones, sont présentés et comparés à des simulations numériques.

Chapitre 6 : Production Améliorée de Radioisotopes en Utilisant une Cible Hélicoïdale avec Tube
Ce chapitre étudie l'application possible des cibles hélicoïdales pour la production de radio-isotopes médicaux, en se concentrant sur la sélection en énergie, grâce aux cibles hélicoïdales, des particules alpha générées par les réactions de fusion proton-bore.

Chapitre 7 : Autres applications intéressantes
Ce chapitre présente deux travaux en cours sur l'application des cibles hélicoïdales pour le chauffage protonique isochore et la production de neutrons. La démarche pour la production de neutrons est similaire à celle décrite au chapitre 6, où l'on cherche à sélectionner les protons en énergie afin d'augmenter la production de neutrons. Concernant le chauffage isochore, nous visons à modeler le spectre des protons afin d'optimiser le dépôt d'énergie dans la cible.

Chapitre 8 : Conclusions et Perspectives
Le dernier chapitre résume les résultats clés de la thèse, mettant en évidence les avantages des cibles hélicoïdales pour l'accélération des particules par laser dans différents régimes d'intensité laser. Le chapitre se termine par les applications possibles, y compris le chauffage isochorique des protons et la production de neutrons ou de radio-isotopes, et présente les perspectives pour

les travaux futurs.

Dans ce manuscrit, toutes les simulations présentées, à l'exception des simulations Monte-Carlo (Sec. 6 et 7), et tous les développements analytiques, hors état de l'art (Sec. 3), ont été réalisés par mes soins. De plus, mon implication expérimentale se situait au niveau du dimensionnement de l'expérience, du montage de cibles, de la participation au montage expérimental, de la réalisation des tirs et du traitement de données de la parabole de Thomson. L'idée d'étendre l'étude aux ions plus lourds comme les α et les ions carbones étaient aussi de mon fait. Bien entendu, la recherche est une discpline collaborative, et la contribution expérimentale d'Elias Catrix, de Simon Vallière, de Sylvain Fourmaux et de Didier Raffestin a été importante pour le bon déroulement de ces travaux. Tout comme l'implication de Vladimir Tikhonchuk sur le plan analytique et de Thomas Carrière et Ronan Lelièvre pour les simulations Monté-Carlo. Enfin, la supervision éclairée d'Emmanuel d'Humières, de Patrizio Antici et de Matthieu Bardon sur chacune de ces étapes a été indispensable.

Chapter 2

Introduction-English

Sommaire

2.1 Particle acceleration

Particle accelerators are experimental instruments that accelerate charged particles, such as electrons, protons, and ions, to speeds approaching the light velocity. The basic principle of particle accelerators relies on the use of electric fields to accelerate charged particles and magnetic fields to confine and direct them as desired. Major discoveries have been made, and applications, particularly in medicine, have emerged, such as cancer treatment, where they are used to precisely deliver high-energy radiation to tumors, a technique known as radiotherapy. Accelerators are also used to produce medical radioisotopes for imaging and diagnostics, such as fluorine-18, used in positron emission tomography (PET scans).

On another hand, high-intensity lasers are one of the most powerful tools used in modern physics. These lasers are able to deliver extremely high power to very small areas, allowing researchers to explore fundamental processes in matter and enabling a wide range of applications, such as laser-driven particle acceleration such as electron acceleration by wakefield, made possible through the use of ultra-short laser pulses which are able to produce extremely intense accelerator fields in the plasma (Laser Wakefield Acceleration, LWFA). This goal is permitted thanks to Chirped Pulse Amplification [13] (CPA), which saw its inventors, G. Mouroux and D. Strickland be awarded the Nobel Prize in physics in 2018.

A high-intensity laser is one that produces a beam of light with a power density large enough to cause significant effects on matter such as ablation or ionisation. The key factors in determining the intensity of a laser are its energy E, pulse duration τ, and the area over which it is focused (focal spot).

The power of a laser can be expressed as $P = \frac{E}{\tau}$ where P is the power of the pulse. For high-intensity lasers, the goal is typically to compress the energy in time and to focus it into a very small spot, creating extremely high intensity, which can reach intensities of 10^{18} W/cm^2 or more, which permit some laser-driven particle acceleration mechanisms such as LWFA for electrons or Target Normal Sheath Acceleration (TNSA) for ions.

High-intensity lasers use pulsed laser systems, where the energy is delivered in extremely short pulses (tenth of femtoseconds to nanosecond scale). When these pulses are focused, it results in a high peak intensity (above TW), which is critical for triggering nonlinear effects in matter. These effects can include phenomena such as ionization (see Sec. 3.2).

2.2 Laser-Plasma Acceleration

One of the most promising applications of high-intensity lasers is laser-plasma acceleration, a technique that uses high-power laser pulses to accelerate charged particles to very high energies. The laser pulse interacts with the plasma, creating strong electric fields that can accelerate particles to relativistic speeds in a very short distance.

Laser-plasma acceleration offers the potential for more compact and less expensive, which could complement traditional particle accelerators for many applications, such as medical treatments and radiation sources.

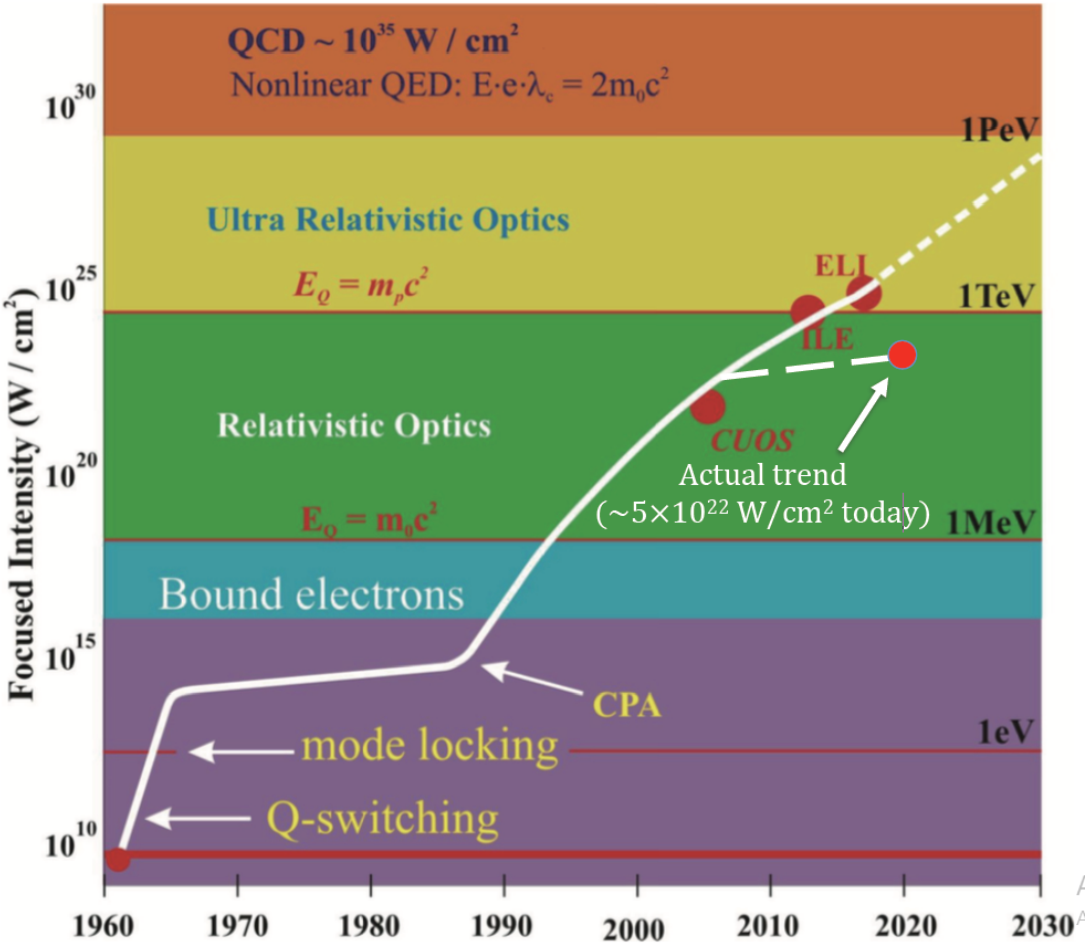

Figure 2.1 – The growing of laser intensities since its invention in 1960. This figure is extracted and adapted from G. A. Mourou, T. Tajima S. V. Bulanov, "Optics in the relativistic regime" [1]

In this PhD work we focused mainly on laser ion acceleration.

2.2.1 Radiation Pressure Acceleration (RPA)

Radiation Pressure Acceleration (RPA) [14,15] relies on the direct transfer of laser momentum to a thin target. The laser pressure pushes the front of the target, accelerating first electrons, and then due to the charge separation, ions in a nearly monochromatic manner. This mechanism promises extremely high yields (effectivness of severeal tenth of percents) and narrow energy spreads($\pm$10 MeV) [16], provided that the laser pulse has high temporal contrast and the target remains intact during the interaction.

2.2.2 Collisionless Shock Acceleration (CSA)

Collisionless Shock Acceleration (CSA) [17] is a mechanism where ions are accelerated at the front of an electrostatic shock without collision, typically in an overdense plasma. The electrostatic shock is typically driven by an RPA piston that propagates through the overdense plasma. The shock wave reflects ions upstream, accelerating them to speeds equal to twice the shock velocity. This process heavily relies on a well-controlled plasma profile with significant

gradients and high laser contrast to ensure stable shock formation and efficient ion reflection.

2.2.3 Issues of CSA and RPA

Despite their attractive features, CSA and RPA suffer from practical limitations. CSA requires precise adaptation of the density gradient and is sensitive to pre-pulse effects that can destroy the desired profile. RPA is highly sensitive to laser contrast and target surface quality; any early plasma expansion or target deformation can significantly degrade the beam quality. Furthermore, both mechanisms typically operate under demanding experimental conditions (gradient density control, laser contrast, etc) that are difficult to maintain in realistic environments or high-repetition-rate systems.

Given these constraints, **Target Normal Sheath Acceleration (TNSA)** offers a more robust and easier-to-implement alternative.

2.2.4 Target Normal Sheath Acceleration

Target Normal Sheath Acceleration (TNSA) is one of the most widely studied mechanisms of laser ion acceleration.

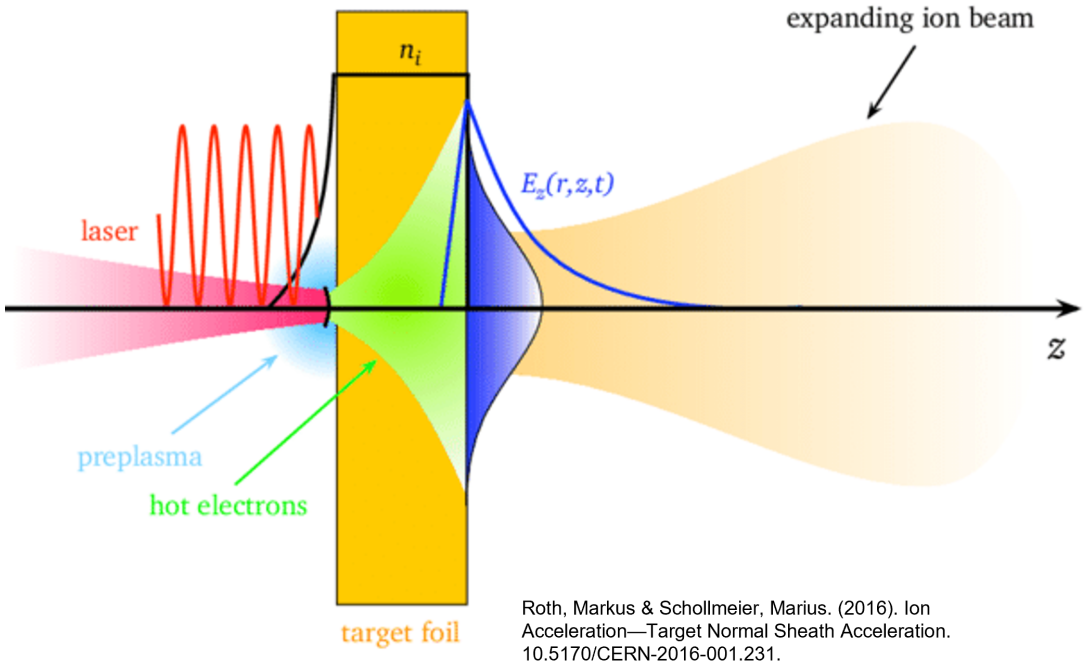

Figure 2.2 – Scheme of Target Normal Sheath Acceleration (TNSA) process. Reproduced from Roth, M., Schollmeier, M. (2013). "Ion acceleration: TNSA. In Laser-Plasma Interactions and Applications" [2]

This phenomenon occurs when a high-intensity (10^{18} W/cm^2 to above 10^{22} W/cm^2), short-pulse (picosecond) laser interacts with a solid target. Upon laser irradiation, the laser's electric field ionizes the target surface, creating a dense cloud of electrons and ions in a region known as the "sheath" (represented in bleu in Fig. 2.2). The key processes involved in TNSA are:

- **Laser-Plasma Interaction**: When the pre-pulse of the laser interacts with the surface of the target, it creates a dense plasma. The main pulse of the laser accelerates the electrons at the target's surface, creating a hot electron cloud, while the heavier ions remain mostly unaffected.
- **Sheath Formation**: The rapid acceleration of the electrons creates a charge separation between the electrons and the ions, leading to the formation of an intense electric field at the rear surface.
- **Acceleration of Ions**: The electric fields created by the sheath can accelerate ions in the target's normal direction (perpendicular to the surface), leading to high-energy ion acceleration. The ions are typically accelerated to energies of up to several MeV, depending on the laser intensity, the target material, and the experimental setup. The electrons with enough energy (above 1 MeV) can escape from the electric field.

Recent studies have highlighted the capability of high-energy laser facilities to generate high-quality ion beams. For instance, using multi-hundreds of femtosecond to multi-picoseconds, kilojoule-class lasers such as PETAL or LFEX, up to 10^{13} protons have been achieved with cutoff energies of 30–50 MeV [18, 19]. In contrast, femtosecond-scale systems delivering only a few joules typically produce 10^{11} protons with cutoff energies of 6–7 MeV but at a much higher repetition rate (up to 0.5 Hz on ALLS) [20]. High-energy lasers thus offer strong single-shot performance but low repetition rates (a few shots per day), whereas high-repetition systems enable greater stability and reproducibility.

Finally, the goal of this research field is to make laser-driven ion sources competitive with conventional accelerators, particularly for medical applications, by offering a more compact, cost-effective, and versatile alternative.

2.3 Helical coil

Helical targets have gained significant attention in the field of laser-driven particle acceleration, particularly for proton post-acceleration and focalization. To overcome the TNSA limitations (too low cutoff energy, high angular dispersion, number of protons exponentially decreasing with their kinetic energy) it was suggested to propagate the ions through a helical coil (HC) electrically connected to the target by S. Kar et al [3]. Indeed, as explained in Sec. 2.2.4, during the laser-plasma interaction, escaping electrons will create a charge default in the solid target, which then becomes positively charged and, as it neutralizes, it drives a discharge current pulse [4, 21, 22] that propagates through the helix, generating an electromagnetic field that post-accelerates and focuses the TNSA proton beam.

2.4 Research objectives and manuscript structure

The objectives of this thesis are the modeling and optimization of helical targets, the development of an analytical theoretical model for helical targets and the optimization of their

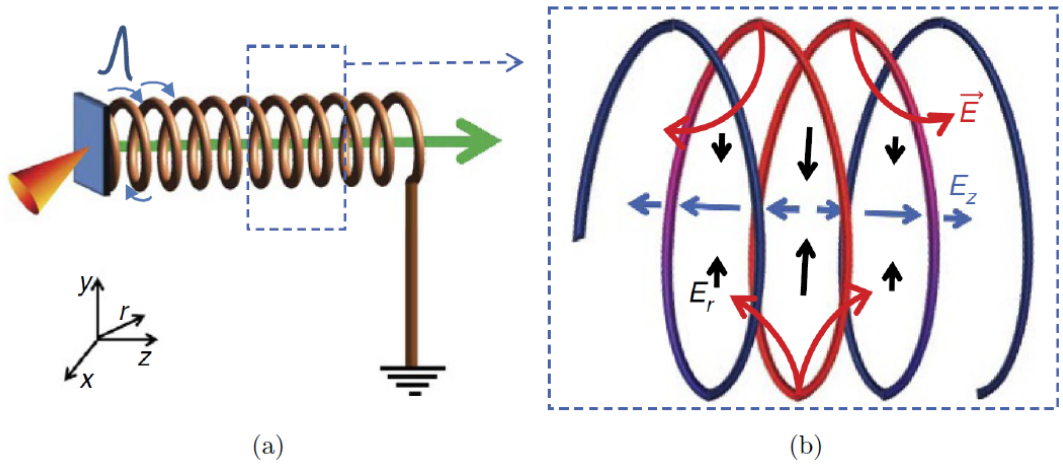

Figure 2.3 – Scheme of (a) a helical coil target and (b) the electric fields generated by the propagation of the discharge current inside the helix. Reproduced from S. Kar, H. Ahmed, R. Prasad, et al., « Guided post-acceleration of laser-driven ions by a miniature modular structure » [3]

geometry to achieve desired proton spectra tailored to specific applications. In a second step, an experimental validation was obtained with the ALLS laser (INRS-EMT, Varennes, Canada). After the validation, we explored higher laser power regimes to extend the applicability of helical targets to more powerful lasers, such as LFEX (Institute of Laser Engineering, Osaka University, Japan), to study ion acceleration in both TW (ALLS) and PW (LFEX) regimes. The final step, has been the investigation of the potential of helical targets for energy bunching for several applications such as radioisotope and neutron production or isochoric heating. This PhD develops an analytical model, Particle-in-Cell (PIC) simulations and lead experiments to provide a complete and robust study.

The thesis is structured into six chapters as follows:

Chapter 3: General theoretical context

This chapter presents the mechanism that come into play during the laser-solid interaction, responsible for the ionization of matter. Next, I describe the fields responsible for the acceleration by TNSA as well as the charge of escaped electrons, being the principal source of the discharge current recovered by the helical target. Finally, I present an analogy between helical targets and traveling wave tubes.

Chapter 4: Theoretical model of current propagation in a helical coil with varying geometry and screen tube

This chapter details the development of an analytical theoretical model for helical targets. The model describes the propagation of a pulsed current in the helical target, focusing on the generation of electric fields and the resulting acceleration of ions. It also includes optimization, via variation of helical target geometry, to obtain specific proton spectra suitable for different applications.

Chapter 5: Experimental Investigation of the Impact of Helical Coil on Laser-driven Protons and Ions

This chapter focuses on the experimental validation of the theoretical and numerical simulation models. Using the ALLS laser facility at INRS-EMT in Varennes, Canada, experiments were conducted with optimized helical targets to test their performance in the 150 TW laser regime. Significant results from these experiments, including proton and carbon spectra, are presented and compared to numerical simulations.

Chapter 6: Enhanced Radioisotope Production Using Helical Coil Target with Tube

Building on the results obtained in Chapter 3, this chapter investigates the potential applications of helical targets for medical radioisotope production. Specifically, the chapter focuses on energy bunching, thanks to the helical coil, of alpha particles generated through proton-boron fusion reactions. By selecting particles with specific energies, it becomes possible to optimize the reaction cross-section for producing desired radioisotopes, demonstrating a promising application of helical targets in nuclear medicine.

Chapitre 7 : Other Interesting applications

This chapter presents two ongoing studies on the application of helical targets for isochoric proton heating and neutron production. The approach for neutron production is similar to that described in Chapter 6, where the goal is to select the proton energy in order to enhance neutron yield. For isochoric heating, our objective is to shape the proton spectrum to optimize energy deposition in the target.

Chapter 8: Conclusions and Perspectives

The final chapter summarizes the key findings of the thesis, highlighting the advantages of helical targets for laser-driven particle acceleration across different regimes of laser intensity. The chapter concludes with potential applications, including proton isochoric heating and neutron or radioisotope production.

In this manuscript, all simulations presented, except for the Monte Carlo simulations (Sec. 6 and 7), as well as all analytical developments, excluding the state-of-the-art review (Sec. 3), were carried out by myself. In addition, my experimental involvement included the design of the experiment, target preparation, participation in the experimental setup, execution of laser shots, and data analysis from the Thomson parabola spectrometer. The idea of extending the study

to heavier ions, such as α particles and carbon ions, also originated from my own initiative. Of course, research is a collaborative work, and the experimental contributions of Elias Catrix, Simon Vallières, Sylvain Fourmaux, and Didier Raffestin were essential to the successful completion of this work. Likewise, the investment of Vladimir Tikhonchuk for the analytical work and the Monte Carlo simulations performed by Thomas Carrière and Ronan Lelièvre were of great importance. Finally, the insightful supervision of Emmanuel d'Humières, Patrizio Antici, and Matthieu Bardon at every stage of this project was indispensable.

Chapter 3

General theoretical context

Sommaire

3.1 Introduction

To gain a clear, step-by-step understanding of the ion acceleration process, it is necessary to introduce some theoretical background. The Target Normal Sheath Acceleration (TNSA) mechanism involves several distinct physical phenomena. First, a high-intensity laser pulse is typically composed of a low-intensity pre-pulse, followed by the main pulse. For sufficiently intense laser systems, the pre-pulse carries enough energy to ionise the solid target upon interaction. This is why, in Section 3.2, we present the Keldysh ionisation model, which explains how the laser interacts with the solid target to produce a plasma.

Secondly, the main laser pulse accelerates electrons, which in turn generate strong electrostatic fields capable of accelerating protons. The associated fields and the various processes involved are described in Section 3.3.

Finally, in Section 3.4, we introduce the concept of Travelling Wave Tubes (TWT), due to their analogy with our helical coil targets. The underlying physics governing both systems is remarkably similar, and this comparison provides useful insights for the interpretation of our results.

3.2 Keldysh Ionization Model

In this chapter, we present the basic equations of the Keldysh model for the target ionization in the presence of a strong laser field [23]. The model, developed by the Soviet physicist Igor Keldysh in 1965, is widely used to describe the ionization of atoms or molecules by strong electromagnetic fields.

The ionization process in the presence of an intense laser field can be categorized into two distinct regimes: the multiphoton ionization regime and the tunnel ionization regime. The transition between these two regimes is determined by the so-called *Keldysh parameter* γ, which is a dimensionless quantity that depends on the laser field strength, the atomic binding energy, and the photon energy.

3.2.1 Phenomenology of the two ionization processes

In the TNSA experiments, the laser is focused onto a target that is initially in a solid state. Upon irradiation, the intense laser field ionizes the atoms composing the target, leading to the formation of a plasma. Two primary ionization mechanisms can occur simultaneously.

The first is the multiphoton ionization [24], in which a bound electron absorbs multiple photons simultaneously, gaining enough energy to escape from the atomic potential. This process operates at low laser intensities.

The second mechanism is the tunnel ionization [25], where the electric field of the laser is sufficiently strong to distort the Coulomb potential seen by the atomic electrons. As a result, the potential barrier becomes narrow enough for the electron to quantum-mechanically tunnel through it. When the laser field becomes so intense that the barrier is completely suppressed

below the binding energy of the electron, the process transitions into what is known as the Over-the-Barrier Ionization (OBI) [26].

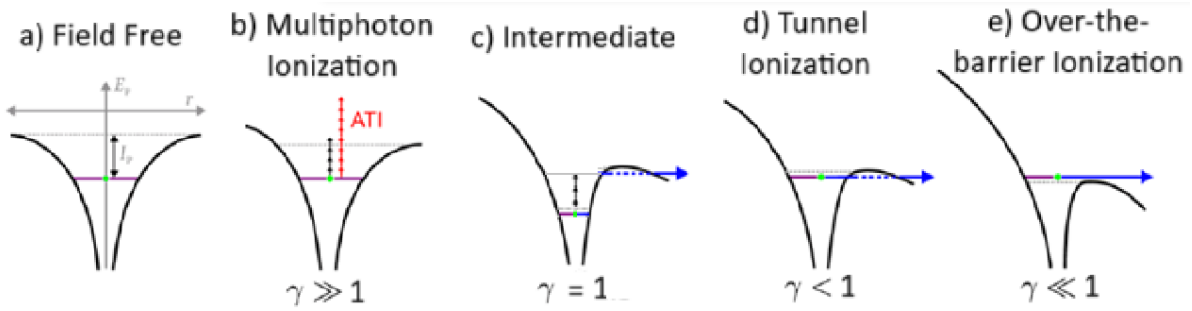

Figure 3.1 – Overview of different process of ionization explained thanks to Keldysh's theory

These ionization processes are schematically illustrated in Fig. 3.1. Other ionization mechanisms exist, such as the Above-threshold-ionization (ATI) or the double ionization [27] which correspond to an intermediate ionization mechanism between multiphoton ionization and tunnel ionization, but we will not discuss it in this theoretical introduction.

3.2.2 Computation of Ionization Rate

To be separated from the atom, the electrons must acquire in the laser field an energy E_{ion}, the energy of ionization. In the tunnel ionization case, it is given by:

$$E_{ion} = eE_{\text{laser}} l_{\text{tunnel}} = \frac{1}{2} m_e \langle v_e \rangle^2, \tag{1.1.13}$$

where E_{laser} is the electric field of the laser, l_{tunnel} the characteristic length (as the order of the Bohr radius) that the electron must cross by tunneling through the potential barrier modified by the laser field, and m_e and $\langle v_e \rangle$ are respectively the electron mass and electron average velocity.

The tunnel frequency, which is the characteristic frequency associated with the tunnel ionization process, is given by:

$$\nu_{\text{tunnel}} = \frac{\langle v_e \rangle}{l_{\text{tunnel}}} = eE_{\text{laser}} \sqrt{2/m_e E_{ion}}. \tag{1.1.14}$$

We can also define the Keldysh parameter γ as:

$$\gamma = \frac{2\omega_L}{\nu_{\text{tunnel}}} = \frac{\omega_L \sqrt{2 m_e E_{ion}}}{eE_{laser}} = \sqrt{\frac{E_{ion}}{\Phi_p}},$$

with, $\Phi_p = \frac{e^2}{4\pi^2 m_e \epsilon_0 c^3} I\lambda^2$ the ponderomotive potential, where I and ω_L are respectively the laser intensity and frequency, λ is the wavelength of the laser, $n = \frac{E_{ion} + 0.5\Phi_p}{\hbar\omega_L} + 1$ is the number of photons required to ionize the atom. .

The Keldysh parameter γ is the ratio of the binding energy of the electron to the ponderomotive energy provided by the laser field. When $\gamma \ll 1$, the binding energy is insufficient to keep the electron bound to the atom, and ionization occurs through tunneling.

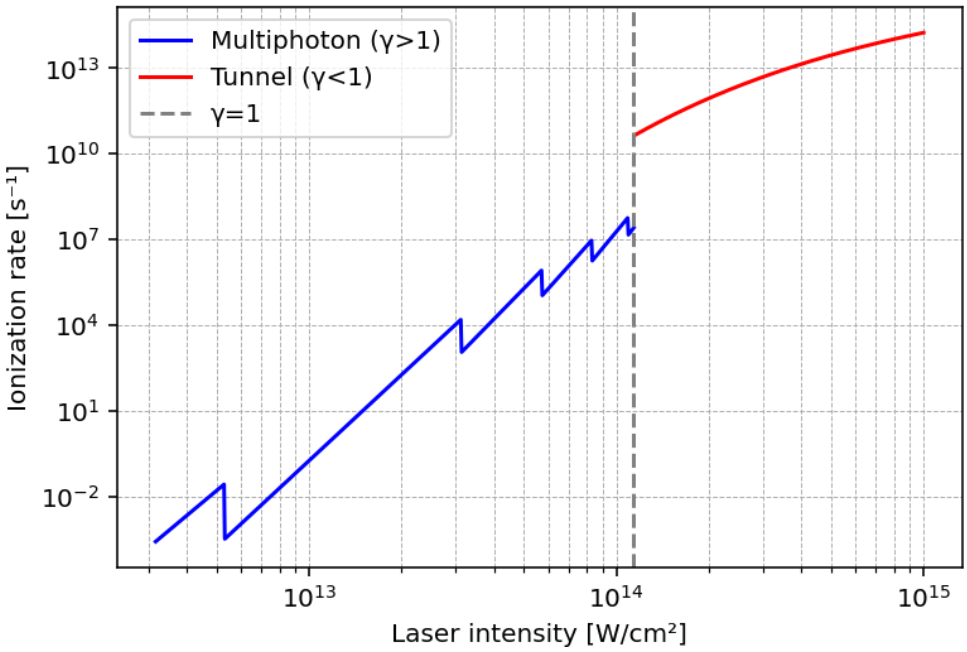

Figure 3.2 – Ionization rate of multiphoton ionization and tunnel ionization as function of laser intensity.

Thanks to this computation, the ionization rates W can be expressed in asymptotic forms in the limits of large or small γ. These asymptotic forms are particularly useful because an exact analytic expression for the full ionization rate is generally too complicated. One gets the ionization rates of the multiphoton ionization for $\gamma \gg 1$:

$$W_{\gamma \gg 1} = \omega \left(\frac{E_{ion}}{\hbar \omega} \right)^{1/2} (2\gamma)^{-2n} \tag{3.2.1}$$

One can also get the tunnel ionization rate for $\gamma \ll 1$:

$$W_{\gamma \ll 1} = \frac{\sqrt{3\pi}}{4} \frac{E_{ion}}{\hbar} \left(\frac{E_{ion}\gamma}{\hbar \omega} \right)^{-1/2} \exp\left(-\frac{4}{3} \frac{E_{ion}\gamma}{\hbar \omega} \right) \tag{3.2.2}$$

.

For $\gamma \gg 1$ (laser energy lower than ionization energy threshold), the prevailing ionization process is the multiphoton ionization. The number of photons required to ionize the atom n is proportional to the energy required to overcome the ionization potential divided by the photon energy. If $\gamma \ll 1$, the ionization is primarily due to the tunneling ionization process (see Fig. 3.2 which presents the ionization rate for hydrogen atom).

3.2.3 Conclusion on Keldysh Model

The Keldysh model provides a framework for understanding the ionization of atoms in strong laser fields. The transition between the tunnel and multiphoton ionization regimes is determined by the Keldysh parameter (see Fig. 3.1 which summarizes it), which depends on both the laser

field strength and the atomic properties. By applying the Keldysh model, one can predict the ionization rate and better understand the interaction between intense laser fields and matter.

This model is the basis for understanding laser based matter ionization and therefore for all the laser-matter applications, such as particle acceleration. In the case of high intensity lasers that we will consider during this thesis, this ionization takes place mainly during the interaction of the target and the pre-pulse of the laser, before the main pulse which is greater than 10^{18} W/cm^2.

3.3 Target Normal Sheath Acceleration

The TNSA mechanism arises when a high-intensity laser pulse (intensity above 10^{18} W/cm^2 and a time of pulse sub-picoseconds) is focused on a solid target [28, 29]. The pre-pulse of the laser ionizes the material, creating an electron population that is accelerated by the main-pulse of the laser [30–32]. These hot electrons then form a sheath at the rear surface of the target, which acts as an electrostatic field that accelerates ions. The acceleration of ions is in the direction normal to the target surface, hence the name "Target Normal Sheath Acceleration." The energy gained by the ion is mainly determined by the electrostatic potential created by the hot electrons at the rear surface. The ion energy E_i in the TNSA regime can be expressed as:

$$E_i = -\int_0^{d_{sheath}} Ze\nabla\phi_{th},$$

where, Z is the atomic number of the target material, e is the elementary charge, ϕ_{th} is the electric potential created by the hot electron sheath (as the order of the hot electron energy) and d_{sheath} is the acceleration length.

The electric field linked to the potential ϕ_{th} is initially on the order of a few TeV/m and the acceleration length d_{sheath} is on the order of tens of microns to a hundred ($d_{sheath} \sim c/\omega_{pe}$ with $\omega_{pe} = \sqrt{(n_{e_0}e^2/m_e\epsilon_0)}$ the electron plasma frequency, is defined by the density of hot electrons and should be sufficiently short for ions be accelerated during the hot electron lifetime, a few ps), depending on the laser intensity and target properties. This permits to get an estimation of ion energy of tens of MeV.

3.3.1 Electron heating

During the Target Normal Sheath Acceleration (TNSA) process, the interaction of an ultra-intense laser pulse with a solid target leads to the acceleration of a large number of electrons. Several mechanisms contribute to the heating of these electrons: Brunel heating (also known as vacuum heating) [33], the anomalous skin effect [34,35], resonance absorption [36,37], sheath inverse bremsstrahlung absorption [38], stochastic heating by counter-propagating electromagnetic waves [39–41], and $\mathbf{J} \times \mathbf{B}$ heating [42,43].

For laser intensities exceeding 10^{18} W/cm^2, the dominant mechanism is $\mathbf{J} \times \mathbf{B}$ heating. This regime arises when the plasma density is higher than the critical density, preventing the laser

from propagating further than the skin depth. Therefore, the interaction between the laser and the plasma is limited to the surface.

In this context, the magnetic part of the Lorentz force, $\mathbf{v} \times \mathbf{B}$, becomes significant, which is characteristic of relativistic laser intensities. Initially, electrons are accelerated transversely by the electric field of the laser. Simultaneously, the magnetic component of the laser field induces a longitudinal momentum. Since the laser cannot penetrate beyond the overdense plasma surface, the electrons are not reflected back by the magnetic field and instead are injected into the target bulk with the energy acquired during the interaction.

Electrons accelerated through this process follow a thermal distribution [44] and exhibit a semi-angle divergence about fifty degrees [45], mainly due to the Weibel instability [46]. These electrons form an intense current [47] of few tens of kA. The resulting charge separation induces an electrostatic field $E_{th} = -\nabla\phi_{th}$ that slows down lower-energy electrons. Nevertheless, the most energetic ones can traverse the target and escape through the rear side, provided the target is sufficiently thin (a few microns or less).

The energy spectrum of electrons generated via $\mathbf{J} \times \mathbf{B}$ heating follows an exponential profile, and their effective temperature is given by [47]:

$$T_e^{\mathbf{v}\times\mathbf{B}} = \left(\sqrt{1 + \frac{a_0^2}{2}} - 1\right) m_e c^2, \tag{3.3.1}$$

where a_0 is the normalized vector potential of the laser. This corresponds to temperatures ranging from a few to several tens of MeV, depending on the laser intensity.

3.3.2 Sheath Formation

To describe the potential, ϕ_{th} created by the sheath, we use the Poisson equation, the Boltzmann distribution function for the electron density and we consider that the ions are trapped in the solid target (it correspond to a Heaviside function distribution $n_i = n_c H(x)$, where $x = 0$ defines the target surface):

$$\epsilon_0 \Delta\phi_{\text{th}} = e\left[n_i - n_c \exp\left(\frac{e\phi_{\text{th}}}{T_h}\right)\right]$$

where e is the electron charge, ϵ_0 is the vacuum dielectric permittivity, $n_c = \epsilon_0 m_e \omega_L^2 / e^2$ the critical density and T_h the hot electron temperature. This hypothesis is valid as long as the characteristic scale of the ion density is smaller than the hot electron Debye length.

This equation has a divergent solution for the potential in one dimension. A. Poye et al [4,31] present a method to determine the potential barrier ϕ_{th}, which is convergent inside and outside the target. Unlike the ion acceleration problem, where only the electric field at the surface matters, the problem of electron escape requires knowledge of the whole potential profile. In the one-dimensional model, we obtain the following electron density distribution:

$$n_e(x) = \begin{cases} n_c \exp\left(-\exp\left(-\frac{\xi x}{\lambda_D}\right)\right), & x > 0 \\ n_c \left(\exp(0.5) - \frac{x}{\lambda_D}\right)^{-2}, & x < 0 \end{cases}$$

where $\lambda_D = \frac{\epsilon_0 T_h}{n_c e^2}$ is the hot electron Debye length and $x = 0$ define the target surface, $x < 0$ is the sheath and $x > 0$ is the plasma as represented in Fig. 3.3. The coefficient $\xi = 0.9288$ is calculated to conserve electroneutrality.

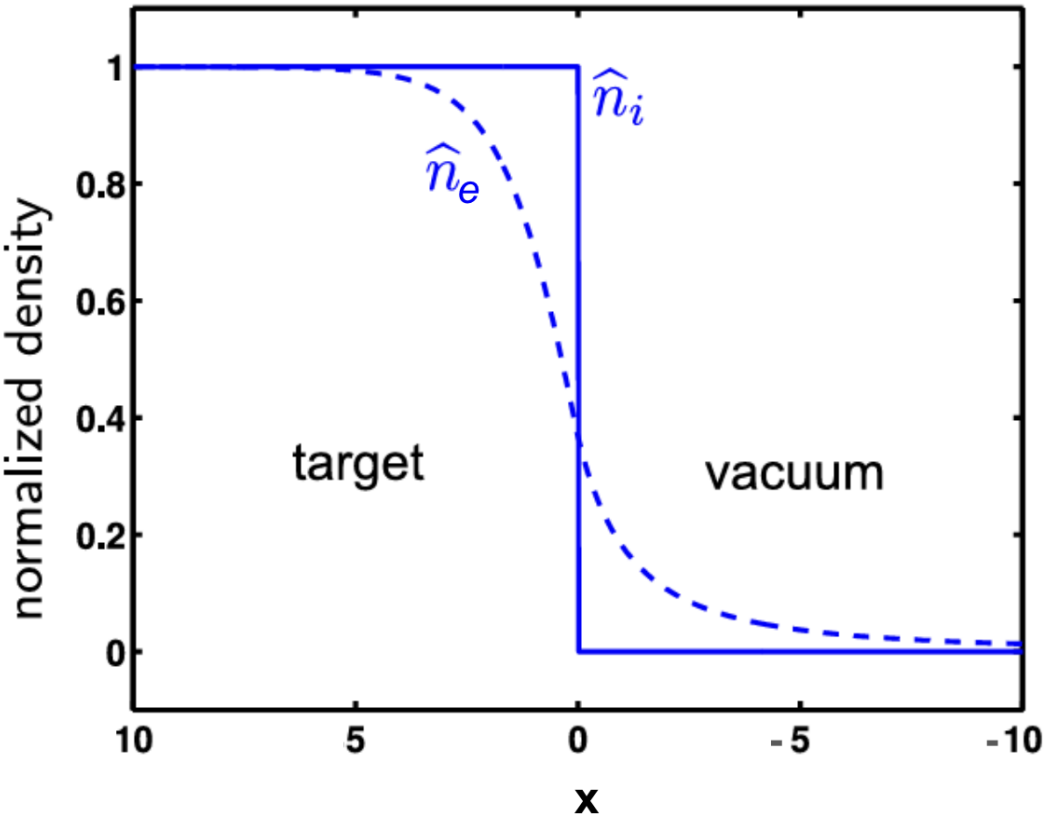

Figure 3.3 – Normalized electron density $\hat{n}_e$ and ion density $\hat{n}_i$ as function of the x axis where $x = 0$ represent the rear surface of the solid target [4]

The potential $\phi_{th}(r, x)$ obtained is finally:

$$\phi_{\text{th}}(r, x) = \frac{e}{4\pi\varepsilon_0} \int \frac{[n_i(x') - n_e(x')]\, dx' r' dr' d\theta}{\sqrt{(x - x')^2 + r^2 + r'^2 - 2rr' \cos\theta}}. \tag{3.3.2}$$

where one particle of cylindrical coordinates (x', y') create the potential in cylindrical coordinates (x, y). This strong potential is due to the charge separation, and is responsible for the ion acceleration.

3.3.3 Ion acceleration

The field computation previously presented in Sec. 3.3.2 has been developed by Wilks *et al.* [29] and Mora [31]. In this section, we will present some scaling laws which have been

experimentally validated by Snavely *et al.* [28] and Fuchs *et al.* [48].

The maximum energy E_{max} of the accelerated ions in the TNSA regime can be expressed as a function of the hot electron temperature T_h and a normalized acceleration duration t_p:

$$E_{max} = 2T_h \left[\ln\left(t_p + \sqrt{t_p^2 + 1}\right)\right]^2, \tag{3.3.3}$$

where $t_p = \omega_{pi}\tau_{acc}/\sqrt{2e}$, and $\omega_{pi} = \sqrt{Z_i e^2 n_{e0}/m_i \varepsilon_0}$ is the ion plasma frequency, with Z_i the ion charge state, n_{e0} the hot electron density at the rear surface, and τ_{acc} the effective acceleration time. Fuchs *et al.* [48] empirically found $\tau_{acc} \simeq 1.3\tau_{laser}$ where τ_{laser} is the pulse duration of the laser pulse.

The temperature of the hot electrons can be estimated using the relativistic ponderomotive scaling law introduced by Wilks *et al.* [29]:

$$T_h = m_e c^2 \left(\sqrt{1 + \frac{I\lambda^2[\mu\mathrm{m}^2]}{1.37 \times 10^{18}\ \mathrm{W\,cm^{-2}}}} - 1\right), \tag{3.3.4}$$

where I is the laser intensity and λ its wavelength.

The total number of hot electrons contributing to the sheath field is estimated by:

$$N_e = \frac{f_e E_{laser}}{T_h}, \tag{3.3.5}$$

with E_{laser} the laser pulse energy and f_e the fraction of absorbed laser energy, which follows the empirical scaling law

$$f_e = 1.2 \times 10^{-15} I^{0.74} \tag{3.3.6}$$

with I in W.cm^{-2} [48]. Typically, f_e ranges from 10% to 40% in the TNSA regime.

The hot electrons interact with the ions in a volume $V = c\tau_{laser} S_{sheath}$, where S_{sheath} denotes the sheath surface area at the rear side, approximated as:

$$S_{sheath} = \pi \left(r_0 + d\tan\theta\right)^2, \tag{3.3.7}$$

with r_0 the laser focal spot radius, d the target thickness, and θ the divergence angle of the electron beam.

This gives access to the hot electron density n_{e0}, enabling the use of the analytical model of Mora [31] to derive the ion energy spectrum:

$$\frac{dN}{dE} = \left(\frac{n_{e0} c_s \tau_{acc} S_{sheath}}{\sqrt{2ET_h}}\right) \exp\left(-\sqrt{\frac{2E}{T_h}}\right), \tag{3.3.8}$$

where $c_s = \sqrt{Z_i k_B T_h/m_i}$ is the ion acoustic velocity.

This model reproduces the experimentally observed features of TNSA-accelerated ion beams:

a Maxwellian-like energy spectrum with a high-energy cut-off typically ranging from a few to tens of MeV, depending on the laser intensity and pulse duration [28, 29, 48, 49].

3.3.4 Ejected Electron Charge

The electron dynamics is due to the interaction of the laser pulse with the target surface, it accelerates electrons and propels them into the material. As these electrons penetrate the target, they gradually lose energy, and exit the target if it is thin enough, leading to the formation of an electric potential at the target surface. This potential acts as a barrier that accelerated electrons must surpass in order to escape entirely [50]. The charge left behind on the target is determined by the number of electrons that successfully escape [4].

A key element in this model is the estimation of the potential barrier, which ultimately dictates the maximum number of escaping electrons. The primary contribution to this barrier arises from the electron sheath potential, ϕ_{th}, as described in Sec. 3.3.2. High-energy electrons that possess sufficient energy can overcome this barrier and leave the target.

To determine the target charge after laser irradiation, we now integrate the various components of the model. Considering the normalized potential barrier ϕ_{th} computed in eq. 3.3.2, the electron temperature T_h and the total number of hot electrons N_e respectively given from the scaling law eq. 3.3.4 and eq. 3.3.5 and the electron distribution, according to the Maxwell-Jüttner distribution :

$$f_e(\varepsilon_e) = \frac{\gamma p}{\mathcal{A}} \exp\left(-\frac{\varepsilon_e}{T_h}\right), \tag{3.3.9}$$

where ε_e is the electron kinetic energy, γ the relativist factor, p the electron momentum and $\mathcal{A}$ is the normalization factor such that $\int_0^\infty f_e(\varepsilon_e)d\varepsilon_e = 1$. One can directly evaluate the total charge that successfully escapes beyond the potential barrier :

$$Q_{th} = eN_e \int_{e\Delta\phi_{th}}^{\infty} f_e(\varepsilon_e)d\varepsilon_e \tag{3.3.10}$$

However, the residual positive charge on the target surface subsequently produces a global background potential, ϕ_{bg}, which extends across the target surface. This positive charge distributes across the entire target surface, introducing a target size-dependent effect. For infinitely large or sufficiently extended targets, the background potential remains negligible because the surface charge density is low. Conversely, for smaller targets, the charge becomes more concentrated at the surface, leading to the development of a significant background potential, which may surpass the potential barrier. To assess the influence of the background potential on the target charge, we consider the surface charge to be homogeneously distributed over a disk of time-dependent radius $R_p(t', t)$, where t' is the time $t - dt$ and t the observation time. The disk radius evolves according to:

$$R_p(t', t) = R_h(t') + c(t - t'), \qquad \text{with } 0 < t' < t, \tag{3.3.11}$$

where $R_h(t')$ is the hot electron emission spot radius at the time of ejection and c the speed of light. The hot electron current is then defined as the flux of electrons with sufficient energy and appropriate direction, crossing the surface πR_h^2. It is given by:

$$J_h(t) = e f_\beta n_h(t) \pi R_h^2(t) \int_{|e\Delta\phi(t)|}^{+\infty} f_e(\varepsilon_e) v(\varepsilon_e)\, d\varepsilon_e, \tag{3.3.12}$$

where $f_e(\varepsilon_e)$ is the electron energy distribution (cf. Eq. (3.3.9)) and $v(\varepsilon_e)$ the corresponding electron velocity and assuming an ejection cone of half-angle β, we define the geometric factor $f_\beta = \frac{1-\cos\beta}{2}$. Thanks to this, one gets the electrostatic background potential:

$$\phi_{bg}(t,x) = \int_0^t dt' \, \frac{J_h(t')}{2\pi\epsilon_0 R_p^2(t',t)} \left(R_p^2(t',t) + x^2 - |x|\right). \tag{3.3.13}$$

Finally, the effective potential reads:

$$\Delta\phi(t) = \phi_{th}(t, x=0) + \phi_{bg}(t, x=0) - \min\left\{\phi_{bg}(t, x_{\min}) + \phi_{\mathrm{th}}(t, x_{\min}), 0\right\}, \tag{3.3.14}$$

and therefore, we are able to compute Q the total ejected electron charge :

$$Q = eN_e \int_{e\Delta\phi}^{\infty} f_e(\varepsilon_e) d\varepsilon_e \tag{3.3.15}$$

This ejection of electronsof several hundreds of nC is responsible for a discharge current of several kA that we will retrieve thanks to our helical coil and create a secondary electromagnetic field of GV/m presented in Chap. 4 which in turn will post-accelerate and focus protons. In previous articles [4,22,50], this discharge current is described as the neutralisation of the missing charge in the target himself due to the electron emission. The electrons emitted during the TNSA process must be distinguished from the electrons in the sheath described in Sec. 3.3.2. While the sheath electrons are responsible for proton acceleration, the emitted electrons are those with enough energy to escape the sheath potential given in Eq. 3.3.2.

3.4 Traveling Wave Tubes

Traveling Wave Tubes (TWTs), are vacuum electron devices belonging to the same family as klystrons and carcinotrons. They address two major needs in telecommunications: wide operational bandwidth and access to very high frequencies. Due to their robustness, high electrical efficiency and compactness, TWTs are the main radio-frequency (RF) amplifiers used in space telecommunications [51–53].

They are composed of an electron gun (such as presented in Sec.3.4.1) that injects a beam used to amplify the signal, a periodic waveguide known as a slow-wave structure (as presented in Sec.3.4.2) or delay line, through which the RF signals propagate, and a collector that captures the electrons exiting the tube. A schematic of a standard TWT is shown in Figure 3.4.

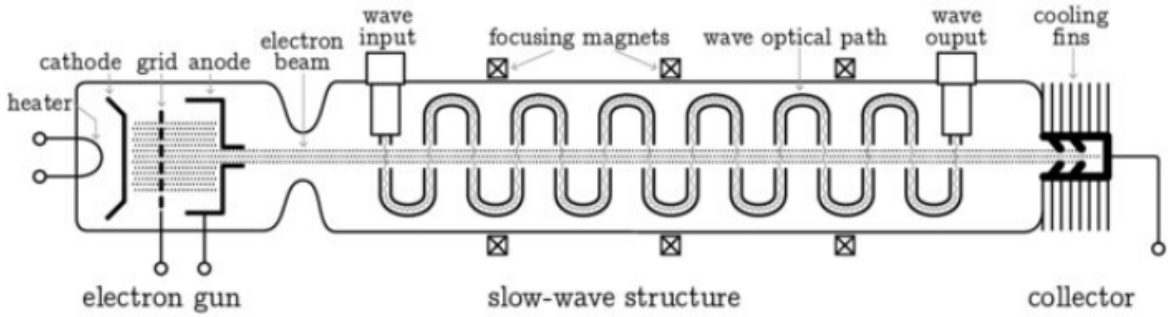

Figure 3.4 – Schematic of the main components of a TWT where the oscillating pipe represent the slow wave structure which is an helix, and the grey lines represent the electron beam. This structure is longer than helical coils, about hundreds of centimetres compare to tenth of millimetres for helical coils, however, the pitch and the radius are the same.

In the helical coil target considered in this manuscript, the electron gun is replaced by the protons accelerated by TNSA, the slow waves structure is replaced by a helical coil and the current that propagates through the coil is produced by the electrons escaped from the target during TNSA. This is why, in Sec.3.4.1 we introduce the electron gun and in Sec.3.4.2 the slow wave structure. However, for the helical coil targets, the objective is to use the electromagnetic fields to post-accelerate and focus protons while for TWT, these are the particles (electrons) which give energy to the field.

3.4.1 Electron Gun

The electron gun injects a uniform, mono-energetic, and focused electron beam along the tube axis. Most TWTs use Pierce-type guns vacuum diodes composed of a cathode (emission), an anode (acceleration), and a focusing electrode (beam shaping). The beam, accelerated by the anode-cathode voltage V_0, generally has a current density insufficient for amplification [54], and diverges due to space-charge effects. Focusing electrodes optimize the beam cross-section at the exit, increasing current density, though this is limited by electron trajectory crossing, with area ratios rarely exceeding 100 [52, 55].

The beam shape depend on the slow-wave line geometry, commonly cylindrical ($a_\mathrm{b} \sim a/3$, where a_b and a are respectively the radii of the electron beam and the slow wave structure), but may also be rectangular (e.g., folded waveguides). More complex guns (e.g., multi-beam [56], pulsed [57]) are also used.

One can assume a uniform, mono-energetic beam traveling at a velocity

$$v_0 = \sqrt{2|e|V_0/m_e}, \tag{3.4.1}$$

with e the electron charge and m_e its mass. Yet, due to space-charge and dimensional reduction, the effective velocity seen by RF waves is slightly lower.

3.4.2 Slow-Wave Structure

Before describing the amplification mechanism in a TWT, it is important to note that wave-particle interaction requires synchronism: the electron beam velocity must match the wave phase velocity. Since reaching relativistic speeds is costly, the phase velocity of the wave is reduced using a slow-wave structure (SWS), which:

- guides electromagnetic waves along the tube,
- slows them down so that $v_\varphi \approx v_0$ where v_ϕ is the axial phase velocity of the electromagnetic waves and v_0 is the electron velocity.

In vacuum tubes like TWTs, this slowing is achieved by introducing periodic metallic structures. Common SWS types include helices, coupled cavities, and folded waveguides each exhibiting periodicity along the axis.

The most widely used structure is the helical SWS, especially in space applications. It consists of a metalic helix (copper or tungsten) supported by dielectric rods. Key geometric parameters include the pitch h, tunnel radius a, and wire thickness a_c, with $a/a_c \gg 1$.

The helical structure supports many propagation modes, but only the fundamental ($m = 0$) interacts with the beam. It has a wave vector k and a dispersion relation $\omega(k)$. For example, the relation dispersion for a single helix [58] is given by:

$$\omega^2 = k^2 c^2 \left(1 + \cot^2 \Psi \, \frac{I_1(\alpha a) K_1(\alpha a)}{I_0(\alpha a) K_0(\alpha a)}\right)^{-1} . \tag{3.4.2}$$

and for a travelling wave tube [59] it is given by:

$$\omega^2 = k^2 c^2 \left(1 + \cot^2 \Psi \, \frac{I_1(\alpha a) I_0(\alpha b) \left(K_1(\alpha b) I_1(\alpha a) - I_1(\alpha b) K_1(\alpha a)\right)}{I_0(\alpha a) I_1(\alpha b) \left(K_0(\alpha b) I_0(\alpha a) - I_0(\alpha b) K_0(\alpha a)\right)}\right)^{-1} . \tag{3.4.3}$$

where $\alpha(\omega) = \sqrt{k^2 - \omega^2/c^2}$ is the radial propagation constant, b is the radius of the tube and I_n and K_n are respectively the modified Bessel functions of order n of first and second kind. These dispersion relations will be used to validate our equations of helical coil target in Chap. 4, which demonstrate the analogy presented in this chapter between TWT and helical coil target.

A major advantage of the helix is its low dispersion. The axial phase velocity is approximately

$$v_\varphi = c \sin(\Psi) , \tag{3.4.4}$$

with the helix angle $\Psi = \arctan\left(\frac{h}{2\pi a}\right)$. This allows synchronization over a wide frequency range, by decreasing the propagation velocity of the current along the helix axis to match to the electron velocity , enabling amplification over up to three octaves [60]. However, helical structures sustain lower RF voltage and power than coupled cavities, which are preferred for high-power, narrowband applications.

Another key parameter is the interaction impedance Z_c, which quantifies the coupling between

the axial electric field and the beam:

$$Z_c = \frac{|E_z|^2}{2k^2 P}. \tag{3.4.5}$$

To interpret this, we compute the axial electric field as function of the voltage V and consider a Fourrier space ($\partial_z = -ik$):

$$E_z = -\partial_z V = ikV, \tag{3.4.6}$$

and relate the RF power to this voltage and an equivalent current I:

$$P = \frac{1}{2}|VI| = \left|\frac{-i}{2}\frac{E_z}{k}I\right| = \frac{|E_z|^2}{2k^2 Z_c}. \tag{3.4.7}$$

The helical slow-wave structure, central to the energy transfer in TWTs, finds a direct analogy in helical coil targets used in laser-driven ion acceleration. While TWTs inject energy into RF waves and slow down electrons in the beam, helical coil targets can retrieve the return discharge current produced during the TNSA process (see Chap. 4) to generate similar RF fields to post-accelerate, energy bunch and focus ions.

3.5 Conclusion

While Target Normal Sheath Acceleration (TNSA) remains a robust and experimentally accessible ion acceleration mechanism, it suffers from key limitations. These include a broad energy spectrum (from 1 MeV to several tenth of MeV), significant beam divergence (± 20) and a number of protons that decreases exponentially with the energy.

To overcome these issues, one promising approach involves coupling the TNSA source to a secondary structure inspired by Traveling-Wave Tubes (TWTs), the so called the helical coil target. In this configuration, the intense discharge current generated during the laser-target interaction propagates along the coil, producing a strong, transient RF field. Rather than amplifying an electromagnetic wave as in a conventional TWT, this setup transfers energy from the RF field to the trailing protons, enabling both post-acceleration, energy bunching and focusing.

This inverted operation, where a charged particle beam receives energy from the wave instead of generating it, is based on beam-wave interaction physics similar to RF devices. It opens new perspectives for compact, staged acceleration schemes and tailored beam shaping, bridging laser-plasma acceleration with microwave engineering concepts.

Chapter 4

Theoretical model of current propagation in a helical coil with varying geometry and screen tube

Sommaire

4.1 Foreword

As described in Chapter 3, the laser first ionizes the solid target, then accelerates electrons and creates a sheath field at the rear surface of the target. Electrons with sufficient energy escape from the target and generate a discharge current which is retrieved by an helical coil.

This chapter presents the development of an analytical model [61] designed to compute the various components of the electromagnetic field (E_r, E_θ, E_z, B_r, B_θ, B_z) generated by the propagation of a current pulse along a helical conductor. The model expresses these fields as functions of the helix parameters, namely the radius (a) and pitch (h).

The proposed model is two-dimensional, axisymmetric, and spatiotemporal, and is applicable to helices with either constant or longitudinally varying pitch and diameter ($a(z)$ and $h(z)$), with or without an electromagnetic shielding tube surrounding the structure. The validity domain of the model is restricted to thin and infinitely long helices ($L \gg a$, where L is the helix length), as the physical cross-section of the wire is neglected.

A preliminary version of this analytical model, limited to constant-pitch, constant-diameter helices without shielding, had been implemented in the `DoPPLIGHT` code (see Bardon et al., *PACMAN* 2020 [21], and Arthur Hirsch-Passicos's PhD thesis [62]). The extended formulation developed in this work, significantly more complete and robust, has also been integrated into the same code framework. The objective is to provide a fast and efficient numerical tool to investigate wave–particle interaction phenomena along the helix and to enable rapid optimization of the system geometry. The key figure of merit for this optimization is the particle (protons, ions) energy distribution at the helix output.

The first part of this chapter is devoted to the presentation of the analytical developments underlying the electromagnetic model. The second part addresses its numerical validation, performed through direct comparison with results from `SOPHIE`, a 3D particle-in-cell (PIC) code developed at CEA [63].

4.2 Theoretical model of current propagation in a helical coil with varying geometry and screen tube

4.2.1 Introduction

Traveling-wave tube amplifiers are devices used to amplify radio frequency (RF) signals in the microwave range. First electromagnetic models of TWT were presented in 1947 [64], followed by analytical models in the 1950s [58, 59, 65, 66]. This device is a wave-particle interaction system that involves an electron beam and an RF signal propagating in a conducting helix. The waveguide is engineered to create a phase velocity smaller than the speed of light ($c/10$), enabling wave-particle interactions when the wave phase velocity nearly matches the particle velocities. Electrons are slowed down to amplify the signal that is transmited to an antenna. In a helical coil target, as shown in Fig. 4.1(a), during the laser-plasma interaction, escaping electrons are charging positively the target, which drives a discharge current pulse through the

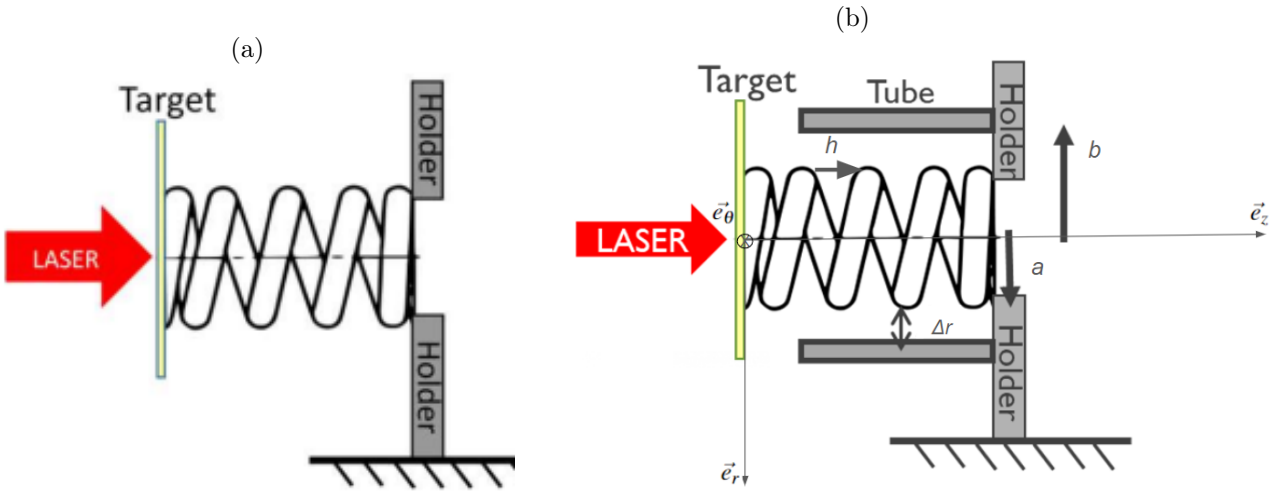

Figure 4.1 – (a) Scheme of a single helical coil, (b) a helical coil with a tube. In the model, the helix is replaced with a thin cylinder which is symmetric by rotation around the z-axis. Reproduced from A. Hirsch-Passicos et al. "Helical coil design with controlled dispersion for bunching enhancement of protons generated by the target normal sheath acceleration," Phys. Rev. E, 109, 025211 (2024) [5] with permission from American Physical Society. The tube is symmetric by rotation around the symmetry axis.

helix, generating an electromagnetic pulse (EMP) that post-accelerates and focuses the TNSA proton beam. The physics of the current propagation in the helix is analogous to what occurs in coupled transmission systems [58, 65]. However, optimizations are needed for an efficient proton post-acceleration. The current pulse dispersion limits the length on which the wave-particle interaction is efficient [21] and the use of longer helical coil (HC) does not produce higher ion energies. Similar issues have been observed in coupled transmission systems [59, 66]. It was suggested that the helix dispersion be controlled by adding a conducting tube around it. The current dispersion was found to depend on the distance between the helix and the tube.

A scheme of a helical coil with a screening tube (HCT) is shown in Fig. 4.1(b). Similarly to the conventional TWT shown in Fig. 3.4, a conducting tube is set around the helical coil [5]. Differently from the low-current TWT, one can not use ties to support the helical coil because of high current, typically of a few kA, that might generate electrical breakdown inside the ties. The HCT configuration reduces the current dispersion, increases the ion maximum energy, and produces a beam bunching [5]. The choice of HC radius and pitch defines the propagation velocity of the electromagnetic fields, which can be synchronized with the ion velocity. The electromagnetic fields accelerate ions within a specific energy range depending on the field amplitude and resonance condition. For a helix with a constant pitch and radius, and a screening tube, scaling laws have been defined [5] to design an optimal geometry function of the proton input spectrum.

The resonance coupling of the ion beam with the current can be improved by varying the helix geometry along the propagation direction (z axis) to accelerate the current pulse to maintain synchronization with the accelerated protons. Here, we consider two geometries shown in Fig. 4.2. The pitch of the helix and/or its radius varies, thus providing an extended length of

synchronization. We refer to a helix with varying geometry and with a tube as VHCT.

Pitch-tapering is a common feature of TWTs, but the current codes used for TWT simulation, such as CST [67], KARAT [68], or MAFIADIMOHA [69], DIMOHA [53], MVTRAD [70], CHRISTINE [71], or BWIS [72], do not effectively account for it.

The main objectives of the analytical model developed in this chapter are the understanding of the physics of current dispersion and the optimization of VHCT geometry for an efficient ion acceleration and bunching. Compared to direct particle-in-cell (PIC) simulations, the analytical model allows us to consider a large parameter space and save computation time. Using this model, one may increase the cut-off ion energy, optimize the beam bunching, and increase the number of high-energy ions. The model is applied for the optimization of a laser-driven ion beamline such as the one that can be obtained on commercially available multi-hundred TW laser systems, e.g. the ALLS laser facility at INRS EMT [73]. In this facility, the ion beamline is driven by a Ti:sapphire laser system generating pulses with an on-target energy of 3.3 J, a pulse duration of 22 fs, a repetition rate of 2.5 Hz, a central wavelength of 800 nm and a focal spot of 5 µm. The peak intensity on target is approximately 1.3×10^{20} W/cm^2.

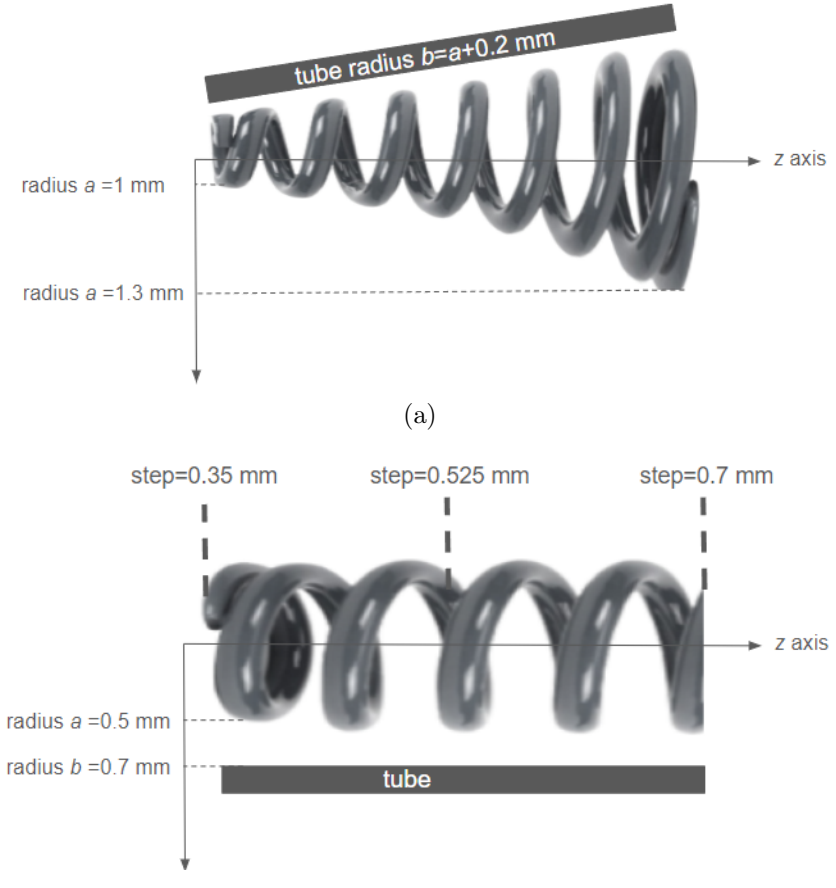

Figure 4.2 – Examples of geometries of the helical coil with varying (a) radius and (b) pitch along the z-axis. The tube is symmetric by rotation around the symmetry axis.

This work is based on the theoretical model of a helical coil developed in Refs. [58,59,65,66], and further applied to HC in Refs [5,21]. Expressions for the electromagnetic fields are derived

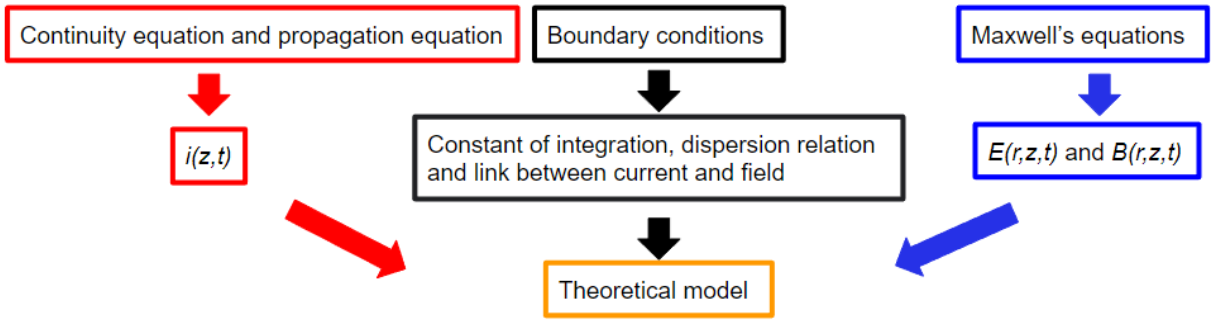

Figure 4.3 – Schema of the model construction.

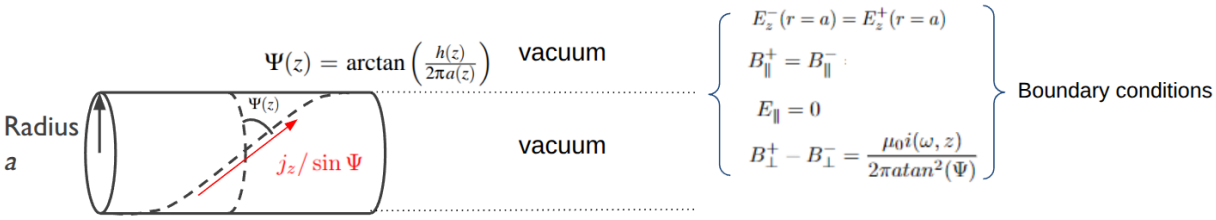

Figure 4.4 – Diagram showing the direction of current propagation at the surface of a cylinder at an angle Ψ to the azimuthal direction and the different boundry conditions at $r = a$.

from Maxwell's equations in vacuum with the boundary conditions linking fields to the surface of the helix and the tube. The helix parameters, the pitch and radius, are assumed to vary slowly along the z axis, so the fields are calculated using the Wentzel, Kramers, and Brillouin approximation (WKB). The dispersion relations are obtained in the Fourier space, and then expressions for the fields in real space are analyzed.

4.2.2 Coupling the current to electromagnetic fields

A general scheme of the model development is presented in Fig. 4.3. The first step consists in the definition of the current propagating in the helix considered as an infinitely thin perfect conductor. It then defines the inner and external electromagnetic fields through the boundary conditions. The electromagnetic fields are computed from the differential equations for the electrostatic and vector potentials. The equation for the current propagation in the helix is given in Sec. 4.2.2.1. Following Ref. [58], the helix is modeled as a continuous cylinder with a current propagating in an azimuthal direction (see Fig. 4.4). Equations for the electromagnetic fields are given in Sec. 4.2.2.2 in the Fourier representation. The boundary conditions for the VHC case (without tube) are given in Sec. 4.2.2.3. They determine a connection between the current and the electromagnetic fields, as well as the dispersion relation. Expressions for the electromagnetic field for VHC in the real space are obtained in Sec. 4.2.2.4. The same process is then repeated for the VHCT geometry – a helix screened with a conducting tube. The boundary conditions and the dispersion equation are given in Sec. 4.2.2.5, and the electromagnetic fields in the real space are given in Sec. 4.2.2.6. The analytical model is compared with PIC simulations in Sec. 4.2.3.

4.2.2.1 Current pulse propagation

Following the original sheath helix model [58], we assume the current is propagating along a thin cylindrical surface of a radius a in the direction defined by the angle Ψ with respect to the azimuthal axis θ. This angle defines a relation between the helix radius a and pitch h:

$$h = 2\pi a \tan \Psi, \tag{4.2.1}$$

as shown in Fig. 4.4.

As the current is only propagating within the helix, we can define the full current propagating along the wire as $j_z/\sin\Psi$. Therefore, it is sufficient to consider only the z component of the current, $j_z(t,z)$. It is related to the charge density per unit length q by the continuity equation:

$$\partial_z j_z = -\partial_t q + 2j_0(t)\delta(z),$$

where the second term on the right-hand side is the source term j_0 prescribed at the origin $z = 0$, and $\delta(z)$ is the Dirac function. The helix is represented as a lossless transmission line with the conductance C and inductance L per unit length. The charge and the current are related by the telegraph equation:

$$-C^{-1}\partial_z q = L\partial_t j_z.$$

Taking the derivative of the continuity equation on z, injecting it in the propagation equation, and performing the Fourier transform in time, we obtain the following equation for the current:

$$\partial_z^2 j_z(\omega,z) + k^2(\omega,z) j_z(\omega,z) = 2j_0(\omega)\delta'(z), \tag{4.2.2}$$

where $k^2 = LC\omega^2$ and ω is the frequency. The value of LC depends on the transmission line structure and may depend on frequency and coordinate.

To solve this equation, we assume that $k(\omega,z)$ is a slow function of the coordinate and represent the current wave number in the WKB approximation, $j_z = A\,\mathrm{e}^{i\phi}$, where $A(\omega,z)$ is slowly varying amplitude and $\phi(\omega,z)$ is the phase. Injecting this expression in Eq. (4.2.2), we neglect the second derivative of A being of third order. Conversely, the phase ϕ varies strongly with z, and its derivative ϕ' is of the first order, same as k. Consequently, we obtain two equations for the amplitude and phase:

$$(\phi')^2 = k^2, \quad \text{and} \quad 2iA'\phi'\mathrm{e}^{i\phi} + i\phi'' A\mathrm{e}^{i\phi} = 2j_0\delta'(z). \tag{4.2.3}$$

Solving the first equation as $\phi = \int_0^z k(\omega, z_\eta)dz_\eta$, we obtain the following expression for the current:

$$j_z = j_0\kappa(\omega)\, g(z), \tag{4.2.4}$$

where $j_0 = j_z(\omega, z=0)$, $k_0 = k(\omega, z=0)$, $\kappa(\omega) = 1 - ik_0'/2k_0^2$, and function g describes the

current variation along the helix axis:

$$g(z) = \sqrt{k_0/k}\,\exp\left[i\int_0^z k(\omega, z_\eta)dz_\eta\right]. \tag{4.2.5}$$

4.2.2.2 Propagation of the electromagnetic fields

Starting from the Maxwell equations, one obtains differential equations for the axial components of the electric and magnetic fields. They are solved by performing variables separation in radius and z axis $E_z = f(r)g(z)$ and $B_z = h(r)g(z)$, where function $g(z)$ (4.2.5) describes the field distribution along the propagation direction in the WKB approximation. A general solution for the radial dependence of the field components in the axisymmetric geometry can be represented as a linear combination of two modified Bessel functions, $f(r) = B_1 I_0(\alpha r) + B_2 K_0(\alpha r)$ and $h(r) = B_3 I_0(\alpha r) + B_4 K_0(\alpha r)$, where B_i are constants defined by the boundary conditions and

$$\alpha(\omega, z) = \sqrt{k^2 - \omega^2/c^2} \tag{4.2.6}$$

is the radial propagation constant. Using these notations, expressions for all field components can be written as follows:

$$E_z = g(z)\,[B_1 I_0(\alpha r) + B_2 K_0(\alpha r)], \tag{4.2.7}$$

$$E_r = i(k/\alpha)\,\Lambda\, g(z)\,[-B_1 I_1(\alpha r) + B_2 K_1(\alpha r)], \tag{4.2.8}$$

$$B_\theta = -\,i(\omega/\alpha c^2)\,\aleph\, g(z)\,[B_1 I_1(\alpha r) - B_2 K_1(\alpha r)], \tag{4.2.9}$$

$$B_z = g(z)\,[B_3 I_0(\alpha r) + B_4 K_0(\alpha r)], \tag{4.2.10}$$

$$B_r = i(k/\alpha)\,\Lambda\, g(z)\,[-B_3 I_1(\alpha r) + B_4 K_1(\alpha r)], \tag{4.2.11}$$

$$E_\theta = i(\omega/\alpha)\, g(z)\,[B_3 I_1(\alpha r) - B_4 K_1(\alpha r)], \tag{4.2.12}$$

where $\Lambda(\omega, z) = 1 + ik'/2k^2$ and $\aleph(\omega, z) = 1 + k''/2k\omega^2 - 3(k')^2/4k^2\omega^2$.

4.2.2.3 Dispersion relation without tube

The constants B_i are defined by the boundary conditions. Since the current sheet is localized at $r = a$, there are two distinct zones, $r < a$ and $r > a$, inside and outside the helix where the constants take different values. They are noted with superscripts $-$ and $+$, respectively.

First, we apply the condition that fields should decrease to zero far away from the helix, at $r \to \infty$. Taking expressions for E_z and B_z (4.2.7) and (4.2.10), we find:

$$B_1^+ = 0 \quad \text{and} \quad B_3^+ = 0. \tag{4.2.13}$$

Another condition is that the fields must have finite values at the helix axis, $r = 0$. Taking expressions for E_z and B_z given by Eqs. (4.2.7) and (4.2.10), we find:

$$B_2^- = 0 \quad \text{and} \quad B_4^- = 0 \tag{4.2.14}$$

Two more conditions apply to the electric field at the position of the current sheet $r = a$. The tangential electric field must be continuous and perpendicular to the current. By applying the continuity condition to the components E_z and E_θ and accounting for Eqs. (4.2.13) and (4.2.14), we find:

$$B_2^+ = B_1^- \frac{I_0(\alpha a)}{K_0(\alpha a)} \quad \text{and} \quad B_3^- = -B_4^+ \frac{K_1(\alpha a)}{I_1(\alpha a)} \tag{4.2.15}$$

The component of the electric field parallel to the current reads:

$$E_\parallel = E_\theta \cos\Psi + E_z \sin\Psi. \tag{4.2.16}$$

Setting to zero this field at $r = a$, we find:

$$B_4^+ = -iB_2^+ \frac{\alpha}{\omega} \frac{K_0(\alpha a)}{K_1(\alpha a)} \tan\Psi. \tag{4.2.17}$$

Thus, applying these boundary conditions, we expressed all eight constants $B_i^\pm$ through one, B_1^-, which is proportional to the current amplitude j_0. However, we have one more continuity condition that applies to the component of the magnetic field parallel to the current: $B_\parallel^+(r = a) = B_\parallel^-(r = a)$. Taking expressions for B_z and B_θ given by Eqs. (4.2.9) and (4.2.10) along with Eqs. (4.2.13) and (4.2.14), we obtain a relation between the frequency ω and wave number k, which is the dispersion relation:

$$\omega^2 = k^2 c^2 \frac{1 + \left(\frac{3(k')^2}{4k^4} - \frac{k''}{2k^3}\right) \cot^2\Psi \, \frac{I_1(\alpha a)K_1(\alpha a)}{I_0(\alpha a)K_0(\alpha a)}}{1 + \cot^2\Psi \, \frac{I_1(\alpha a)K_1(\alpha a)}{I_0(\alpha a)K_0(\alpha a)}}. \tag{4.2.18}$$

The dispersion relation is plotted in red in Fig. 4.5 the helix angle $\Psi = 6.36°$. At large values of wave number, $ka \gg 1$, the dispersion is negligible and $\omega \approx kc \sin\Psi$, where $c \sin\Psi$ is the velocity of the electric current propagation along the z axis. By contrast, the dispersion effects are important at wavelengths comparable with the helix radius, and the phase velocity ω/k approaches the light velocity. Moreover, the second term in the numerator in Eq. (4.2.18) is supposed to be smaller than 1 in the domain of validity of the WKB approximation. The limits of validity are discussed further in Sec. 4.2.4. Out of these limits, we neglect the first and second derivatives of k in the equations.

To find a relation of the remaining constant B_1^- with the current j_0, we apply the condition of discontinuity of the tangential component of the magnetic field perpendicular to the direction of the electric current at $r = a$. According to the Ampere theorem, it reads:

$$B_\perp^+(r = a) - B_\perp^-(r = a) = (\mu_0/h)\, j_0 \cot\Psi, \tag{4.2.19}$$

where $h/\cos\Psi$ is the length of the current path over one period, $j_0/\sin\Psi$ is the full current propagating along the wire, and μ_0 is the vacuum magnetic permeability. Considering expressions

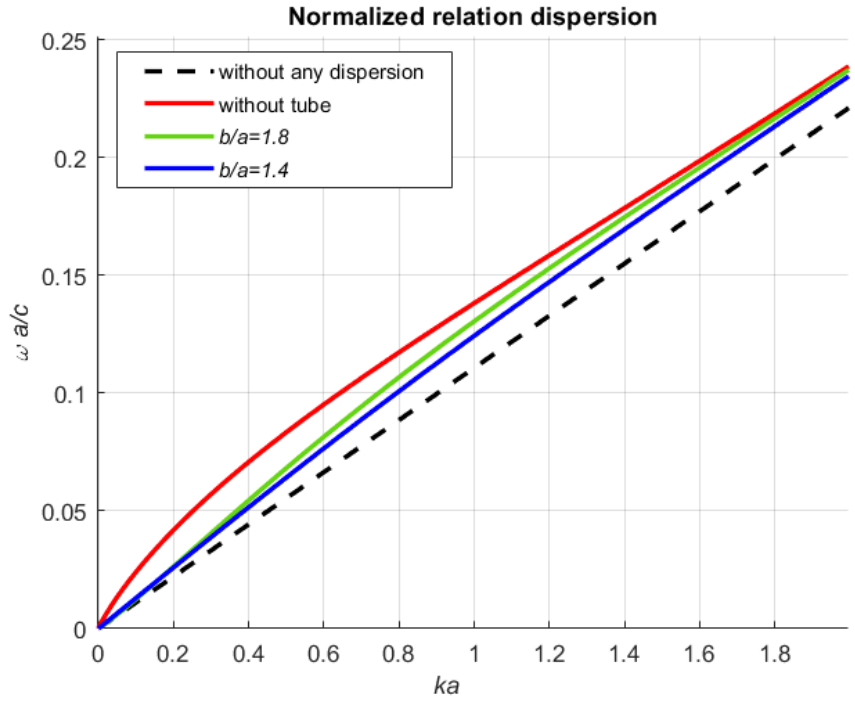

Figure 4.5 – Dependence of the frequency ω on the wave number k for HC with a radius of $a = 0.5$ mm and linearly varying pitch (on a length of $l_c = 40$ mm) of $h = 0.35$ mm to 0.7 mm, without tube (red), with a tube of a radius $b/a = 1.4$ (blue), and $b/a = 1.8$ (green), and in a perfect case without any dispersion (dashed black).

for B_z and B_θ given by Eqs. (4.2.9) and (4.2.10), we find:

$$B_1^- = -\frac{i\omega\mu_0 j_0 \kappa}{2\pi a\alpha} \frac{I_1(\alpha a)K_1(\alpha a)}{I_0(\alpha a)J(\alpha a)} \cot^3\Psi \ \cos\Psi, \tag{4.2.20}$$

where $J(\alpha a) = K_1(\alpha a)I_0(\alpha a) + K_0(\alpha a)I_1(\alpha a)$. Knowing all constants and the dispersion relation, we obtain expressions for electric and magnetic fields as a function of time.

4.2.2.4 Expressions for fields without tube

Performing the inverse Fourier transform of Eqs. (4.2.7) - (4.2.12) with appropriate values of constants, we obtain expressions for the electric and magnetic fields in the function of r, z and t. Here, we show the expressions for E_z and B_z for $r < a$:

$$E_z^-(r,z,t) = -\frac{i\mu_0}{2\pi^2 a}\int_0^\infty d\omega \, \frac{j_0\omega\kappa}{\alpha}\sqrt{\frac{k_0}{k}}\frac{I_1(\alpha a)K_1(\alpha a)}{I_0(\alpha a)J(\alpha a)} \times \cot^3\Psi \ \cos\Psi \ I_0(\alpha r) \exp\left[i\int_0^z k(\omega, z_\eta)dz_\eta - i\omega t\right], \tag{4.2.21}$$

$$B_z^-(r,z,t) = \frac{\mu_0}{2\pi^2 a}\int_0^\infty d\omega \, j_0\kappa\sqrt{\frac{k_0}{k}}\frac{K_1(\alpha a)}{J(\alpha a)}I_0(\alpha r) \times \cot^2\Psi \ \cos\Psi \ \exp\left[i\int_0^z k(\omega, z_\eta)dz_\eta - i\omega t\right]. \tag{4.2.22}$$

Expressions for other components of the electric and magnetic fields are given in Sec. 4.2.5.

4.2.2.5 Dispersion relation with tube

Here, we calculate the constants B_i for a helix with the screening tube (VHCT). Considering the tube as an ideal conducting cylinder of radius b, the boundary conditions correspond to zero electric and magnetic fields at $r = b$. Taking expressions for E_z and B_z (4.2.7) and (4.2.10), we find:

$$B_2^+ = -B_1^+ \frac{I_0(\alpha b)}{K_0(\alpha b)} \quad \text{and} \quad B_4^+ = B_3^+ \frac{I_1(\alpha b)}{K_1(\alpha b)}. \tag{4.2.23}$$

The condition on the fields at the helix axis, $r = 0$, is unchanged and given by Eq. (4.2.14). The conditions on the electric field at the position of the current sheet $r = a$ are also the same as in the case without tube, Eqs. (4.2.15) and (4.2.17). The condition (4.2.17) remains unchanged, and, accounting for the conditions (4.2.23) at the tube, we can represent Eqs. (4.2.15) as follows:

$$B_1^+ = B_1^- \frac{K_0(\alpha b) I_0(\alpha a)}{K_0(\alpha b) I_0(\alpha a) - I_0(\alpha b) K_0(\alpha a)}, \tag{4.2.24}$$

$$B_3^+ = B_3^- \frac{K_1(\alpha b) I_1(\alpha a)}{K_1(\alpha b) I_1(\alpha a) - I_1(\alpha b) K_1(\alpha a)}. \tag{4.2.25}$$

Thus, applying these boundary conditions, we expressed all eight constants $B_i^{\pm}$ through one, B_1^-, which is proportional to the current amplitude j_0. Using then the continuity condition for the component of the magnetic field parallel to current: $B_{\parallel}^+(r = a) = B_{\parallel}^-(r = a)$. Taking expressions for B_z and B_θ given by Eqs. (4.2.9) and (4.2.10) along with Eqs. (4.2.23), we obtain a dispersion relation for the helix with tube:

$$\omega^2 = k^2 c^2 \frac{1 + \left(\frac{3(k')^2}{4k^4} - \frac{k''}{2k^3}\right) \cot^2 \Psi \; \frac{I_1(\alpha a) I_0(\alpha b) J(\alpha a) N(\alpha a)}{I_0(\alpha a) F(\alpha a)}}{1 + \cot^2 \Psi \; \frac{I_1(\alpha a) I_0(\alpha b) J(\alpha a) N(\alpha a)}{I_0(\alpha a) F(\alpha a)}} \tag{4.2.26}$$

where $F(\alpha a) = K_0(\alpha b) I_0(\alpha a) - I_0(\alpha b) K_0(\alpha a)$ and

$$N(\alpha a) = \frac{K_1(\alpha b) I_1(\alpha a) - I_1(\alpha b) K_1(\alpha a)}{I_1(\alpha b) J(\alpha a)}.$$

It is plotted in Fig. 4.5 for the ratios $b/a = 1.4$ (blue curve) and $b/a = 1.8$ (green curve). As one can see, the dispersion decreases as the tube approaches the coil.

To find a relation of the remaining constant B_1^- with the current j_0, we apply the condition of discontinuity of the tangential component of the magnetic field perpendicular to the direction of the electric current at $r = a$ given by Eq. (4.2.19). Considering expressions for B_z and B_θ given by Eqs. (4.2.9) and (4.2.10), we find:

$$B_1^- = \frac{i\omega\mu_0 j_0 \kappa}{2\pi a \alpha} \frac{I_1(\alpha a) N(\alpha a)}{I_0(\alpha a)} \cot^3 \Psi \; \cos \Psi. \tag{4.2.27}$$

4.2.2.6 Expressions for the fields with tube

Performing the inverse Fourier transform of Eqs. (4.2.7) and (4.2.10) with the corresponding expressions for constants B_i, we obtain the electric and magnetic fields in the real space. As

an example, we show below expressions for E_z^- and B_z^-. Other components of the electric and magnetic fields are given in Sec. 4.2.5.

$$E_z^-(r,z,t) = \frac{i\mu_0}{2\pi^2 a}\int_0^\infty d\omega\, \frac{j_0\omega\kappa}{\alpha}\sqrt{\frac{k_0}{k}}\frac{I_1(\alpha a)N(\alpha a)}{I_0(\alpha a)}\ \cos\Psi$$
$$\times \cot^3\Psi\ I_0(\alpha r)\exp\left[i\int_0^z k(\omega,z_\eta)dz_\eta - i\omega t\right], \tag{4.2.28}$$

$$B_z^-(r,z,t) = -\frac{\mu_0}{2\pi^2 a}\int_0^\infty d\omega\, j_0\kappa\sqrt{\frac{k_0}{k}}N(\alpha a)\cot^2\Psi\ \cos\Psi$$
$$\times I_0(\alpha r)\exp\left[i\int_0^z k(\omega,z_\eta)dz_\eta - i\omega t\right] \tag{4.2.29}$$

The electric and magnetic fields in the coil given by Eqs. (4.2.21), (4.2.22), (4.2.28), and (4.2.29) are calculated with the DoPPLIGHT code described in the next subsection.

4.2.3 Model validation: comparison to PIC simulations

The analytical model describing the current propagation along the helix and electromagnetic fields, is implemented in the DoPPLIGHT code [74], introduced in Sec. 4.2.3.2), and compared to the results obtained with a PIC code, SOPHIE [63], presented in Sec. 4.2.3.1. The model validation consists of the comparison of expressions for electromagnetic fields and dispersion equations with known formulas for specific conditions [59,65] (Eq. 3.4.2 and 3.4.3) and numerical simulations presented in Sec. 4.2.3.3. Furthermore, the proton energy distributions obtained with DoPPLIGHT and from PIC simulations are compared in Sec. 4.2.3.4.

4.2.3.1 Description of the SOPHIE code

The PIC code SOPHIE [63], developed at CEA-CESTA, solves Maxwell's equations for the electric and magnetic fields in 3D geometry in matter with boundary conditions defined at surfaces of arbitrary shape made of conducting, dielectric, or magnetic materials. Maxwell's equations are solved on the Yee mesh with centered electric and magnetic fields using the finite-difference time-domain (FDTD) method [75]. The particles are moved according to the relativistic dynamic equations using a Boris solver [76]. Self-consistence is achieved using a Buneman currents collector. The Buneman instability occurs when electrons move significantly faster than ions, generating electrostatic waves that enhance energy transfer and current dissipation. In a PIC-FDTD code like SOPHIE, the implementation of Buneman current collectors refers to a technique ensuring consistency between the current carried by charged particles and the current induced in the electromagnetic grid of the simulation. This helps accurately model plasma-conductor interactions and prevent numerical artifacts related to improper current representation.

SOPHIE is not designed to simulate laser-plasma interaction which requires to resolve the laser wavelength. It is complementary to laser-plasma interaction PIC codes such as CALDER [77] or Smilei [78]. It is used to model the current propagation in matter on large spatial scales (of

the order of several cm) and long-time scales (of the order of a few ns). The code is benchmarked on test cases and compared with other similar codes.

In our SOPHIE simulations, a helical coil is positioned at the rear side of a foil target. The target, coil, and holder are considered perfect conductors and are meshed at full scale with a cell size of $\Delta x = \Delta y = \Delta z = 20$ μm, yielding a total of 2×10^9 cells across a volume of 72 cm^3. The electrons and the protons are represented using 10 million macroparticles each.

Inputs for ion energy and angular distributions are taken from experimental data obtained with TNSA without HC. The input proton energy distribution is obtained experimentally in previous experiment [20]. The angular distribution is modeled using a super-Gaussian function given by $dN_p/d\theta \propto \exp\left[-(\theta/\theta_p)^{10}/2\right]$, where $\theta_p = 19°$. The temporal emission profile dN/dt follows a Gaussian shape with a full-width at half-maximum (FWHM) duration τ of a 3.5 ps. The emission zone for the protons is set to a transverse size of 200 μm.

The dynamic of the protons within the helical coil are determined solely by the electromagnetic fields generated by the discharge current. To simulate this current, electrons are emitted isotropically with an energy distribution similar to that of the protons. The transverse size of the electron emission zone matches that of the protons and carbon ions (200 μm).

In these simulations, the electron charge emission is set to 160 nC, while the proton charge emission is 12 nC, both emitted over a duration of 3.5 ps.

4.2.3.2 Description of the DOPPLIGHT code

DoPPLIGHT [74] is a numerical realization of a model describing charge particle motion in a coil with prescribed electric and magnetic fields varying in space and time. It is used to run fast computations for a large number of cases. The scheme of this code is presented in Fig. 4.6. It includes the following steps:

- The first input is the parameters (a, h, L) of the helix geometry.
- The second input is the current as a function of time $i(t)$ at the beginning of the helix ($z = 0$)
- The final input is the particle source term defined in terms of particle density depending on time along with the angular and energy distributions.
- At the same time, the particles' source terms are defined in terms of particle density depending on time along with the angular and energy distribution.
- DoPPLIGHT then performs the Fourier transform of the current and uses it to calculate the fields according to the equations given in Sec. 4.2.2.
- It then calculates the space charge fields [62,74] assuming a Gaussian-shaped non-relativistic proton beam.
- Finally, the protons and electrons are injected in the coil, and their trajectories are calculated using the Boris pusher [79] using the fields interpolated at every time step on each particle's position.

This numerical model operates in a 2D-axisymmetric geometry. It is time-resolved and, contrary to a PIC code, not self-consistent. It is a very efficient code that runs in few minutes

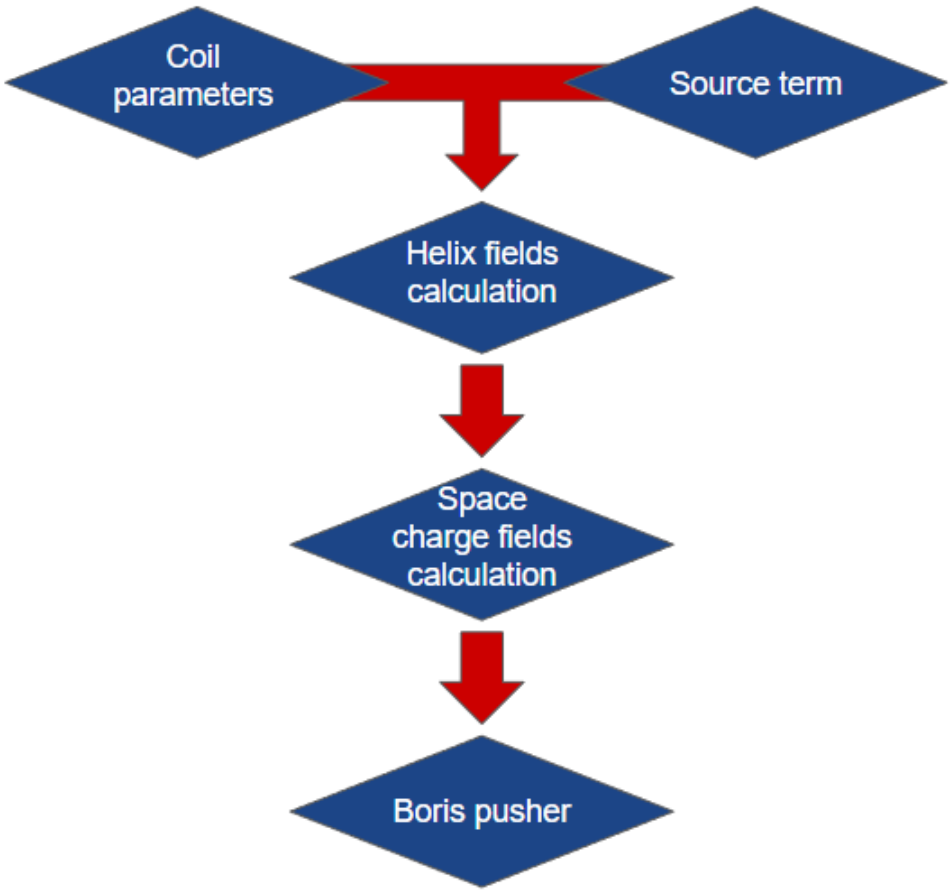

Figure 4.6 – Diagram of DoPPLIGHT code. The coil parameters correspond to the radius a, the pitch h and the length L. The source term provides the distribution of particles in energy, angle, and time. The electric and magnetic fields in the helix are calculated according to Eqs. (4.2.28) and (4.2.29). The space charge fields account for Coulomb repulsion. Particle displacement is calculated with the Boris pusher.

on a laptop computer which allows to perform hundreds of simulations for the helix geometry optimization. Its simplicity enables the use of many diagnostics, such as the proton spectrum at the HC exit or values of the electromagnetic fields at the particle trajectory at every time step. Exactly like SOPHIE, DoPPLIGHT is not designed to simulate laser-plasma interaction. The source term (input of the simulation) is the emission of particles (electrons and ions) from the target. The characteristics of this emission (temporal, angular, time distributions) are defined either by a first PIC simulation (Smilei or Calder) that models the laser-plasma interaction, or by the experimental results obtained during a TNSA shot (without helical coil). In the next subsection, the results obtained with this code are compared with the PIC simulations using SOPHIE.

4.2.3.3 Comparisons

Coil with a constant pitch and radius

By considering k independent of the coordinate, our results can be compared with known analytic expressions. Dispersion equation (4.2.18) for a helix without tube reads:

$$\omega^2 = k^2 c^2 \left(1 + \cot^2 \Psi \, \frac{I_1(\alpha a) K_1(\alpha a)}{I_0(\alpha a) K_0(\alpha a)}\right)^{-1}.$$

It agrees with the dispersion equation given in Refs. [58, 65]. Similarly, for a coil with tube, Eq. (4.2.26) agrees with Refs. [59, 66].

A simple expression can be obtained for the magnetic field on the coil axis in the case of a DC current $j(z,t) = J_0$. Inserting this expression in Eq. (4.2.22) we find:

$$B_z = (\mu_0/h) J_0 \cos \Psi.$$

In particular, in the case of small pitch, $\Psi \to 0$, this expression reduces to the well-known formula for the magnetic field of a solenoid, $B_z = \mu_0 N J_0$, where $N = 1/h$ is the number of turns per unit length.

Figure 4.7(a) presents a comparison of the z-component of the electric field on the axis calculated with DoPPLIGHT and SOPHIE for an input current of $j_0 = J_0 \exp\left[-(t-t_0)^2/2t_p^2\right]$, where $J_0 = 800$ A, $t_0 = 16$ ps is the time delay between the proton emission and the current emission and $t_p = 3$ ps is the pulse duration FWHM. The temporal distribution of the current is responsible for the different frequencies of the pulse, which is itself in charge of the current dispersion, as explained in Secs. 4.2.2.3 and 4.2.2.5. Our model estimates that the electric field component is 300 MV/m for the radial and axial components and 20 MV/m for the azimuthal component. Concerning the magnetic field, the estimations, given by DoPPLIGHT, are of the order of 5 T for the axial component and 150 mT for the radial and azimuthal components. These estimates indicate that the radial and axial electric fields dominate the particle motion in the helix. These parameters correspond to the coil used in an experiment on proton acceleration on the ALLS facility [5]. Good agreement between the PIC simulation and the reduced model is

evident. A similar comparison for the helix with a tube of radius $b/a = 1.4$ is presented in Fig. 4.7(b). Agreement is also good, thus confirming the consistency of our model.

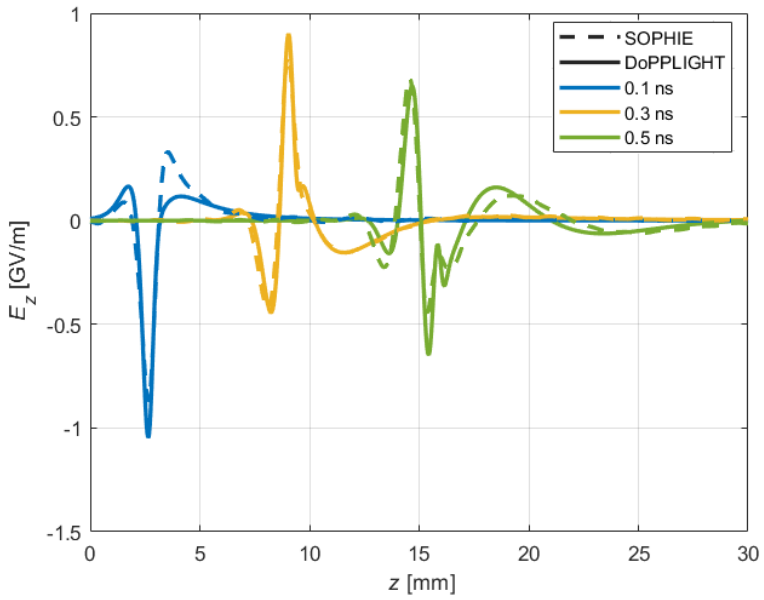

(a)

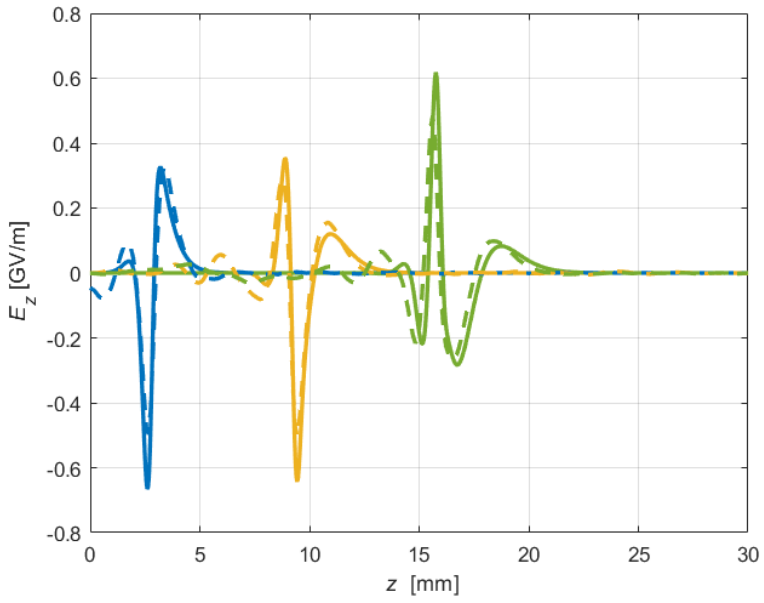

(b)

Figure 4.7 – Coordinate dependence of the axial electric field E_z at $r = 0.2$ mm for the coil without (a) and with tube (b) at 0.1 ns after emission time (blue curve), at 0.3 ns (yellow curve) and at 0.5 ns (green curve). Dashed lines show the result of the PIC simulation (SOPHIE), and solid lines are obtained with DoPPLIGHT code. The helix radius is 0.5 mm, the pitch 0.35 mm, and the tube radius is 0.7 mm.

One can see in Fig. 4.7(a) that the velocity of pulse propagation reduces with time. This is the dispersion effect. By contrast, the presence of the tube in panel (b) mitigates dispersion, and the pulse propagates faster. This has a positive effect on the proton acceleration and bunching,

as shown in the next subsection.

Small differences between the model and PIC simulation can be explained by the limits of the sheath helix model requiring a small helix angle Ψ [58] . However, these differences are smaller than the typical shot-to-shot variations in experiments [20, 22], which are on the order of 25%. Furthermore, we estimate the current from the ejected electrons and protons measured during experiments [73]. The average error of our model is within 20%, smaller than the measurement error.

The comparison between SOPHIE and DoPPLIGHT for the radial electric field and the current is presented in Sec. 4.2.7. Good agreement confirms the validation of our model for the case of constant helix parameters.

Coil with a tube and varying pitch

Here, we consider a coil of length of $l_c = 40$ mm with pitch linearly varying from $h_0 = 0.35$ mm to $h_1 = 0.70$ mm, such that

$$h(z) = h_0 + (h_1 - h_0)z/l_c. \tag{4.2.30}$$

The coil and tube radii are $a = 0.5$ mm and $b = 0.7$ mm. The axial electric field $E_z(0, z)$ is shown in Fig. 4.8 for the coils without (VHC) and with tube (VHCT).

Comparison of the solid and dashed lines demonstrates good agreement between the model and the PIC simulations for the axial component of the electric field. A similar level of agreement for the radial electric fields is demonstrated in Sec. 4.2.7. The average error of 20% is smaller than the typical measurement errors [20]. Small differences between the model and PIC simulation can be explained by the approximation made in the solution of Maxwell's equations. The separation of variables in r and z direction is not exact if the coil parameters vary along the axis. Also, the WKB approximation implies a slow variation of the coil parameters.

Other comparisons not shown here confirm the capacity of the model to describe the electromagnetic fields in the coil with sufficient accuracy, including the pulse propagation velocity and the field amplitude. DoPPLIGHT is able to compute the electric fields as a function of z and r in a few minutes, compared to some ten thousand CPU hours for PIC simulations.

4.2.3.4 Energy distribution of protons accelerated in coil

In this subsection, we show the capacity of our model to calculate the proton acceleration in the coil by comparing the results obtained with SOPHIE and DoPPLIGHT. The proton spectrum entering the coil is taken from experiments conducted at the ALLS facility [20, 80]. It is approximated by an exponential distribution

$$dN_p/d\varepsilon = (N_p/T_p)\,\exp(-\varepsilon/T_p), \tag{4.2.31}$$

with the total number of protons $N_p = 7.5 \times 10^{10}$, effective temperature $T_p = 1$ MeV, cutoff energy of 7 MeV, and angular divergence of $\pm$ 20°. The protons are propagated through the coil

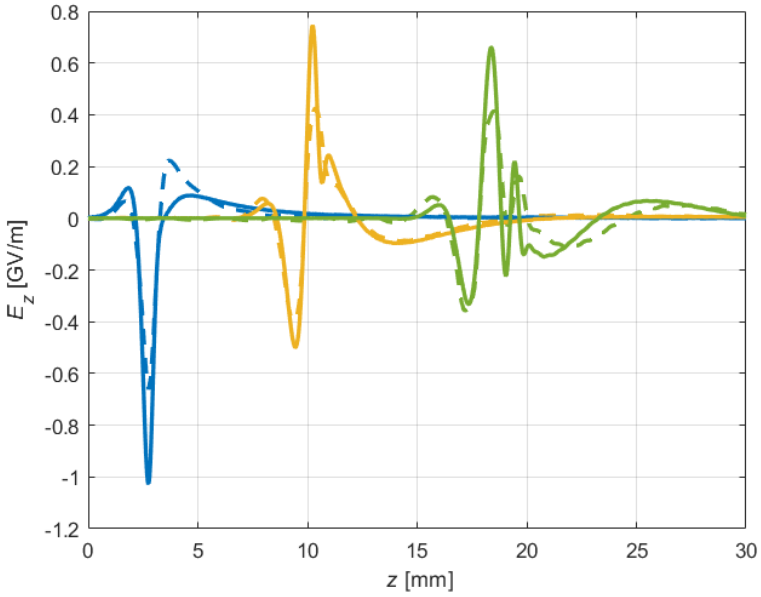

(a)

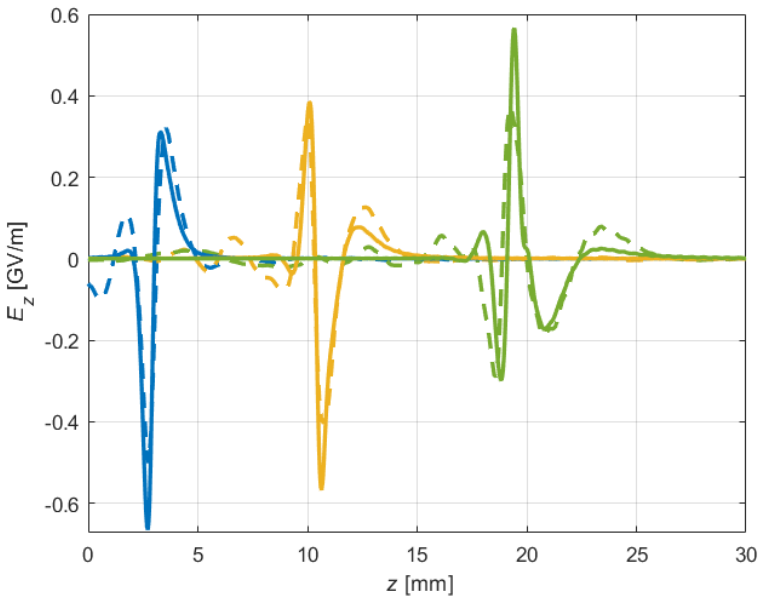

(b)

Figure 4.8 – Coordinate dependence of the axial electric field E_z at $r = 0.2$ mm for the coil without (a) and with tube (b) and pitch varying linearly with the coordinate (4.2.30) at 0.1 ns after emission time (blue curve), at 0.3 ns (yellow curve) and at 0.5 ns (green curve). Dashed lines show the results of PIC simulations (SOPHIE), and solid lines are obtained with the DoPPLIGHT code. Other parameters are given in the text.

of length $l_c = 14$ mm, radius $a = 0.5$ mm, and pitch varying linearly from $h_0 = 0.35$ mm to $h_1 = 0.4725$ mm. The spectra of protons exiting the coil are shown in Fig. 4.9 for the cases without (panel a) and with tube of radius $b = 0.7$ mm (panel b).

In spite of some differences related to a simplified description of the particle dynamics in the model, the proton spectra obtained with DoPPLIGHT and SOPHIE show similarities concerning

(a)

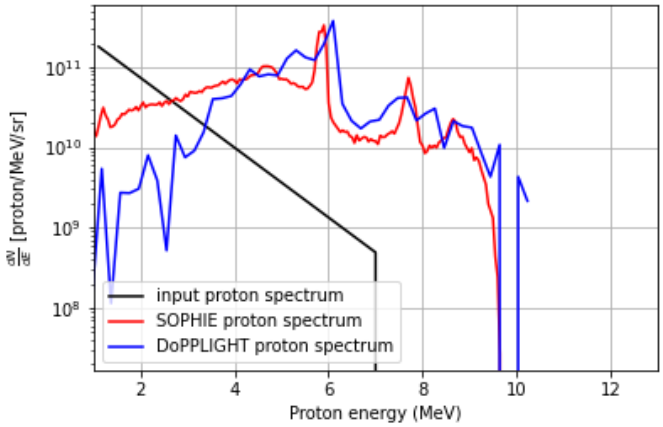

(b)

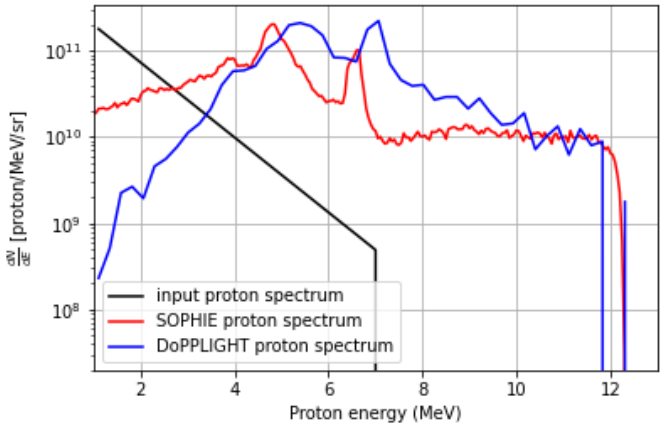

(c)

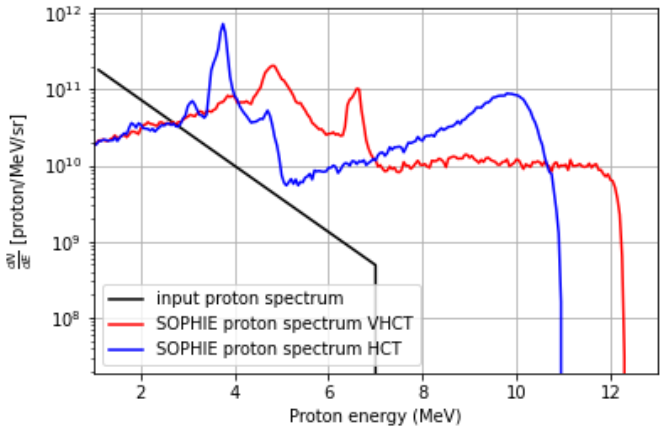

Figure 4.9 – Energy distribution of the protons accelerated in the helical coil without tube (a) and with tube (b) calculated with SOPHIE code (red line) and DoPPLIGHT code (blue line) with a linearly varying pitch. Panel (c) compare the case of a linearly varying pitch and the constant pitch. Black line shows the input proton spectrum. The parameters of the coil and the current are given in the text.

the cut-off energy, position of peaks, and the overall shape for energies above 4 MeV. A similar agreement for the coils with a constant pitch can be seen in Sec. 4.2.8. A comparison of panels (a) and (b) in Fig. 4.9 shows that the use of a tube allows an increase in the cut-off energy from 10 MeV to 12 MeV. This is explained by the mitigation of the coil dispersion by the tube and a better coupling between the field and the particles. Moreover, the number of protons with energies above 3.5 MeV is increased by a factor of 20 compared to the input spectrum. This example shows the potential of coils with a tube and varying geometry to shape the proton spectrum according to the desired application. A comparison of the obtained result for a helical coil with tube and a varying helical coil with tube in Fig. 4.9 (c) shows a cut-off energy up to 12 MeV for the VHCT which is higher than the HCT cut-off. The total number of protons at the HC exit is only few percents of the input TNSA proton. However, because of the focusing effect of the radial electric field, we get a higher number of protons per solid angle unit. Confirm that the total number of particles at the exit is less or equal to the number of injected particles. Figure 4.9 illustrates the positive effect of the tube, but I do not see any effect of the pitch variation. It is desirable to show it.

Once again, this underlines the reliability of our model. The differences between our model and SOPHIE simulations is acceptable because of the shot-to-shot fluctuation in the experiments. As demonstrated in earlier publications [4, 5], the measurement error attributed to shot-to-shot fluctuations, induced by variations in laser beam energy or laser-plasma interaction, typically ranges between 25 and 50 %. In our study, we observe an error margin of 31 to 44 %. Furthermore, we suspect that this error comes from, in part, the computation of the space charge in DoPPLIGHT [62]. This similarity in error magnitude suggests consistency in the computational outcomes of our model.

A comparison between DoPPLIGHT and SOPHIE results concerning proton acceleration confirms the acceptable accuracy of our model. It enables the performance of a large number of simulations and facilitates the exploration of a broad range of coil geometries. Although SOPHIE and DoPPLIGHT give similar results for the HC geometries presented in this chapter, there are three major differences between these two codes. The first one comes from the particle retroaction. Actually, the effect on the electromagnetic field of particles acceleration/deceleration is not taken into account in DoPPLIGHT, contrary to SOPHIE. The second one comes from the space charge modelling. It is found from solving the Poisson equation in SOPHIE while in DoPPLIGHT it is described as a field created by a charged axi-symmetric ellipsoid. The third one comes from the reflections during the pulse propagation along the helix. SOPHIE describes the real helical structure of helix with a wire of a finite thickness. So, in addition to the fields induced by the current, it accounts for the secondary fields induced by reflections from conducting surfaces.

4.2.4 Limits of the model

In this part, we discuss the limits of the model related to the geometry variation, the range of wave vectors, and the issue of the variable separation.

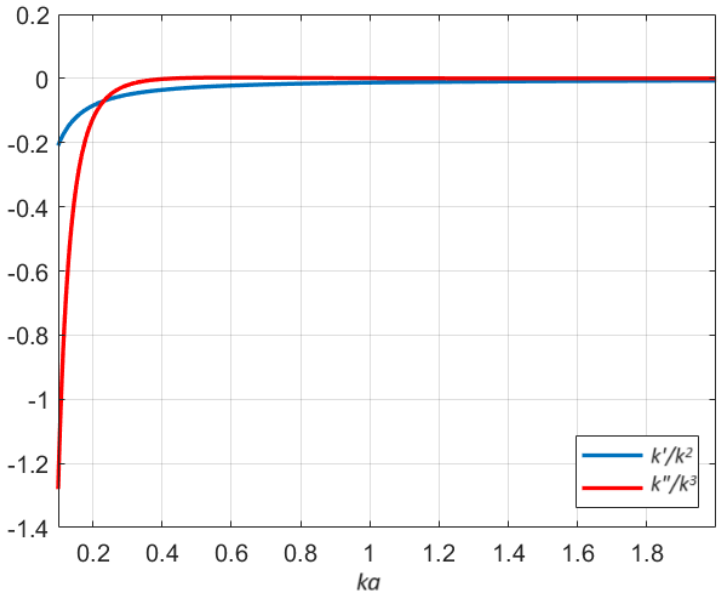

Figure 4.10 – Dependence of the WKB validity conditions (4.2.33), on the wave number k for the simulation parameters used in this work.

The WKB approximation implies a slow variation of the coil parameters. This allows us to neglect the second derivative of the current amplitude in Eq. (4.2.3). However, according to this equation, A'' is proportional to the derivatives of k:

$$A'' = j_0\sqrt{k_0}\kappa k^{3/2}\left(\frac{3(k')^2}{4k^4} - \frac{k''}{2k^3}\right). \tag{4.2.32}$$

Comparing this expression with the two other terms retained in Eq. (4.2.3), the conditions of slow variation of the wave number read:

$$|k'| \ll k^2 \quad \text{and} \quad |k''| \ll k^3. \tag{4.2.33}$$

These conditions are presented in Fig. 4.10 for the parameters considered in this work. For $ka \lesssim 0.3$, the conditions are not respected and the model is not valid in this domain. Alternatively, attempts were made to achieve linear variation in segments, describing a quadratic variation with distinct linear components. However, the discontinuity of k' at the connecting points causes additional errors. A small variation between the linear segments is necessary to ensure the validity of Eqs. (4.2.33).

We also note that the coordinate dependence of wave vector k introduces an error in the variable separation. Indeed, the z dependence of k implies that α (4.2.6) also depends on z. Reciprocally, the link between k, ω, and α results in imperfect variable separation and errors in the fields. These errors are small if the WKB criteria (4.2.33) are valid.

4.2.5 Expressions of the other components of the electromagnetic fields in real space

4.2.5.1 Field expressions without tube

Taking the inverse Fourier transforms of Eqs. (4.2.8) and (4.2.10) and injecting Eqs. (4.2.13) and (4.2.20), we obtain the fields in real space for $r < a$:

$$E_r^-(r,z,t) = \frac{i\mu_0}{2\pi^2 a}\int_0^\infty \frac{j_0\omega\sqrt{k\ k_0}}{\alpha^2}\kappa\Lambda\frac{I_1(\alpha a)K_1(\alpha a)}{I_0(\alpha a)J(\alpha a)}\ \cos\Psi \times \cot^3\Psi\ I_1(\alpha r)\exp\left[i\int_0^z k(\omega,z_\eta)dz_\eta - i\omega t\right], \tag{4.2.34}$$

$$B_\theta^-(r,z,t) = \frac{\mu_0}{2\pi^2 a c^2}\int_0^\infty \frac{j_0\omega^2\kappa\aleph}{\alpha^2}\sqrt{\frac{k_0}{k}}\frac{I_1(\alpha a)K_1(\alpha a)}{I_0(\alpha a)J(\alpha a)}\ \cos\Psi \times \cot^3\Psi\ I_1(\alpha r)\exp\left[i\int_0^z k(\omega,z_\eta)dz_\eta - i\omega t\right], \tag{4.2.35}$$

$$B_r^-(r,z,t) = \frac{\mu_0}{2\pi^2 a}\int_0^\infty \frac{j_0\sqrt{k\ k_0}}{\alpha}\kappa\Lambda\frac{K_1(\alpha a)}{J(\alpha a)}\cot^2\Psi \cos\Psi\ \times I_1(\alpha r)\exp\left[i\int_0^z k(\omega,z_\eta)dz_\eta - i\omega t\right], \tag{4.2.36}$$

$$E_\theta^-(r,z,t) = -i\frac{\mu_0}{2\pi^2 a}\int_0^\infty \frac{j_0\omega\kappa}{\alpha}\sqrt{\frac{k_0}{k}}\frac{K_1(\alpha a)}{J(\alpha a)}\cot^2\Psi \times \cos\Psi\ I_1(\alpha r)\exp\left[i\int_0^z k(\omega,z_\eta)dz_\eta - i\omega t\right]. \tag{4.2.37}$$

Similar expressions for the fields are obtained for $r > a$:

$$E_r^+(r,z,t) = -\frac{i\mu_0}{2\pi^2 a}\int_0^\infty \frac{j_0\omega\sqrt{k\ k_0}}{\alpha^2}\kappa\Lambda\frac{I_1(\alpha a)K_1(\alpha a)}{K_0(\alpha a)J(\alpha a)}\ \cos\Psi \times \cot^3\Psi\ K_1(\alpha r)\exp\left[i\int_0^z k(\omega,z_\eta)dz_\eta - i\omega t\right], \tag{4.2.38}$$

$$B_\theta^+(r,z,t) = -\frac{\mu_0}{2\pi^2 a c^2}\int_0^\infty \frac{j_0\omega^2\kappa}{\alpha^2}\sqrt{\frac{k_0}{k}}\aleph\frac{I_1(\alpha a)K_1(\alpha a)}{K_0(\alpha a)J(\alpha a)}\ \cos\Psi \times \cot^3\Psi\ K_1(\alpha r)\exp\left[i\int_0^z k(\omega,z_\eta)dz_\eta - i\omega t\right], \tag{4.2.39}$$

$$B_r^+(r,z,t) = \frac{\mu_0}{2\pi^2 a}\int_0^{+\infty} \frac{j_0\sqrt{k\ k_0}}{\alpha}\kappa\Lambda\frac{I_1(\alpha a)}{K_1(\alpha a)J(\alpha a)}\ \cos\Psi \times \cot^2\Psi\ K_1(\alpha r)\exp\left[i\int_0^z k(\omega,z_\eta)dz_\eta - i\omega t\right], \tag{4.2.40}$$

$$E_\theta^+(r,z,t) = -i\frac{\mu_0}{2\pi^2 a}\int_0^{+\infty} \frac{j_0\omega\kappa}{\alpha}\sqrt{\frac{k_0}{k}}\frac{I_1(\alpha a)}{K_1(\alpha a)J(\alpha a)}\ \cos\Psi \times \cot^2\Psi\ K_1(\alpha r)\exp\left[i\int_0^z k(\omega,z_\eta)dz_\eta - i\omega t\right]. \tag{4.2.41}$$

4.2.6 Expressions for the fields in coil with tube

Taking the inverse Fourier transforms of Eqs. (4.2.7) and (4.2.12) and injecting Eqs. (4.2.23) and (4.2.27), we obtain the following expressions for the fields for $r < a$:

$$E_r(r,z,t)^- = -\frac{i\mu_0}{2\pi^2 a}\int_0^\infty \frac{j_0\omega\sqrt{k\ k_0}}{\alpha^2}\kappa\Lambda\frac{I_1(\alpha a)N(\alpha a)}{I_0(\alpha a)}\ \cos\Psi$$
$$\times\cot^3\Psi\ I_1(\alpha r)\exp\left[i\int_0^z k(\omega,z_\eta)dz_\eta - i\omega t\right], \tag{4.2.42}$$

$$B_\theta^-(r,z,t) = -\frac{\mu_0}{2\pi^2 a c^2}\int_0^\infty \frac{j_0\omega^2\kappa\aleph}{\alpha^2}\sqrt{\frac{k_0}{k}}\frac{I_1(\alpha a)N(\alpha a)}{I_0(\alpha a)}\ \cos\Psi$$
$$\times\cot^3\Psi\ I_1(\alpha r)\exp\left[i\int_0^z k(\omega,z_\eta)dz_\eta - i\omega t\right], \tag{4.2.43}$$

$$B_r(r,z,t)^- = -\frac{\mu_0}{2\pi^2 a}\int_0^{+\infty} \frac{j_0\sqrt{k\ k_0}}{\alpha}\kappa\Lambda N(\alpha a)\cot^2\Psi$$
$$\times\cos\Psi\ I_1(\alpha r)\exp\left[i\int_0^z k(\omega,z_\eta)dz_\eta - i\omega t\right], \tag{4.2.44}$$

$$E_\theta^-(r,z,t) = \frac{i\mu_0}{2\pi^2 a}\int_0^{+\infty} \frac{j_0\omega\kappa}{\alpha}\sqrt{\frac{k_0}{k}}N(\alpha a)\cot^2\Psi\ \cos\Psi$$
$$\times I_1(\alpha r)\exp\left[i\int_0^z k(\omega,z_\eta)dz_\eta - i\omega t\right]. \tag{4.2.45}$$

Similar expressions for the fields are obtained for $r > a$:

$$E_r^+(r,z,t) = \frac{i\mu_0}{2\pi^2 a}\int_0^\infty \frac{j_0\omega\sqrt{k\ k_0}}{\alpha^2}\kappa\Lambda I_1(\alpha a)K_0(\alpha b)N(\alpha a)$$
$$\times\left(-I_1(\alpha r) + \frac{I_0(\alpha b)}{K_0(\alpha b)}K_1(\alpha r)\right)I_1(\alpha a)K_0(\alpha b)\ \cos\Psi$$
$$\times\cot^3\Psi\ \frac{N(\alpha a)}{F(\alpha a)}\exp\left[i\int_0^z k(\omega,z_\eta)dz_\eta - i\omega t\right], \tag{4.2.46}$$

$$B_\theta^+(r,z,t) = -\frac{\mu_0}{2\pi^2 a c^2}\int_0^\infty \frac{j_0\omega^2\sqrt{k_0}}{\alpha^2\sqrt{k}}\kappa\aleph I_1(\alpha a)K_0(\alpha b)N(\alpha a) \times \frac{I_1(\alpha a)K_0(\alpha b)N(\alpha a)}{F(\alpha a)}\left(I_1(\alpha r) - \frac{I_0(\alpha b)}{K_0(\alpha b)}\right) \times \cot^3\Psi\ \cos\Psi\ \exp\left[i\int_0^z k(\omega, z_\eta)dz_\eta - i\omega t\right], \tag{4.2.47}$$

$$B_r^+(r,z,t) = -\frac{\mu_0}{2\pi^2 a}\int_0^\infty \frac{j_0\sqrt{k\ k_0}}{\alpha}\kappa\Lambda\frac{K_1(\alpha b)I_1(\alpha a)}{I_1(\alpha b)J(\alpha a)} \times \left(-I_1(\alpha r) + \frac{I_1(\alpha b)}{K_1(\alpha b)}K_1(\alpha r)\right) \times \cot^2\Psi\ \cos\Psi\ \exp\left[i\int_0^z k(\omega, z_\eta)dz_\eta - i\omega t\right], \tag{4.2.48}$$

$$E_\theta^+(r,z,t) = \frac{i\mu_0}{2\pi^2 a}\int_0^\infty \frac{j_0\omega\kappa}{\alpha}\sqrt{\frac{k_0}{k}} \times \frac{K_1(\alpha b)I_1(\alpha a)}{I_1(\alpha b)J(\alpha a)}\left(I_1(\alpha r) - \frac{I_1(\alpha b)}{K_1(\alpha b)}K_1(\alpha r)\right) \times \cot^2\Psi\ \cos\Psi\ \exp\left[i\int_0^z k(\omega, z_\eta)dz_\eta - i\omega t\right]. \tag{4.2.49}$$

4.2.7 Comparison of the model and PIC simulations

Here, we present the comparison of simulations performed with DoPPLIGHT and SOPHIE for $E_r(r,z,t)$, the radial electric field which is responsible for the focusing of the proton beam, in Fig. 4.11(a) for HC, (b) for HCT, (c) for VHC and (d) for VHCT. We also present the current propagating in the helical coil $j_0/\sin\Psi$, the discharge current, which creates the electric and magnetic fields, is shown in Fig. 4.12(a) for HC, (b) for HCT, (c) for VHC and (d) for VHCT. The calculation parameters are described in Sec. 4.2.3.3 for a helical coil of radius $a = 0.5$ mm and of pitch $h = 0.35$ mm. The radius of the tube for HCT and VHCT, is $b/a = 1.4$. The graphs show good consistency between the model and the PIC simulations in the case of VHC and VHCT. The average error is of the order of 20% for Figs. 4.11(a) to 4.12(b) and of 33% for Figs. 4.12(c) and (d). It is always smaller than the typical measurement errors.

4.2.8 Proton acceleration in the helix

In this subsection, we apply the electric fields to accelerate protons and compare the spectrum at the end of the coil computed by SOPHIE and DoPPLIGHT. We present results for VHC in Fig. 4.13(a) and VHCT in (b). The average error of 33% is smaller than the errors of measurements as discussed above. A comparison of panels (a) and (b) shows that the use of a tube allows an increase in the cut-off energy from 10 MeV to 11 MeV and a bunching effect for the protons at 10 MeV. This is explained by the suppression of the coil dispersion by the tube and a better coupling between the field and the particles. Moreover, the number of protons with energies above 3.5 MeV is increased by a factor of 20 compared to the input spectrum. The bunch at high energy is due to the accelerator field at the front of the current pulse (see Fig. 4.7) and the bunch at low energy is due to the decelerator field at the back of the current pulse. More results

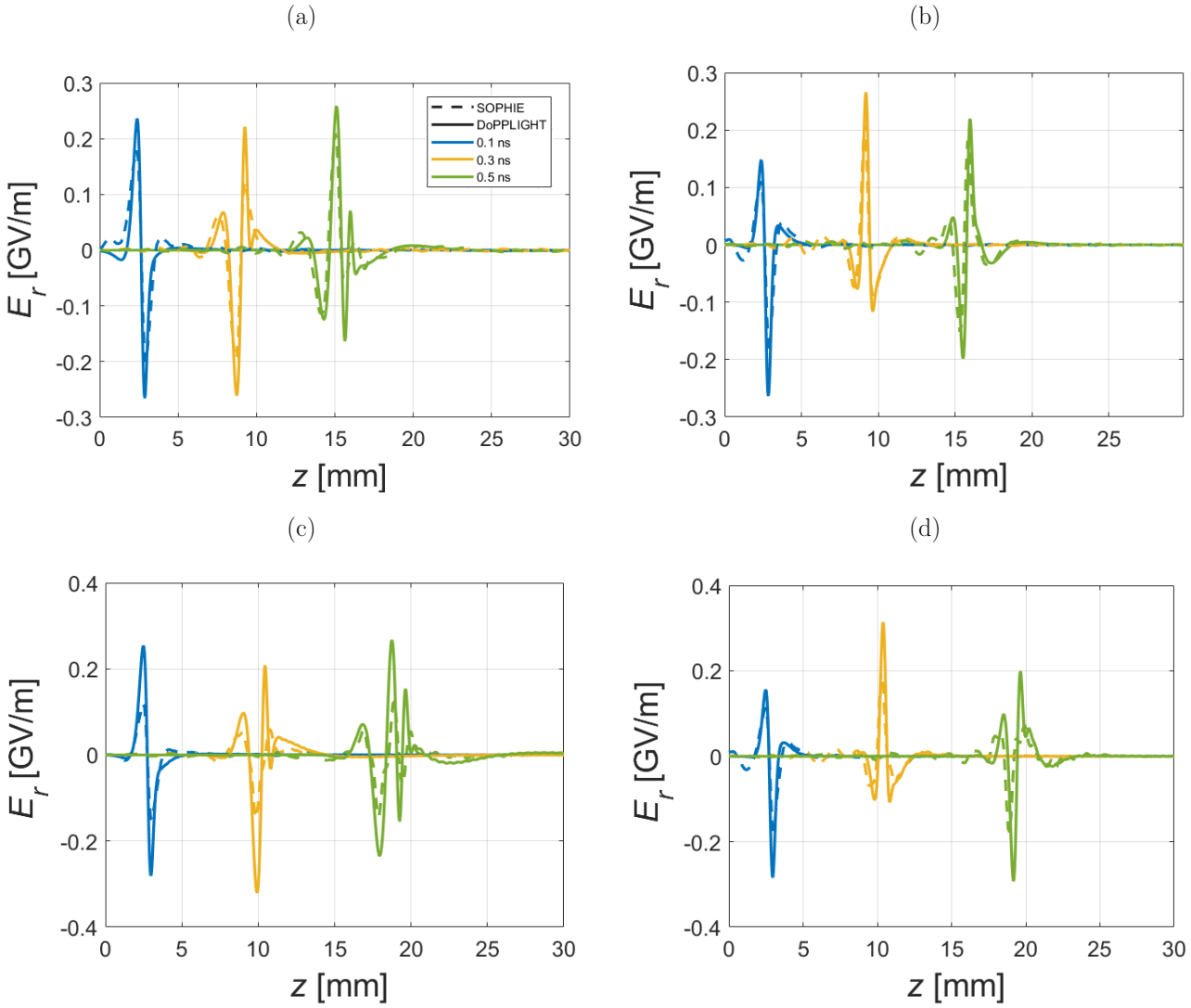

Figure 4.11 – Coordinate dependence of the axial electric field E_r at $r = 0.2$ mm for the coil without (a) and with tube (b), and for a pitch varying linearly for the coil without (c) and with tube (d) at 0.1 ns after emission time (blue curve), at 0.3 ns (yellow curve) and at 0.5 ns (green curve). Dashed lines show the result of the PIC simulation (SOPHIE), and solid lines are obtained with DoPPLIGHT code. The helix radius is 0.5 mm, the pitch 0.35 mm, and the tube radius is 0.7 mm.

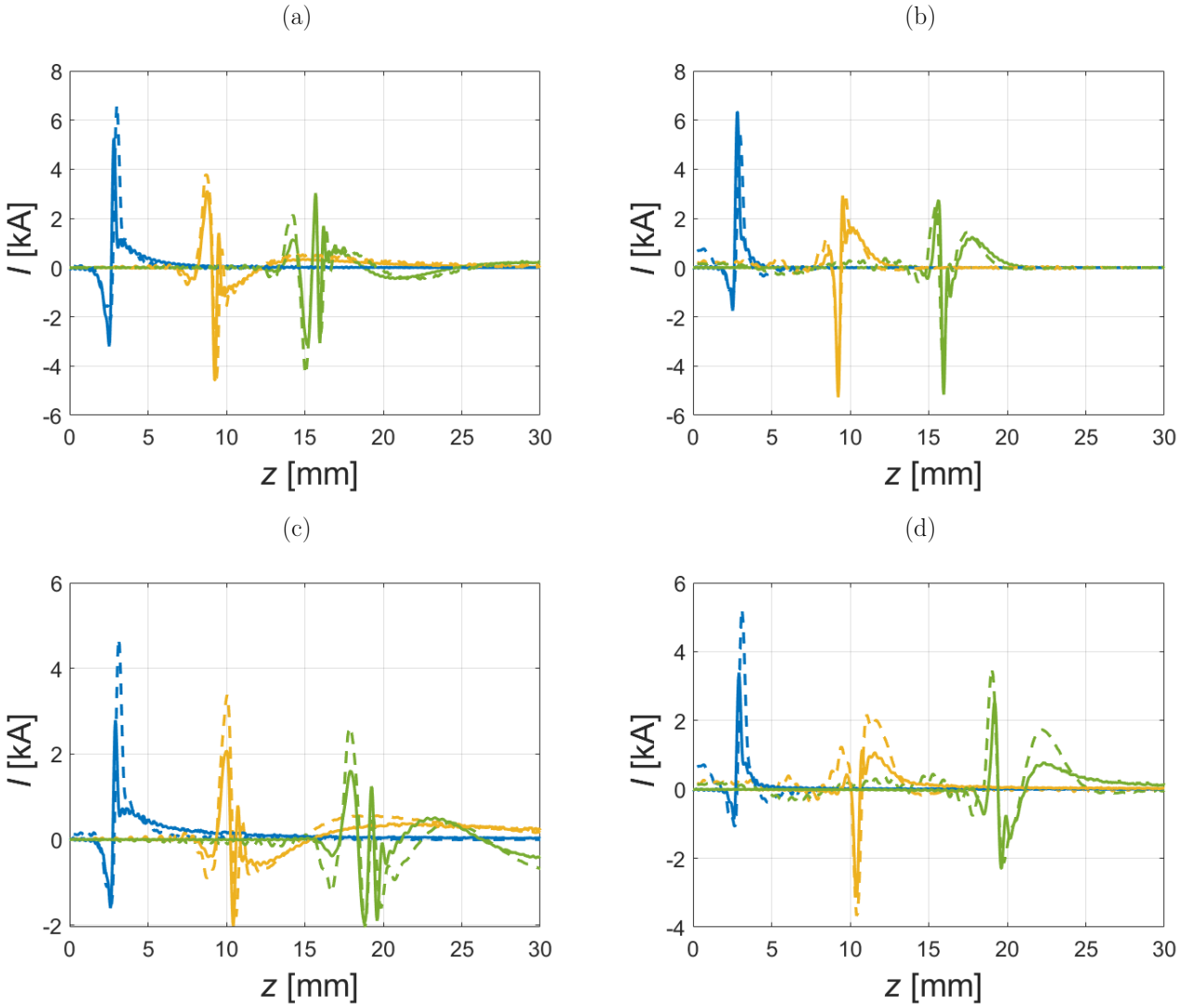

Figure 4.12 – Coordinate dependence of the current that propagate in the helix $j_0/\sin\Psi$ for the coil without (a) and with tube (b), and for a pitch varying linearly for the coil without (c) and with tube (d) at 0.1 ns after emission time (blue curve), at 0.3 ns (yellow curve) and at 0.5 ns (green curve). Dashed lines show the result of the PIC simulation (SOPHIE), and solid lines are obtained with DoPPLIGHT code. The helix radius is 0.5 mm, the pitch 0.35 mm, and the tube radius is 0.7 mm.

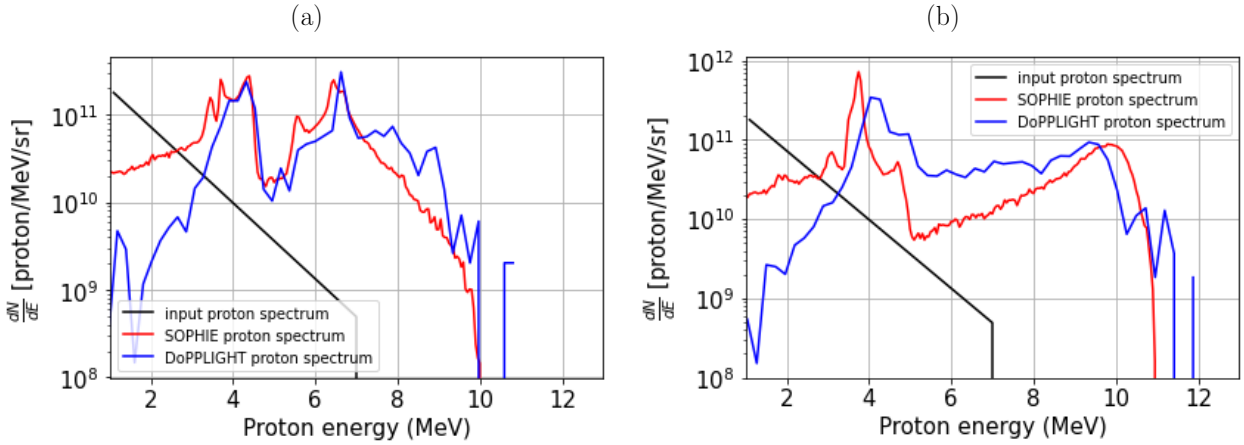

Figure 4.13 – Energy distribution of the protons accelerated in the helical coil without tube (a) and with tube (b) calculated with SOPHIE code (red line) and DoPPLIGHT code (blue line). Black line shows the input proton spectrum. The parameters of the coil and the current are given in the text.

and comparisons between HC and HCT are given in Ref. [5].

The proton spectra obtained with both DoPPLIGHT and SOPHIE are quite similar, see Figs. 4.13(a) and (b). As depicted in Fig. 4.9, the number of protons with energy larger than 3.5 MeV is increased by a factor of 20 compared to the TNSA spectrum. The positions of peaks in the energy spectrum and the cut-off energies are similar in DoPPLIGHT and SOPHIE calculations.

Discrepancies between our model and SOPHIE simulations are deemed acceptable due to shot-to-shot fluctuations observed in experiments and discussed in section III. This similarity in error magnitude suggests consistency in the computational outcomes of our model.

4.2.9 Optimization of the pitch variation for a synchronized field with protons

4.2.9.1 Fields variation with helix parameters

In the objective to know the pitch variation, we need to understand how the fields depend on the coil parameters (radius a and pitch h). Fig. 4.14 show that the longitudinal electric field and the radial electric field, which are respectively responsible for the post-acceleration and the focusing of the protons, are maximum at low radius (Fig. 4.14.a) and pitch (Fig. 4.14.b). Indeed, Fig. 4.14 show that the maximum electric field decreases exponentially with both the helix radius and pitch. However, the decrease is more pronounced with the pitch, as indicated by the steeper slope. To maximize the effect of the helical coil on the proton beam, both the radius and pitch should be minimized. Nevertheless, for a given characteristic energy, reducing the pitch is more effective than reducing the radius, and should therefore be prioritized in the coil design.

Indeed, the geometry of the helical target directly controls the amplitude of the electric fields experienced by the ions. In particular, reducing the radial electric field for instance by increasing the pitch or the radius of the helical coil leads to a weaker transverse focusing of the proton beam.

Similarly, increasing the pitch or the radius of the helical target reduces the longitudinal electric field, which is responsible for the post-acceleration of the ions. As a consequence, a weaker longitudinal field results in a reduced post-acceleration efficiency and therefore in a lower proton cut-off energy. A careful balance must therefore be found in the target design to simultaneously ensure the synchronism between ions and the pulse without too much mitigation of the electric field.

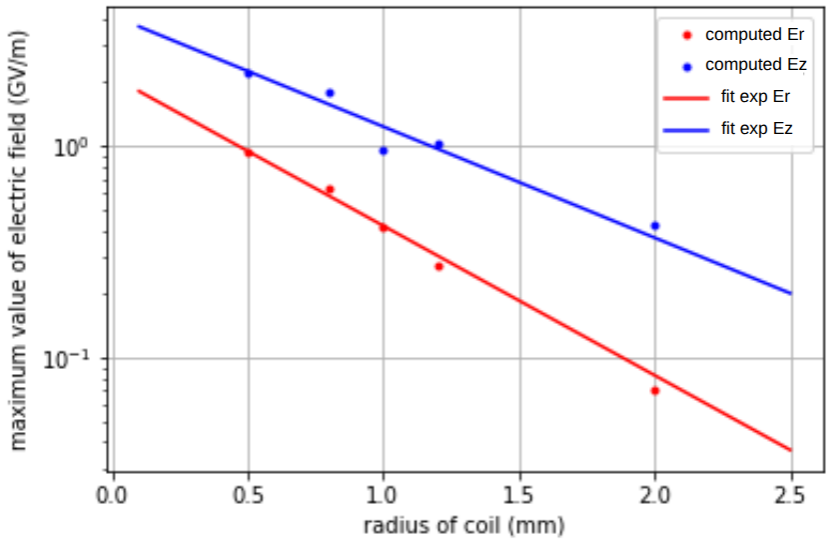

(a)

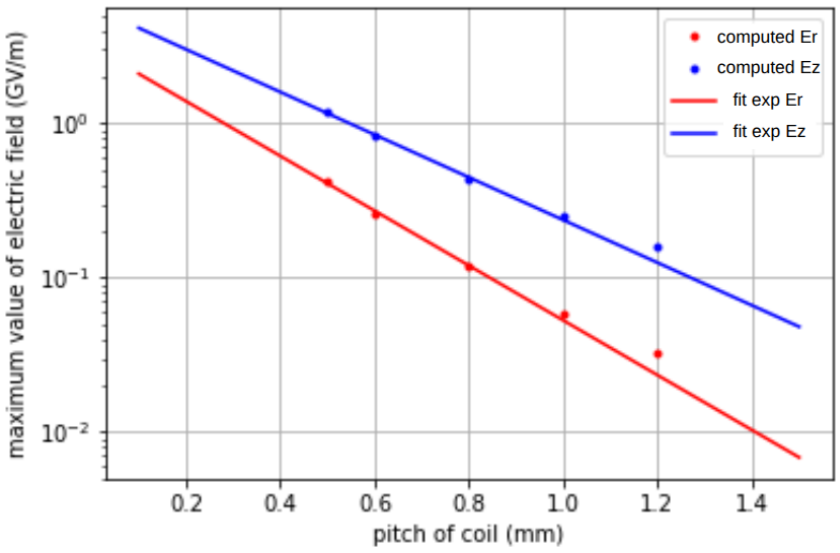

(b)

Figure 4.14 – Dependence of the computed maximum electric fields generated by the helical coil on its geometrical parameters. (a) Computed (using the analytical model presented in this chapter) longitudinal (E_z, blue curve) and radial (E_r, red curve) electric fields as a function of the coil radius a. (b) Computed longitudinal (E_z, blue curve) and radial (E_r, red curve) electric fields as a function of the coil pitch h. The dots represent the analytical values of the electric fields and the solid line represent the exponentially decreasing fit.

Although reducing the coil pitch is more effective than reducing the coil radius for enhancing

the electric fields, practical fabrication constraiunts limit the extent to which the radius can be decreased. In particular, the finite thickness of the wire used to construct the helical target imposes a lower bound on the achievable radius, making further reduction technically complicated. To address this limitation, we develop an analytical model aimed at synchronizing the maximum of the electric field with a selected population of protons. This model account for the proton acceleration dynamics as they propagate along the helical structure. Such a synchronization approach could provide a novel path to optimize the helical coil post-acceleration without relying solely on geometric minimization of its parameters.

4.2.9.2 Description of analytical expression

In this analytical work, we would like to get an equation to synchronize the electric field with a proton during all its propagation inside the helical coil. To do it, we are starting from energy conservation:

$$(\gamma - \gamma_0)mc^2 = \int_0^z eE_z dz \tag{4.2.50}$$

,

with $\gamma = \frac{1}{\sqrt{1-\frac{v_p^2}{c^2}}}$ the Lorentz factor associated to the proton velocity v_p, $\gamma_0 = \frac{1}{\sqrt{1-\frac{v_p(z=0)^2}{c^2}}}$, E_z the longitudinal electric field, m_p the proton mass, e the elementary charge. In our case of synchronization of the fields with the protons, we search for the wave phase velocity $v_\phi = v_p$. Therefore, one can express the phase velocity such as :

$$v_\phi(z) = c\sqrt{1 - \frac{1}{\left(\frac{e}{m_p c^2}\int_0^z E_z dz + \left(1 - \frac{v_{\phi 0}^2}{c^2}\right)^{-1/2}\right)^2}} \tag{4.2.51}$$

Thanks to equation 4.2.51 and knowing that $v_\phi(z) = \frac{c}{\sqrt{1+(\frac{2\pi a}{h(z)})^2}}$ one can know the expression of the pitch $h(z)$:

$$h(z) = \frac{2\pi a}{\sqrt{\frac{1}{1-\frac{1}{\left(\frac{e}{m_p c^2}\int_0^z E_z dz + \left(1-\frac{v_{\phi 0}^2}{c^2}\right)^{-1/2}\right)^2}} - 1}} \tag{4.2.52}$$

4.2.9.3 Proton spectrum results

To compute numerically the eq. 4.2.52, we have to compute the maximum electric field as function of z in DoPPLIGHT with a constant pitch first. Then, we recompute the electric field knowing $h(z)$. With some iterations, it converges to the pitch profile shown in Fig. 4.15.a and the corresponding characteristic energy of the helical coil in Fig. 4.15.b. The impact of this pitch on proton spectra, computed using DoPPLIGHT and presented in red in Fig. 4.15.c, is to increase the proton energy up to the maximal characteristic energy such as described in the

(a)

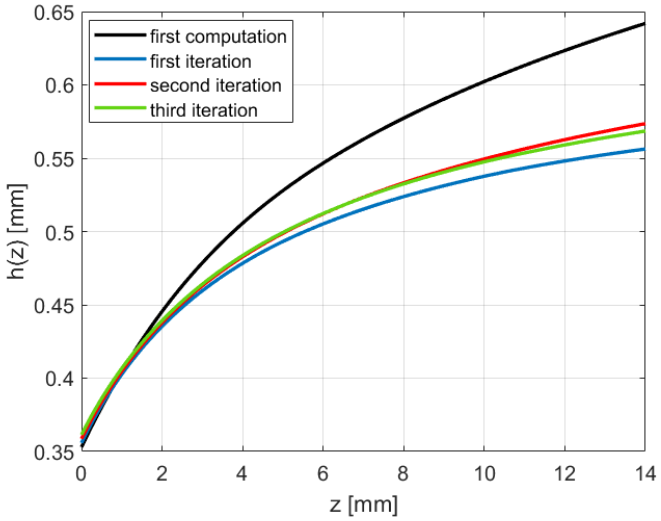

(b)

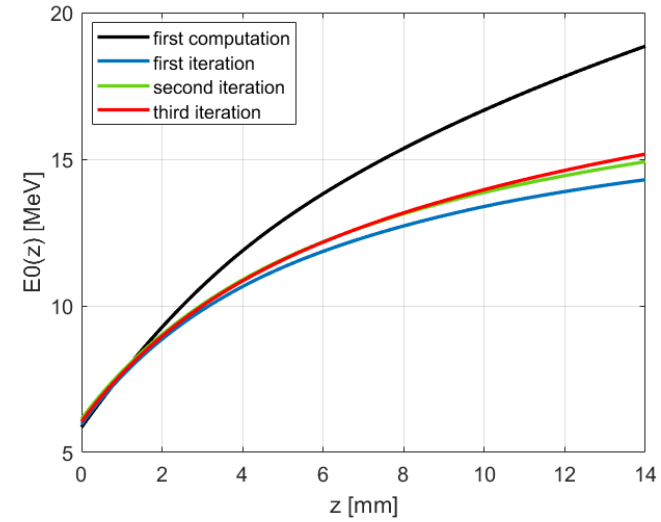

(c)

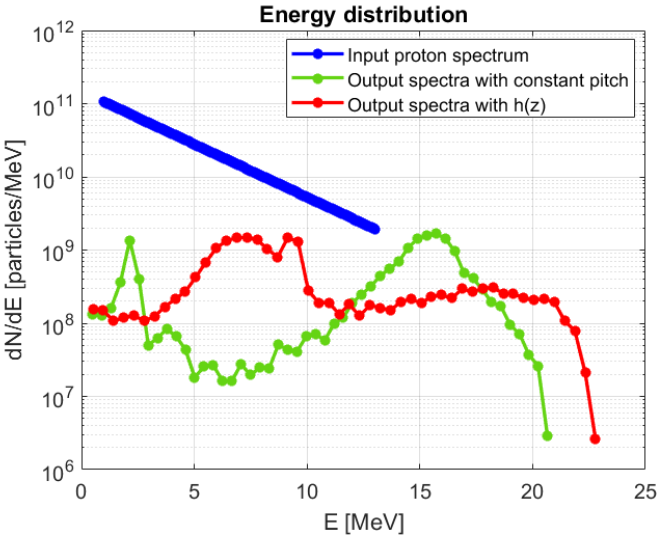

Figure 4.15 – a) Pitch and b) characteristic energy variation get thanks to the model described in eq. 4.2.52 for a current discharge corresponding to an electron emission of 600 nC. c) Proton spectra get with TNSA (blue curve), varying pitch (red curve) and constant pitch (green curve).

model. However, if we compare to the constant pitch (green curve), we see a lower bunching effect in energy of the varying pitch. Indeed, the theoretical model, takes into account only one proton and does not take into account the dynamic effect of the beam, such as the space charge. The space charge is higher at high energy (above characteristic energy), therefore, the number of protons which is synchronized with the electric field decreases. To increase the bunching energy with a varying pitch, the discharge pulse should be of higher intensity to compensate the effect of the space charge. But in experiments, if we increase the discharge current, we also increase the number of protons at high energy and therefore, the space charge, and finally, we cannot get a better result with this theoretical model.

4.2.10 Conclusion

In this work, we develop an analytic description of the current propagation in a helical coil with a screening tube and varying geometry. The tube mitigates the coil dispersion and maintains a quasi-constant pulse shape and propagation velocity. In addition, a gradual increase of the coil pitch allows to accelerate the pulse along the propagation direction and maintain resonance with the accelerated particles over a longer distance.

The model is implemented numerically in the code DoPPLIGHT, and its accuracy is demonstrated by comparing it with the results of PIC simulations. Good agreement is obtained for coils with a constant pitch and radius with and without a tube. Furthermore, the comparison is extended to the case of a linearly varying pitch.

We demonstrated that coil screening and pitch stretching allows optimizing the proton acceleration. An increase in the number of high-energy protons by an order of magnitude was observed, together with an increase in the maximum proton energy by 20% and a focusing of the particles on the coil axis.

Thanks to this model, we optimize of the helical coil geometries to increase the cut-off energy and the number of high energy protons (note that [81] propose another approach to synchronize the fields). We have seen that the radial and longitudinal electric fields decrease exponentially with increasing pitch and radius of the helical targets. Accordingly, an optimization was proposed that accounts for these field reductions while maintaining the synchronization of the protons with the discharge current throughout the post-acceleration. The utilization of a more powerful laser beam could also be interesting because of an increased discharge current and so, a better proton acceleration and focusing.

Further future improvements of the model foresee taking into account the current reflection due to the helix inhomogeneity along the propagation direction. Currently, the model neglects the coil resistance, and the retro-action of the particles on the electric field. The perfect conductor is a good approximation because the resistance of a realistic coil is about 10 mΩ (accounting for the skin effect), so, the resistive electric field is much smaller than the inductive electric field. Adding the retro-action of particles will slow down the performances of the DoPPLIGHT code, and, in our cases, this contribution is negligible [82].

Nevertheless, the model is sufficiently accurate and allows to perform a large number of

simulations in a few minutes. It is an excellent tool for optimizing the helical coil geometry for the proton post-acceleration, bunching and focusing.

Building on these insights, it is essential to confront the predictions with experimental validation in order to assess both the robustness of the models and their practical relevance. In this context, an experimental campaigns were carried out and reported in next chapter.

Chapter 5

Experimental Investigation of the Impact of Helical Coil on Laser-driven Protons and Ions

Sommaire

5.1 Foreword

Thanks to the modeling work presented in the previous chapter, we were able to design new helical targets specifically tailored for the experiment conducted at the ALLS laser facility at INRS (Canada). The primary objective of this experiment was to achieve an experimental validation of helical coil targets with a screening tube (HCT). Unfortunately, due to assembly issues, such as misalignment between the tube and the coil, and possible physical contact between them, as well as a lower-than-expected current generation, this initial goal could not be achieved.

However, the performance of helical coil targets without tubes was successfully demonstrated, and good agreement between simulations and experimental results was observed [83]. The second objective of the experiment was to implement, for the first time, a Thomson parabola (TP) as the main diagnostic tool to measure the proton energy spectrum at the coil exit. Until this experiment, in all experiments involving helical targets, only radiochromic films (RCFs) had been used for this purpose. RCFs are considerably easier to implement than a TP, since the focused nature of the proton beam exiting the coil ($\pm 2^\circ$ divergence) requires extremely precise alignment between the coil and the TP. This technical challenge was successfully overcome, allowing the observation also for the first time of a significant effect of the coil field on carbon ions [83].

Following this experiment, new helical targets were optimized to focus, post-accelerate, and bunch carbon ions [83]. This chapter presents the experimental setup and procedures employed in this campaign, as well as the main experimental results obtained on proton and carbon ion focusing and post-acceleration. The simulation input parameters used to align numerical results with measurements are also detailed. The chapter concludes with a presentation of simulation results for new helical geometries optimized for carbon ion manipulation.

5.2 Methodology

In this experiment, we used solid tantalum foils of $2\,\mu$m thickness as interaction targets for producing the ion acceleration. The choice of a tantalum target is motivated by the ion beam stability demonstrated in a previous study [20]. A schematic of the experimental setup for the ion acceleration using HC is depicted in Fig. 5.1. The helical coil target setup was assembled by inserting a circular piece of foil with a radius equal to the radius of the helical coil, which had been cut out of a $2\,\mu$m tantalum foil by ultrafast laser micromachining. The use of a screening tube does not permit an alignment by the rear side of the foil. The laser cutting of the tantalum foil allows to align the helical coil target by the front side. In this alignment process, the laser beam must be focused on the front side of the target foil but also on the coil center. Therefore, the coil edges must not be hidden by the foil. Fig. 5.2 shows the helical coil without (a) and with (b) the target foil. The method for the target foil cutting is presented in Sec. 5.2.1 and the ion acceleration experiment with HC using a Ti:Sapphire laser is presented in Sec. 5.2.2.

5.2.1 Laser cutting of the TNSA target

Femtosecond laser micromachining is a universal tool allowing for very precise processing of any material thanks to the extremely short interaction time of the laser beam with the material [84]. Thermal diffusion is suppressed in this regime and thus reduces the formation of a heat affected zone even in high thermal conductivity materials such as metals [85]. Moreover, transparent materials like dielectrics can be modified very locally in the bulk by non-linear absorption within the laser focus [86].

For the target fabrication, micro-cutting of small disks of 1 to 3 mm diameter out of a 2 μm thickness tantalum foil has been performed (see Fig. 5.2b.) using a commercially available Yb-doped femtosecond laser source (Tangor 100, Amplitude) operating at 1030 nm wavelength [87] coupled to a home-built micro-machining station [88]. The cutting process was performed using a repetition rate of 20 kHz and an average power of 0.67 W, corresponding to a fluence of 8.5 J/cm^2. The trajectories for cutting the circles out of the metal foil were done using a galvo scanner (IntelliScan III-14, Scanlab) equipped with a focusing lens of 100 mm. The scanning velocity was 10 mm/s, and the cutting process was done in a single pass. The sample was held self-supported using two spring pliers with a distance of 12 mm between the pliers. Once the samples have been cut, the disks fall down into a plastic cup. Then all disks are sorted with a micro-suction device and stored in a membrane box. Finally, the dimensions of the disks have been measured with a measuring microscope equipped with a 20x objective (MF-B1010D Mitutoyo).

This target fabrication method, by ultrafast laser processing, allows for extremely precise cutting without causing damage, thereby preserving the quality of the TNSA during the experiments. The TNSA process relies on perfectly flat targets with minimal imperfections, which optimize the acceleration process during TNSA. In other cutting processes, targets may become folded, creased, or torn, which can disrupt the laser-plasma interaction, reducing the ion energy cut-off and the number of accelerated ions

5.2.2 Experimental setup for ion acceleration

The experiments were performed on the laser-driven ion acceleration beamline of the Advanced Laser Light Source (ALLS) at the INRS in Varennes, Canada. We used the ALLS 150 TW Ti:Sapphire laser (λ_0 = 800 nm) system delivering 3.2 J on target with a pulse duration of τ_{FWHM} = 22 fs at Full-Width-Half-Maximum (FWHM). The experimental setup (Fig. 5.1) uses an $f/3$ off-axis parabola (OAP) to focus the 95 $\times$ 95 mm^2 beam (at e^{-2}) down to a spot size of $w_{\mathrm{FWHM}} \approx 5$ μm. Parabola alignment and wavefront optimization, using a feedback loop between a wavefront sensor and a deformable mirror, are both performed at full laser power, which allows to compensate aberrations arising from thermalization in the laser system. This results in a peak intensity I_0 around 1.3×10^{20} W/cm^2 [20, 73]. Prior to entering the second Chirped Pulse Amplification(CPA) [13] amplification stage, a cross-wave polarizer (XPW) and a booster stage relying on a saturable absorber are employed to clean the incoming laser beam,

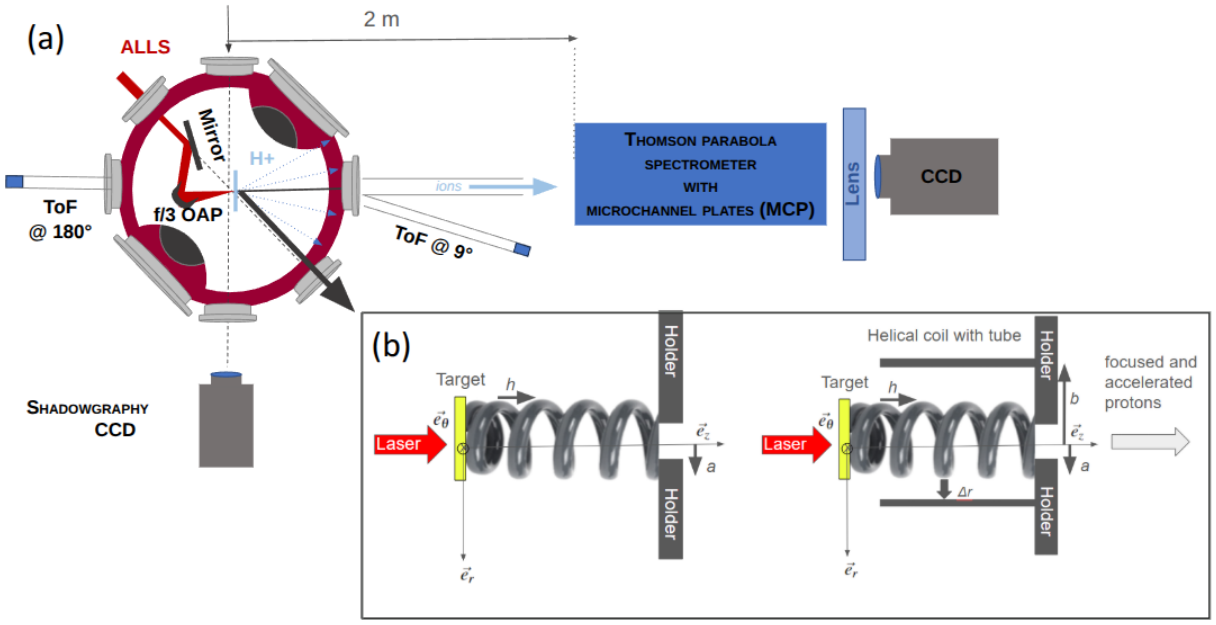

Figure 5.1 – a) Top-view of the experimental setup for the laser-driven ion acceleration using helical coil targets. b) Scheme of a single helical coil and a helical coil with a tube. The tube is axially symmetric.

achieving an Amplified Spontaneous Emission (ASE) pre-pulse contrast $<10^{-10}$ at -100 ps before the main pulse, along with a steep power rise with contrast $<10^{-6}$ at -3 ps.

The p-polarized laser pulses are incident at an angle of 20°, to avoid specular reflections, with respect to the target-normal on the circular 2-μm-thick tantalum foils at the tip of the helical coils to produce ion beams using the TNSA regime. The energy distribution of the accelerated ions is measured using a calibrated Thomson Parabola (TP) spectrometer positioned at 0° with respect to the target-normal axis, employing a double Micro-Channel Plate (MCP) [73] detector in Chevron configuration with a P43 phosphor screen, allowing to acquire images of the ion spectra for each laser shot. The Thomson parabola spectrometer is used to identify ions and measure their energy by dispersing charged particles according to their charge-to-mass ratio and kinetic energy using both electric and magnetic fields. The resulting parabolic traces on the detector allow simultaneous species discrimination and energy-resolved ion spectroscopy. Additionally, Time-of-Flight (ToF) spectrometers are employed at 9° and 180° from the main axis, monitoring the number of protons and their energies in correlation with the TP spectrometer. These ToF spectrometers are primarily used to get an on-line verification of the laser-plasma interaction during high repetition rate experiments [89]. This diagnostic is used to characterize proton emission by measuring the arrival time of particles at a detector placed at a known distance from the interaction point. Finally, we employed RadioChromic Films (RCF) of type EBT3 to measure the angular distribution of the ion beam. We position the RCF at the distance of 50 cm centered on the proton beam axis. After irradiation, the RCF were scanned with an Epson Perfection 2450 scanner.

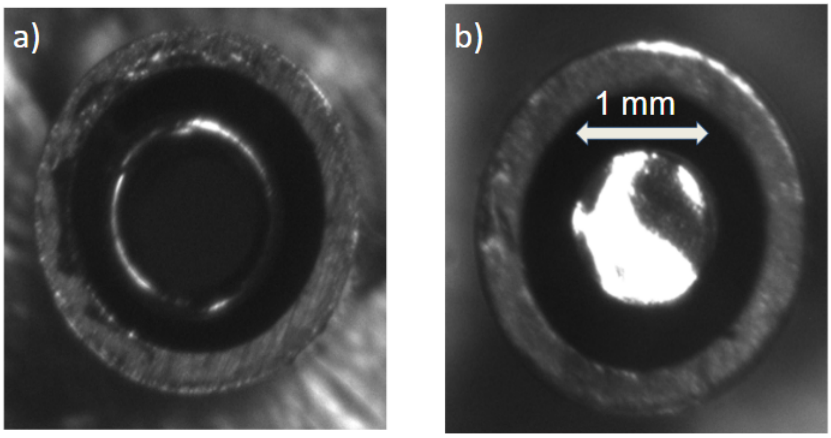

Figure 5.2 – Microscope image of the helical coil a) without target b) with cut out target filed and pasted on the helical coil.

5.3 Experimental results

5.3.1 Proton acceleration and focusing

Figure 5.3.a presents the proton spectrum measured for an HC of 5 mm length (red curve), compared to the classical TNSA spectra obtained on the same day at INRS (black curve) and to the background noise (blue curve). The HC geometry has been chosen based on previous simulations [5, 61] to synchronize the electric field propagation velocity with proton velocity having energy $E_{HC} = \frac{1}{2} m_p V_{HC}^2 = 4$ MeV (stable energy within the proton spectrum for the ion beamline at ALLS), where $V_{HC} = hc/\sqrt{h^2 + 4\pi^2 a^2}$ is the phase velocity and m_p is the proton mass.

One can see, that the use of the helical coil increases the cut-off energy from 4 MeV to 5 MeV, enhances the fluence for protons above 2.4 MeV, and reduces the number of low-energy protons. This reduction of low-energy protons is attributed to space charge effects, as discussed in previous work [5, 62].

Figure 5.3.b depicts an RCF, placed at 50 cm from the TNSA target, which clearly shows a reduced angular dispersion, about 2.3° with our HC compared to 20° as obtained for classical TNSA. The opening angle of the helical coil is 6.8°, which confirms that the angular dispersion is reduced thanks to the focusing effect of the helical coil and not just a filtering effect.

5.3.2 Carbon ions measurement

During the TNSA process, multiple ion species are accelerated, predominantly protons and carbon ions. Until now, no laser experiments have demonstrated an effect of helical coil targets on carbon ions. This is likely because, in most cases, these experiments were conducted with a stack of RCF as a unique diagnostic tool, without the use of a Thomson parabola spectrometer. Carbon spectra are presented in Fig.5.4.a. Dotted lines represent carbon ions spectra under the influence of HC, while the solid line shows the spectra without the influence of the HC. The black solid line denotes the background noise for carbon ions. This figure shows a decreased number

(a)

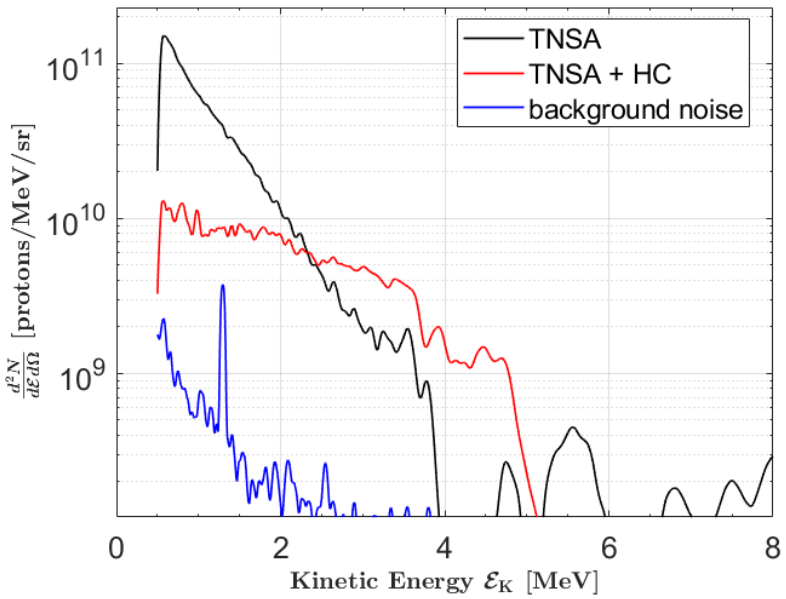

(b)

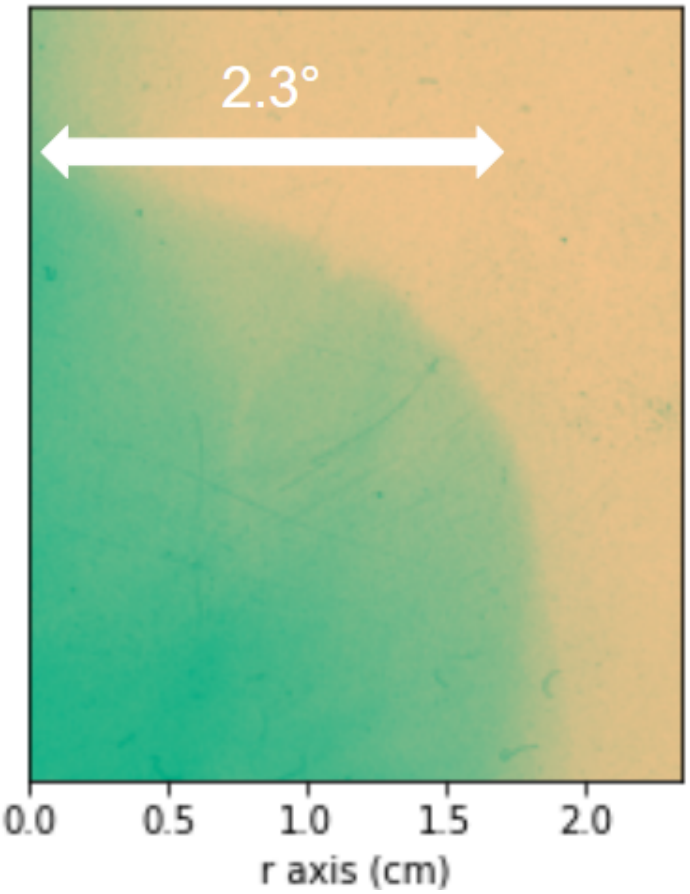

Figure 5.3 – a) Comparison of proton spectra between a helical coil of radius a =0.6 mm, step h =0.35 mm and length L =5 mm and standard TNSA proton spectra (2 μm tantalum foil). b) RCF scan showing the beam radius and highlight the focusing effect, reducing the angular dispersion from 20° half angle obtained with TNSA, compared to 2.3° obtained with an HC.

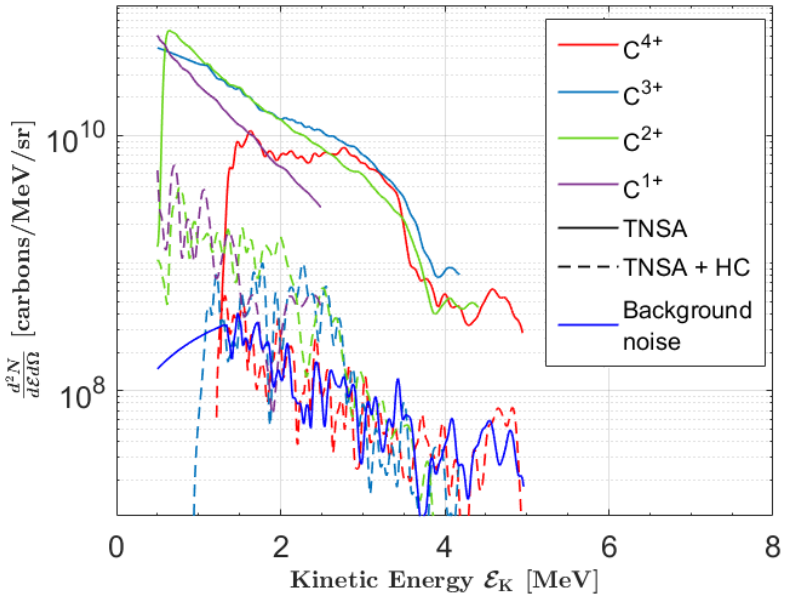

(a)

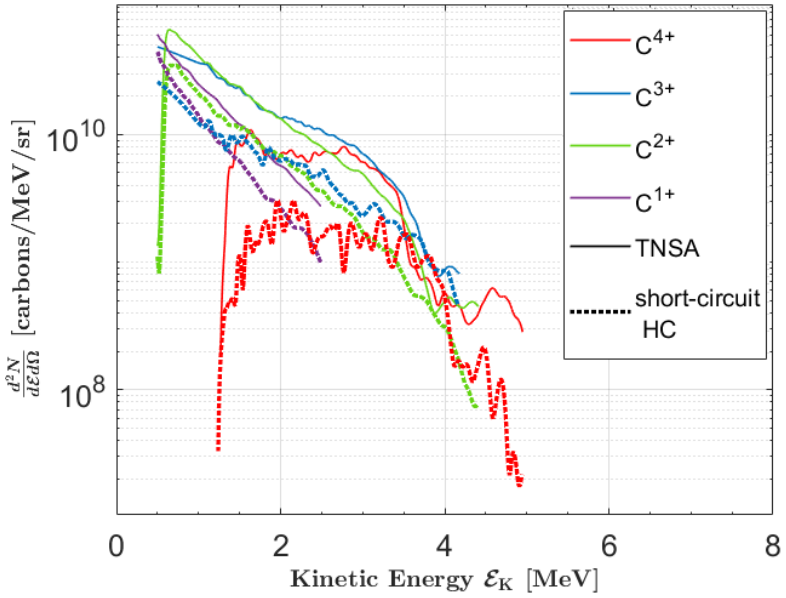

(b)

Figure 5.4 – Comparison of carbon spectra between a) a helical coil (dashed line) of radius a =0.6 mm, pitch h =0.35 mm and length L =5 mm b) a short-circuited helical coil (dotted lines) and the TNSA carbon spectra (solid lines).

of carbon ions, from 10^{10} without to 10^{9} with HC. The cutoff energy of the TNSA carbons is 2.5 MeV for C^{1+} and 4 MeV for C^{2+}, C^{3+}, C^{4+}. In contrast, with the HC, the signals above 2.5 MeV are indistinguishable from the background noise.

Figure 5.4.b shows the carbon ions spectra using a short-circuited HC (dotted lines) and the comparison to the TNSA without HC (solid lines). A short-circuited HC means that the HC is present but connected to the tube. Therefore, the major part of the current pulse does not propagate through the helix but in the tube. The short-circuited helical coil serves as a reference

to isolate the effect of the coil itself. If the number of carbon ions observed with a short-circuited helical coil is similar to the background noise, it indicates that the degradation of laser-plasma interaction quality caused by the helical coil is responsible for the reduced number of carbon ions, as shown in Fig. 5.4.a. Conversely, if the carbon ion yield with the short-circuited coil is comparable to that of the TNSA process, the reduced carbon ion production can be attributed to the discharge current propagating through the coil.

Figure 5.4.b demonstrates that the cutoff energy of carbon ions remains similar between the HC and TNSA cases, while the total number of carbon ions is reduced by a factor of two.

These comparisons reveal a clear effect of the HC on the carbon ions. In the short-circuited HC case, a carbon ion spectra similar to TNSA without HC is observed. However, when HC are employed, the number of carbon ions becomes comparable to the background noise level, illustrating a notable suppression of carbon ion. This suppression of carbon ion results from the increased space charge induced by the helical coil [62]. The HC focuses ions and de-focuses electrons, which induces a beam de-neutralization. This creates a significant space charge effect, causing the dispersion of the ions non-synchronized with the discharge current, which induces an explosion of the ion beam. For particles synchronized with the discharge current, the radial electric field generated by the current propagation through the helix [61] partially compensates for the space charge. However, for non-synchronized particles (i.e. the carbons, which are slower because their are heavier), no such compensation occurs, leading to beam dispersion and a reduction in the number of carbon ions by approximately a factor of 100. Finally, the particle beam produced at helix exit is composed of only one ion species: the protons. This helical coil property can be very usefull for medical applications.

5.4 Simulations

To shed light onto the current propagation within the helix we used the code SOPHIE [63]. SOPHIE is a 3D FDTD-PIC simulation code developed to solve Maxwell's equations in both vacuum and material environments. The code supports boundary conditions for perfect electric conductors, dielectrics, and magnetic materials. Relativistic particle motion in vacuum is governed by Newton's second law, solved using the Boris algorithm [90]. To ensure self-consistency, Buneman current collectors are implemented.

An important feature of SOPHIE is its ability to simulate current propagation through a helix using boundary conditions, such as perfect electric conductors, without requiring macroparticles. This design choice reduces computational constraints and facilitates large-scale simulations. Unlike traditional codes that resolve the laser wavelength, SOPHIE is optimized for simulations on grids spanning several centimeters and time intervals on the nanosecond scale. These capabilities make SOPHIE an optimal tool for studying the physics of Helical Coil Targets (HCT).

In our SOPHIE simulations, a helical coil is positioned at the rear side of a foil target. The target, coil, and holder are considered perfect conductors and are meshed at full scale with a cell size of $\Delta x = \Delta y = \Delta z = 20$ μm, yielding a total of 2×10^9 cells across a volume of 72 cm^3.

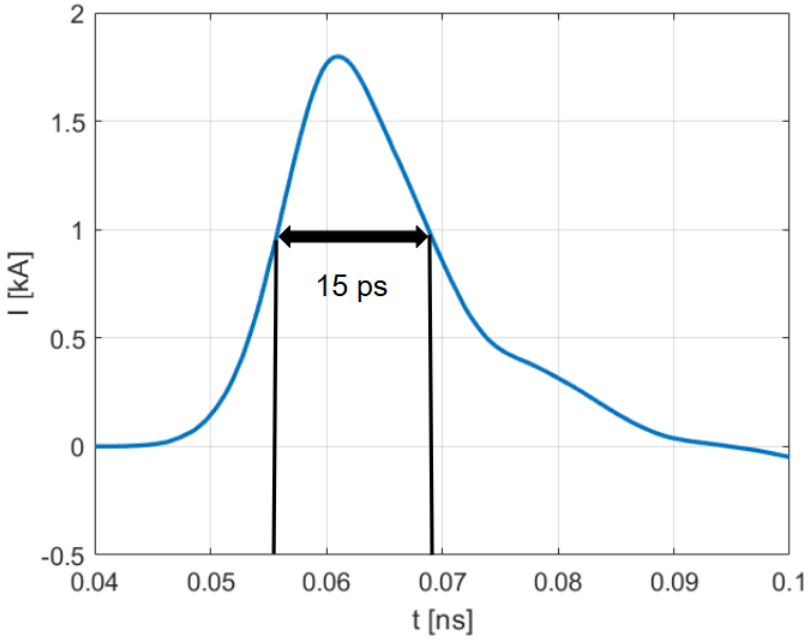

Figure 5.5 – Discharge current measurement in the SOPHIE simulation at the entrance of the helical coil as function of time.

Electrons, protons, and carbon ions are represented using 10 million macroparticles each.

Inputs for ion energy and angular distributions are taken from experimental data obtained with TNSA without HC. The input proton energy distribution is the one represented by the black curve in Fig. 5.3.a, and the ion ones are represented in blue and red curves respectively for C^{3+} and C^{4+} in Fig. 5.4.a. The angular distribution is modeled using a super-Gaussian function given by $dN_p/d\theta \propto \exp\left[-(\theta/\theta_p)^{10}/2\right]$, where $\theta_p = 19°$. The temporal emission profile dN/dt follows a Gaussian shape with a full-width at half-maximum (FWHM) duration τ of a 7 ps. The emission zones for protons and carbon ions are both set to a transverse size of 200 μm.

The proton and carbon ion dynamics within the helical coil are determined solely by the electromagnetic fields generated by the discharge current. To simulate this current, electrons are emitted isotropically with an energy distribution similar to that of the protons. The transverse size of the electron emission zone matches that of the protons and carbon ions (200 μm).

In these simulations, to fit with experimental results, the electron charge emission is set to 40 nC, while the proton charge emission is 5.6 nC, both emitted over a duration of 7 ps. Carbon ions are emitted with a total charge of 6.9 nC and 3.8 nC respectively for C^{3+} and C^{4+} over the same emission duration than protons.

The electron emission induces a discharge current in the helix of amplitude 1.8 kA and a pulse duration of 15 ps (FWHM), which matches perfectly with the values reported in the experiment of S. Kar et al [3] who measured 60 nC of electron charge and 15 ps of pulse duration for the discharge current. This current profile is shown in Fig. 5.5 where a rise time of 5 ps and a decay time of 10 ps are highlighted, which corresponds again to the experiment of S. Kar et al. [3]. The simulation results are shown in Fig. 5.6.a (blue curve).

In Fig. 5.6.a, the proton cut-off energy in the simulation is overestimated compared to the

(a)

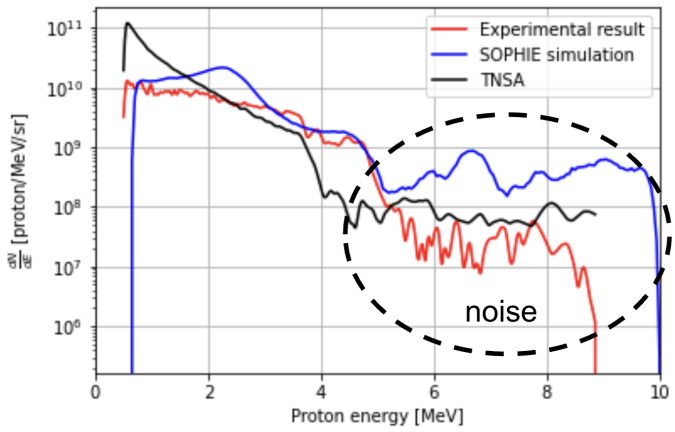

(b)

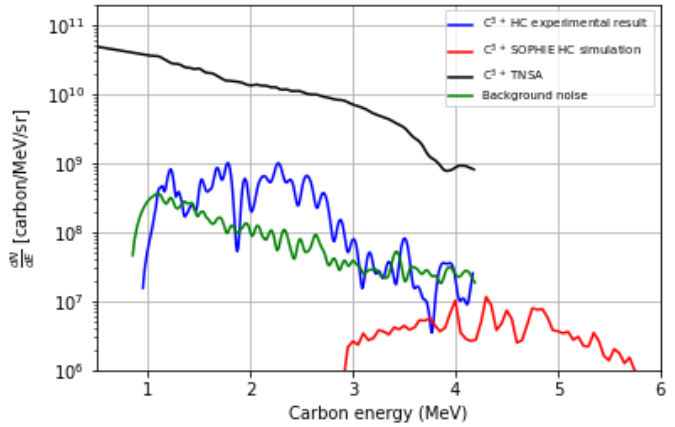

(c)

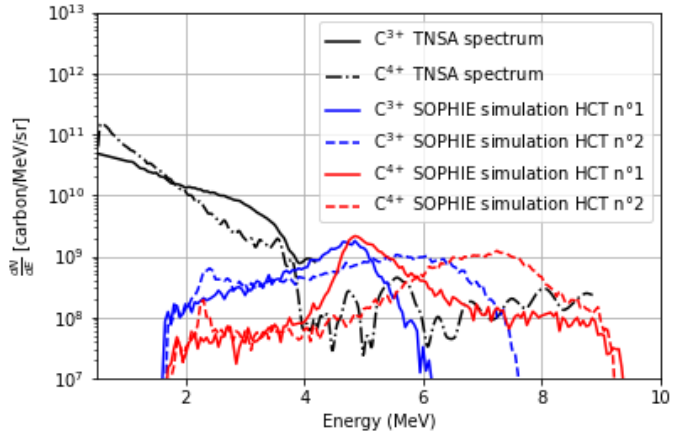

Figure 5.6 – a) Comparison of proton spectra between an experimental result using an helical coil (red line) of radius a =0.6 mm, step h =0.35 mm and length L =5 mm and the experimental TNSA proton spectra (black line) and the SOPHIE simulation for a current of 1.75 kA, of 15 ps at FWHM. b) Comparison of carbon spectra between an experimental result of helical coil (red line) of radius a =0.6 mm, step h =0.35 mm and length L =5 mm and the TNSA proton spectra (black line), the SOPHIE simulation which is comparable to the background noise in green. c) Comparison of carbon spectra between a helical coil simulated with SOPHIE of radius a =1.5 mm and a tube of radius $b = 2$ mm for HCT n°1 (solid line) or 1.8 mm and $b = 2.3$ mm for HCT n°2 (dotted line), step h =0.35 mm and length L =15 mm and the input carbon spectra (black line).

experimental data. During the experiments, the laser-plasma interaction creates a charge separation generating an electric field that accelerates the protons, and the most energetic electrons escape. However, for the simulations, we have to take into account a particle emission similar to that obtained by TNSA. Therefore, we create a fictive TNSA-like electric field which slightly accelerates protons on a distance of a few hundreds of micrometers with a field at the order of a hundred of GV/m. This added field is an artifact, but it cannot be removed from the simulation. To conclude, Fig. 5.6.a shows a good agreement between the experimental measurements and the simulations, with both showing the same number of protons in the plateau level and a cut-off energy of 5 MeV. This strong correlation validates the accuracy of our input parameters, enabling us to robustly and reliably design helical coils, specifically for carbon acceleration. In both the experimental data and the simulations, the proton spectrum above 5 MeV is dominated by noise. Consequently, the effective cut-off energy is 5 MeV, and higher-energy features are not considered physically meaningful.

In Fig. 5.6.b, the SOPHIE results show a decreased number of carbon ions, lower than the background noise level. Experimentally, the number of carbon ions obtained with the HC designed for the protons is of the same order as the background noise. This comparison confirms the validity of the results presented in Fig. 5.6.a and the input data used in the SOPHIE simulations.

Now that we have demonstrated that HC is not only acting on protons, but also on carbon ions, we can design new HCT geometries adapted to carbons. To optimize the HC geometries for accelerating protons, the phase speed V_{HC}, which corresponds to the longitudinal speed of a current pulse propagating at the speed of light along the helical coil, is computed. Its expression is given by $V_{HC} = hc/\sqrt{h^2 + 4\pi^2 a^2}$, where h is the pitch and a is the radius of the helix. This phase speed determines the group of particles that is synchronized with the electromagnetic pulse, having an initial energy $E_{HC} = \frac{1}{2} m_i V_{HC}^2$, where m_i is the ion mass. To predict the final energy of the ion bunch, we apply the scaling law presented in our previous work [5]. Here, we propose to use the same methodology we used for the design of new HCT geometries optimized for carbon ion acceleration, focusing and bunching.

Sophie simulations were performed using the same input datas as the ones who enabled us to recover the experimental spectra on protons and carbons (see Fig. 5.4.b). Figure 5.6.c presents the potential effects of the helical coil with a HCT on carbon ions, showing an increase in energy up to 9 MeV, energy bunching up to 7 MeV, and improved focusing, as indicated by the increased number of carbon ions per solid angle. This simulation result, based on experimental input data, demonstrates that HCT can also accelerate, focus and bunch carbon ions.

5.5 Conclusion

This study shows the impact of helical coil (HC) targets on the shaping of proton and carbon ion beams in laser-driven ion acceleration experiments. By employing the ALLS laser facility, we observed improvements in proton acceleration, increased cut-off energy, and enhanced

beam focusing. These results align with our previous theoretical and simulation-based studies, confirming the potential of HC targets for optimizing proton acceleration schemes.

This experiment is also the first one that demonstrates that helical coil targets can act on heavy ions. During the HC acceleration scheme, electrons are de-focused, which produces a de-neutralization of the particle beam and creates a strong space charge. If the HC is designed for protons, the propagation of the radial electric field produced by the HC is not synchronized with the one of carbon ions. Therefore, these ions are only subjected to their space charge, which de-focuses and suppresses them from the main particle beam. As observed during this experiment, the particle beam at the helix exit is a pure, mono-species, beam only composed of protons.

Our new PIC simulations, based on experimental input data measured during this experiment, suggest that proper tuning of the HC geometry can selectively synchronize with ion species, enabling energy bunching, focusing, and post-acceleration of carbon ions.

The use of helical coils has shown great potential in producing pure, mono-species, ion beams, which is of great interest for medical applications. Their ability to double the energy of carbon ions is especially beneficial for oncological applications. Cancer treatments involving ion therapy require both precise energy control and high carbon ion energies to effectively target and treat deep-seated tumors. Achieving doubled carbon ion energy on petawatt (PW) laser facilities could represent a significant step forward in meeting these stringent requirements [91]. This breakthrough would enable enhanced energy modulation capabilities, making laser-driven carbon ion acceleration a promising approach for advanced oncological treatments.

However, oncological applications (hadron therapy) require ion energies on the order of 100 MeV/u, whereas the results presented in this chapter reach only about 1 MeV/u. Nevertheless, laser-driven acceleration has already demonstrated carbon-ion energies up to 50 MeV/u [92]. Combining helical coil schemes with optimized laser parameters could potentially allow further energy gains, for instance by approximately doubling the achievable ion energy.

In particular, the experiments have revealed a clear effect of the helical coil target on heavy ions, suggesting that similar mechanisms could be exploited for α particles. This opens the perspective of optimizing radioisotope production, shaping the spectra of α particles. In the next chapter, this perspective is developed.

Chapter 6

Enhanced Radioisotope Production Using Helical Coil Target with Tube

Sommaire

6.1 Foreword

The work done in the previous chapter shows the possibility to have post-acceleration and focalization on heavy ions. This chapter investigates the effect of the helical coil on α ions produced during pitcher catcher experiments. We show a significant effect on α particle spectra and an increase in radioisotope production, using interaction of a cadmium secondary target with the post-accelerated and focused α particles or proton, with helical coil compared to without [93]. The FLUKA simulations were conducted by Thomas Carrière during his PhD.

6.2 β decay

Beta decay is a radioactive process in which an unstable nucleus emits a beta particle (β^- or β^+) accompanied by a neutrino or an antineutrino. This phenomenon is a manifestation of the weak interaction and allows nuclei to transform into a more stable state.

6.2.1 Beta Minus Decay (β^-)

Beta minus decay (β^-) occurs when a neutron in an unstable nucleus is converted into a proton according to the following reaction:

$$n \rightarrow p + e^- + \bar{\nu}_e \tag{6.2.1}$$

In this reaction, a neutron (n) is transformed into a proton (p) with the emission of an electron (e^-), called a beta particle, and an electron antineutrino ($\bar{\nu}_e$). This type of decay occurs in nuclei with an excess of neutrons and leads to an increase in atomic number Z, thereby changing the chemical element.

A typical example of β^- decay is that of carbon-14:

$$^{14}_{6}C \rightarrow ^{14}_{7}N + e^- + \bar{\nu}_e \tag{6.2.2}$$

6.2.2 Beta Plus Decay (β^+)

Beta plus decay (β^+) occurs when a proton in an unstable nucleus is converted into a neutron according to the following reaction:

$$p \rightarrow n + e^+ + \nu_e \tag{6.2.3}$$

Here, a proton (p) is transformed into a neutron (n) with the emission of a positron (e^+), also called a positon, and an electron neutrino (ν_e). This process occurs in nuclei with an excess of protons and results in a decrease in atomic number Z, thus altering the chemical element.

A typical example of β^+ decay is that of fluorine-18:

$$^{18}_{9}F \rightarrow ^{18}_{8}O + e^+ + \nu_e \tag{6.2.4}$$

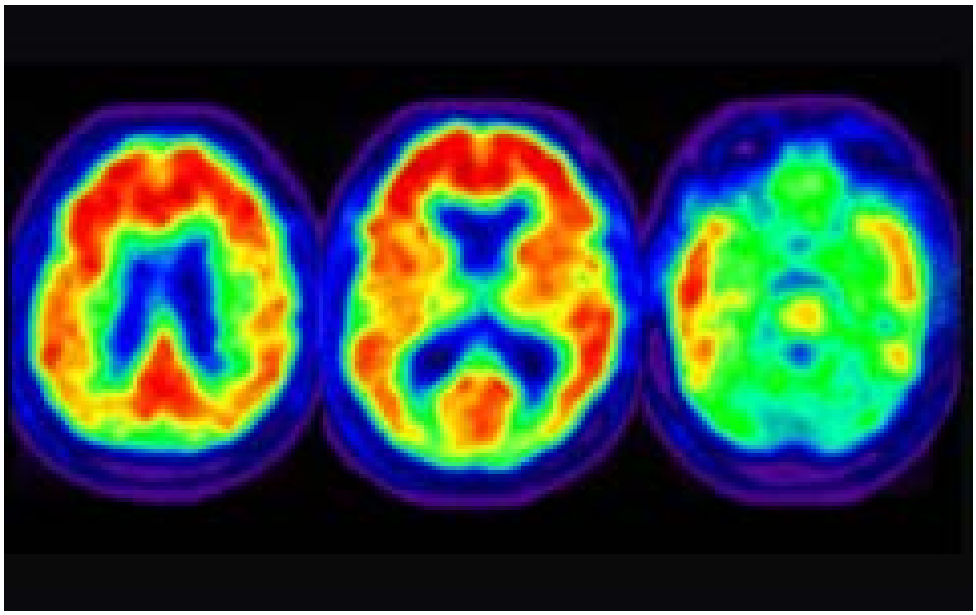

Figure 6.1 – Three different PET scan images of a brain. https://vitalim.ca/awareness/diagnostic-tests/pet-scan/

Beta decay is an essential phenomenon in the evolution of unstable nuclei. These processes play a crucial role in astrophysics, nuclear physics, and nuclear medicine, particularly in positron emission tomography (PET).

6.2.3 PET

Positron Emission Tomography (PET) is a medical imaging technique that uses the principles of β^+ decay. In PET scans, a radiotracer containing a positron-emitting radionuclide, such as fluorine-18, is introduced into the body. When a positron is emitted, it quickly encounters an electron, leading to annihilation and the production of two gamma photons of 511 keV moving in opposite directions.

The PET scanner detects these gamma photons and reconstructs a three-dimensional image of the tracer's distribution in the body. This technique is widely used in oncology for detecting tumors, in neurology for studying brain function, and in cardiology for assessing heart conditions. The Fig. 6.1 show an example of images that is possible to get thanks to this technique.

6.3 Enhanced Laser-Driven Radioisotope Production Using a Helical Coil Target with Tube

6.3.1 Introduction

Radioisotopes, natural or synthetic, are unstable nuclides because of an excess of nuclear energy. Around 90% of radioisotopes are used for medical diagnostic purposes, mainly β^+ (like ^{18}F, ^{43}Sc or ^{44}Sc) and short-life emitters (like ^{123}I or ^{99m}Tc) whereas β^- (^{47}Sc, ^{177}Lu, ^{131}I or ^{90}Y) and alpha emitters (^{225}Ac, ^{211}At, ...) are exploited for medical therapy [94]. They

are produced either with cyclotrons [95] by nuclear reactions induced by protons, alphas, or heavier ions or with nuclear reactors by reactions initiated by neutrons. The supply of medical radioisotopes is a sector in constant tension. The main problem is related to the cost of the necessary infrastructures and their aging. A compact and versatile laser-plasma accelerator able to produce protons or α-particle beams of several tens of MeV in the same place could answer this issue.

One of the most widely used methods for laser-driven ion acceleration is the Target Normal Sheath Acceleration (TNSA) scheme [28, 29]. In this regime, a high-intensity laser interacts with a solid target, inducing electron expulsion from the target's front to its rear surface via the ponderomotive force. This process leads to charge separation within the target material and, when these electrons exit the back side of the target in vacuum, results in the generation of a static electric field reaching several TV/m. Consequently, protons from surface contaminants on the initially undisturbed rear surface are accelerated to energies in the MeV range. However, for radioisotope production, the generated proton beam presents one major drawback: a broadband energy distribution that is exponentially decreasing with a cutoff energy increasing with the laser intensity. These features do not allow for efficient aiming of the maximums of the cross-section reaction. Moreover, the generation of protons at unsuitable energies might produce undesired radioisotopes.

Meanwhile, the concept of proton-boron (pB) fusion, envisioned as early as the 1930s [96], was realized through laser-induced fusion [97]. This fusion reaction, $p^+ + {}^{11}B \rightarrow 3\alpha + 8.7$ MeV, offers distinct advantages, notably neutron-free production of α particles. The absence of neutrons simplifies system design and reduces radiation protection costs. Moreover, pB fusion holds promise for medical radioisotope production. However, a notable drawback of pB fusion for radioisotope production, or any application relying on α particle beams, is the quasi-isotropic nature of the α-particle flux. Another drawback is, as for TNSA, a broad energy spectrum of the α particle beam that does not allow efficient radioisotope production and might also produce undesired (harmful) radioisotopes.

To address the limitations on proton beam, several improvements have been studied such as helical coils [3] or self-guiding through low density plasmas [98]. We propose to use a new design of helical coil targets with tubes (HCT) that we have developed [5] to overcome the limitations on α particle beams. The acceleration scheme using helical coil targets was first proposed by S. Kar [3] et al. to focus, post-accelerate, and bunch a proton beam generated by TNSA. During the laser-foil target interaction, the expulsion of hot electrons triggers a discharge current [22] that propagates through the helix connected to the target's rear side. In this configuration, an electromagnetic pulse (EMP) is generated inside the helix, and the longitudinal component of the electric field post-accelerates and bunches the proton beam, whereas the radial component focuses it. This concept was demonstrated in several experiments [3, 21, 99–101], but the efficiency of this scheme in terms of energy bunching and post-acceleration remains limited due to the current dispersion during its propagation through the helix [21]. To address this issue, A. Hirsch-Passicos et al. have recently proposed adding a conducting tube around the helix to mitigate dispersion

and produce a bunching effect [5]. In this chapter, we propose, for the first time, using HCT to shape not only the proton beam but also the α particle beam generated in the pB fusion reaction in a pitcher-catcher configuration. In that setup, protons and α-particles are focused using HCT on a secondary calcium (Ca) target to produce scandium (Sc) isotopes (see Figs 7.4 and **??**). This chapter presents preliminary simulation results for optimizing radioisotope production using HCT. The purpose of this study is to provide a comparative analysis of radioisotope production using HCT with protons versus HCT with α-particles, with the objective of identifying the optimal approach to increase the number of produced radioisotopes and select the desired radioisotope.

As a first step, the different reactions for radioisotope production and their cross sections, as well as the strategy to optimize the radioisotope production, are presented in Sec. 6.3.2. The setup for protons is described in Sec. 6.3.3.1 and the one for the α-particles in Sec. 6.3.3.2. Section 6.3.4 is dedicated to the description of the simulation chain. Finally, the results of simulations are presented in Sec. 6.3.5. An evaluation of the number of produced radioisotopes, with or without HCT, is performed for proton and α configurations.

The objectives of this work are to demonstrate our ability to post-accelerate, focus and select in energy (bunch) laser-produced proton and α particle beams using HCT, and to identify the most effective way to produce radioisotopes by laser-plasma interaction.

6.3.2 Radioisotope production

This chapter focuses on the production of scandium isotopes, specifically ^{43}Sc, ^{44}Sc, and ^{47}Sc, due to their potential in various medical applications [94].

^{43}Sc and ^{44}Sc are positron-emitting radioisotopes that are highly suitable for use in positron emission tomography (PET) [102], a powerful diagnostic tool in oncology and other medical fields. Compared to conventional PET radioisotopes such as ^{18}F or ^{68}Ga, scandium isotopes offer advantages such as longer half-lives and more favorable decay properties, which allow extended imaging time windows and simplified logistics for radio-pharmaceutical preparation and delivery [95, 103, 104].

^{47}Sc, on the other hand, is a particularly promising β^- emitter for targeted radiotherapy, where it can deliver therapeutic doses while also allowing real-time imaging through gamma emission [105, 106]. This makes ^{47}Sc an excellent choice for radiation therapy applications, including radiolabeled drugs for treating tumors.

Furthermore, $^{43/44}$Sc and ^{47}Sc being isotopes of the same atom, their chemical properties are identical: they can be incorporated within the same vector molecules. Thus, a macroscopical amount of the patient-injected radio-pharmaceutical can be made such that it contains useful quantities of both types of isotopes. This allows for the theranostic technique [107] but using the same radio-pharmaceutical for both diagnostic and treatment. This method of using pairs of matched isotopes allows for personalized medicine, *ie.* more efficient patient-optimized deposition of dose [108].

6.3.2.1 Reactions

To produce scandium isotopes, we use incident protons or α particles to interact with a calcium target. For protons, the reactions of interest are:

$$^{43}\mathrm{Ca} + p \rightarrow n + ^{43}\mathrm{Sc}$$
$$^{44}\mathrm{Ca} + p \rightarrow 2n + ^{43}\mathrm{Sc}$$
$$^{44}\mathrm{Ca} + p \rightarrow n + ^{44}\mathrm{Sc}$$
$$^{48}\mathrm{Ca} + p \rightarrow 2n + ^{47}\mathrm{Sc}$$

and for α particle, the reactions are:

$$^{40}\mathrm{Ca} + \alpha \rightarrow p + ^{43}\mathrm{Sc}$$
$$^{42}\mathrm{Ca} + \alpha \rightarrow X + ^{43}\mathrm{Sc}$$
$$^{42}\mathrm{Ca} + \alpha \rightarrow X + ^{44}\mathrm{Sc}$$
$$^{43}\mathrm{Ca} + \alpha \rightarrow X + ^{44}\mathrm{Sc}$$
$$^{44}\mathrm{Ca} + \alpha \rightarrow p + ^{47}\mathrm{Sc}$$

where X means other products, such as protons, neutrons, etc. The ^{40}Ca represents 97 % of the natural Ca, ^{44}Ca represents 2 %, ^{42}Ca represents 0.6 %, ^{48}Ca represents 0.2 %, and ^{43}Ca represents 0.1 %. These ratios are important for the interpretation results of Sec. 6.3.5.

6.3.2.2 Cross-sections

The proton-calcium cross section is shown in Fig.6.2.a. A production of ^{43}Sc and ^{44}Sc can begins for proton energies above 5 MeV while ^{47}Sc needs 10 MeV. A cross section for ^{44}Sc starts at 15 MeV of proton energy. Also, because cross sections are quite narrow in energy, energy bunching of particles is as important as post-acceleration to select the desired cross-section and produce the wanted radioisotope.

The cross sections presented in Fig. 6.2.b for incident α particles show two points that must be taken into account. First, production of ^{47}Sc and ^{43}Sc only needs 10-25 MeV alphas energy while ^{44}Sc needs 20-40 MeV. Second, one can observe that the cross sections are also quite narrow in energy. Therefore, energy bunching is mandatory.

6.3.2.3 Strategy

The growing interest in scandium-based isotopes has motivated efforts to develop efficient production methods using laser-driven ion acceleration. In this context, we explore how the implementation of advanced target technologies, such as the helical coil target (HCT), can op-

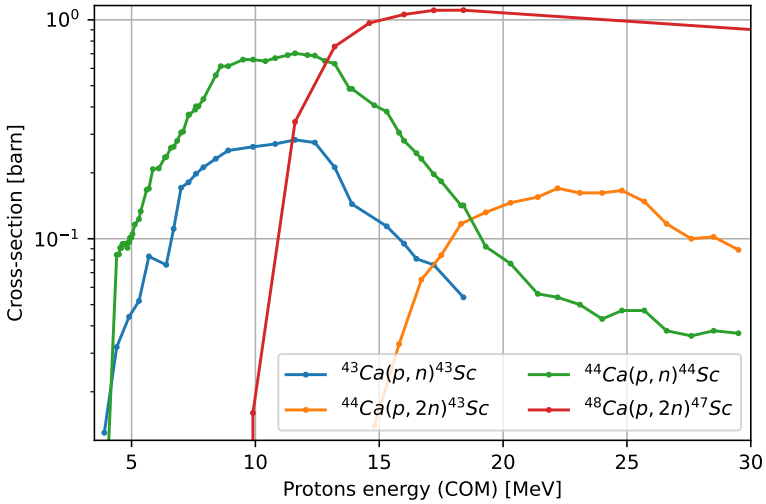

(a)

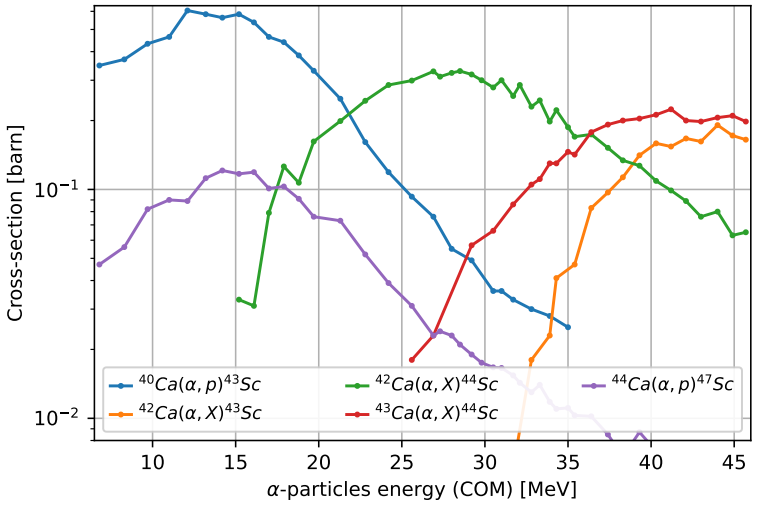

(b)

Figure 6.2 – Cross-sections of the main reactions between calcium and (a) protons or (b) α to produce different scandium radioisotopes depending on the energy of the incident particles in the Center Of Mass (COM).

timize ion acceleration to enhance radioisotope yields. This approach not only aims to validate simulation predictions but also paves the way for scalable production methods for medical radioisotopes.

The implementation of the HCT allows for the creation of a concordance between the energy range of bunched protons and the reaction cross section. For that, we use the capability of the HCT to post-accelerate and energy bunch proton spectra to increase the number of produced radioisotopes. The same principle can be applied to heavier ions. Indeed, the work performed by the electric field, defined as $W = \int_0^l qEdl$, is solely dependent on the charge and not on the particle's mass. Consequently, the energy gain of the α particles should exceed that of protons. Our challenge is to design, for the first time, an HCT geometry to post-accelerate and bunch α

particles within the energy range of the nuclear reaction cross section (refer to Fig.6.2). To do this, we focus on the production of protons and α above 10 MeV.

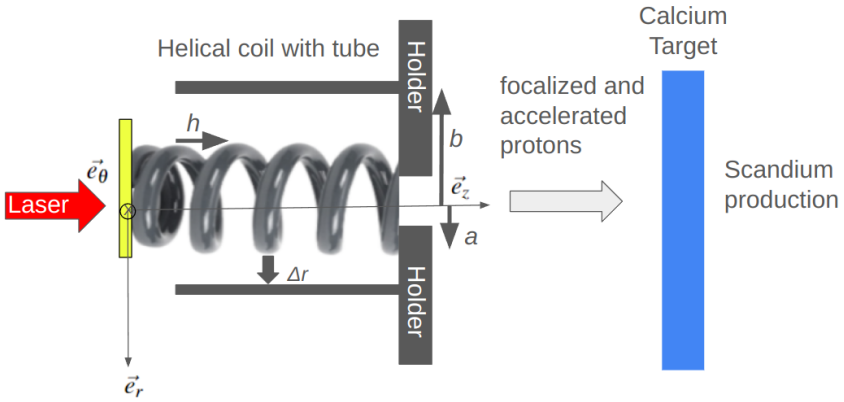

Figure 6.3 – Scheme of a helical coil with tube where the laser beam interacts with a foil target, accelerates protons and creates a discharge current. The latter propagates in the HCT, post-accelerates, energy bunches and focuses protons on a calcium target and produces radioisotopes. The helix is surrounded with a thin cylinder which is symmetric by rotation around the z-axis.

6.3.3 Setup

6.3.3.1 Proton setup

We present the conventional HCT configuration in Fig. 6.3. This setup facilitates the generation of protons and discharge current. The discharge current propagates along the helical coil, inducing longitudinal and radial electric fields, which lead to proton bunching, acceleration, and focusing. The electromagnetic field is described in Chap. 4. In the final stage, these accelerated protons interact with the calcium target to produce scandium radioisotopes. The calcium target is close enough from the TNSA target (0.5 cm) to interact with the entire proton beam.

6.3.3.2 α setup

In the α configuration, a pitcher-catcher geometry is used as shown in Fig. 6.4). The laser-pitcher interaction triggers protons and a discharge current pulse. Protons interact with the catcher (boron target) and produce α particles through fusion reactions, while the current pulse propagates through a wire to the HCT. In the third stage, the discharge current propagates through the helical coil and bunches, accelerates, and focuses the α particles. In the final step, α particles interact with a calcium target to produce scandium radioisotopes (^{43}Sc, ^{44}Sc or ^{47}Sc).

6.3.4 Simulation chain

6.3.4.1 Method

The simulation chain is composed of a three-dimensional (3D) particle-in-cell (PIC) code SOPHIE [63] to model the particle-wave interaction inside the HCT and the code FLUKA [109], a Monte Carlo transport code to evaluate the number of produced radioisotopes. In

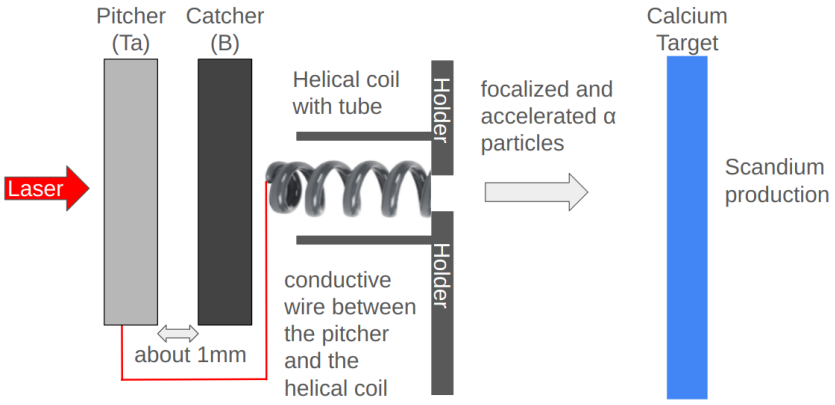

Figure 6.4 – Scheme of a pitcher-catcher configuration where the laser interacts with the pitcher to accelerate protons which in turn interact with the catcher and produce α particles. A wire conducts the discharge current produced by the pitcher and injects it on a HCT, to focus and post-accelerate α particles which interact with a calcium target to produce scandium radioisotopes.

this study, TNSA proton spectra are derived from experimental measurements in two different facilities (INRS/ALLS and ILE/LFEX). They are used as input for SOPHIE simulations. These experimental data also serve as input in FLUKA to evaluate the reference case without HCT. The main SOPHIE output is the proton spectrum at the helix exit, which serves as input for FLUKA simulations.

Simulations in Sec 6.3.5.1 were performed using the ALLS ion acceleration beamline parameters. The Ti:Sapphire ALLS 150 TW laser, operates at a repetition rate of 2.5 Hz with a central wavelength of 800 nm. The system delivers laser pulses with an on-target energy of 3.3 J, duration of 22 fs, and peak intensity of about $1.3 \times 10^{20} W/cm^2$. These simulations are directly linked with Chap. 4 and 5 where we demonstrated the HCT capability to bunch protons around the energy of the maximum cross-section reaction with ^{43}Ca, ^{44}Ca, and ^{48}Ca (see Fig. 6.2.a). Other simulations were carried out with the data obtained at LFEX (Laser for Fast Ignition Experiment) laser [110]. The LFEX laser was engineered to achieve specific parameters: a pulse duration ranging from 1 to 10 ps with an output energy of 1 kJ. Operating at a wavelength of 1.05 μm, the laser achieves a focal spot diameter of 50 μm. In our simulations, we use 1 kJ and 1 ps for the energy and duration of the LFEX laser.

For α particles, we take as a starting point simulations of α particle production data from the LFEX campaign [111,112]. The baseline simulation of a 200 μm boron target irradiated with a TNSA proton beam is performed with FLUKA [112]. The α spectrum shown in Fig. 6.5 is taken at the rear side of the catcher target and used as input for SOPHIE simulations. This spectrum also serves as input in FLUKA to establish a reference case without HCT. The SOPHIE output spectrum is injected into FLUKA to model the interaction with the calcium target. Thanks to this simulation chain, the number of produced radioisotopes can be evaluated, with and without HCT, for proton and α configurations. Simulations for α particles were conducted exclusively using LFEX parameters. Due to ALLS's lower energy, the α particles produced with it do not have sufficient energy to trigger the reactions whose cross-sections are shown in Fig. 6.2.

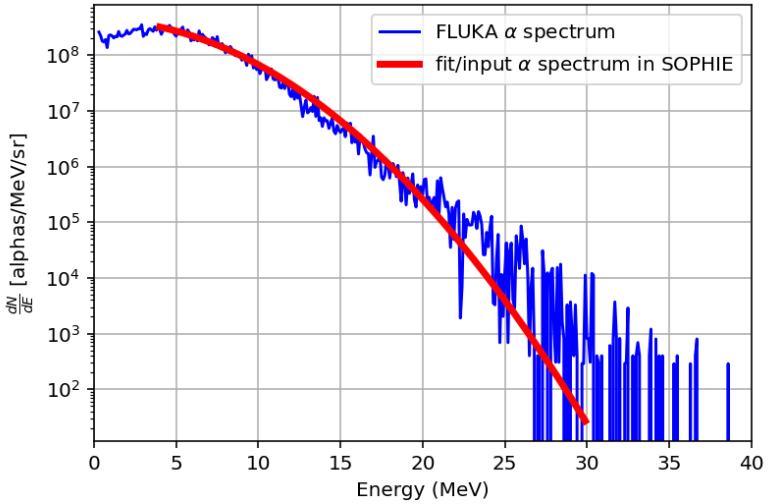

Figure 6.5 – α energy distribution obtained with FLUKA (blue curve) and the exponential fitting used for SOPHIE input (red curve).

Additionally, the lower number of particles generated by ALLS means that there are not enough α particles to use the HCT effectively. As discussed in Sec. 6.3.5.1, HCT introduces significant particle losses, so a large initial number of particles is required before applying the HCT.

6.3.4.2 SOPHIE

In the simulations, we consider a helical coil attached to the rear side of a foil target. The target, coil, and holder are modeled as perfect conductors and meshed at real scale (about $20 \times 6 \times 6$ mm^3) with a cell size of $\Delta x = \Delta y = \Delta z = 20$ μm, resulting in 2×10^9 cells distributed over a volume of 72 cm^3. Electrons, protons, and α-particles are represented using 10 million macroparticles.

The energy and angular distributions of the injected protons are based on experimental measurements with TNSA without a helical coil. The energy distribution corresponds to the black curve in Fig. 6.6.a and b, respectively, for the ALLS and LFEX facilities, while the α-particle energy distribution is shown in red in Fig. 6.5. The angular distribution follows a super-Gaussian function $dN_p/d\theta \propto \exp\left[-(\theta/\theta_p)^{10}/2\right]$, with $\theta_p = 19°$ for protons and $\theta_p = 90°$ for α-particles. The temporal profile of the particle emission dN_p/dt is modeled as a Gaussian function with a full-width at half-maximum (FWHM) duration τ of a few ps. Although its exact value is unknown, it remains negligible compared to the proton transit time (> 100 ps) through the coil and their final bunch duration caused by time-of-flight dispersion. The transverse size of the particle emission zone is set to 200 μm.

The proton and α-particle dynamics inside the helical coil are governed solely by the electromagnetic fields generated by the discharge current. To model this discharge current, isotropically emitted electrons are introduced with an energy distribution similar to that of the protons. The electron emission zone matches the protons' transverse size of 200 μm.

For the ALLS facility, the electron emission is set to 160 nC, while proton emission is 12 nC, both with an emission duration of 7 ps [5, 20]. For the LFEX facility, the electron emission is 1600 nC, the proton emission is 1200 nC [18, 111], and the α-particle emission is 4.5 nC, all with an emission duration of 14 ps.

In this study, the ALLS simulations were performed assuming an optimal (best focus) electron emission of 160 nC and an optimal (best focus) TNSA proton spectrum (6 MeV of cut-off, 12 nC [20]), whereas the experimental results presented is Fig. 5.3 corresponded to a significantly lower emitted electron charge of about 40 nC, a lower emitted proton charge of 5.6 nC and a lower cut-off energy of 4 MeV. Therefore, we also use an helical coil characteristic energy of about 5.7 MeV in the simulations instead of 4 MeV in the experimental case.

6.3.4.3 FLUKA

The FLUKA code [109, 113] stands as a versatile Monte Carlo simulation tool designed to comprehensively model the interaction and transport of particles across various mediums. Its development is rooted in the aspiration to incorporate the most robust and precise physics models, ensuring a microscopic approach where each computational step is underpinned by sound physical principles.

This code exists in two versions: one from CERN and one from INFN. Here, the version from INFN [114] was used with 200 million particles per simulation. The target size is $5 \times 5 \times 2$ mm of $^{\text{nat}}$Ca inside a very large vacuum region, with 2 mm being in the beam direction. This length is sufficient because the most energetic α particles of up to 60 MeV only go through two-thirds of the target. The input used is the proton and alpha spectrum sampled in bins of 0.1 MeV, which is then used for Monte-Carlo type calculation. The 2021 version of the code was used because special Fortran routines were developed that used MGDRAW results as SOURCE for FLUKA simulations. These are here needed when using α particle simulation results as input. The evaporation, coalescence and peanut model modules are activated along with heavy ions transport. Radioactive decay uses the semi-analogue model for Monte-Carlo sampling of the physical distribution. Results are then obtained using the RESNUCLE, or Residual nuclei module, which gives a number of each isotope per code unit. We present in 6.3.5.2 the total number of radioisotopes obtained.

6.3.5 Results

6.3.5.1 SOPHIE simulations

To determine the helix parameters, radius a and pitch h, we compute the phase speed V_{HC}, corresponding to the longitudinal speed of a current pulse going at the speed c along the helical coil such that $V_{HC} = hc/\sqrt{h^2 + 4\pi^2 a^2}$. This phase speed determines the population of particles synchronized with the electromagnetic pulse having an initial energy $E_{HC} = \frac{1}{2} m_i V_{HC}^2$, where m_i is the ion mass. To determine the final energy of the bunch, one can then use the scaling law given in our previous publication [5]. Thanks to this scaling law, we know that we have to use

an helical coil of characteristic energy $E_{HC} = 0.8E_{cut-off}$, where $E_{cut-off}$ is the TNSA cut-off energy.

Proton setup

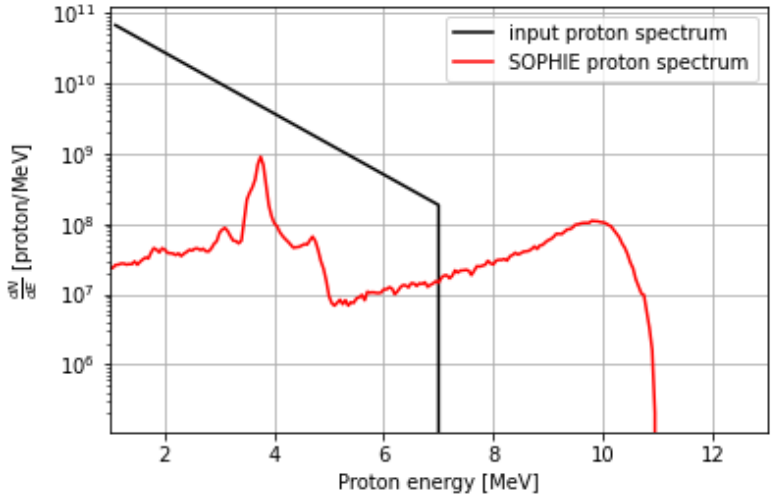

(a)

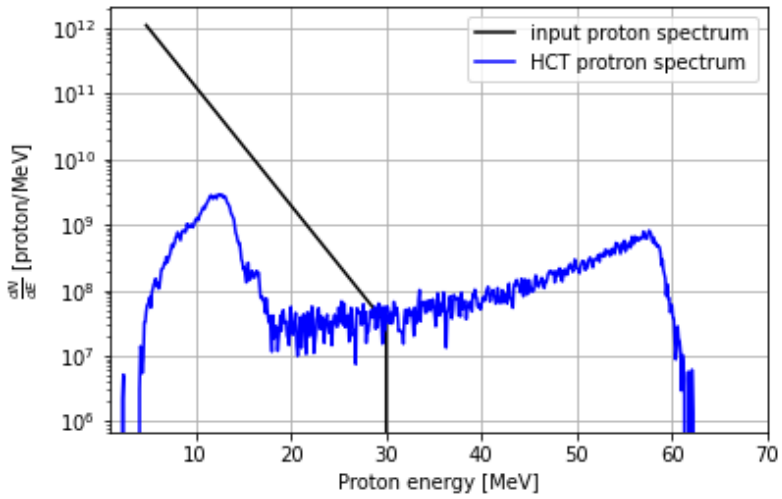

(b)

Figure 6.6 – Energy distribution of the accelerated protons at the HCT exit for ALLS (a) and LFEX (b) calculated with the SOPHIE code. Black lines show the input proton spectrum at the HCT entrance. HCT parameters are: a radius $a = 0.5$ mm, a pitch $h = 0.35$ mm, a tube of radius $b = 0.7$ mm and a length $L = 15$ mm for the ALLS facility, and a radius $a = 0.6$ mm, a pitch $h = 0.864$ mm, a tube of radius $b = 1$ mm and a length $L = 15$ mm for the LFEX facility.

To synchronize the phase speed V_{HC} with the proton velocities, two distinct geometries are required for ALLS and LFEX. For the ALLS facility, the geometry needs to be optimized for lower energy protons (with a maximum energy of 7 MeV), so we must decrease the pitch h or increase the radius a to reduce V_{HC}. In contrast, for the LFEX facility, due to the higher proton

energies, we need to increase V_{HC}, which can be achieved by reducing the radius or increasing the pitch. SOPHIE simulations showcase the capability to achieve energy bunching around 3.5 MeV and 10 MeV (refer to Fig. 6.6.a). The input of this SOPHIE simulation is the classical TNSA spectrum measured on this facility (black curve). In the same way, for the LFEX facility, using the classical TNSA spectrum obtained on this facility (black curve) as input of the SOPHIE simulation, then adding a helical coil we get a first bunch at 12 MeV and a second one at 57 MeV (see Fig.6.6.b). For both cases, one can observe that the number of protons at the HCT exit is low (yield of about 1%) compared those at the entrance (black curves). This HCT limit is discussed in Chap. 4. However, what is not shown in these graphics is the number of protons/MeV/sr which has increased due to the focusing effect of the HCT. These HCT proton spectra are used as input datas for FLUKA simulations.

α setup

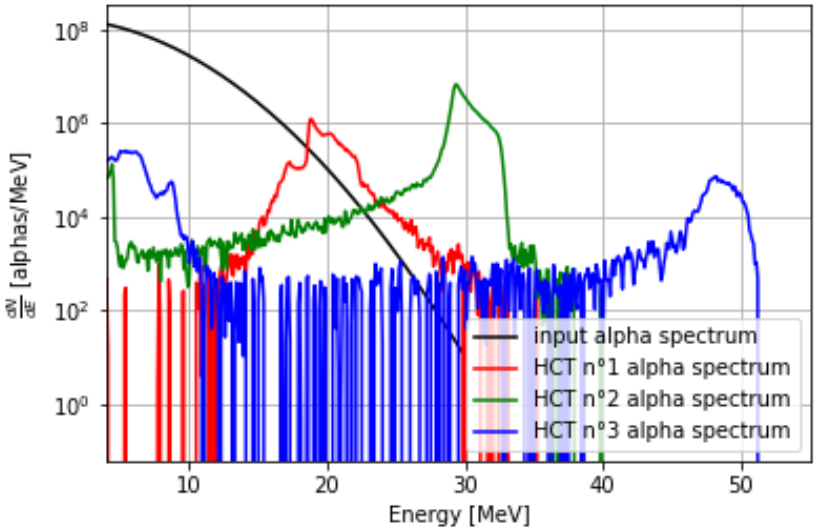

Figure 6.7 – Energy distribution of the α particles accelerated in different HCT geometries. The black line shows the input α spectrum at the HCT entrance. In this figure, we show three different HCT geometries $a = 0.9$ mm $h = 0.3$ mm and $b = 1.3$ mm (red curve, HCT n°1), $a = 0.8$ mm $h = 0.4$ mm and $b = 1$ mm (green curve, HCT n°2), $a = 0.5$ mm $h = 0.35$ mm and $b = 0.9$ mm (blue curve, HCT n°3) and a length $L = 15$ mm.

With SOPHIE, we can simulate the propagation and acceleration of α particles in the HCT. Figure 6.7 demonstrates that, even if the number of exiting α particles remains low, the HCT facilitates significant energy bunching within the range of 20 to 50 MeV, dependent on parameters such as the radius a and pitch h. What this figure does not show is the increase in the number of α per solid angle (decreasing the angular dispersion from 45° to 1°), in the energy range of the bunch, compared to the input α spectrum. These findings represent a pivotal contribution of this chapter: they demonstrate, our ability to manipulate heavy (heavier than protons) ion energies using the HCT configuration. These HCT α spectra are used as input datas for FLUKA

N/shot	^{43}Sc	^{44}Sc	^{47}Sc
no coil LFEX	44	1144	36
coil LFEX	634	2400	288
no coil ALLS	5	31	None
coil ALLS	170	962	None

Table 6.1 – Number of radioisotope atoms per shot, obtained using our simulation chain for each facility, with and without HCT, using the proton setup.

simulations.

6.3.5.2 FLUKA simulations

Proton setup

Radioisotope production of scandium from natural calcium has been looked at for two distinct proton acceleration laser systems: ALLS and LFEX. The two regimes give varying proton spectra ranging from 10 to 50 MeV. As such, we numerically study the radioisotope production, with and without HCT, and compare to the number of protons per shot.

As seen in Table 6.1, for both facilities, the yield is significantly increased with the HCT configuration. In the case of the LFEX laser, the number of radioisotopes is increased by a factor 2 to 14 (2 for ^{44}Sc, 8 for ^{47}Sc, and 14 for ^{43}Sc). For the INRS case, we get an increase factor of 30 for the two isotopes: ^{43}Sc and ^{44}Sc. Due to the low energy range of protons, no ^{47}Sc are produced with or without HCT, in the INRS case.

These increases come from the fact that with the helical coil in the INRS setup, we increase the proton cut-off energy up to 10 MeV. Thanks to this, one can reach the peak of the cross-sections for ^{43}Ca(p,n)^{43}Sc and ^{44}Ca(p,n)^{44}Sc reactions (see respectively blue and green curve in Fig. 6.2.a) which were unattainable without helical coil. Concerning LFEX setup, we trigger ^{44}Ca(p,2n)^{43}Sc, ^{44}Ca(p,n)^{44}Sc, ^{48}Ca(p,2n)^{47}Sc reactions (see respectively green, orange and red curve in Fig. 6.2.a). The high-energy protons lose energy propagating inside the calcium target and increase their probability of interaction, enhancing the yield even more. Additionally, thanks to the helical coil, we increase the number of protons for energies above 20 MeV, which is approximately the cross-section peak of ^{44}Ca(p,n)^{44}Sc and ^{48}Ca(p,2n)^{47}Sc reactions.

α setup

Cross-sections for the production of different calcium isotopes are shown Fig. 6.2; these indicate which energy ranges should be aimed for with the α particles spectrum. SOPHIE simulations have showcased great advance for α particles bunching and acceleration which can

N/shot	^{43}Sc	^{44}Sc	^{47}Sc
no coil	1181	0.1	1
HCT n°1	53000	0.4	6
HCT n°2	46000	342	114
HCT n°3	8260	242	159

Table 6.2 – Number of radioisotope atoms per shot, obtained using our simulation chain for each facility, with and without HCT, using the α setup

greatly increase the yield of radioisotopes.

As shown in Table 6.2 for ^{43}Sc and ^{44}Sc we have obtained respectively a multiplication by 50 and 3000 using HCT. ^{47}Sc yields have also been improved by factors 100 for the HCT n°2 and n°3. One can therefore conclude that the energy bunching effect compensates for the reduction in the number of incident particles, and that, thanks to the helical coil, the number of produced radioisotopes can be greatly increased.

Indeed, with the HCT n°1, one can increase the number of particles with energy above 15 MeV which correspond to the maximum of the ^{40}Ca(α,p)^{43}Sc and ^{44}Ca(α,p)^{47}Sc cross-sections (see respectively blue and purple curves on Fig. 6.2,b). With the HCT n°2 and 3 one can trigger the ^{42}Ca(α,X)^{43}Sc, ^{42}Ca(α,X)^{44}Sc and ^{43}Ca(α,X)^{44}Sc reactions (see respectively orange, green and red curves on Fig. 6.2,b), which was unattainable without helical coil. Similarly to protons in the previous paragraph, α particles of energies higher than those near the peak of the cross-sections (above 30 MeV) slow down propagating inside the calcium target: their energy is reduced to more optimal values and thus their probability of reaction is increased. This also allows to trigger the ^{44}Ca(α,p)^{47}Sc reaction whose cross-section peak is at lower energies.

α particles are more efficient than protons at producing ^{43}Sc, primarily due to the natural proportion of calcium isotopes. Protons react with ^{43}Ca, which constitutes only 0.1 % of natural calcium, whereas α particles react with ^{40}Ca, which makes up 97 % . Additionally, to fully understand these results, it is crucial to consider the differences in reaction cross-sections for the respective processes such as it as been done in this work.

6.3.6 Conclusion

Nuclear reactions require specific energies to take place, and it is necessary to have bunches of particles at the maximum of the cross-section reaction in order to obtain the highest number of products. HCT gives the opportunity to correct that aspect in laser-accelerated proton and α spectra as these are usually too broad to aim for a specific nuclear reaction.

Our numerical study unveils a potential advancement in α particle manipulation enabled by the innovative helical coil target (HCT) configuration. Through Particle-In-Cell simulations

using SOPHIE, we have demonstrated the possibility of controlling the energy distribution of α particle bunches. Moreover, our findings highlight the potential of the HCT for radioisotope production, with yields exhibiting a significant enhancement ranging from 50 to 3 000 times greater compared to classical laser plasma acceleration methods.

Furthermore, we have shown the interest of different setups such as the HCT configuration with protons to produce ^{44}Sc and the HCT configuration with α to produce ^{43}Sc. To produce ^{47}Sc, both α and protons with HCT are interesting, multiplying the number of produced radioisotopes by a factor 100 and 10 respectively.

This enhancement holds promise for various fields reliant on radioisotopes, including medicine, industry and scientific research. Moving forward, the HCT presents a transformative avenue for advancing α particle acceleration techniques with high intensity lasers, offering opportunities for further exploration and application in diverse scientific and technological domains.

However, 10^{11} scandium isotopes are required per patient [115]. Consequently, significant technological progress is still needed to make laser-driven radioisotope production using helical coils viable, in particular by increasing both the laser repetition rate and the operational shot rate of the helical coil.

Currently, radioisotopes are produced using high-energy proton or alpha beams generated by large cyclotrons, such as ARRONAX in Nantes (France), which can deliver proton currents of approximately 10^{15} protons per second. In contrast, large-scale laser facilities can produce up to 10^{14} protons per shot via laser-driven acceleration, although the repetition rate is limited to a few shots per day. To achieve comparable production rates, a promising alternative is to use medium-intensity lasers operating at higher repetition rates. For instance, at INRS with the ALLS laser facility, more than 10^{12} protons per shots can be produced at 2.5 Hz. Continuous advancements are being made in both laser intensity and repetition rate, driven by numerous companies active in the development of laser technologies. Additionally, parallel efforts are focused on increasing the proton yield per shot through optimization of laser parameters and target design. Indeed, the primary target could be optimized to yield more protons and the secondary target could be enriched in relevant isotopes for more reactions.

Eventually, to implement the helical coil in a high repetition rate setup, its setup will be adapted, and its multi shot capabilities will be assessed in a future experiment.

Chapter 7

Other interesting applications

Sommaire

In this chapter, we present two complementary work in progress carried out during this PhD. The first one, detailed in Sec. 7.1, concerns isochoric heating, where the Varying Helical Coil Target (VHCT) is investigated as a way to shape the proton spectrum in order to optimize the heating of a sample for warm dense matter studies. The second one, described in Sec. 7.2, focuses on neutron production. This study explores the use of VHCT to enhance neutron yield. The approach is similar to that discussed in Chap. 6 on radioisotope production, where the helical coil target serves to bunch the proton energy at the value corresponding to the maximum cross-section of the reaction (^{7}Li(p, n)^{7}Be). The FLUKA simulations were conducted by Thomas Carrière during his PhD, and the Geant4 simulations were performed by Ronan Lelièvre during his PhD.

7.1 Isochoric heating

7.1.1 Introduction

Isochoric heating using laser-driven proton beams has emerged as a promising technique to study matter under extreme conditions, particularly in the context of warm dense matter (WDM). In contrast to traditional volumetric heating methods, isochoric proton heating enables rapid and localized energy deposition on timescales shorter than the material's hydrodynamic response. This makes it possible to heat the target while keeping its density nearly unchanged, thereby facilitating controlled and well-characterized experiments to study high-energy-density (HED) states.

Over the past two decades, significant progress has been made in generating high-intensity, short-duration proton bursts using the TNSA mechanism. These protons, typically in the multi-MeV energy range, efficiently couple their energy to solid-density samples. Studies such as [116,117] have demonstrated that proton beams can heat solid foils from several eV to tens of eV within a few picoseconds, enabling access to WDM regimes with temporal and spatial resolutions that are difficult to achieve using traditional x-ray or optical heating methods. Despite these advances, several challenges remain such as the spatial uniformity of heating and the control of proton spectra.

We propose to use a new design of varying helical coil targets with tubes (VHCT) that we have developed [61] to shape the proton spectra for the isochoric heating.

7.1.2 Strategy

The growing interest in isochoric heating has motivated efforts to develop efficient investigation methods using laser-driven ion acceleration. In this context, we explore how the implementation of advanced target technologies, such as the varying helical coil with tube (VHCT), can optimize ion acceleration to enhance the homogeneity and the intensity of the isochoric heating. This approach not only aims to validate simulation predictions but also paves the way for scalable investigation methods for material equation of state. For that, we use the capability of

the VHCT to post-accelerate and energy shape proton spectra to increase the temperature and homogenize the energy deposition in the sample.

7.1.3 Setup

We present the VHCT configuration in Fig. 7.1. In this setup, to get a flat proton spectrum in energy, we use a varying pitch [61]. The varying pitch permits a higher cutoff energy without energy bunch. Thanks to this, one can get a more homogeneous heating in the target thickness.

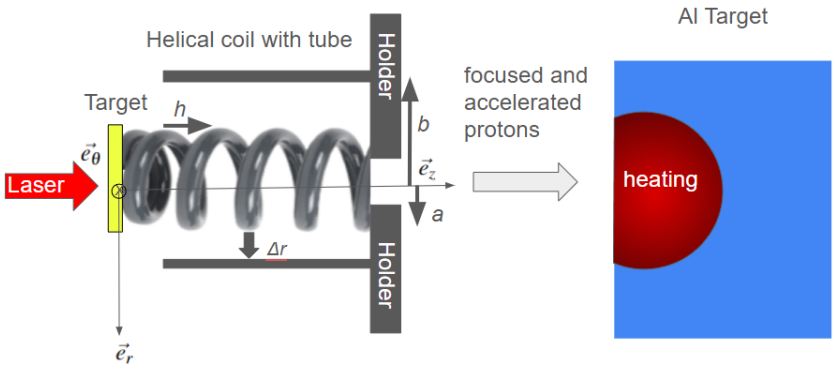

Figure 7.1 – Scheme of a helical coil with tube where the laser beam interacts with a foil target, accelerates protons and creates a discharge current. The latter propagates in the HCT, post-accelerates, energy bunches and focuses protons on a aluminium target to heat it. The helix is surrounded with a thin cylinder which is symmetric by rotation around the z-axis.

The TITAN laser at Lawrence Livermore National Laboratory is a high-power, short-pulse laser facility comparable to PETAL and LFEX, which were presented previously. TITAN delivers laser pulses with energies of the order of 150–200 J on target and pulse durations in the picosecond regime (typically 1 ps), corresponding to peak powers in the hundred-terawatt range. When focused onto solid targets, intensities exceeding 10^{19} W/cm^2 can be achieved.

7.1.4 Simulation chain

Method

The simulation chain is composed of the three-dimensional (3D) particle-in-cell (PIC) code SOPHIE [63] to model the particle-wave interaction inside the HCT and the code FLUKA [109], a Monte Carlo transport code to evaluate the deposited energy. In this study, TNSA proton spectra are derived from experimental measurements for the JLF Titan facility [118]. They are used as input for SOPHIE simulations. These experimental data also serve as input in FLUKA to evaluate the reference case without VHCT. The main SOPHIE output is the proton spectrum at the helix exit, which serves as input for FLUKA simulations.

SOPHIE

In the simulations, we consider a helical coil attached to the rear side of a foil target. The target, coil, and holder are modeled as perfect conductors and meshed at real scale with a cell

size of $\Delta x = \Delta y = \Delta z = 20$ μm, resulting in 2×10^9 cells distributed over a volume of 72 cm^3. Electrons, protons, and α-particles are represented using 10 million macroparticles.

The energy and angular distributions of the injected protons are based on experimental measurements with TNSA without a helical coil. The energy distribution corresponds to the black curve in Fig. 7.2 and the angular distribution follows a super-Gaussian function $dN_p/d\theta \propto \exp\left[-(\theta/\theta_p)^{10}/2\right]$, with $\theta_p = 19°$. The temporal profile of the particle emission dN_p/dt is modeled as a Gaussian function with a full-width at half-maximum (FWHM) duration τ of a few ps. Although its exact value is unknown, it remains negligible compared to the proton transit time (> 100 ps) through the coil and their final bunch duration caused by time-of-flight dispersion. The transverse size of the particle emission zone is set to 200 μm.

The proton dynamics inside the helical coil are governed solely by the electromagnetic fields generated by the discharge current. To model this discharge current, isotropically emitted electrons are introduced with an energy distribution similar to that of the protons. The electron emission zone matches the protons' transverse size of 200 μm.

The electron charge emission is 1600 nC taken by analogy with PETAL experiment [18] and the proton charge emission is 1200 nC taken from previous experimental campaign [118].

FLUKA

In these simulations, the version from INFN [114] was used with 200 million particles per simulation. The target size is $5 \times 5 \times 20$ mm of $^{\text{nat}}$Al inside a very large void region, with 20 mm being in the beam direction. This length is sufficient because the most energetic protons of up to 60 MeV only go through two-thirds of the target. The input used is the proton spectrum sampled in bins of 0.1 MeV, which is then used for Monte-Carlo type calculation. Results are then obtained using the USRBIN, or energy deposition module, which gives the deposited energy in GeV/cm^3/unit primary weight. To get the temperature, we have to multiply by the unit primary weight and divide by the calorific capacity and the density of the aluminum. We present in 7.1.5 the produced heating.

7.1.5 Results

SOPHIE simulations

To determine the helix parameters, radius a and pitch h, we compute the phase speed V_{HC}, corresponding to the longitudinal speed of a current pulse going at the speed c along the helical coil such that $V_{HC} = hc/\sqrt{h^2 + 4\pi^2 a^2}$. This phase speed determines the population of particles synchronized with the electromagnetic pulse having an initial energy $E_{HC} = \frac{1}{2} m_i V_{HC}^2$, where m_i is the ion mass. To determine the variation of the pitch, one can try different variations and choose the best compromise between number of protons and energy spectra. Figure 7.2 shows that the linear variation case results in a flatter proton spectrum in its energy distribution and an increased cutoff energy from 40 MeV to 63 MeV. These VHCT-modified proton spectra are used as input data for the FLUKA simulations.

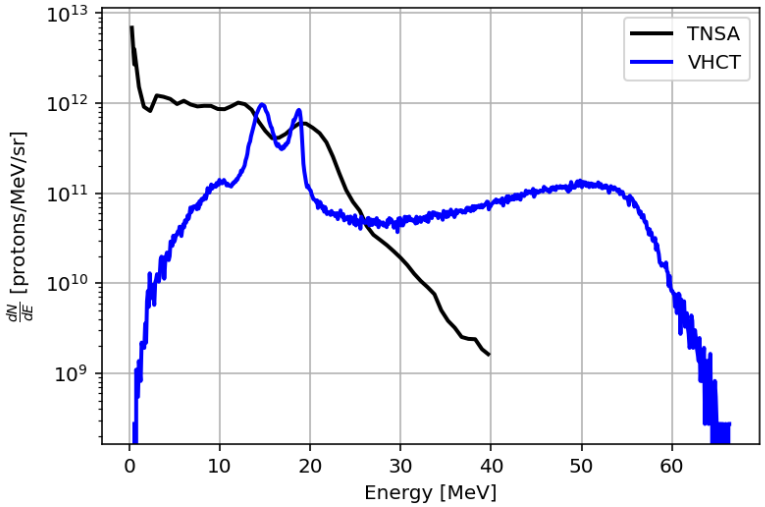

Figure 7.2 – Energy distribution of the accelerated protons at the HCT exit for Titan facility, calculated with the SOPHIE code. Black lines show the input proton spectrum at the HCT entrance. HCT parameters are: a radius $a = 0.6$ mm, a linearly varying pitch $h = 0.864$ to 1.15 mm, a tube of radius $b = 1$ mm and a length $L = 15$ mm for the JLF Titan facility.

FLUKA simulations

By injecting the linear variation results obtained from SOPHIE or the TNSA spectra (shown in Fig. 7.2 and used as a reference) into the FLUKA code, the temperature distribution shown in Fig. 7.3 is obtained. The isochoric heating induced by TNSA alone is presented in Fig. 7.3.a, while the case combining TNSA with VHCT is shown in Fig. 7.3.b. Finally, Fig. 7.3.c displays the temperature difference between the VHCT-enhanced TNSA and the standard TNSA configuration.

The results clearly highlight a lower maximum temperature with VHCT case, decreasing from 10^7 K (TNSA case) to 10^5 K, along with an overall temperature drop for target thicknesses below 0.6 mm. This is attributed to the reduced number of low-energy protons. However, with the implementation of VHCT, the temperature increases and becomes more homogeneous in the 0.6–1.2 mm region. Additionally, the helical coil contributes to reducing the temperature gradient, leading to a more uniform heating profile.

The results obtained with the TNSA is in agreement with previous experimental results in the Gekko laser facility [119]. Indeed, RA. Snavely et al [119] obtained 100 eV of isochoric heating with an intensity of 3×10^{18} W/cm^2.With the JLF Titan intensity, which is a similar laser beam, with 5×10^{19} W/cm^2 we should easily get a factor 10 higher temperature [8].

Furthermore, one can estimate the temperature $T = \frac{N_p E_p}{C_p^{Al} \rho_{Al} V_{dep}}$, where N_p is the number of protons, E_p is the mean energy of protons, C_p^{Al} the specific heat capacity of the aluminium, ρ_{Al} the density of the aluminium and V_{dep} the volume of energy deposition. Thanks to PSTAR [120], one gets a mean penetration length of protons in aluminium of 7.4 μm. Knowing the radius of the proton beam after 0.5 cm of propagation (radius$==\tan(20\pi/180) \times 5 \times 10^{-3}$), we are able to estimate the temperature:

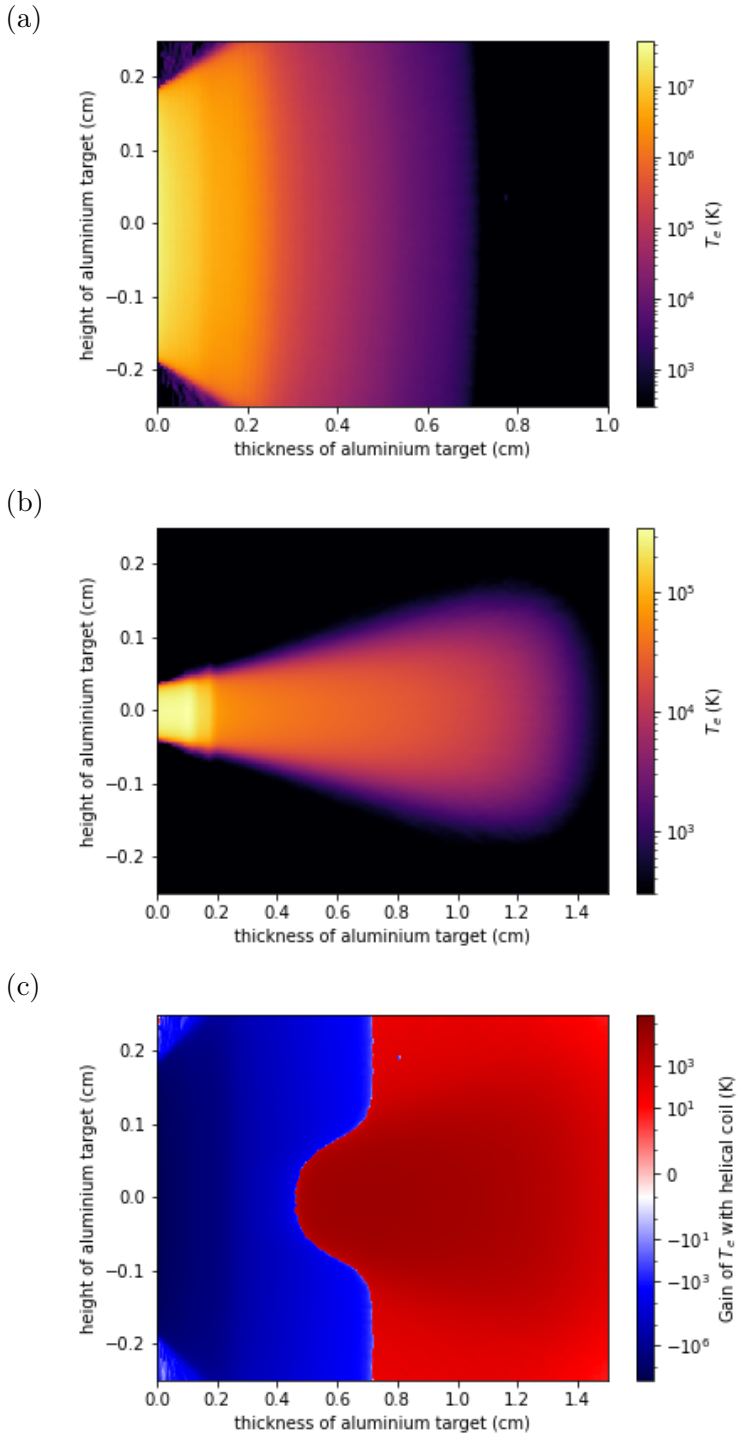

Figure 7.3 – Isochoric heating in °K obtained with TNSA a) and a helical coil b) at JLF Titan. c) Represents the difference of temperature between the TNSA with helical coil and the TNSA without helical coil.

$$\frac{1\times10^{18}\times1.6\times10^{-19}}{897\times2.7\times10^{-3}\times\pi\left(\left(\tan\left(20\cdot\frac{\pi}{180}\right)\cdot5\times10^{-3}\right)^2\cdot74\times10^{-6}\right)} = 8.6\times10^7 K$$

which corresponds to the simulated values.

7.1.6 Conclusion

In this work, we have investigated the use of Varying Helical Coil Targets (VHCT) to improve the spectral and spatial characteristics of proton beams generated via Target Normal Sheath Acceleration (TNSA), with the goal of optimizing isochoric heating of solid targets. Through electromagnetic simulations, we demonstrated that a linearly varying pitch in the VHCT leads to significant enhancement in proton energy distribution, including an increase in cutoff energy and improved spectral flatness.

These modified proton spectra were then used in FLUKA simulations to model energy deposition in aluminium. The results showed a clear improvement in heating performance compared to standard TNSA spectra, with lower peak temperatures but a more uniform temperature distribution. It shows a particular interest in the 0.6–1.2 mm thickness region of the target.

In this study, we showed that the number of protons which is reduced in the HC case is detrimental for the application of isochoric heating. The next step will be to increase the efficiency of the helical coil to compensate the loss in number of protons. Furthermore, different spectra have to be tested and above all, hydrodynamic simulations as ESTHER have to be used to take into account the temporality of the proton heating, phase changing and heat propagation in the sample. These simulations are necessary to have a complete study.

7.2 Neutron production

7.2.1 Introduction

The development of compact, high-flux neutron sources is of growing interest for a wide range of applications, including nuclear physics, materials science, non-destructive testing, medical diagnostics, and security screening. In recent years, laser-driven ion acceleration has emerged as a promising alternative to conventional accelerator technologies for the generation of short-pulse, high-intensity neutron bursts. In particular, the Target Normal Sheath Acceleration (TNSA) mechanism can accelerate protons to several tens of MeV, making it suitable for initiating nuclear reactions with light or heavy converter materials to produce neutrons.

In this context, neutron generation typically relies on the interaction of laser-accelerated protons with secondary converter targets such as lithium, beryllium, or deuterated materials. The nuclear reactions involved—such as $^{7}\mathrm{Li(p,n)}^{7}\mathrm{Be}$, $^{9}\mathrm{Be(p,n)}^{9}\mathrm{B}$, or $\mathrm{D(p,n)pp}$—have relatively low reaction thresholds and can be efficiently driven by the broad proton spectra produced via TNSA. The resulting neutron yield and spectral characteristics depend on various factors, including the laser parameters, the proton beam energy and angular distribution, and the geometry and composition of the converter target.

Advances in high-power laser systems and target engineering have significantly improved the performance of laser-driven neutron sources, achieving neutron fluxes exceeding 10^{7} neutrons per shot [121] or 10^{5} neutrons per shot with high repetition rate of 0.5 Hz [89]. Moreover, the ultrashort duration and high brightness of the generated neutron pulses make them particularly

attractive for time-resolved measurements and probing dynamic processes at the nanoscale.

In certain facilities, such as ALLS (INRS-Canada), 22 fs of pulse duration and 3.2 J of energy, the maximal proton cut-off energy, obtained thanks to the TNSA mechanism, is too low to maximize the neutron production (is not in the agreement with the ^{7}Li(p, n)^{7}Be cross-section). However, these kinds of facility, which present a high repetition rate, are interesting to produce neutron sources at the Hz repetition rate.

In this work, we investigate numerical approaches for optimizing neutron production using helical coil targets. For that, we use the capability of a varying radius of VHCT to post-accelerate and energy shape proton spectra to increase the neutron production. The idea is to increase the agreement between proton energy and $^7Li(p,n)^7Be$ cross-section. To do it, we will use DoPPLIGHT [74] to simulate the proton spectra and a Monte Carlo code named GEANT4 to simulate the proton transport inside the target and the neutron conversion.

7.2.2 Strategy

Setup

We present the VHCT configuration in Fig. 7.4. In this setup, to get an energy bunch in the energy proton spectra, we use a varying radius [61]. The varying radius permits a higher retrieved number of protons at the exit of the coil.

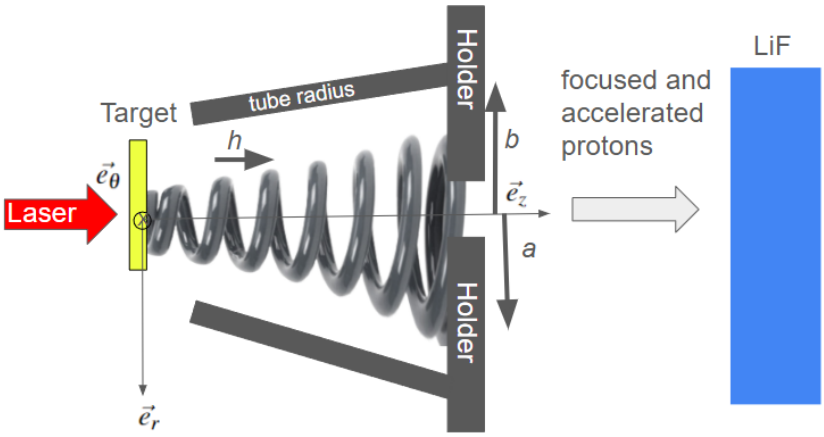

Figure 7.4 – Scheme of a helical coil with tube and a varying radius where the laser beam interacts with a foil target, accelerates protons and creates a discharge current. The latter propagates in the HCT, post-accelerates, energy bunches and focuses protons on a LiF target leading to the generation of neutrons. The helix is surrounded with a thin cone which is symmetric by rotation around the z-axis.

7.2.3 Simulation chain

Method

Neutron production via laser-driven proton acceleration is a prominent method in nuclear physics research. This approach uses the accelerated protons from TNSA to interact with lithium

fluoride (LiF) targets. Neutrons are produced primarily through the ^{7}Li(p,n)^{7}Be reaction. This reaction is characterized by a significant cross-section (see Fig. 7.5,a), making LiF an efficient neutron converter. The cross-section for this reaction varies with proton energy, influencing the neutron yield. Understanding the proton-LiF interaction cross-sections is crucial for optimizing neutron production in experimental setups. Another possibility is to use the ^{19}F(p,n)^{19}Ne reactions.

To compute the neutron production, we propose to first, use DoPPLIGHT [74] to model the particle-wave interaction inside the HCT and a code GEANT [122, 123], a Monte Carlo transport code to evaluate the neutron yield. In this study, TNSA proton spectra are derived from experimental measurements for the ALLS laser facility (already presented in Chap. 4, 5 and 6). They are used as input for SOPHIE simulations. These experimental data also serve as input in GEANT4 to evaluate the reference case without VHCT. The main SOPHIE output is the proton spectrum at the helix exit, which serves as input for FLUKA simulations.

DoPPLIGHT

In the simulations, we consider a helical coil attached to the rear side of a foil target. The energy and angular distributions of the injected protons are based on experimental measurements with TNSA without a helical coil. The energy distribution corresponds to the green curve in Fig. 7.5,b and the angular distribution follows a super-Gaussian function $dN_p/d\theta \propto \exp\left[-(\theta/\theta_p)^{10}/2\right]$, with $\theta_p = 19°$. The temporal profile of the particle emission dN_p/dt is modeled as a Gaussian function with a full-width at half-maximum (FWHM) duration τ of a few ps. Although its exact value is unknown, it remains negligible compared to the proton transit time (> 100 ps) through the coil and their final bunch duration caused by time-of-flight dispersion. The transverse size of the particle emission zone is set to 200 μm.

The proton dynamics inside the helical coil are governed solely by the electromagnetic fields generated by the discharge current. To model this discharge current, we use as input the current presented in dotted line in Fig. 4.12, such as the one computed in Chap. 4 with ChoCoLaT [4] (optimistic theoretical discharge current).

GEANT4

GEANT4 (Geometry and Tracking) is a Monte Carlo simulation toolkit developed by an international collaboration under the coordination of CERN. It is designed for simulating the passage of particles through matter and is widely used in high-energy physics, astrophysics, medical physics, and radiation shielding applications [122, 123].

The toolkit offers a comprehensive set of functionalities for modeling complex geometries, particle tracking, material definitions, magnetic and electric fields, and detector response. It includes an extensive library of physical models to simulate electromagnetic, hadronic, optical, and decay processes over a broad energy range, from a few eV to several TeV.

In the context of laser-driven neutron generation, GEANT4 is particularly suited for simulating the interaction of laser-accelerated protons with secondary converter targets such as lithium,

(a)

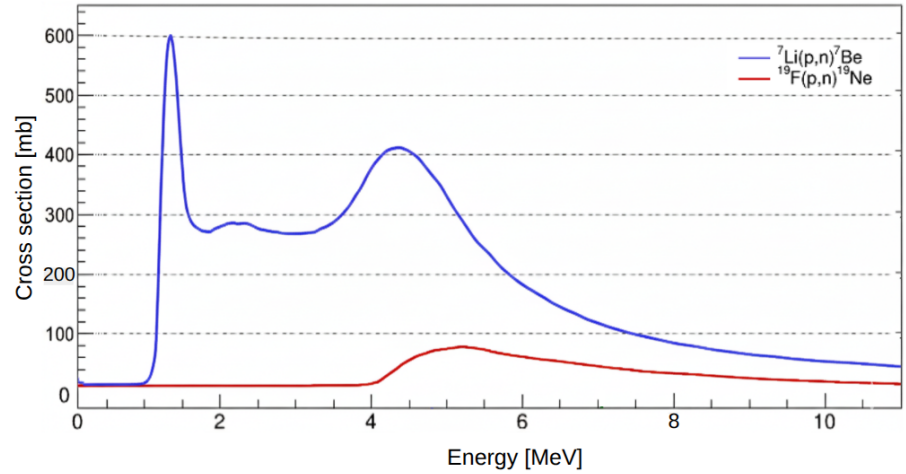

(b)

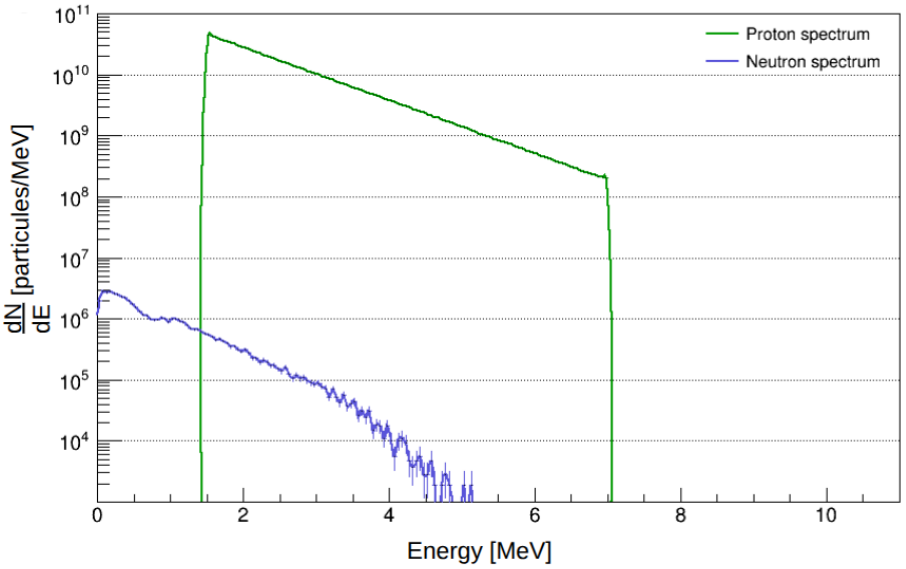

(c)

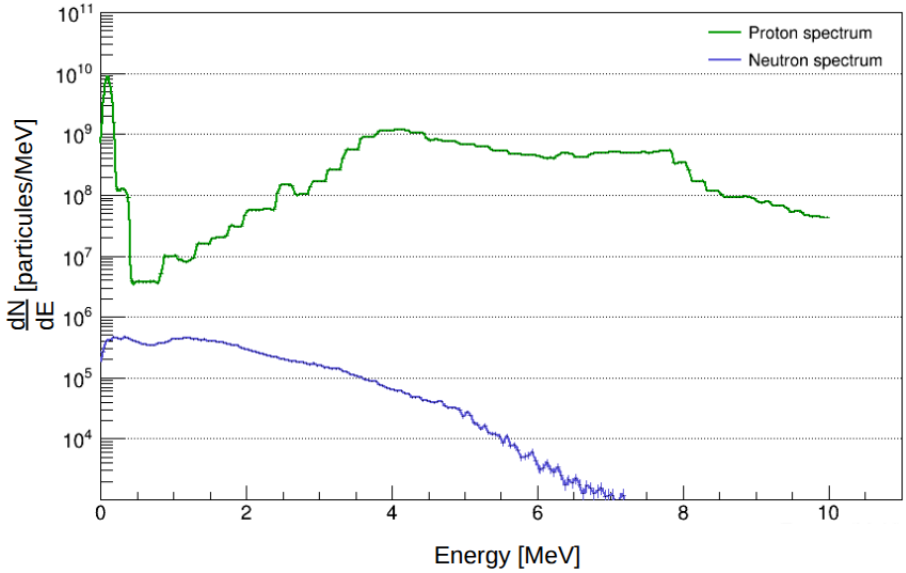

Figure 7.5 – a) Cross sections of the ^{7}Li(p,n)^{7}Be and the ^{19}F(p,n)^{19}Ne reactions, as given by the ENDF/B-VIII.0 [6] and TENDL-2019 libraries [7], respectively. Proton and neutron spectra obtained with TNSA b) and VHCT c) in Geant4 simulations. The Geant4 simulations were carried out by Ronan Lelièvre during his PhD.

beryllium, or deuterated compounds. It allows for the calculation of neutron yields and spectra from nuclear reactions such as ^{7}Li(p, n)^{7}Be, ^{9}Be(p, n)^{9}B, or D(p, n)pp, taking into account the full 3D geometry of the setup and the angular and energy distribution of the incident proton beam.

GEANT4 offers modular physics lists that allow users to select appropriate models for their specific application. For neutron production in the 1–100 MeV proton energy range, physics lists such as `QGSP_BIC_HP` or `FTFP_BERT_HP` are commonly used. These combine intranuclear cascade models (Binary Cascade or Bertini) for hadronic interactions with high-precision neutron transport based on evaluated nuclear data libraries (e.g., ENDF/B-VII [124], JEFF [125], JENDL [126]), ensuring accurate modeling of neutron interactions and transport down to thermal energies.

7.2.4 Simulation Results

The neutron production using the TNSA proton spectrum is illustrated in blue in Fig. 7.5.b, which presents a Geant4 simulation performed by R. Lelièvre during his PhD. Additional experimental results can be found in [89, 127]. However, optimizing the proton spectrum could enhance the interaction between protons and the LiF target by considering proton deceleration and the ^{7}Li(p,n)^{7}Be reaction cross-section. This philosophy is exactly the same as in Chap. 6. The proton and neutron spectra using VHCT are shown in Fig. 7.5.c respectively in green and blue solid line. This figure presents an proton spectrum obtained using VHCT (DoPPLIGHT simulations) at the ALLS facility, along with the corresponding neutron spectrum. The latter exhibits a neutron yield reduced by a factor of two, but with an increased neutron cutoff energy (rising from 4 MeV to 6 MeV). This result demonstrates that, for this class of laser facilities (100TW), helical coil targets are not relevant for the neutron production. However, for larger scale facilities (PW-class laser), they could be relevant if they allow to increase the proton cut-off in order to reach the spallation regime (above 100 MeV).

Spallation is a nuclear reaction in which a high-energy particle, typically a proton with energies above a few hundred MeV, strikes a heavy nucleus, causing the ejection of multiple secondary particles, including neutrons. This process is widely used for neutron production in accelerator-driven systems and is an essential mechanism in applications such as neutron sources for research reactors, medical isotope production, and transmutation of nuclear wastes. Unlike fusion or fission, spallation allows for a continuous and controllable neutron flux by adjusting the incident proton energy and target material, commonly lead, tungsten, or uranium.

7.3 Additional results

A similar work than the one presented in Sec. 7.2.4 has been performed with FLUKA. This time, a SOPHIE simulation has been used as input for the helical coil to get a more robust study. The input proton spectrum is the one presented in Fig. 7.5.a, the green curve. The results presented in Fig. 7.6 confirm the Geant4 simulations, with a similar number of produced

neutrons with and without helical coil, but with a higher neutron cut-off energy using HCT (3 MeV with TNSA and 6 MeV with VHCT). Furthermore, one get two times more neutrons in total with the HCT.

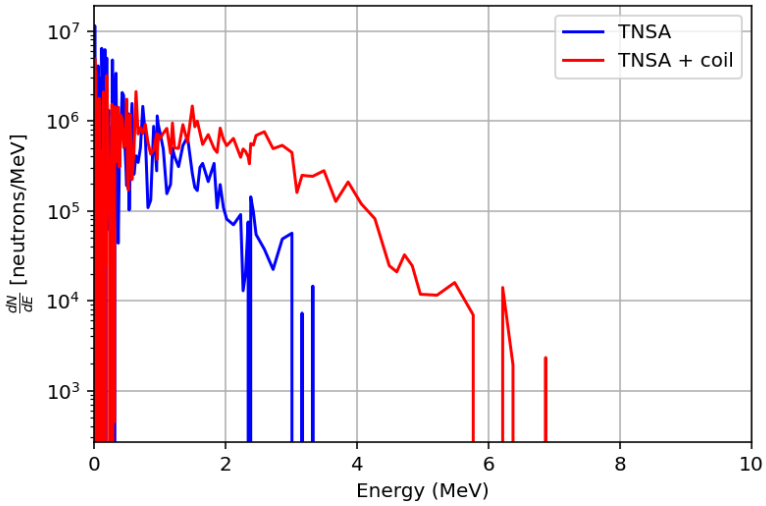

Figure 7.6 – Proton and neutron spectra obtained with TNSA (blue curve) and VHCT (red curve) in FLUKA simulations. The FLUKA simulations were conducted by Thomas Carrière during his PhD.

7.3.1 Conclusion

The use of varying helical coil with tube (VHCT) for laser-driven neutron generation shows significant potential for tailoring the neutron spectrum through proton beam shaping. Simulations indicate that the proton spectrum generated with VHCT, although leading to a slightly lower total neutron yield when interacting with a LiF converter, results in a higher neutron cutoff energy (from 4 MeV to 6 MeV). This spectral extension is beneficial for applications requiring fast neutrons, such as active interrogation [128] or time-resolved materials probing.

These findings suggest that VHCT can be a valuable strategy for optimizing neutron sources, especially when coupled with appropriate converter materials. While LiF remains effective for low-energy neutron production via the $^7\mathrm{Li}(\mathrm{p},\mathrm{n})^7\mathrm{Be}$ reaction, the VHCT-enhanced proton spectrum could be more advantageous for spallation-based approaches, which require higher proton energies and favor heavy-element converters like tungsten or lead.

In summary, although the use of VHCT does not maximize the neutron yield in LiF targets, its ability to shape the proton energy distribution opens new pathways for designing laser-based neutron sources with tailored spectral properties. Future work should explore its integration with spallation targets and investigate the trade-off between yield, energy distribution, and repetition rate for practical applications.

Chapter 8

Conclusion et Perspectives

Sommaire

This PhD work has laid the foundation for a deeper understanding of the potential of helical coil targets in the context of laser-driven proton acceleration. Throughout the thesis, the helical coil concept was investigated from complementary perspectives, combining theoretical analysis, numerical simulations, and first experimental studies. On the theoretical and numerical side, we developed analytical models of current propagation within a varying helical coil with a tube, supported by extensive simulations. On the experimental side, initial campaigns have demonstrated the influence of the helical coil on ion dynamics, in particular highlighting its effect on carbon ions and suggesting its potential as a multi-species filter. These results also indicate possible applications of the coil in domains such as medical radioisotope production, where the electromagnetic fields generated by the HC can selectively enhance the yield of protons and α particles in the relevant energy range. Taken together, these achievements provide a consistent picture of the helical coil's ability to act as both a spectral shaper and a post-accelerator, paving the way for more advanced studies. Building on this groundwork, the following perspectives are dedicated to addressing the main challenges that remain to fully exploit the helical coil targets such as improving its efficiency through coupling with advanced target designs, adapting it to high-repetition-rate laser systems, and exploring its potential for practical applications such as isochoric heating, neutron production, and medical uses.

8.1 High-repetition rate

The development of helical coil targets compatible with high-repetition-rate laser systems represents a crucial step toward advancing laser-driven proton acceleration and its applications. During this PhD, the helical coil targets were often optimized for single-shot experiments, which limits their suitability for future applications. To fully exploit the benefits of the helical coil, it is essential to design and implement helical targets that can operate reliably at high repetition rates. High-repetition-rate operation is indispensable for practical applications such as medical applications (radioisotope production for medicine, oncology ...). A major limitation, however, is that in the conventional helical coil schema, the Target Normal Sheath Acceleration (TNSA) targer is destroyed after each laser shot, preventing the reuse of HC.

To overcome this limitation, one promising approach is to decouple the sources of protons and electrons. In the standard helical coil configuration, the laser simultaneously accelerates protons and generates the fast electrons responsible for the discharge current. By employing two separate target systems, one dedicated to proton generation and another to electron acceleration, it may be possible to sustain high-repetition-rate operation. The proton source could be implemented as a matrix of TNSA targets, as demonstrated in [20], while the electron source could rely on a second TNSA matrix optimized for current generation. Such a scheme would allow for continuous alignment of the proton targets while retaining the laser-driven current discharge.

Another possibility is the direct development of helical coil target matrices, where each coil is combined with a small TNSA foil. However, this technique requires highly precise fabrication in order to ensure that the laser beam remains properly focused when translating from one target

to the next.

8.2 Coupling helical coil

One of the key issues with proton acceleration in laser-driven experiments is the energy conversion efficiency. Typically, a few tens of percent of the laser energy is transferred to the electrons, but only a small percentage, around a few percent, goes to the ions, including protons. This low conversion rate presents a significant limitation in maximizing the overall efficiency of proton acceleration. It is a critical area of focus in my research, as improving this conversion rate is essential for advancing of fast ignition. To do it, I suggest optimizing the design of the helical coil target using curved foils or foams.

8.2.1 Curved foil

Curved foils are a technique used in laser-driven ion acceleration to enhance certain aspects of acceleration dynamics (see Fig. 8.1). In laser ion acceleration setups, curved foils stand out from conventional flat targets, offering advantages in terms of control and efficiency of ion acceleration. When the laser beam hits a curved target, the geometry of the foil allows the electric field to be concentrated at the rear of the target (where the ions are accelerated). This creates a focalization field and enhances ion acceleration. The curvature can reduce the angular divergence of the ions, leading to a more collimated and concentrated ion beam [8, 129].

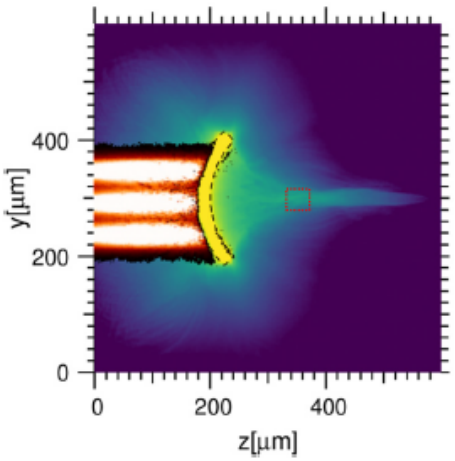

Figure 8.1 – 2D PIC simulation of TNSA laser–ion acceleration off a curved foil. Three laser beams are incident on a 20 μm thick, 200 μm wide solid density foil with a curvature radius of 140 μm. Reproduced from A. Kemp, S. Wilks, and M. Tabak, "Laser-to-proton conversion efficiency studies for proton fast ignition," Physics of Plasmas 31 (2024). [8]

8.2.2 Foam

The use of foams (see Fig. 8.2) in laser-driven ion acceleration is a technique that has gained attention due to its potential advantages in improving the efficiency and control of the acceleration process. Foam is an underdense target which can be used as a target in ion acceleration and

is highly studied in simulations [130] and in experiments [131] because it can enhance the conversion of laser energy into electron and ion energy. The structure of the foam allows for a longer interaction between the laser beam and the material, which can increase the efficiency of energy conversion. Furthermore, foam targets have a much lower density (10^{19} to 10^{21} cm^{-3}) [9] compared to solid targets. This can reduce reflection effects and allow for more effective absorption of the laser beam, thereby facilitating ion acceleration [132].

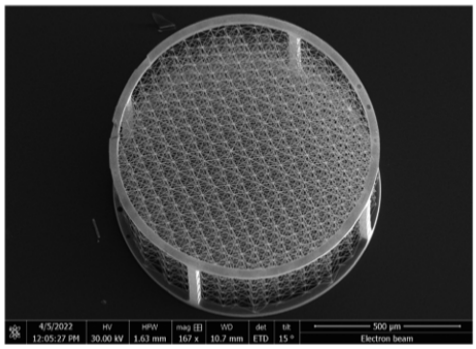

Figure 8.2 – Example of a laser-printed target for use in high-power laser–plasma interaction experiments. Reproduced from V. Tikhonchuk and S. Weber, "Physics of porous materials under extreme laser-generated conditions," Matter and Radiation at Extremes 9 (2024). [9]

8.2.3 Idea of combination

The two previously discussed schemes enhance laser-driven accelerated particles through different mechanisms. The curved foil targets improve proton focusing, while foam targets increase absorption efficiency.

When coupled to a helical coil target, the proton focusing provided by the curved foil can increase the number of protons injected into the coil, thereby enhancing the space charge. As already discussed in Chap. 5, the space charge plays an important role in raising the cut-off energy thanks to HC.

Similarly, the use of foam targets to enhance laser absorption contributes by increasing both the number and the energy of accelerated protons and electrons. Coupled with a helical coil target, the higher number of injected protons further increases the space charge and thus the cut-off energy. In addition, a larger population of accelerated electrons generates a stronger discharge current, which in turn improves the focusing and post-acceleration of the proton beam.

Therefore, combining these two techniques with helical coil targets could provide improved performance and broaden the range of potential applications.

8.3 General conclusion

From Chap. 7, it is clear that considerable work remains to be done in order to fully exploit the potential of the helical coil for laser-driven proton acceleration. During this PhD, our study has established a solid theoretical and numerical foundation, developping the physical understanding

of the current propagation through the helix and the acceleration process. Yet, the transition towards practical, high-impact applications will require extensive experimental validation. In particular, a campaign of experiments at high repetition rate and with increased laser energy is necessary to achieve higher proton energies and to evaluate the long-term stability and robustness of the acceleration process. Such efforts have to be done to investigate the impact of laser parameters on the reproducibility and the robustness of the proton beam.

Beyond the purely theoretical and numerical achievements, the first experimental results obtained during this PhD have demonstrated the effect of the helical coil on carbon ions, opening the way for further multi-species studies. These findings suggest a new potential role for the helical coil target: acting as a species filter. In parallel, simulations have been performed to highlight the potential of the helical coil for specific applications, notably in the field of medical radioisotope production. These studies indicate that the electromagnetic fields generated by the coil can significantly increase the number of protons and α particles in the energy range relevant for radioisotope generation. Depending on the chosen helical coil geometry, we are able to select the desired energy to increase the desired radioisotope production. Once again, experimental work has to support these results.

However, much work remains to adapt the helical coil to other promising applications such as isochoric heating and neutron production. In these cases, the efficiency of proton collection with the coil, which currently stands at approximately 1%, must be substantially increased in order to obtain significant results. To do it, the combination of the helical coil with other target designs could be explored. For example, coupling the coil to curved-foil targets [129] or to low-density foams [9,132] could enhance the target absorption which increase in turn, the number and energy of accelerated protons and the intensity of the discharge current. Another considered way to increase the helical coil efficiency is to use Artificial Intelligence (AI). Using lots of SOPHIE or DoPPLIGHT simulations we could train an AI model to optimize the helical coil target geometry in the same manner as it was previously done for ICF target optimization [133].

Bibliography

[1] G. A. Mourou, T. Tajima, and S. V. Bulanov, "Optics in the relativistic regime," *Reviews of modern physics*, vol. 78, no. 2, pp. 309–371, 2006.

[2] M. Roth and M. Schollmeier, "Ion acceleration: Tnsa," in *Laser-Plasma Interactions and Applications*, pp. 303–350, Springer, 2013.

[3] S. Kar, H. Ahmed, R. Prasad, M. Cerchez, S. Brauckmann, B. Aurand, G. Cantono, P. Hadjisolomou, C. L. Lewis, A. Macchi, *et al.*, "Guided post-acceleration of laser-driven ions by a miniature modular structure," *Nat. Commun.*, vol. 7, p. 1, 2016.

[4] A. Poyé, J.-L. Dubois, F. Lubrano-Lavaderci, E. d'Humiéres, M. Bardon, S. Hulin, M. Bailly-Grandvaux, J. Ribolzi, D. Raffestin, J. Santos, *et al.*, "Dynamic model of target charging by short laser pulse interactions," *Phys. Rev. E*, vol. 92, no. 4, p. 043107, 2015.

[5] A. Hirsch-Passicos, C. Lacoste, F. André, Y. Elskens, E. D'Humières, V. Tikhonchuk, and M. Bardon, "Helical coil design with controlled dispersion for bunching enhancement of protons generated by the target normal sheath acceleration," *Phys. Rev. E*, vol. 109, no. 2, p. 025211, 2024.

[6] D. A. Brown, M. B. Chadwick, R. Capote, A. Kahler, A. Trkov, M. Herman, A. Sonzogni, Y. Danon, A. Carlson, M. Dunn, *et al.*, "Endf/b-viii. 0: the 8th major release of the nuclear reaction data library with cielo-project cross sections, new standards and thermal scattering data," *Nuclear Data Sheets*, vol. 148, pp. 1–142, 2018.

[7] A. Koning, D. Rochman, J.-C. Sublet, N. Dzysiuk, M. Fleming, and S. Van der Marck, "Tendl: complete nuclear data library for innovative nuclear science and technology," *Nuclear Data Sheets*, vol. 155, pp. 1–55, 2019.

[8] A. Kemp, S. Wilks, and M. Tabak, "Laser-to-proton conversion efficiency studies for proton fast ignition," *Physics of Plasmas*, vol. 31, no. 4, 2024.

[9] V. Tikhonchuk and S. Weber, "Physics of porous materials under extreme laser-generated conditions," *Matter and Radiation at Extremes*, vol. 9, no. 3, 2024.

[10] W. Yao, A. Higginson, J.-R. Marquès, P. Antici, J. Béard, K. Burdonov, M. Borghesi, A. Castan, A. Ciardi, B. Coleman, *et al.*, "Dynamics of nanosecond laser pulse propagation and of associated instabilities in a magnetized underdense plasma," *Physical Review Letters*, vol. 130, no. 26, p. 265101, 2023.

[11] E. Morse, *Inertial Fusion*, pp. 345–412. Cham: Springer International Publishing, 2018.

[12] M. Nakatsutsumi, J. Marques, P. Antici, N. Bourgeois, J. Feugeas, T. Lin, P. Nicolaï, L. Romagnani, R. Kodama, P. Audebert, *et al.*, "High-power laser delocalization in plasmas leading to long-range beam merging," *Nature Physics*, vol. 6, no. 12, pp. 1010–1016, 2010.

[13] D. Strickland and G. Mourou, "Compression of amplified chirped optical pulses," *Optics communications*, vol. 55, no. 6, pp. 447–449, 1985.

[14] A. Macchi, F. Cattani, T. V. Liseykina, and F. Cornolti, "Laser acceleration of ion bunches at the front surface of overdense plasmas," *Physical review letters*, vol. 94, no. 16, p. 165003, 2005.

[15] A. Macchi, S. Veghini, T. V. Liseykina, and F. Pegoraro, "Radiation pressure acceleration of ultrathin foils," *New Journal of Physics*, vol. 12, no. 4, p. 045013, 2010.

[16] A. Macchi and C. Benedetti, "Ion acceleration by radiation pressure in thin and thick targets," *Nuclear Instruments and Methods in Physics Research Section A: Accelerators, Spectrometers, Detectors and Associated Equipment*, vol. 620, no. 1, pp. 41–45, 2010.

[17] L. O. Silva, M. Marti, J. R. Davies, R. A. Fonseca, C. Ren, F. S. Tsung, and W. B. Mori, "Proton shock acceleration in laser-plasma interactions," *Physical Review Letters*, vol. 92, no. 1, p. 015002, 2004.

[18] D. Raffestin, L. Lecherbourg, I. Lantuéjoul, B. Vauzour, P. Masson-Laborde, X. Davoine, N. Blanchot, J. Dubois, X. Vaisseau, E. d'Humières, *et al.*, "Enhanced ion acceleration using the high-energy petawatt petal laser," *Matter and Radiation at Extremes*, vol. 6, no. 5, 2021.

[19] A. Yogo, K. Mima, N. Iwata, S. Tosaki, A. Morace, Y. Arikawa, S. Fujioka, T. Johzaki, Y. Sentoku, H. Nishimura, *et al.*, "Boosting laser-ion acceleration with multi-picosecond pulses," *Scientific reports*, vol. 7, no. 1, p. 42451, 2017.

[20] E. Catrix, F. Boivin, K. Langlois, S. Vallières, C. Y. Boynukara, S. Fourmaux, and P. Antici, "Stable high repetition-rate laser-driven proton beam production for multidisciplinary applications on the advanced laser light source ion beamline," *Rev. Sci. Instrum*, vol. 94, no. 10, 2023.

[21] M. Bardon, J. Moreau, L. Romagnani, C. Rousseaux, M. Ferri, F. Lefévre, I. Lantuéjoul, B. Etchessahar, S. Bazzoli, D. Farcage, *et al.*, "Physics of chromatic focusing, post-acceleration and bunching of laser-driven proton beams in helical coil targets," *Plasma Phys. Control. Fusion*, vol. 62, no. 12, p. 125019, 2020.

[22] F. Consoli, V. T. Tikhonchuk, M. Bardon, P. Bradford, D. C. Carroll, J. Cikhardt, M. Cipriani, R. J. Clarke, T. E. Cowan, C. N. Danson, *et al.*, "Laser produced electromagnetic pulses: generation, detection and mitigation," *High Power Laser Sci. Eng.*, vol. 8, 2020.

[23] L. Keldysh, "Ionization in the field of a strong electromagnetic wave," in *Selected Papers of Leonid V Keldysh*, pp. 56–63, World Scientific, 2024.

[24] M. Göppert-Mayer, "Über elementarakte mit zwei quantensprüngen," *Annalen der Physik*, vol. 401, no. 3, pp. 273–294, 1931.

[25] M. V. Ammosov, N. B. Delone, and V. P. Krainov, "Tunnel ionization of complex atoms and atomic ions in electromagnetic field," in *High intensity laser processes*, vol. 664, pp. 138–141, SPIE, 1986.

[26] P. Gibbon, *Short pulse laser interactions with matter: an introduction.* World Scientific, 2005.

[27] P. B. Corkum, "Plasma perspective on strong field multiphoton ionization," *Physical review letters*, vol. 71, no. 13, p. 1994, 1993.

[28] R. Snavely, M. Key, S. Hatchett, T. Cowan, M. Roth, T. Phillips, M. Stoyer, E. Henry, T. Sangster, M. Singh, *et al.*, "Intense high-energy proton beams from petawatt-laser irradiation of solids," *Phys. Rev. Lett*, vol. 85, p. 2945, 2000.

[29] S. Wilks, A. Langdon, T. Cowan, M. Roth, M. Singh, S. Hatchett, M. Key, D. Pennington, A. Mackinnon, and R. Snavely, "Energetic proton generation in ultra-intense laser-solid interactions," *Phys. Plasmas*, vol. 8, pp. 542–549, 2001.

[30] J. Crow, P. Auer, and J. Allen, "The expansion of a plasma into a vacuum," *Journal of Plasma Physics*, vol. 14, no. 1, pp. 65–76, 1975.

[31] P. Mora, "Plasma expansion into a vacuum," *Physical Review Letters*, vol. 90, no. 18, p. 185002, 2003.

[32] J. Schreiber, F. Bell, F. Grüner, U. Schramm, M. Geissler, M. Schnürer, S. Ter-Avetisyan, B. M. Hegelich, J. Cobble, E. Brambrink, *et al.*, "Analytical model for ion acceleration by high-intensity laser pulses," *Physical review letters*, vol. 97, no. 4, p. 045005, 2006.

[33] F. Brunel, "Not-so-resonant, resonant absorption," *Physical Review Letters*, vol. 59, no. 1, p. 52, 1987.

[34] E. S. Weibel, "Anomalous skin effect in a plasma," *The Physics of Fluids*, vol. 10, no. 4, pp. 741–748, 1967.

[35] E. Gamalii and V. Tikhonchuk, "Effect of intense ultrashort light pulses on a substance," *JETP Letters*, vol. 48, no. 8, 1988.

[36] V. L. Ginzburg, *The propagation of electromagnetic waves in plasmas.* International Series of Monographs in Electromagnetic Waves, Pergamon Press, 1970.

[37] W. L. Kruer, *The Physics of Laser Plasma Interaction.* Addison-Wesley, 1988.

[38] P. Catto and R. M. More, "Sheath inverse bremsstrahlung in laser produced plasmas," *The Physics of Fluids*, vol. 20, no. 4, pp. 704–705, 1977.

[39] J. T. Mendonça, "Threshold for electron heating by two electromagnetic waves," *Physical Review A*, vol. 28, no. 6, p. 3592, 1983.

[40] Z.-M. Sheng, K. Mima, Y. Sentoku, M. S. Jovanovic, T. Taguchi, J. Zhang, and J. Meyer-ter Vehn, "Stochastic heating and acceleration of electrons in colliding laser fields in plasma," *Physical Review Letters*, vol. 88, no. 5, p. 055004, 2002.

[41] A. Bourdier, D. Patin, and E. Lefebvre, "Stochastic heating in ultra high intensity laser-plasma interaction," *Laser and Particle Beams*, vol. 25, no. 1, pp. 169–180, 2007.

[42] W. L. Kruer and K. Estabrook, "$\mathbf{J} \times \mathbf{B}$ heating by very intense laser light," *The Physics of Fluids*, vol. 28, no. 1, pp. 430–432, 1985.

[43] S. C. Wilks, W. L. Kruer, M. Tabak, and A. B. Langdon, "Absorption of ultra-intense laser pulses," *Physical Review Letters*, vol. 69, no. 9, p. 1383, 1992.

[44] G. Malka and J.-L. Miquel, "Experimental confirmation of ponderomotive-force electrons produced by an ultrarelativistic laser pulse on a solid target," *Physical Review Letters*, vol. 77, no. 1, p. 75, 1996.

[45] A. Debayle, J. J. Honrubia, E. d'Humières, and V. T. Tikhonchuk, "Divergence of laser-driven relativistic electron beams," *Physical Review E*, vol. 82, no. 3, p. 036405, 2010.

[46] E. S. Weibel, "Spontaneously growing transverse waves in a plasma due to an anisotropic velocity distribution," *Physical Review Letters*, vol. 2, no. 3, p. 83, 1959.

[47] A. Macchi, *A Superintense Laser-Plasma Interaction Theory Primer*. Springer, 2013.

[48] J. Fuchs, P. Antici, E. d'Humières, *et al.*, "Laser-driven proton scaling laws and new paths towards energy increase," *Nature Physics*, vol. 2, no. 1, pp. 48–54, 2006.

[49] M. Roth, A. Blazevic, M. Geissel, *et al.*, "Energetic ions generated by laser pulses: a detailed study on target properties," *Physical Review Special Topics-Accelerators and Beams*, vol. 5, no. 6, p. 061301, 2002.

[50] A. Poyé, S. Hulin, M. Bailly-Grandvaux, J.-L. Dubois, J. Ribolzi, D. Raffestin, M. Bardon, F. Lubrano-Lavaderci, E. D'Humières, J. J. Santos, *et al.*, "Physics of giant electromagnetic pulse generation in short-pulse laser experiments," *Physical Review E*, vol. 91, no. 4, p. 043106, 2015.

[51] A. Gilmour Jr, *Microwave and millimeter-wave vacuum electron devices: inductive output tubes, klystrons, traveling-wave tubes, magnetrons, crossed-field amplifiers, and gyrotrons*. Artech House, 2020.

[52] R. G. Carter, *Microwave and RF vacuum electronic power sources*. Cambridge Univ. Press, 2018.

[53] D. F. Minenna, Y. Elskens, F. André, A. Poyé, J. Puech, and F. Doveil, "Dimoha: A time-domain algorithm for traveling-wave tube simulations," *IEEE Transactions on Electron Devices*, vol. 66, no. 9, pp. 4042–4047, 2019.

[54] M. C. Converse, J. H. Booske, and S. C. Hagness, "Impulse amplification in a traveling-wave tube-i: Simulation and experimental validation," *IEEE transactions on plasma science*, vol. 32, no. 3, pp. 1040–1048, 2004.

[55] S. E. Tsimring, *Electron beams and microwave vacuum electronics*. John Wiley & Sons, 2006.

[56] G. V. Torgashov, R. A. Torgashov, V. N. Titov, A. G. Rozhnev, and N. M. Ryskin, "Meander-line slow-wave structure for high-power millimeter-band traveling-wave tubes with multiple sheet electron beam," *IEEE Electron Device Letters*, vol. 40, no. 12, pp. 1980–1983, 2019.

[57] D. Shiffler, J. A. Nation, and G. S. Kerslick, "A high-power, traveling wave tube amplifier," *IEEE transactions on plasma science*, vol. 18, no. 3, pp. 546–552, 1990.

[58] J. R. Pierce, "Traveling-wave tubes," *Bell Syst. Tech. J.*, vol. 29, no. 2, pp. 189–250, 1950.

[59] J. Freund, M. Kodis, and N. Vanderplaats, "Self-consistent field theory of a helix traveling wave tube amplifier," *IEEE transactions on plasma science*, vol. 20, no. 5, pp. 543–553, 1992.

[60] R. G. Carter and R. O. Jenkins, "Studies of the transient response of a klystron," in *2008 IEEE International Vacuum Electronics Conference*, pp. 312–313, IEEE, 2008.

[61] C. Lacoste, A. Hirsch, E. d'Humières, V. Tikhonchuk, P. Antici, and M. Bardon, "Theoretical model of current propagation in a helical coil with varying geometry and screen tube," *MRE*, vol. 9, no. 6, 2024.

[62] A. Hirsch-Passicos, *Numerical and experimental study of a new laser-driven proton accelerator*. PhD thesis, Université de Bordeaux, 2023.

[63] O. Cessenat, "SOPHIE, an FDTD code on the way to multicore, getting rid of the memory bandwidth bottleneck better using cache," *arXiv preprint arXiv:1301.4539*, 2013.

[64] R. Kompfner, "The traveling-wave tube as amplifier at microwaves," *Proc. IRE*, vol. 35, no. 2, pp. 124–127, 1947.

[65] G. Kino and S. Paik, "Circuit theory of coupled transmission systems," *J. Appl. Phys*, vol. 33, no. 10, pp. 3002–3008, 1962.

[66] H. S. Uhm and J. Y. Choe, "Properties of the electromagnetic wave propagation in a helix-loaded waveguide," *J. Appl. Phys*, vol. 53, no. 12, pp. 8483–8488, 1982.

[67] D. Safi, P. Birtel, S. Meyne, and A. F. Jacob, "A traveling-wave tube simulation approach with CST particle studio," *IEEE transactions on electron devices*, vol. 65, no. 6, pp. 2257–2263, 2018.

[68] V. Tarakanov, "User's manual for code KARAT," 1992.

[69] T. Weiland, M. Bartsch, U. Becker, M. Bihn, U. Blell, M. Clemens, M. Dehler, M. Dohlus, M. Drevlak, X. Du, *et al.*, "MAFIA version 4," in *AIP Conference Proceedings*, vol. 391, pp. 65–70, AIP, 1997.

[70] P. Waller, *Modélisation numérique de l'interaction et diagnostic expérimental du faisceau d'électrons dans un Tube à Ondes Progressives spatial*. PhD thesis, Paris 7, 1999.

[71] T. M. Antonsen and B. Levush, *CHRISTINE: A multifrequency parametric simulation code for traveling wave tube amplifiers*. Naval Research Laboratory, 1997.

[72] B. Li, Z. H. Yang, J. Q. Li, X. F. Zhu, T. Huang, Q. Hu, Y. L. Hu, L. Xu, J. J. Ma, L. Liao, *et al.*, "Theory and design of microwave-tube simulator suite," *IEEE Transactions on Electron Devices*, vol. 56, no. 5, pp. 919–927, 2009.

[73] S. Vallières, M. Salvadori, P. Puyuelo-Valdes, S. Payeur, S. Fourmaux, F. Consoli, C. Verona, E. d'Humières, M. Chicoine, S. Roorda, *et al.*, "Thomson parabola and time-

of-flight detector cross-calibration methodology on the ALLS 100 tw laser-driven ion acceleration beamline," *Rev. Sci. Instrum*, vol. 91, no. 10, 2020.

[74] M. Bardon and al., "DoPPLIGHT: an efficient model to study and design helical coil targets for laser-driven ion acceleration," *To be submitted*, 2024.

[75] K. Yee, "Numerical solution of initial boundary value problems involving maxwell's equations in isotropic media," *IEEE Trans. Antennas Propag*, vol. 14, no. 3, pp. 302–307, 1966.

[76] J. P. Boris and R. A. Shanny, "Proceedings of the conference on the numerical simulation of plasmas (4th) held at the Naval Research Laboratory, Washington, DC on 2, 3 november 1970," 1971.

[77] E. Lefebvre, N. Cochet, S. Fritzler, V. Malka, M.-M. Aléonard, J.-F. Chemin, S. Darbon, L. Disdier, J. Faure, A. Fedotoff, *et al.*, "Electron and photon production from relativistic laser–plasma interactions," *Nucl. Fusion*, vol. 43, no. 7, p. 629, 2003.

[78] J. Derouillat, A. Beck, F. Pérez, T. Vinci, M. Chiaramello, A. Grassi, M. Flé, G. Bouchard, I. Plotnikov, N. Aunai, *et al.*, "SMILEI: A collaborative, open-source, multi-purpose particle-in-cell code for plasma simulation," *Computer Physics Communications*, vol. 222, pp. 351–373, 2018.

[79] J. P. Boris *et al.*, "Relativistic plasma simulation-optimization of a hybrid code," in *Proc. Fourth Conf. Num. Sim. Plasmas*, pp. 3–67, 1970.

[80] S. Carrier-Vallieres, *Towards reliable, intense and high repetition-rate laser-driven ion beamlines.* PhD thesis, Université de Bordeaux; Institut national de la recherche scientifique, 2020.

[81] C. Li, Y. Li, Y. Yan, Y. Fang, J. Li, M. Wu, C. Lin, and X. Yan, "Design methodology for stable dispersion-suppressed helix post-acceleration in laser proton accelerators," *Physics of Plasmas*, vol. 32, no. 9, 2025.

[82] K. Aliane *et al.*, "Extending a 1-d hamiltonian traveling-wave tube model to laser driven proton acceleration in helical coil targets : Evaluation of self-consistency effects," *submitted to Physics of Plasmas.*

[83] C. Lacoste, E. Catrix, S. Vallières, A. Hirsch-Passicos, T. Guilberteau, M. Lafargue, J. Lopez, I. Manek-Hönninger, S. Fourmaux, D. Raffestin, *et al.*, "Experimental and numerical investigation of the impact of helical coil targets on laser-driven proton and carbon accelerations," *Matter and Radiation at Extremes*, vol. 10, no. 3, 2025.

[84] B. Chichkov, C. Momma, S. Nolte, F. von Alversleben, and A. Tünnermann, "Femtosecond, picosecond and nanosecond laser ablation of solids," *Appel. Phys. A*, vol. 63, p. 109, 1996.

[85] K. Sugioka and Y. Cheng, "Ultrafast lasers—reliable tools for advanced materials processing," *Light Sci. Appl.*, vol. 3, p. e149, 2014.

[86] R. Gattass and E. Mazur, "Femtosecond laser micromachining in transparent materials," *Nature Photonics*, vol. 2, p. 219, 2008.

[87] P. Balage, J. Lopez, G. Bonamis, C. Hönninger, and I. Manek-Hönninger, "Crack-free high-aspect ratio holes in glasses by top–down percussion drilling with infrared femtosecond laser ghz-bursts," *Int. J. Extrem. Manuf.*, vol. 5, p. 015002, 2023.

[88] T. Guilberteau, P. Balage, M. Lafargue, J. Lopez, L. Gemini, and I. Manek-Hönninger, "Bessel beam femtosecond laser interaction with fused silica before and after chemical etching: Comparison of single pulse, mhz-burst, and ghz-burst," *Int. J. Extrem. Manuf.*, vol. 5, p. 015002, 2023.

[89] R. Lelievre, E. Catrix, S. Vallières, S. Fourmaux, A. Allaoua, V. Anthonippillai, P. Antici, Q. Ducasse, and J. Fuchs, "High repetition-rate 0.5 hz broadband neutron source driven by the advanced laser light source," *Physics of Plasmas*, vol. 31, no. 9, 2024.

[90] J. P. Boris and R. A. Shanny, *Proceedings.* Naval Research Laboratory, 1973.

[91] U. Amaldi and G. Kraft, "Radiotherapy with beams of carbon ions," *Reports on progress in physics*, vol. 68, no. 8, p. 1861, 2005.

[92] N. P. Dover, T. Ziegler, S. Assenbaum, C. Bernert, S. Bock, F.-E. Brack, T. E. Cowan, E. J. Ditter, M. Garten, L. Gaus, *et al.*, "Enhanced ion acceleration from transparency-driven foils demonstrated at two ultraintense laser facilities," *Light: Science & Applications*, vol. 12, no. 1, p. 71, 2023.

[93] C. Lacoste, T. Carrière, H. Larreur, D. Batani, D. Raffestin, P. Antici, E. D'Humières, P. Nicolaï, and M. Bardon, "Enhanced laser-driven radioisotope production using a helical coil target with tube," *Physical Review Accelerators and Beams*, vol. 28, no. 9, p. 093401, 2025.

[94] K. A. Domnanich, C. Müller, M. Benešová, R. Dressler, S. Haller, U. Köster, B. Ponsard, R. Schibli, A. Türler, and N. P. van Der Meulen, "47 sc as useful β—emitter for the radiotheragnostic paradigm: a comparative study of feasible production routes," *EJNMMI Radiopharmacy and Chemistry*, vol. 2, pp. 1–17, 2017.

[95] R. Walczak, S. Krajewski, K. Szkliniarz, M. Sitarz, K. Abbas, J. Choiński, A. Jakubowski, J. Jastrzębski, A. Majkowska, F. Simonelli, *et al.*, "Cyclotron production of 43 sc for pet imaging," *EJNMMI physics*, vol. 2, pp. 1–10, 2015.

[96] M. L. E. Oliphant and E. Rutherford, "Experiments on the transmutation of elements by protons," *Proc. R. Soc. Lond. A*, vol. 141, no. 843, pp. 259–281, 1933.

[97] V. Belyaev, A. Matafonov, V. Vinogradov, V. Krainov, V. Lisitsa, A. Roussetski, G. Ignatyev, and V. Andrianov, "Observation of neutronless fusion reactions in picosecond laser plasmas," *Phys. Rev. E*, vol. 72, no. 2, p. 026406, 2005.

[98] M. Streeter, G. Glenn, S. Dilorio, F. Treffert, B. Loughran, H. Ahmed, S. Astbury, M. Borghesi, N. Bourgeois, C. Curry, S. Dann, N. Dover, T. Dzelzainis, O. Ettlinger, M. Gauthier, L. Giuffrida, S. Glenzer, R. Gray, J. Green, G. Hicks, C. Hyland, V. Istokskaia, M. King, D. Margarone, O. McCusker, P. McKenna, Z. Najmudin, C. Parisuaña,

P. Parsons, C. Spindloe, D. Symes, A. Thomas, N. Xu, and C. Palmer, "Stable laser-acceleration of high-flux proton beams with plasma collimation," *Nature Communications*, vol. 16, 2025.

[99] P. Martin, H. Ahmed, O. Cavanagh, S. Ferguson, J. Green, B. Greenwood, B. Odlozilik, M. Borghesi, and S. Kar, "Multi-parametric characterization of proton bunches above 50 mev generated by helical coil targets," *High Power Laser Science and Engineering*, vol. 12, p. e88, 2024.

[100] H. Ahmed, P. Hadjisolomou, K. Naughton, A. Alejo, S. Brauckmann, G. Cantono, S. Ferguson, M. Cerchez, D. Doria, J. Green, *et al.*, "High energy implementation of coil-target scheme for guided re-acceleration of laser-driven protons," *Scientific Reports*, vol. 11, no. 1, p. 699, 2021.

[101] P. Hadjisolomou, H. Ahmed, R. Prasad, M. Cerchez, S. Brauckmann, B. Aurand, A. Schroer, M. Swantusch, O. Willi, M. Borghesi, *et al.*, "Dynamics of guided post-acceleration of protons in a laser-driven travelling-field accelerator," *Plasma Physics and Controlled Fusion*, vol. 62, no. 11, p. 115023, 2020.

[102] R. P. Baum and H. R. Kulkarni, "Theranostics: from molecular imaging using ga-68 labeled tracers and pet/ct to personalized radionuclide therapy-the bad berka experience," *Theranostics*, vol. 2, no. 5, p. 437, 2012.

[103] R. Hernandez, H. F. Valdovinos, Y. Yang, R. Chakravarty, H. Hong, T. E. Barnhart, and W. Cai, "44sc: an attractive isotope for peptide-based pet imaging," *Molecular pharmaceutics*, vol. 11, no. 8, pp. 2954–2961, 2014.

[104] F. Roesch, "Scandium-44: benefits of a long-lived pet radionuclide available from the 44ti/44sc generator system," *Current radiopharmaceuticals*, vol. 5, no. 3, pp. 187–201, 2012.

[105] C. Müller, M. Bunka, S. Haller, U. Köster, V. Groehn, P. Bernhardt, N. van der Meulen, A. Türler, and R. Schibli, "Promising prospects for 44sc-/47sc-based theragnostics: application of 47sc for radionuclide tumor therapy in mice," *Journal of nuclear medicine*, vol. 55, no. 10, pp. 1658–1664, 2014.

[106] C. Champion, M. A. Quinto, C. Morgat, P. Zanotti-Fregonara, and E. Hindié, "Comparison between three promising ß-emitting radionuclides, 67cu, 47sc and 161tb, with emphasis on doses delivered to minimal residual disease," *Theranostics*, vol. 6, no. 10, p. 1611, 2016.

[107] S. Okamoto, T. Shiga, and N. Tamaki, "Clinical perspectives of theranostics," *Molecules*, vol. 26, no. 8, 2021.

[108] S. M. Qaim, B. Scholten, and B. Neumaier, "New developments in the production of theranostic pairs of radionuclides," *Journal of Radioanalytical and Nuclear Chemistry*, vol. 318, pp. 1493–1509, 2018.

[109] T. Böhlen, F. Cerutti, M. Chin, A. Fassò, A. Ferrari, P. G. Ortega, A. Mairani, P. R. Sala, G. Smirnov, and V. Vlachoudis, "The fluka code: developments and challenges for high energy and medical applications," *Nucl. Data Sheets*, vol. 120, pp. 211–214, 2014.

[110] N. Miyanaga, H. Azechi, K. Tanaka, T. Kanabe, T. Jitsuno, J. Kawanaka, Y. Fujimoto, R. Kodama, H. Shiraga, K. Knodo, *et al.*, "10-kj pw laser for the firex-i program," in *J. Phys. IV*, vol. 133, pp. 81–87, EDP sciences, 2006.

[111] D. Margarone, A. Morace, J. Bonvalet, Y. Abe, V. Kantarelou, D. Raffestin, L. Giuffrida, P. Nicolai, M. Tosca, A. Picciotto, *et al.*, "Generation of α-particle beams with a multi-kj, peta-watt class laser system," *Front. Phys.*, vol. 8, p. 343, 2020.

[112] J. Bonvalet, P. Nicolai, D. Raffestin, E. D'humieres, D. Batani, V. Tikhonchuk, V. Kantarelou, L. Giuffrida, M. Tosca, G. Korn, *et al.*, "Energetic α-particle sources produced through proton-boron reactions by high-energy high-intensity laser beams," *Phys. Rev. E*, vol. 103, no. 5, p. 053202, 2021.

[113] G. Battistoni, T. Boehlen, F. Cerutti, P. W. Chin, L. S. Esposito, A. Fasso, A. Ferrari, A. Lechner, A. Empl, A. Mairani, *et al.*, "Overview of the fluka code," *Ann. Nucl. Energy*, vol. 82, pp. 10–18, 2015.

[114] A. Ferrari, J. Ranft, P. R. Sala, and A. Fassò, *FLUKA: A multi-particle transport code (Program version 2005)*. No. CERN-2005-10, Cern, 2005.

[115] F. Jamar, J. Buscombe, A. Chiti, P. E. Christian, D. Delbeke, K. J. Donohoe, O. Israel, J. Martin-Comin, and A. Signore, "Eanm/snmmi guideline for 18f-fdg use in inflammation and infection," *Journal of Nuclear Medicine*, vol. 54, no. 4, pp. 647–658, 2013.

[116] P. K. Patel, A. J. Mackinnon, M. H. Key, T. E. Cowan, M. E. Foord, M. Allen, D. Price, H. Ruhl, P. T. Springer, and R. B. Stephens, "Isochoric heating of solid-density matter with an ultrafast proton beam," *Physical Review Letters*, vol. 91, no. 12, p. 125004, 2003.

[117] M. Roth, T. E. Cowan, M. H. Key, S. P. Hatchett, C. Brown, W. Fountain, J. Johnson, D. M. Pennington, R. A. Snavely, S. C. Wilks, K. Yasuike, H. Ruhl, F. Pegoraro, S. V. Bulanov, E. M. Campbell, M. D. Perry, and H. Powell, "Fast ignition by laser-accelerated proton beams," *Physical Review Letters*, vol. 86, no. 3, pp. 436–439, 2001.

[118] M. Barberio, S. Veltri, M. Scisciо, and P. Antici, "Laser-accelerated proton beams as diagnostics for cultural heritage," *Scientific Reports*, vol. 7, no. 1, p. 40415, 2017.

[119] R. Snavely, B. Zhang, K. Akli, Z. Chen, R. Freeman, P. Gu, S. Hatchett, D. Hey, J. Hill, M. Key, *et al.*, "Laser generated proton beam focusing and high temperature isochoric heating of solid matter," *Physics of Plasmas*, vol. 14, no. 9, 2007.

[120] M. Berger, J. Coursey, and M. Zucker, "Estar, pstar, and astar: Computer programs for calculating stopping-power and range tables for electrons, protons, and helium ions (version 1.21)," 1999.

[121] R. Lelièvre, W. Yao, T. Waltenspiel, I. Cohen, V. Anthonippillai, P. Antici, A. Beck, E. Cohen, D. Michaeli, I. Pomerantz, *et al.*, "A comprehensive characterization of the neutron fields produced by the apollon petawatt laser," *The European Physical Journal Plus*, vol. 139, no. 11, p. 1035, 2024.

[122] S. Agostinelli *et al.*, "GEANT4—a simulation toolkit," *Nuclear Instruments and Methods in Physics Research Section A: Accelerators, Spectrometers, Detectors and Associated Equipment*, vol. 506, no. 3, pp. 250–303, 2003.

[123] J. Allison *et al.*, "Recent developments in GEANT4," *Nuclear Instruments and Methods in Physics Research Section A: Accelerators, Spectrometers, Detectors and Associated Equipment*, vol. 835, pp. 186–225, 2016.

[124] M. Chadwick, M. Herman, and P. Oblozinsky, "" endf/b-vii. 1 nuclear data for science and technology: Cross sections, covariances, fission product yields and decay data", nuclear data sheets, 112 (12): 2887-2996," 2011.

[125] A. J. Plompen, O. Cabellos, C. de Saint Jean, M. Fleming, A. Algora, M. Angelone, P. Archier, E. Bauge, O. Bersillon, A. Blokhin, *et al.*, "The joint evaluated fission and fusion nuclear data library, jeff-3.3," *The European Physical Journal A*, vol. 56, no. 7, p. 181, 2020.

[126] K. Shibata, O. Iwamoto, T. Nakagawa, N. Iwamoto, A. Ichihara, S. Kunieda, S. Chiba, K. Furutaka, N. Otuka, T. Ohsawa, *et al.*, "Jendl-4.0: a new library for nuclear science and engineering," *Journal of Nuclear Science and Technology*, vol. 48, no. 1, pp. 1–30, 2011.

[127] K. Burdonov, R. Lelièvre, P. Forestier-Colleoni, T. Ceccotti, M. Cuciuc, L. Lancia, W. Yao, and J. Fuchs, "Absolute calibration up to 20 mev of an online readout cmos system suitable to detect high-power lasers accelerated protons," *Review of Scientific Instruments*, vol. 94, no. 8, 2023.

[128] J. Bendahan, "Review of active interrogation techniques," *Nuclear Instruments and Methods in Physics Research Section A: Accelerators, Spectrometers, Detectors and Associated Equipment*, vol. 954, p. 161120, 2020.

[129] P. Patel, A. Mackinnon, M. Key, T. Cowan, M. Foord, M. Allen, D. Price, H. Ruhl, P. Springer, and R. Stephens, "Isochoric heating of solid-density matter with an ultrafast proton beam," *Phys. Rev. Lett*, vol. 91, no. 12, p. 125004, 2003.

[130] I. Prencipe, A. Sgattoni, D. Dellasega, L. Fedeli, L. Cialfi, I. W. Choi, I. J. Kim, K. A. Janulewicz, K. Kakolee, H. W. Lee, *et al.*, "Development of foam-based layered targets for laser-driven ion beam production," *Plasma Physics and Controlled Fusion*, vol. 58, no. 3, p. 034019, 2016.

[131] M. Gyrdymov, J. Cikhardt, P. Tavana, N. G. Borisenko, S. Y. Gus´ kov, R. A. Yakhin, G. A. Vegunova, W. Wei, J. Ren, Y. Zhao, *et al.*, "High-brightness betatron emission from the interaction of a sub picosecond laser pulse with pre-ionized low-density polymer foam for icf research," *Scientific Reports*, vol. 14, no. 1, p. 14785, 2024.

[132] S. Shekhanov, A. Gintrand, L. Hudec, R. Liska, J. Limpouch, S. Weber, and V. Tikhonchuk, "Kinetic modeling of laser absorption in foams," *Physics of Plasmas*, vol. 30, no. 1, 2023.

[133] M. Ben Tayeb, V. Tikhonchuk, and J.-L. Feugeas, "Icf target optimization using generative ai," *Physics of Plasmas*, vol. 31, no. 10, 2024.

[134] D. Turnbull, C. Goyon, G. Kemp, B. Pollock, D. Mariscal, L. Divol, J. Ross, S. Patankar, J. Moody, and P. Michel, "Refractive index seen by a probe beam interacting with a laser-plasma system," *Physical Review Letters*, vol. 118, no. 1, p. 015001, 2017.

[135] B. Albertazzi, J. Béard, A. Ciardi, T. Vinci, J. Albrecht, J. Billette, T. Burris-Mog, S. Chen, D. Da Silva, S. Dittrich, *et al.*, "Production of large volume, strongly magnetized laser-produced plasmas by use of pulsed external magnetic fields," *Review of Scientific Instruments*, vol. 84, no. 4, 2013.

[136] D. Higginson, G. Revet, B. Khiar, J. Béard, M. Blecher, M. Borghesi, K. Burdonov, S. Chen, E. Filippov, D. Khaghani, *et al.*, "Detailed characterization of laser-produced astrophysically-relevant jets formed via a poloidal magnetic nozzle," *High Energy Density Physics*, vol. 23, pp. 48–59, 2017.

[137] J. Nuckolls, L. Wood, A. Thiessen, and G. Zimmerman, "Laser compression of matter to super-high densities: Thermonuclear (ctr) applications," *Nature*, vol. 239, no. 5368, pp. 139–142, 1972.

[138] W. L. Kruer, "Intense laser plasma interactions: From janus to nova," *Physics of Fluids B: Plasma Physics*, vol. 3, no. 8, pp. 2356–2366, 1991.

[139] A. Zylstra, O. Hurricane, D. Callahan, A. Kritcher, J. Ralph, H. Robey, J. Ross, C. Young, K. Baker, D. Casey, *et al.*, "Burning plasma achieved in inertial fusion," *Nature*, vol. 601, no. 7894, pp. 542–548, 2022.

[140] P. Michel, S. Glenzer, L. Divol, D. Bradley, D. Callahan, S. Dixit, S. Glenn, D. Hinkel, R. Kirkwood, J. Kline, *et al.*, "Symmetry tuning via controlled crossed-beam energy transfer on the national ignition facility," *Physics of Plasmas*, vol. 17, no. 5, 2010.

[141] J. Lindl, "Development of the indirect-drive approach to inertial confinement fusion and the target physics basis for ignition and gain," *Physics of plasmas*, vol. 2, no. 11, pp. 3933–4024, 1995.

[142] D. S. Montgomery, "Two decades of progress in understanding and control of laser plasma instabilities in indirect drive inertial fusion," *Physics of Plasmas*, vol. 23, no. 5, 2016.

[143] R. Craxton, K. Anderson, T. Boehly, V. Goncharov, D. Harding, J. Knauer, R. McCrory, P. McKenty, D. Meyerhofer, J. Myatt, *et al.*, "Direct-drive inertial confinement fusion: A review," *Physics of Plasmas*, vol. 22, no. 11, 2015.

[144] L. Yin, B. J. Albright, D. J. Stark, W. D. Nystrom, R. F. Bird, and K. J. Bowers, "Saturation of cross-beam energy transfer for multispeckled laser beams involving both ion and electron dynamics," *Physics of Plasmas*, vol. 26, no. 8, 2019.

[145] C. A. Walsh, S. O'Neill, J. Chittenden, A. J. Crilly, B. Appelbe, D. J. Strozzi, D. Ho, H. Sio, B. Pollock, L. Divol, *et al.*, "Magnetized icf implosions: Scaling of temperature and yield enhancement," *Physics of Plasmas*, vol. 29, no. 4, 2022.

[146] P. Chang, G. Fiksel, M. Hohenberger, J. Knauer, R. Betti, F. Marshall, D. Meyerhofer, F. Séguin, and R. Petrasso, "Fusion yield enhancement in magnetized laser-driven implosions," *Physical review letters*, vol. 107, no. 3, p. 035006, 2011.

[147] J. Moody, B. Pollock, H. Sio, D. Strozzi, D.-M. Ho, C. Walsh, G. Kemp, B. Lahmann, S. Kucheyev, B. Kozioziemski, *et al.*, "Increased ion temperature and neutron yield observed in magnetized indirectly driven d 2-filled capsule implosions on the national ignition facility," *Physical Review Letters*, vol. 129, no. 19, p. 195002, 2022.

[148] L. Perkins, D.-M. Ho, B. Logan, G. Zimmerman, M. Rhodes, D. Strozzi, D. Blackfield, and S. Hawkins, "The potential of imposed magnetic fields for enhancing ignition probability and fusion energy yield in indirect-drive inertial confinement fusion," *Physics of plasmas*, vol. 24, no. 6, 2017.

[149] S. H. Glenzer, B. MacGowan, P. Michel, N. Meezan, L. Suter, S. Dixit, J. Kline, G. Kyrala, D. Bradley, D. Callahan, *et al.*, "Symmetric inertial confinement fusion implosions at ultra-high laser energies," *Science*, vol. 327, no. 5970, pp. 1228–1231, 2010.

[150] A. Seaton, L. Yin, R. Follett, B. Albright, and A. Le, "Cross-beam energy transfer in direct-drive icf. ii. theory and simulation of mitigation through increased laser bandwidth," *Physics of Plasmas*, vol. 29, no. 4, 2022.

[151] D. Froula, I. Igumenshchev, D. Michel, D. Edgell, R. Follett, V. Y. Glebov, V. Goncharov, J. Kwiatkowski, F. Marshall, P. Radha, *et al.*, "Increasing hydrodynamic efficiency by reducing cross-beam energy transfer in direct-drive-implosion experiments," *Physical Review Letters*, vol. 108, no. 12, p. 125003, 2012.

[152] J. Marozas, M. Hohenberger, M. Rosenberg, D. Turnbull, T. Collins, P. Radha, P. McKenty, J. Zuegel, F. Marshall, S. Regan, *et al.*, "First observation of cross-beam energy transfer mitigation for direct-drive inertial confinement fusion implosions using wavelength detuning at the national ignition facility," *Physical review letters*, vol. 120, no. 8, p. 085001, 2018.

[153] J. Bates, J. Myatt, J. Shaw, R. Follett, J. Weaver, R. Lehmberg, and S. Obenschain, "Mitigation of cross-beam energy transfer in inertial-confinement-fusion plasmas with enhanced laser bandwidth," *Physical Review E*, vol. 97, no. 6, p. 061202, 2018.

[154] A. Hansen, K. Nguyen, D. Turnbull, B. Albright, R. Follett, R. Huff, J. Katz, D. Mastrosimone, A. Milder, L. Yin, *et al.*, "Cross-beam energy transfer saturation by ion heating," *Physical Review Letters*, vol. 126, no. 7, p. 075002, 2021.

[155] W. Yao, A. Fazzini, S. Chen, K. Burdonov, P. Antici, J. Béard, S. Bolaños, A. Ciardi, R. Diab, E. Filippov, *et al.*, "Laboratory evidence for proton energization by collisionless shock surfing," *Nature Physics*, vol. 17, no. 10, pp. 1177–1182, 2021.

[156] W. Yao, A. Fazzini, S. Chen, K. Burdonov, P. Antici, J. Béard, S. Bolaños, A. Ciardi, R. Diab, E. Filippov, *et al.*, "Detailed characterization of a laboratory magnetized supercritical collisionless shock and of the associated proton energization," *Matter and Radiation at Extremes*, vol. 7, no. 1, 2022.

[157] J. Fuchs, C. Labaune, S. Depierreux, H. Baldis, and A. Michard, "Modification of spatial and temporal gains of stimulated brillouin and raman scattering by polarization smoothing," *Physical Review Letters*, vol. 84, no. 14, p. 3089, 2000.

[158] J. Fuchs, C. Labaune, S. Depierreux, H. Baldis, A. Michard, and G. James, "Experimental evidence of plasma-induced incoherence of an intense laser beam propagating in an underdense plasma," *Physical Review Letters*, vol. 86, no. 3, p. 432, 2001.

[159] D. Froula, D. Bower, M. Chrisp, S. Grace, J. Kamperschroer, T. Kelleher, R. Kirkwood, B. MacGowan, T. McCarville, N. Sewall, *et al.*, "Full-aperture backscatter measurements on the national ignition facility," *Review of scientific instruments*, vol. 75, no. 10, pp. 4168–4170, 2004.

[160] J. Moody, P. Datte, K. Krauter, E. Bond, P. Michel, S. Glenzer, L. Divol, C. Niemann, L. Suter, N. Meezan, *et al.*, "Backscatter measurements for nif ignition targets," *Review of Scientific Instruments*, vol. 81, no. 10, 2010.

[161] S. H. Glenzer, D. H. Froula, L. Divol, M. Dorr, R. L. Berger, S. Dixit, B. A. Hammel, C. Haynam, J. A. Hittinger, J. P. Holder, O. S. Jones, D. H. Kalantar, O. L. Landen, A. B. Langdon, S. Langer, B. J. MacGowan, A. J. Mackinnon, N. Meezan, E. I. Moses, C. Niemann, C. H. Still, L. J. Suter, R. J. Wallace, E. A. Williams, and B. K. F. Young, "Experiments and multiscale simulations of laser propagation through ignition-scale plasmas," *Nature Physics*, vol. 3, p. 716–719, Sept. 2007.

[162] B. J. MacGowan, B. Afeyan, C. Back, R. Berger, G. Bonnaud, M. Casanova, B. Cohen, D. Desenne, D. DuBois, A. Dulieu, *et al.*, "Laser–plasma interactions in ignition-scale hohlraum plasmas," *Physics of Plasmas*, vol. 3, no. 5, pp. 2029–2040, 1996.

[163] J. Fuchs, C. Labaune, S. Depierreux, V. Tikhonchuk, and H. Baldis, "Stimulated brillouin and raman scattering from a randomized laser beam in large inhomogeneous collisional plasmas. i. experiment," *Physics of Plasmas*, vol. 7, no. 11, pp. 4659–4668, 2000.

[164] R. Kodama, K. Okada, and Y. Kato, "Development of a two-dimensional space-resolved high speed sampling camera," *Review of scientific instruments*, vol. 70, no. 1, pp. 625–628, 1999.

[165] B. Fryxell, K. Olson, P. Ricker, F. X. Timmes, M. Zingale, D. Lamb, P. MacNeice, R. Rosner, J. Truran, and H. Tufo, "Flash: An adaptive mesh hydrodynamics code for modeling astrophysical thermonuclear flashes," *The Astrophysical Journal Supplement Series*, vol. 131, no. 1, p. 273, 2000.

[166] J. Buchner, M. Brightman, M. Baloković, K. Wada, F. E. Bauer, and K. Nandra, "Physically motivated x-ray obscurer models," *Astronomy & Astrophysics*, vol. 651, p. A58, 2021.

[167] A. Colaïtis, R. Follett, J. Palastro, I. Igumenschev, and V. Goncharov, "Adaptive inverse ray-tracing for accurate and efficient modeling of cross beam energy transfer in hydrodynamics simulations," *Physics of Plasmas*, vol. 26, no. 7, 2019.

[168] A. Colaïtis, I. Igumenshchev, J. Mathiaud, and V. Goncharov, "Inverse ray tracing on icosahedral tetrahedron grids for non-linear laser plasma interaction coupled to 3d radiation hydrodynamics," *Journal of Computational Physics*, vol. 443, p. 110537, 2021.

[169] A. Colaïtis, D. Turnbull, I. Igumenschev, D. Edgell, R. Shah, O. Mannion, C. Stoeckl, D. Jacob-Perkins, A. Shvydky, R. Janezic, *et al.*, "3d simulations capture the persistent

low-mode asymmetries evident in laser-direct-drive implosions on omega," *Physical Review Letters*, vol. 129, no. 9, p. 095001, 2022.

[170] I. Igumenshchev, V. Goncharov, F. Marshall, J. Knauer, E. Campbell, C. Forrest, D. Froula, V. Y. Glebov, R. McCrory, S. Regan, *et al.*, "Three-dimensional modeling of direct-drive cryogenic implosions on omega," *Physics of Plasmas*, vol. 23, no. 5, 2016.

[171] I. Igumenshchev, D. Michel, R. Shah, E. Campbell, R. Epstein, C. Forrest, V. Y. Glebov, V. Goncharov, J. Knauer, F. Marshall, *et al.*, "Three-dimensional hydrodynamic simulations of omega implosions," *Physics of Plasmas*, vol. 24, no. 5, 2017.

[172] C. McKinstrie, J. Li, R. Giacone, and H. Vu, "Two-dimensional analysis of the power transfer between crossed laser beams," *Physics of Plasmas*, vol. 3, no. 7, pp. 2686–2692, 1996.

[173] W. Kruer, *The physics of laser plasma interactions*. crc Press, 2019.

[174] V. Tikhonchuk, *Particle Kinetics and Laser-plasma Interactions*. Cambridge Scholars Publishing, 2023.

[175] P. Michel, *Introduction to laser-plasma interactions*. Springer Nature, 2023.

[176] C. McKinstrie, A. Kanaev, V. Tikhonchuk, R. Giacone, and H. Vu, "Three-dimensional analysis of the power transfer between crossed laser beams," *Physics of Plasmas*, vol. 5, no. 4, pp. 1142–1147, 1998.

[177] M. Bailly-Grandvaux, B. Winjum, M.-E. Manuel, S. Bolaños, C. Walsh, J. Saret, A. Bogale, J. Strehlow, R. Lee, F. Tsung, *et al.*, "Validation of magnetized gas-jet experiments to investigate the effects of an external magnetic field on laser-plasma instabilities," *Journal of Plasma Physics*, vol. 89, no. 2, p. 175890201, 2023.

[178] B. Winjum, F. Tsung, and W. Mori, "Mitigation of stimulated raman scattering in the kinetic regime by external magnetic fields," *Physical Review E*, vol. 98, no. 4, p. 043208, 2018.

[179] J. Sheffield, D. Froula, S. H. Glenzer, and N. C. Luhmann Jr, *Plasma scattering of electromagnetic radiation: theory and measurement techniques*. Academic press, 2010.

Chapter

Annexes

Sommaire

1

2 Introduction on Laser-Plasma Instabilities

It is important to note that the study of laser–plasma instabilities (LPI) presented in this section is not directly connected to the work on helical coil targets. The investigation of LPI was carried out in parallel, as part of a complementary research activity. In this context, I contributed both to the development of an analytical model and to the experimental campaign aimed at understanding the effect of an external magnetic field on the growth of such instabilities. The motivation behind this effort was to clarify how the presence of a magnetic field can modify processes such as Stimulated Raman Scattering (SRS) and Stimulated Brillouin Scattering (SBS), which are of central importance for laser–plasma coupling in high-energy-density physics. While this topic falls outside the scope of helical target studies, it represents an independent line of research that enriches the broader context of laser–plasma interaction physics explored during this PhD.

2.1 Laser-Plasma Instabilities

Laser-plasma instabilities are fundamental phenomena occurring in high-intensity laser interactions with plasmas. These instabilities can significantly affect energy coupling, plasma heating, and particle acceleration. Among the most studied instabilities are Stimulated Raman Scattering (SRS), Stimulated Brillouin Scattering (SBS), and Cross-talk effects such as Cross-Beam Energy Transfer (CBET).

2.2 Stimulated Raman Scattering (SRS)

Stimulated Raman Scattering (SRS) is a parametric instability where an incident laser photon (ω_1, k_1) decays into a scattered photon (ω_0, k_0) and an electron plasma wave (ω_e, k_e). This process is governed by the resonance condition:

$$\omega_1 = \omega_0 + \omega_e, \quad \mathbf{k}_1 = \mathbf{k}_0 + \mathbf{k}_e. \tag{2.1}$$

SRS can lead to significant energy losses as the scattered photons escape the plasma, and the plasma waves can accelerate electrons to high energies, potentially leading to preheating in inertial confinement fusion (ICF) experiments.

2.3 Stimulated Brillouin Scattering (SBS)

Stimulated Brillouin Scattering (SBS) is another parametric instability where an incident laser photon decays into a scattered photon and an ion-acoustic wave (ω_s, k_s). The resonance condition is:

$$\omega_1 = \omega_s + \omega_0, \quad \mathbf{k}_1 = \mathbf{k}_s + \mathbf{k}_0. \tag{2.2}$$

SBS is particularly detrimental in laser-plasma interactions because the ion-acoustic wave can reflect and redirect laser energy, leading to poor energy deposition and instabilities in fusion applications.

2.4 Cross-talk and Cross-Beam Energy Transfer (CBET)

Cross-talk (CT) refers to the interaction between multiple laser beams in a plasma, leading to interference effects and unintended redistribution of laser energy. A specific manifestation of cross-talk is Cross-Beam Energy Transfer (CBET), where energy is transferred from one beam to another via ion-acoustic waves. This effect is especially significant in ICF experiments, where CBET can lead to nonuniform energy deposition and reduced compression efficiency.

The CBET process follows the energy and momentum matching conditions similar to SBS:

$$\omega_1 - \omega_2 = \omega_s, \quad \mathbf{k}_1 - \mathbf{k}_2 = \mathbf{k}_s. \tag{2.3}$$

This transfer mechanism can be mitigated through techniques such as polarization smoothing and beam phasing strategies.

Laser-plasma instabilities, including SRS, SBS, and CBET, play a crucial role in high-intensity laser interactions with plasmas. Understanding and mitigating these effects are essential for optimizing laser-driven fusion and plasma-based accelerators. Future research aims to develop advanced simulation tools and experimental diagnostics to better control these instabilities.

2.5 Magnetized Inertial Confinement Fusion

Despite its potential, magnetized ICF faces several challenges:

- Precise control and stability of the magnetic field throughout implosion.
- Understanding and mitigating undesired MHD instabilities.
- Increasing the ion temperature of the fuel.

Future research aims to address these challenges through advanced simulations, improved experimental techniques, and interdisciplinary collaboration between plasma physics and fusion science.

Magnetized ICF represents a promising avenue for enhancing inertial fusion performance. By leveraging external magnetic fields, it is possible to reduce heat losses, and optimize energy gain. Continued theoretical and experimental efforts will be essential in determining the feasibility of this approach for future fusion energy applications.

3 Investigation of Laser Plasma Instabilities driven by Coupled High-Power Laser Beams in Magnetized Underdense Plasmas

Plasma, recognized as a nonlinear medium [134], exhibits a diverse array of phenomena that significantly influence laser-plasma interactions (LPI) [135, 136] in inertial confinement fusion

[137–139] (ICF) environments. Among these phenomena, Stimulated Raman Scattering (SRS), Stimulated Brillouin Scattering (SBS), cross-talk (CT) between laser beams [12] and Cross-Beam Energy Transfer (CBET) [140] play pivotal roles in shaping the dynamics of energy deposition within fusion targets. In indirect-drive ICF [141], for instance, CT facilitates the redirection of laser energy, which is critical for achieving the desired symmetry in energy distribution [140,142]. However, it is not the case in direct-drive ICF [143], where it complicates the homogeneous implosion. The interplay between these processes is complex, with CT saturation linked closely to the excitation of SRS, occurring on a rapid timescale of approximately 10 picoseconds [144]. Thus, understanding the mechanisms underlying these interactions is vital for optimizing energy deposition in fusion experiments.

Recent advancements, simulations [145] and experimental validations [146], in magnetized plasma research have revealed that external magnetic fields can significantly alter the behavior of plasma and its interactions with laser light. The incorporation of magnetization into ICF experiments has been shown to enhance fuel temperature and yield [147,148]. Moreover, magnetization can improve the stability and propagation of laser beams in plasma, potentially mitigating the detrimental effects of cross-talk and energy transfer losses. However, a deeper investigation of its effects on local plasma physics remains critical to harnessing these benefits fully.

Cross Talk is fundamental and widespread wave-coupling processes that occur alongside other LPI effects like SBS, SRS, and Two-Plasmon Decay (TPD). These mechanisms can facilitate energy transfer between laser pulses, particularly in indirect-drive ICF where they help control hohlraum energy deposition and implosion symmetry [140,149]. Controlling CT has become a priority in indirect-drive ICF, as highlighted by recent NIF experiments aiming to enhance implosion performance [150]. To reduce CT effects, various approaches have been proposed, including beam diameter reduction [151], wavelength detuning [152], and bandwidth enhancement [153]. However, these investigations are largely based on unmagnetized plasma.

The first direct measurements of CT saturation through ion heating at OMEGA identified CT's sensitivity to ion temperature [154], suggesting CT can be mitigated by local plasma heating. Our prior experiments indicate that such heating can be effectively induced through external magnetic fields, offering a promising pathway to control CT effects in magnetized ICF setups [10]. This experiment have demonstrated notable improvements in light transmission and enhanced smoothing of high-power laser beams. We also observed increased SRS backscattering, attributed in our kinetic simulations to the confinement of hot electrons within the magnetized plasma environment.

Through a combination of experimental investigations and theoretical modeling, we seek to establish a clearer study of how magnetization affects cross-talk and energy transfer processes in laser-plasma interactions. By addressing these critical aspects, our work aims to contribute to the ongoing efforts to enhance the efficiency and effectiveness of ICF, paving the way for future advancements in fusion energy research.

This study aims to explore the implications of cross-talk within a magnetized plasma back-

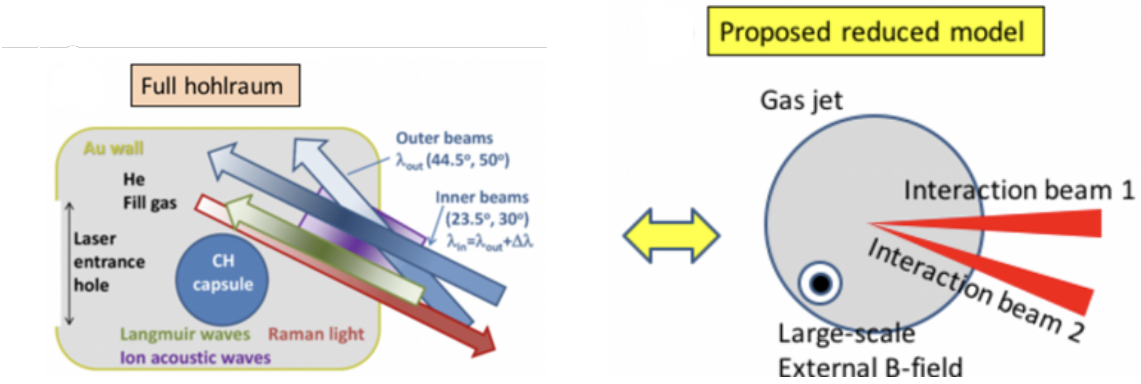

(a) (b)

Figure S1 – Concept of the experiment: (a) Cross-Energy Beam Transfer (CBET) is occurring in hohlraums near the Laser Entrance Hole (LEH), between beams that are part of different irradiation cones. (b) Our proposed mock-up: We will use a gas jet to mimic the atmosphere in the hohlraums and send two long-pulse laser beams that will intersect within the gas jet. On top of this, we will have the capability to apply a large-scale magnetic field to the setup, with dimensions on the order of centimeters, compared to the millimeter-scale of the gas jet, as demonstrated in our previous work [10]. Reproduced from E. Morse, "Inertial fusion," in Nuclear Fusion (Springer International Publishing, Cham, 2018) pp. 345–412. [11] with permission.

ground, using a experimental platform specifically designed for investigating strongly magnetized plasmas. This platform has enabled us to delve deeper into the effects of magnetization on the dynamics of laser propagation and plasma instabilities, highlighting the importance of understanding these interactions.

The magnetization platform itself, developed over the past decade [135, 136], has been deployed at major laser facilities, to study astrophysically-relevant plasma dynamics [155, 156] or ICF [12, 157, 158].

To conduct this work, we will first present the experimental setup and process in Sec. 4, followed by the development and explanation of our analytical theory in Sec. 5. In Sec. 5.1, we will derive the equations governing the SBS (Sec. 5.1.1) and the SRS (Sec. 5.1.2) for a single laser beam. In Sec. 5.2, we will extend this analysis to the case of two interacting laser beams, examining the impact on SBS and SRS instabilities. Finally, we will discuss in Sec. 5.3 the implications of the analytical model in predicting how magnetic fields and the number of laser beam influences these instabilities based on the given assumptions. In the final section (Sec. 6), we will present the experimental results and compare them to the predictions made by the analytical model, allowing us to assess the model's accuracy.

4 Experimental process

4.1 Diagnostics

The used diagnostics have been thoroughly evaluated to measure the plasma conditions (density, temperature), the backscattered light and the transmitted light, as illustrated in Fig.S3.

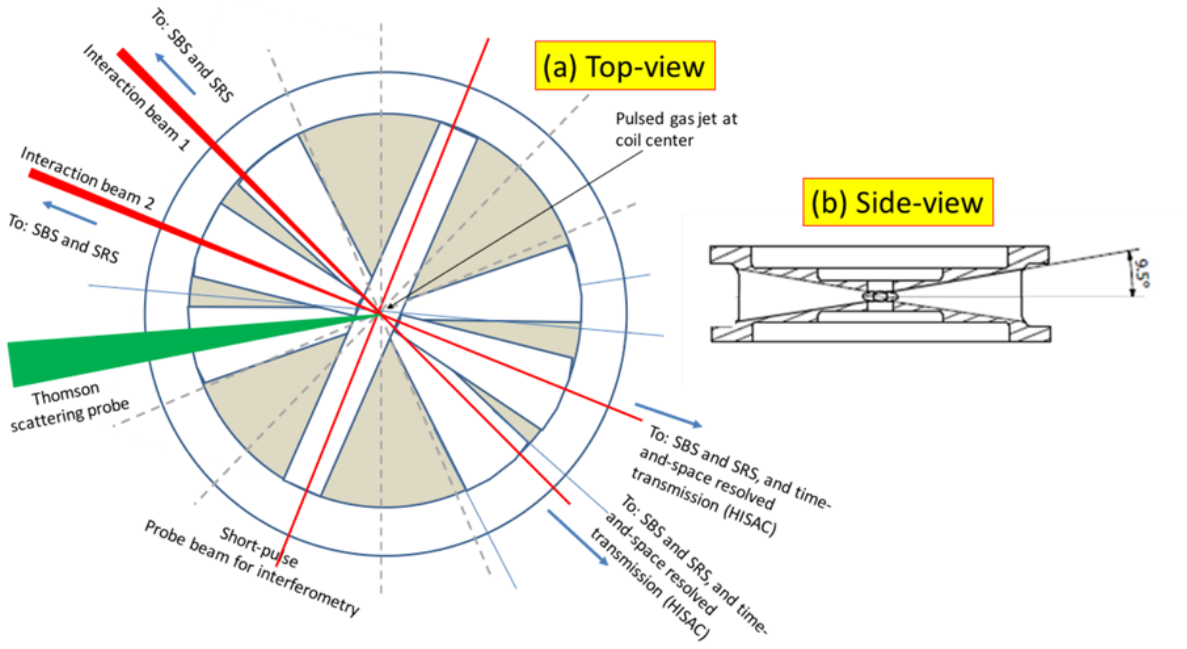

Figure S2 – (a) Proposed setup, illustrating the arrangement of laser beams inside the magnetic field coil, along with the intended diagnostics. This is a top-view cut in the equatorial plane. (b) Side view of the same coil, displaying the conical access to the coil for the beams. The coil employed is identical to the one utilized in our previous studies on magnetized Laser-Plasma Interactions (LPI) [10].

These examples demonstrate that each diagnostic can yield detectable signals under the proposed experimental conditions [10]. The selected diagnostics include:

- Thomson Scattering: This involves scattering off the ion and electron waves, resolved in time through the use of streak cameras. It allows for the assessment of the temporal dynamics of heating and energy transfer [155, 157] (see example in Fig.S3a). Therefore, we are able to measure the plasma temperature. This diagnostic used a probing auxiliary laser beam, featuring a wavelength of 526.5 nm and delivering up to 15 J of energy, with a pulse length of 3 ns.
- Mach-Zehnder Interferometry: This diagnostic uses a few mJ, 8 ns laser available in the LULI area with a wavelength of 532 nm [136]. A Kentech fast gating (50 ps opening time) unit, coupled to Andor cameras, allowed to capture snapshots of the plasma and quantify the plasma electron density (see example in Fig.S3b).
- SBS and SRS Measurements: To quantify the levels of backward Stimulated Brillouin Scattering (SBS) and Stimulated Raman Scattering (SRS) occurring in the plasma [159, 160], time-resolved photodiodes were employed. These measurements were performed by collecting the backscattered light over the full aperture of the focusing optics, following standard procedures in inertial confinement fusion (ICF) experiments to characterize laser–plasma instabilities (LPI) [161]. Two photodiodes with different spectral sensitivity ranges were used in combination with suitable optical filters positioned in front of each. This configuration ensured selective detection: one photodiode, sensitive from 0.2 to 1.1 µm, was dedicated

to SBS, while the other, sensitive from 0.8 to 1.7 µm, was dedicated to SRS. Optical filters were employed to block the unwanted spectral components for each diode. For SBS detection, a bandpass filter centered at the laser wavelength (λ_0) with a ±10 nm full width at half maximum (FWHM) was used to suppress the SRS-shifted light, which occurs around $\omega_1 - \omega_{pe}$ (where ω_1 is the laser frequency and ω_{pe} the plasma frequency) corresponding to wavelengths in the 1.1–1.2 μm range for the plasma densities considered. Conversely, for SRS detection, a silicon filter was used to block all wavelengths below 1.05 μm, effectively eliminating SBS signals, which are shifted by approximately ±10 Åaround λ_0 [162, 163].

- Laser Transmission Measurement: Time-and-space-resolved measurement of the laser transmission using the High-Speed 2D Spatially-Resolved Sampling Camera (HISAC) diagnostic. HISAC allows capturing snapshots of the 2D distribution of the laser with 30ps resolution [10, 12, 164] (see example in Fig.S3d).

The first two diagnostics will be used to quantify plasma conditions, including density and temperature, which are essential inputs for our analytical model or for hydro-radiative (hydro-rad) and Particle-in-Cell (PIC) simulations, as demonstrated in previous studies [10]. The latter two sets of diagnostics will facilitate a thorough assessment of the energetic aspects of the laser interaction with the plasma and the associated energy transfer.

4.2 Experimental setup

In this study, we aim to evaluate the impact of external magnetization on Cross-Talk (CT) and systematically investigate the phase space parameters. Our experimental setup, illustrated in Fig.S1b, takes full advantage of the capabilities offered by LULI2000 facility, particularly its capacity to accommodate multiple long-pulse, high-energy beams.

The two interacting beams had a wavelength of 1.053 μm, with energy levels reaching up to 100 J, and pulse durations of 15 ns. Each beam was focused using an f/8 lens, but was deliberately kept out of focus at the interaction point, with a spot diameter of approximately 300 µm in the gas jet. This defocusing ensured a stable and well-overlapped interaction region between the two beams within the plasma. Under these conditions, each beam reached an on-target intensity of 6×10^{12} W/cm^2. Both beams were linearly polarized along the z-axis and propagated 0.75 mm above the nozzle exit. They were arranged with a crossing angle of 20°, consistent with configurations commonly used in Inertial Confinement Fusion (ICF) facilities such as the National Ignition Facility (NIF). The two laser beam propagate along the x-axis and is polarized along the z-axis, was shot on the hydrogen gas jet, itself at the center of a coil which is responsible for the magnetic field of 20 T (see Fig. S2). The plasma profile had a full-width at half-maximum (FWHM) length of 1.5 mm, with the peak electron density adjustable in the range $n_e = 0.0015$ to $0.015\ n_c$ by modifying the backing pressure of the gas jet system. This underdense plasma replicates the hohlraum environment, where laser-plasma interaction (LPI) processes predominantly occur in indirect-drive inertial confinement fusion (ICF).

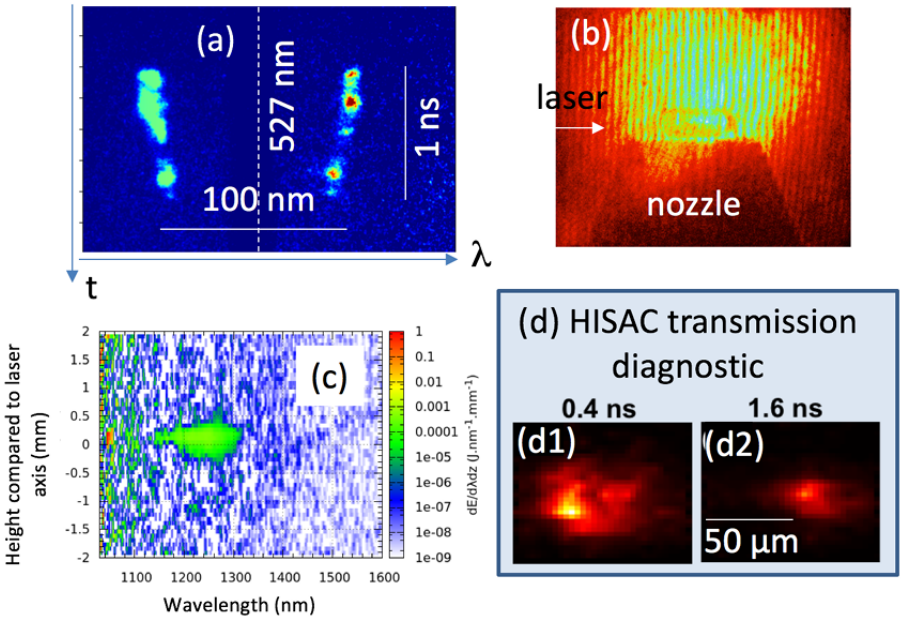

Figure S3 – Examples of raw data for the proposed diagnostics in the experiment, demonstrating our capability to measure the targeted observables under very similar conditions [10], where only one propagating laser beam was used instead of two, as proposed here: (a) Ion Thomson Scattering Spectrum: Time-resolved using an S20 streak camera to measure ion and electron temperatures. The central wavelength (at 527nm, indicated by the white dashed line) of the probe beam is blocked by a notch filter. (b) Interferometry: Used to measure the plasma density. (c) Stimulated Raman Scattering (SRS) Signal: Registered by an InGaAs camera. (d) Two snapshots of the laser beam profile after propagation through the gas jet, reconstructed from the HISAC transmission diagnostic [10, 12]. Each snapshot is integrated over 30 picoseconds. The two snapshots are taken at 0.4 and 1.6 nanoseconds within the evolution of a 2-ns long-pulse, illustrating the diagnostic's ability to resolve filamentation and self-focusing.

5 Theoretical explanation

To simulate Cross-Talk (CT) or Cross-Beam Energy Transfer (CBET), we typically rely on FLASH [165] or GORGON [166] for hydro-radiative (hydro-rad) modeling and use SMILEI [78] for Particle-In-Cell (PIC) simulations [10]. In cases where no external magnetic field is applied, CT dynamics can also be explored with the IFRIIT code [167], which integrates seamlessly with the ASTER [168, 169] radiation hydrodynamics framework [170, 171]. However, an analytical theoretical approach for CT or CBET behavior in the presence of external magnetic fields remains undeveloped.

For our analytical model, we propose to analyze Stimulated Raman Scattering (SRS) and Stimulated Brillouin Scattering (SBS) as separate processes. By incorporating the magnetic field into the SBS equations [172], we derive the interaction between two electromagnetic fields, while noting that the Maxwell wave equation remains unchanged [173, 174]:

$$\left(\partial_t^2 + \omega_{pe}^2 - c^2\nabla^2\right) A = -\omega_{pe}^2 n_l A \tag{5.1}$$

,

and the ion-acoustic (sound) wave equation becomes:

$$\left(\chi\partial_t^2 - c_s^2\nabla^2 + \gamma\partial_t\right) n_l = \frac{c_s^2}{2}\nabla^2 A^2 \tag{5.2}$$

.

with $\chi = Z\left(d\tilde{n_i}/d\tilde{n_e}\right) = 1 + k^2\lambda_D^2$, $\gamma = \left(Zm_e/m_i\right)\left(1-\chi_B\right)\omega_c + 2\gamma_s^B$, $\lambda_D = \sqrt{\epsilon_0 k_B T_e/n_e}$ is the Debye length, A is the electromagnetic potential , $\omega_{pe} = \sqrt{\left(n_{e_0}e^2/m_e\epsilon_0\right)}$ is the electronic plasma frequency, $\omega_c = \left(eB/m_e\right)$ is the cyclotron frequency, B is the external magnetic field, m_e and m_i are respectively the electron and the ion mass, e is the elementary charge, Z the degree of ionization, $n_e = n_{e_0} + \tilde{n_e}$ and $n_i = n_{i_0} + \tilde{n_i}$ are respectively the electron and ion density, $n_l = \tilde{n_e}/n_{e_0}$, $\tilde{n_i}$ and $\tilde{n_e}$ are respectively the low fluctuation of the ion and electron density derived assuming a Boltzmann distribution, as described in Ref. [174], n_{e_0} and n_{i_0} are respectively the uniform background electronic and ionic density, $c_s = \sqrt{ZT_e/m_i}$ is the ion acoustic velocity, $\gamma_s = \sqrt{\frac{\pi}{8}}kv_s\left(\omega_{pi}/\omega_{pe} + c_s^3/v_{Ti}^3\exp\left(-v_s^2/2v_{Ti}^2\right)\right)$ is the Landau damping frequency due to electrons and ions, $\gamma_{se} = \sqrt{\frac{\pi}{8}}\omega_{pe}/\left(k\lambda_D\right)^3\exp\left(-3/2 - 1/2\left(k\lambda_D\right)^2\right)$ is the Landau damping frequency due to electrons [174, 175], $\omega_{pi} = \sqrt{Z^2e^2n_{i_0}/m_i\epsilon_0}$ is the ion plasma density, $v_s = \sqrt{\frac{ZT_e+3T_i}{m_i}}$ is the sound speed, $v_{Ti} = \sqrt{T_i/m_e}$ the thermal ion velocity, k is the wave vector, ϵ_0 is the vacuum permittivity and k_B is the Boltzmann constant. χ_B and χ_{noB} are respectively the ion-to-electron fluctuation density with and without magnetic-field, γ_{se}^B and γ_{se}^{noB} are respectively the electronic Landau damping with and without magnetic-field and γ_s^B and γ_s^{noB} are respectively the Landau damping frequency due to electrons and ions with and without magnetic-field.

Adding the magnetic field in the equations of SRS [173], we conserve the Maxwell's wave equation (eq. 5.1) but we replace the ion-acoustic wave by the electronic wave equation:

$$\left(\partial_t^2 + \omega_{pe}^2 - c_e^2\nabla^2 + \left(\omega_c + 2\gamma_s^B\right)\partial_t\right) n_l = \frac{c_e^2}{2}\nabla^2 A^2 \tag{5.3}$$

.

where $c_e = c_s\sqrt{\frac{m_i}{Zm_e}}$ is the electronic thermal velocity. We propose then to describe 4 different cases, for each SBS and SRS, consider the cases with one and two beams.

5.1 One laser beam

In the study of only one laser beam, one consider:

$$\begin{aligned} A =& A_1(\epsilon,\eta,t)\times\exp\left[i\left(k_1 r - \omega_1 t\right)\right] \\ &+ A_0(\epsilon,\eta,t)\times\exp\left[i\left(k_0 r - \omega_0 t\right)\right] \end{aligned} \tag{5.4}$$

and

$$n_l = \tilde{n_e}/n_{e_0} = n(\epsilon,\eta,t)\times\exp\left[i\left(k_1 - k_0\right)r\right] \tag{5.5}$$

with $\omega_{1L} = \omega_1 - \omega_0$ and where A_1, ω_1 and k_1 are respectively the electromagnetic potential, the frequency and the wave vector of the laser beam and A_0, ω_0 and k_0 are respectively the electromagnetic potential, the frequency and the wave vector of the scattered beam.

Making the slowly varying envelope approximation, one can show that:

$$\partial_x A_1 = -i\left(\omega_{pe}^2/2\omega_1 v_1\right) n A_0 \exp\left[i\omega_{1L}t\right] \tag{5.6}$$

$$\partial_y A_0 = -i\left(\omega_{pe}^2/2\omega_0 v_0\right) n^* A_1 \exp\left[-i\omega_{1L}t\right] \tag{5.7}$$

where $v_1 = \frac{d\omega_1}{dk_1}$ is the group velocity of the laser beam and v_0 is the group velocity of the backscattered wave.

5.1.1 One beam - Stimulated Brillouin Scattering

In the one beam SBS case, the ion-acoustic wave equation becomes:

$$\left(\chi\partial_t^2 + \omega_{s_1}^2 + \gamma\partial_t\right) n = -\omega_{s_1}^2 A_1 A_0^* \exp\left[-i\omega_{1L}t\right] \tag{5.8}$$

.

If, in eq. 5.8, we take B=0 and $\frac{d\tilde{n_i}}{d\tilde{n_e}} = 1/Z$, to found the equations presented in previous publications [173]. To finish, one can compute α_j and β_j coefficients, which are respectively the real and imaginary parts of the ion-acoustic response to the ponderomotive force. Such that:

$$\partial_x A_1 = \left(i\alpha_{1-1L-SBS} - \beta_{1-1L-SBS}\right) A_1 |A_0|^2 \tag{5.9}$$

$$\partial_y A_0 = \left(i\alpha_{0-1L-SBS} + \beta_{0-1L-SBS}\right) |A_1|^2 A_0 \tag{5.10}$$

and here, injecting eq. 5.8 in eq. 5.6 and 5.7, one get:

$$\alpha_{j-1L-SBS} = \frac{\omega_{pe}^2 \omega_{s_1}^2 \left(\omega_{s_1}^2 - \chi\omega_{1L}^2\right)}{2\omega_j v_j \left[\left(\omega_{s_1}^2 - \chi\omega_{1L}^2\right)^2 + \omega_{1L}^2\gamma^2\right]} \tag{5.11}$$

$$\beta_{j-1L-SBS} = \frac{\omega_{pe}^2 \omega_{s_1}^2 \gamma\omega_{1L}}{2\omega_j v_j \left[\left(\omega_{s_1}^2 - \chi\omega_{1L}^2\right)^2 + \omega_{1L}^2\gamma^2\right]} \tag{5.12}$$

with $\omega_{s_1} = c_s \left(k_1 - k_0\right)$ the ion-accoustic wave frequency for one beam.

5.1.2 One beam - Stimulated Raman Scattering

In the one beam SRS case, the electronic wave equation becomes:

$$\begin{aligned}\left(\partial_t^2 + \omega_{pe}^2 + \omega_{e_1}^2 + \left(\omega_c + 2\gamma_s^B\right)\partial_t\right) n \\ = -\omega_{e_1}^2 A_1 A_0^* \exp\left[-i\omega_{1L}t\right]\end{aligned} \tag{5.13}$$

.

To finish, one can compute α_j and β_j coefficients, which are respectively the real and imaginary parts of the ion-acoustic response to the ponderomotive force. Such that:

$$\partial_x A_1 = \left(i\alpha_{1-1L-SRS} - \beta_{1-1L-SRS}\right) A_1 |A_0|^2 \tag{5.14}$$

$$\partial_y A_0 = \left(i\alpha_{0-1L-SRS} + \beta_{0-1L-SRS}\right) |A_1|^2 A_0 \tag{5.15}$$

and here, injecting eq. 5.13 in eq. 5.6 and 5.7, one get:

$$\alpha_{j-1L-SRS} = \frac{\omega_{pe}^2 \omega_{e_1}^2 \left(\omega_{1L}^2 - \omega_{pe}^2 - \omega_{e_1}^2\right)}{2\omega_j v_j \left[\left(\omega_{1L}^2 - \omega_{pe}^2 - \omega_{e_1}^2\right)^2 + \omega_{1L}^2 \left(\omega_c + 2\gamma_s^B\right)^2\right]} \tag{5.16}$$

$$\beta_{j-1L-SRS} = \frac{\omega_{pe}^2 \omega_{e_1}^2 \left(\omega_c + 2\gamma_s^B\right) \omega_{1L}}{2\omega_j v_j \left[\left(\omega_{1L}^2 - \omega_{pe}^2 - \omega_{e_1}^2\right)^2 + \omega_{1L}^2 \left(\omega_c + 2\gamma_s^B\right)^2\right]} \tag{5.17}$$

with $\omega_{e_1} = c_e \left(k_1 - k_0\right)$ the thermal electronic wave frequency for one beam.

5.2 Two laser beams

In the study of two laser beams, one considers:

$$\begin{aligned} A =& A_1(\epsilon, \eta, t) \times \exp\left[i\left(k_1 r - \omega_1 t\right)\right] \\ &+ A_2(\epsilon, \eta, t) \times \exp\left[i\left(k_2 r - \omega_2 t\right)\right] \end{aligned} \tag{5.18}$$

and

$$n_l = \tilde{n_e}/n_{e_0} = n(\epsilon, \eta, t) \times \exp\left[i\left(k_1 - k_2\right) r\right] \tag{5.19}$$

with $\omega_{2L} = \omega_1 - \omega_2$, where A_2, ω_2 and k_2 are respectively the electromagnetic potential, the frequency and the wave vector of the second laser beam. Making the slowly varying envelope approximation, one can show that:

$$\partial_x A_1 = -i\left(\omega_{pe}^2/2\omega_1 v_1\right) n A_2 \exp\left[i\omega_{2L} t\right] \tag{5.20}$$

$$\partial_y A_2 = -i\left(\omega_{pe}^2/2\omega_2 v_2\right) n^* A_1 \exp\left[-i\omega_{2L} t\right] \tag{5.21}$$

where $v_2 = \frac{d\omega_2}{dk_2}$ is the group velocity of the lower-frequency beam and $v_1 \approx v_2$ is the group velocity of the higher-frequency beam.

5.2.1 Two beams - Stimulated Brillouin Scattering

In the two beam SBS case, the ion-acoustic wave equation becomes:

$$\left(\chi\partial_t^2 + \omega_{s_2}^2 + \gamma\partial_t\right) n = -\omega_{s_2}^2 A_1 A_2^* \exp\left[-i\omega_{2L} t\right] \tag{5.22}$$

.

If, in eq. 5.22, we take B=0, so $\frac{d\tilde{n_i}}{d\tilde{n_e}} = 1/Z$, to found the equations presented in previous publications [172]. To finish, one can compute α_j and β_j coefficients, which are respectively the real and imaginary parts of the ion-acoustic response to the ponderomotive force. Such that:

$$\partial_x A_1 = \left(i\alpha_{1-2L-SBS} - \beta_{1-2L-SBS}\right) A_1 |A_2|^2 \tag{5.23}$$

$$\partial_y A_2 = \left(i\alpha_{2-2L-SBS} + \beta_{2-2L-SBS}\right) |A_1|^2 A_2 \tag{5.24}$$

and here, injecting eq. 5.22 in eq. 5.20 and 5.21, one get:

$$\alpha_{j-2L-SBS} = \frac{\omega_{pe}^2 \omega_{s_2}^2 \left(\omega_{s_2}^2 - \chi\omega_{2L}^2\right)}{2\omega_j v_j \left[\left(\omega_{s_2}^2 - \chi\omega_{2L}^2\right)^2 + \omega_{2L}^2\gamma^2\right]} \tag{5.25}$$

$$\beta_{j-2L-SBS} = \frac{\omega_{pe}^2 \omega_{s_2}^2 \gamma\omega_{2L}}{2\omega_j v_j \left[\left(\omega_{s_2}^2 - \chi\omega_{2L}^2\right)^2 + \omega_{2L}^2\gamma^2\right]} \tag{5.26}$$

with $\omega_{s_2} = c_s\left(k_1 - k_2\right)$ the ion-accoustic wave frequency for two beams.

5.2.2 Two beams - Stimulated Raman Scattering

In the two beam SRS case, the electronic wave equation becomes:

$$\left(\partial_t^2 + \omega_{pe}^2 + \omega_{e_2}^2 + \left(\omega_c + 2\gamma_{se}^B\right)\partial_t\right) n = -\omega_{e_2}^2 A_1 A_2^* \exp\left[-i\omega_{2L}t\right] \tag{5.27}$$

.

To finish, one can compute α_j and β_j coefficients, which are respectively the real and imaginary parts of the ion-acoustic response to the ponderomotive force. Such that:

$$\partial_x A_1 = \left(i\alpha_{1-2L-SRS} - \beta_{1-2L-SRS}\right) A_1 |A_2|^2 \tag{5.28}$$

$$\partial_y A_2 = \left(i\alpha_{2-2L-SRS} + \beta_{2-2L-SRS}\right) |A_1|^2 A_2 \tag{5.29}$$

and here, injecting eq. 5.27 in eq. 5.20 and 5.21, one get:

$$\alpha_{j-2L-SRS} = \frac{\omega_{pe}^2 \omega_{e_2}^2 \left(\omega_{2L}^2 - \omega_{pe}^2 - \omega_{e_2}^2\right)}{2\omega_j v_j \left[\left(\omega_{2L}^2 - \omega_{pe}^2 - \omega_{e_2}^2\right)^2 + \omega_{2L}^2\left(\omega_c + 2\gamma_{se}^B\right)^2\right]} \tag{5.30}$$

$$\beta_{j-2L-SRS} = \frac{\omega_{pe}^2 \omega_{e_2}^2 \left(\omega_c + 2\gamma_{se}^B\right)\omega_{2L}}{2\omega_j v_j \left[\left(\omega_{2L}^2 - \omega_{pe}^2 - \omega_{e_2}^2\right)^2 + \omega_{2L}^2\left(\omega_c + 2\gamma_{se}^B\right)^2\right]} \tag{5.31}$$

with $\omega_{e_2} = c_e\left(k_1 - k_2\right)$ the thermal electronic wave frequency for two beams.

5.3 Model discussion

The responsible for growth rate of instabilities is the β coefficient [176]. This is why, we reason with this coefficient to understand the behavior of the instabilities in the different cases that we treat.

5.3.1 Discussion on SBS

For SBS with only one laser:

$$\frac{\beta_{1L-SBS}^{noB}}{\beta_{1L-SBS}^{B}} = \frac{2\gamma_s^{noB}\left[\left(\omega_{s_1}^2 - \chi_B\omega_{1L}^2\right)^2 + \gamma^2\omega_{1L}^2\right]}{\gamma\left[\left(\omega_{s_1}^2 - \chi_{noB}\omega_{1L}^2\right)^2 + 4\gamma_s^{noB^2}\omega_{1L}^2\right]}$$

.

If $\frac{\beta_{1L-SBS}^{noB}}{\beta_{1L-SBS}^{B}} > 1$ the SBS will decrease under the effect of magnetic field, else the SBS will increase under the effect of magnetic field.

For SBS with two lasers:

$$\frac{\beta_{2L-SBS}^{noB}}{\beta_{2L-SBS}^{B}} = \frac{2\gamma_s^{noB}\left[\left(\omega_{s_2}^2 - \chi_B\omega_{2L}^2\right)^2 + \gamma^2\omega_{2L}^2\right]}{\gamma\left[\left(\omega_{s_2}^2 - \chi_{noB}\omega_{2L}^2\right)^2 + 4\gamma_s^{noB^2}\omega_{2L}^2\right]}$$

.

If $\frac{\beta_{1L-SBS}^{noB}}{\beta_{1L-SBS}^{B}} \times \frac{\beta_{2L-SBS}^{noB}}{\beta_{2L-SBS}^{B}} > 1$, the magnetic field will decrease the SBS under the effect of two beams, else the magnetic field and the two beams will increase the SBS.

5.3.2 Discussion on SRS

For SRS with only one laser:

$$\frac{\beta_{1L-SRS}^{noB}}{\beta_{1L-SRS}^{B}} = \frac{2\gamma_{se}^{noB}\left[\left(\omega_{1L}^2 + \omega_{pe}^2 - \omega_{e_1}^2\right)^2 + \left(\omega_c + 2\gamma_{se}^{B}\right)^2\omega_{1L}^2\right]}{\left(\omega_c + 2\gamma_{se}^{B}\right)\left[\left(\omega_{1L}^2 + \omega_{pe}^2 - \omega_{e_1}^2\right)^2 + 4\gamma_{se}^{noB^2}\omega_{1L}^2\right]}$$

.

One gets $\frac{\beta_{1L-SRS}^{noB}}{\beta_{1L-SRS}^{B}} > 1$, if $\omega_c > \frac{\left(\omega_{1L}^2 - \omega_{pe}^2 - \omega_{e_1}^2\right)^2}{2\gamma_{se}^{noB}\omega_{1L}^2} - 2\gamma_{se}^{B}$ and so, the magnetic field will decrease the SRS else $\frac{\beta_{1L-SRS}^{noB}}{\beta_{1L-SRS}^{B}} < 1$ therefore, the magnetic field will increase the SRS.

For SRS with two laser beams:

$$\frac{\beta_{2L-SRS}^{noB}}{\beta_{2L-SRS}^{B}} = \frac{2\gamma_{se}^{noB}\left[\left(\omega_{2L}^2 - \omega_{pe}^2 - \omega_{e_2}^2\right)^2 + \left(\omega_c + 2\gamma_{se}^{B}\right)^2\omega_{2L}^2\right]}{\left(\omega_c + 2\gamma_{se}^{B}\right)\left[\left(\omega_{2L}^2 - \omega_{pe}^2 - \omega_{e_2}^2\right)^2 + 4\gamma_{se}^{noB^2}\omega_{2L}^2\right]}$$

.

One gets $\frac{\beta_{1L-SRS}^{noB}}{\beta_{1L-SRS}^{B}} \times \frac{\beta_{2L-SRS}^{noB}}{\beta_{2L-SRS}^{B}} > 1$, if:
$\omega_c \notin \left[\frac{\left(\omega_{2L}^2+\omega_{pe}^2-\omega_{e_2}^2\right)^2}{2\gamma_{se}^{noB}\omega_{2L}^2} - 2\gamma_{se}^{B}, \frac{\left(\omega_{1L}^2+\omega_{pe}^2-\omega_{e_1}^2\right)^2}{2\gamma_{se}^{noB}\omega_{1L}^2} - 2\gamma_{se}^{B}\right]$
the magnetic field will decrease the SRS else $\frac{\beta_{1L-SRS}^{noB}}{\beta_{1L-SRS}^{B}} \times \frac{\beta_{2L-SRS}^{noB}}{\beta_{2L-SRS}^{B}} < 1$ therefore, the magnetic field will increase the SRS. One can understand that the effect of the magnetic field depends directly on the Landau damping, which is higher at low plasma density and high plasma temperature [174, 175].

5.3.3 Discussion on Cross-Talk without magnetic field

The CT SRS behavior without magnetic field is defined using:

$$\frac{\beta_{1L-SRS}^{noB}}{\beta_{2L-SRS}^{noB}} = \frac{\omega_2 v_2 \omega_{e1}^2 \omega_{1L} \left[\left(\omega_{2L}^2 - \omega_{pe}^2 - \omega_{e_2}^2\right)^2 + \omega_{2L}^2 \left(2\gamma_{se}^{noB}\right)^2\right]}{\omega_1 v_1 \omega_{e2}^2 \omega_{2L} \left[\left(\omega_{1L}^2 - \omega_{pe}^2 - \omega_{e_1}^2\right)^2 + \omega_{1L}^2 \left(2\gamma_{se}^{noB}\right)^2\right]}$$

One gets $\frac{\beta_{1L-SRS}^{noB}}{\beta_{2L-SRS}^{noB}} > 1$, if $4\left(\gamma_{se}^{noB}\right)^2 > \frac{\omega_{e2}^2\omega_{2L}\left(\omega_{1L}^2-\omega_{pe}^2-\omega_{e1}^2\right)^2 - \frac{\omega_2 v_2}{\omega 1 v_1}\omega_{e1}^2\omega_{1L}\left(\omega_{2L}^2-\omega_{pe}^2-\omega_{e2}^2\right)^2}{\frac{\omega_2 v_2}{\omega 1 v_1}\omega_{e1}^2\omega_{2L}^2\omega_{1L} - \omega_{e2}^2\omega_{1L}^2\omega_{2L}}$, we reduce the SRS with two beam compared with only one.

The CT SBS behaviour without magnetic field is defined using:

$$\frac{\beta_{1L-SBS}^{noB}}{\beta_{2L-SBS}^{noB}} = \frac{\omega_2 v_2 \omega_{s1}^2 \omega_{1L} \left[\left(\omega_{s_2}^2 - \chi_{noB}\omega_{2L}^2\right)^2 + \omega_{2L}^2 \left(2\gamma_{s}^{noB}\right)^2\right]}{\omega_1 v_1 \omega_{s2}^2 \omega_{2L} \left[\left(\omega_{s_1}^2 - \chi_{noB}\omega_{1L}^2\right)^2 + \omega_{1L}^2 \left(2\gamma_{s}^{noB}\right)^2\right]}$$

One gets $\frac{\beta_{1L-SBS}^{noB}}{\beta_{2L-SBS}^{noB}} > 1$, if $4\left(\gamma_{s}^{noB}\right)^2 > \frac{\omega_{s2}^2\omega_{2L}\left(\omega_{s1}^2-\chi_{noB}\omega_{1L}^2\right)^2 - \frac{\omega_2 v_2}{\omega 1 v_1}\omega_{s1}^2\omega_{1L}\left(\omega_{s2}^2-\chi_{noB}\omega_{2L}^2\right)^2}{\frac{\omega_2 v_2}{\omega 1 v_1}\omega_{s1}^2\omega_{2L}^2\omega_{1L} - \omega_{s2}^2\omega_{1L}^2\omega_{2L}}$, we reduce the SBS with two beam compared with only one.

with γ_s^B and γ_s^{noB} are respectively the Landau damping frequency due to electrons and ions with and without magnetic-field.

5.3.4 Discussion on Cross-Talk beam with magnetic field

The CT SRS behavior with magnetic field can be define using:

$$\frac{\beta_{1L-SRS}^{B}}{\beta_{2L-SRS}^{B}} = \frac{\omega_2 v_2 \omega_{e1}^2 \omega_{1L} \left[\left(\omega_{2L}^2 - \omega_{pe}^2 - \omega_{e_2}^2\right)^2 + \omega_{2L}^2 \left(2\gamma_{se}^{B}\right)^2\right]}{\omega_1 v_1 \omega_{e2}^2 \omega_{2L} \left[\left(\omega_{1L}^2 - \omega_{pe}^2 - \omega_{e_1}^2\right)^2 + \omega_{1L}^2 \left(2\gamma_{se}^{B}\right)^2\right]}$$

One gets $\frac{\beta_{1L-SRS}^{B}}{\beta_{2L-SRS}^{B}} > 1$, if $\left(\omega_c + 2\gamma_{se}^{B}\right)^2 > \frac{\omega_{e2}^2\omega_{2L}\left(\omega_{1L}^2-\omega_{pe}^2-\omega_{e1}^2\right)^2 - \frac{\omega_2 v_2}{\omega 1 v_1}\omega_{e1}^2\omega_{1L}\left(\omega_{2L}^2-\omega_{pe}^2-\omega_{e2}^2\right)^2}{\frac{\omega_2 v_2}{\omega 1 v_1}\omega_{e1}^2\omega_{2L}^2\omega_{1L} - \omega_{e2}^2\omega_{1L}^2\omega_{2L}}$, we reduce the SRS with two beam compared with only one.

The CT SBS behaviour with magnetic field can be defined using:

$$\frac{\beta_{1L-SBS}^{B}}{\beta_{2L-SBS}^{B}} = \frac{\omega_2 v_2 \omega_{s1}^2 \omega_{1L} \left[\left(\omega_{s_2}^2 - \chi_{B}\omega_{2L}^2\right)^2 + \omega_{2L}^2 \left(2\gamma_{s}^{B}\right)^2\right]}{\omega_1 v_1 \omega_{s2}^2 \omega_{2L} \left[\left(\omega_{s_1}^2 - \chi_{B}\omega_{1L}^2\right)^2 + \omega_{1L}^2 \left(2\gamma_{s}^{B}\right)^2\right]}$$

One gets $\frac{\beta_{1L-SBS}^{B}}{\beta_{2L-SBS}^{B}} > 1$, if $4\left(\gamma_{s}^{B}\right)^2 > \frac{\omega_{s2}^2\omega_{2L}\left(\omega_{s1}^2-\chi_{B}\omega_{1L}^2\right)^2 - \frac{\omega_2 v_2}{\omega 1 v_1}\omega_{s1}^2\omega_{1L}\left(\omega_{s2}^2-\chi_{B}\omega_{2L}^2\right)^2}{\frac{\omega_2 v_2}{\omega 1 v_1}\omega_{s1}^2\omega_{2L}^2\omega_{1L} - \omega_{s2}^2\omega_{1L}^2\omega_{2L}}$, we reduce the SBS with two beam compared with only one.

5.3.5 Expected results

	SRS	SBS
two beams versus one beam (CT effect)	decrease if $1 > \frac{\omega_{e2}^2\omega_{2L}\left(\omega_{1L}^2-\omega_{pe}^2-\omega_{e1}^2\right)^2-\frac{\omega_2 v_2}{\omega_1 v_1}\omega_{e1}^2\omega_{1L}\left(\omega_{2L}^2-\omega_{pe}^2-\omega_{e2}^2\right)^2}{\left(\frac{\omega_2 v_2}{\omega_1 v_1}\omega_{e1}^2\omega_{2L}^2\omega_{1L}-\omega_{e2}^2\omega_{1L}^2\omega_{2L}\right)4(\gamma_{se}^{noB})^2}$ else increase	decrease if $1 > \sqrt{CT_{SBS}}/2\gamma_s^{noB}$ else increase, with $CT_{SBS} = \frac{\omega_{s2}^2\omega_{2L}\left(\omega_{s1}^2-\chi_{noB}\omega_{1L}^2\right)^2-\frac{\omega_2 v_2}{\omega_1 v_1}\omega_{s1}^2\omega_{1L}\left(\omega_{s2}^2-\chi_{noB}\omega_{2L}^2\right)^2}{\frac{\omega_2 v_2}{\omega_1 v_1}\omega_{s1}^2\omega_{2L}^2\omega_{1L}-\omega_{s2}^2\omega_{1L}^2\omega_{2L}}$
two beams and B-field versus one beam with B-field (CT effect)	decrease if $1 > \frac{\omega_{e2}^2\omega_{2L}\left(\omega_{1L}^2-\omega_{pe}^2-\omega_{e1}^2\right)^2-\frac{\omega_2 v_2}{\omega_1 v_1}\omega_{e1}^2\omega_{1L}\left(\omega_{2L}^2-\omega_{pe}^2-\omega_{e2}^2\right)^2}{\left(\frac{\omega_2 v_2}{\omega_1 v_1}\omega_{e1}^2\omega_{2L}^2\omega_{1L}-\omega_{e2}^2\omega_{1L}^2\omega_{2L}\right)(\omega_c+2\gamma_{se}^B)^2}$ else increase	decrease if $1 > \sqrt{\frac{\omega_{s2}^2\omega_{2L}\left(\omega_{s1}^2-\chi_B\omega_{1L}^2\right)^2-\frac{\omega_2 v_2}{\omega_1 v_1}\omega_{s1}^2\omega_{1L}\left(\omega_{s2}^2-\chi_B\omega_{2L}^2\right)^2}{\frac{\omega_2 v_2}{\omega_1 v_1}\omega_{s1}^2\omega_{2L}^2\omega_{1L}-\omega_{s2}^2\omega_{1L}^2\omega_{2L}}}/2\gamma_s^B$ else increase
one beam with B-field versus one beam	decrease if $\omega_c > \frac{\left(\omega_{1L}^2-\omega_{pe}^2-\omega_{e_1}^2\right)^2}{2\gamma_{se}^{noB}\omega_{1L}^2} - 2\gamma_{se}^B$ else increase	decrease if $\frac{\gamma_s^B}{\gamma_s^{noB}}\frac{\left(\omega_{s1}^2-\chi_B\omega_{1L}^2\right)^2+4{\gamma_s^B}^2\omega_{1L}^2}{\left(\omega_{s1}^2-\chi_{noB}\omega_{1L}^2\right)^2+4{\gamma_s^{noB}}^2\omega_{1L}^2} > 1$ else increase
two beams with B-field versus one beam	decrease if $\omega_c \notin \left[\frac{\left(\omega_{1L}^2-\omega_{pe}^2-\omega_{e_1}^2\right)^2}{2\gamma_{se}^{noB}\omega_{1L}^2} - 2\gamma_{se}^B, \frac{\left(\omega_{2L}^2-\omega_{pe}^2-\omega_{e_2}^2\right)^2}{2\gamma_{se}^{noB}\omega_{2L}^2} - 2\gamma_{se}^B\right]$ else increase	decrease if $\left(\frac{\gamma_s^B}{\gamma_s^{noB}}\right)^2\frac{\left(\omega_{s1}^2-\chi_B\omega_{1L}^2\right)^2+4{\gamma_s^B}^2\omega_{1L}^2}{\left(\omega_{s1}^2-\chi_{noB}\omega_{1L}^2\right)^2+4{\gamma_s^{noB}}^2\omega_{1L}^2}\times\frac{\left(\omega_{s2}^2-\chi_B\omega_{2L}^2\right)^2+4{\gamma_s^B}^2\omega_{2L}^2}{\left(\omega_{s2}^2-\chi_{noB}\omega_{2L}^2\right)^2+4{\gamma_s^{noB}}^2\omega_{2L}^2} >$ 1 else increase

Table S1 – Summary table of the different behaviours of SRS, SBS and of the effect of CT on the latter

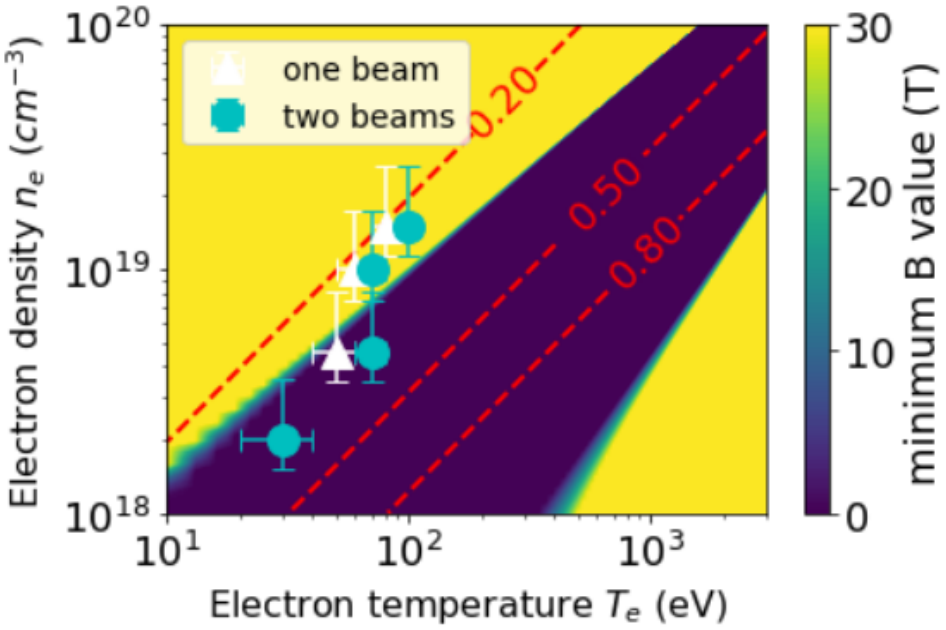

Figure S4 – Map of the minimum magnetic field required to achieve a decrease single-beam SRS, and correspondingly a two-beam SRS increase, as a function of the plasma electron density and temperature, when magnetizing the plasma. The red doted lines correspond to iso-values of the $k\lambda_D$ factor. The colormap is capped at 30 T to enhance readability.

Considering SRS and SBS separately, we are able to clarify the effect of the magnetic field on the instabilities. If the magnetic field affects plasma density, and above all, the ion to electron fluctuation density (i.e., χ), SBS is likely modified. To modify it, the magnetic field can play a important role on plasma temperature and/or density.

Thanks to this model, we are also able to predict that the effect of the magnetic field on the SRS depends directly on the Landau damping. If the Landau damping is high, the effect of the magnetic field will tend to reduce the SRS. The Landau damping is higher with a high $k\lambda_D$ [174], which corresponds to a low plasma density and/or a high plasma temperature. Indeed, in previous publications [10], the effect of magnetic field on the SRS was attributed to a trapping of electrons in the plasma, which is indeed similar to the Landau damping. Regarding the analytical model and these previous publications, one can attribute an effect of the magnetic field on the Landau damping.

All these predicted results have been summarized in Tab. S1. Furthermore, thanks to the SRS conditions presented in this table, one gets the Fig. S4 where the yellow color indicates the (n_e, T_e) values where the B-field increases the one beam SRS and decreases the two beam SRS, and the blue/green indicates the (n_e, T_e) values where the B-field decreases the one beam SRS and increases the two beam SRS. This figure is totally fitting with previous numerical simulation results [177, 178] where the B-field helps to mitigate the SRS. It is also fitting with previous experimental and numerical results where the B-field increased SRS with one beam [10].

One also gets the Fig. S5 where the values higher than 1 indicates the (n_e, T_e) values where the CT with B-field increases the SBS, and the values lower than 1 reciprocally where the CT

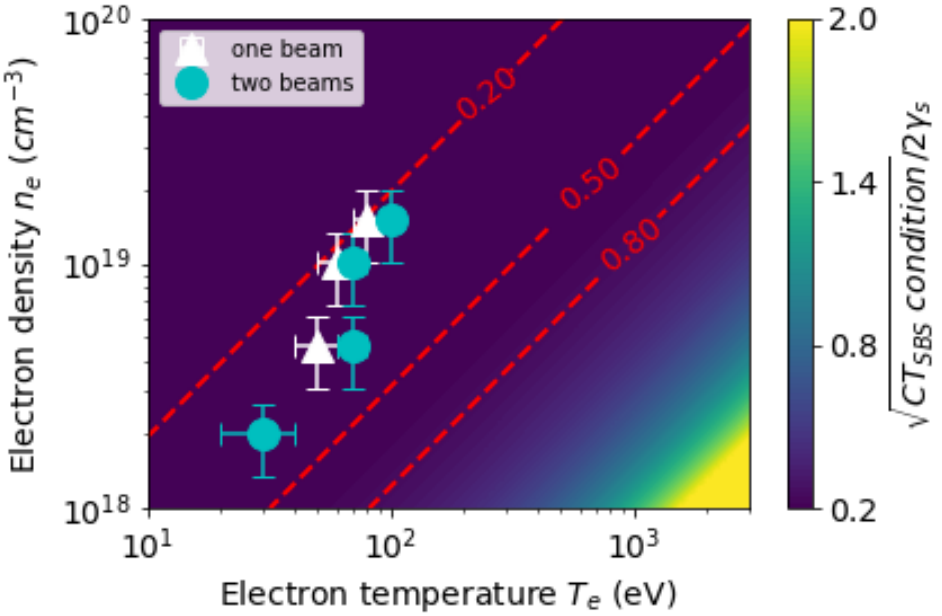

Figure S5 – Map of the the square root of the condition for SBS growth, based on our model, in Cross-Talk (CT) conditions, normalized to the Landau damping (as defined in Tab. S1). The red doted lines correspond to iso-values of the $k\lambda_D$ factor.

with B-field decreases the SBS. The numerical application of the CT SRS conditions imply always that CT reduces the SRS and it is again reduces using B-field.

6 Experimental results

6.1 HISAC reconstructed images

Fig.S6 presents a sequence of plasma images reconstructed from the High-Speed 2D Spatially-Resolved Sampling Camera (HISAC) diagnostic, showcasing both scenarios without and with the application of the magnetic field. The images depict the conditions when solely the South Laser is active and when both the South and North Lasers are operational at 75 bar pressure.

In Fig.S7, the mean intensity profile evolution over approximately 15 nanoseconds is displayed for different laser and magnetic field configurations at 75 bar pressure. In the absence of the magnetic field, irrespective of the laser configuration, there is a reported peak intensity around 9 ns after plasma formation, followed by a continuous decline. However, with the application of the magnetic field, an increase in the intensity change rate is observed after 9 ns. The most significant difference in intensity without/with the magnetic field is observed between 6-11 ns when only the South beam is operating.

The information provided highlights the findings from Fig.S8, which focuses on light transmission analysis from HISAC raw images under various experimental conditions and time windows. Specifically concerning the south beam (S), in the initial nanosecond (first ns), better transmission is observed when only the south beam is applied with an external magnetic field (B=20 T). However, this improved transmission in the first ns does not follow a consistent trend for the

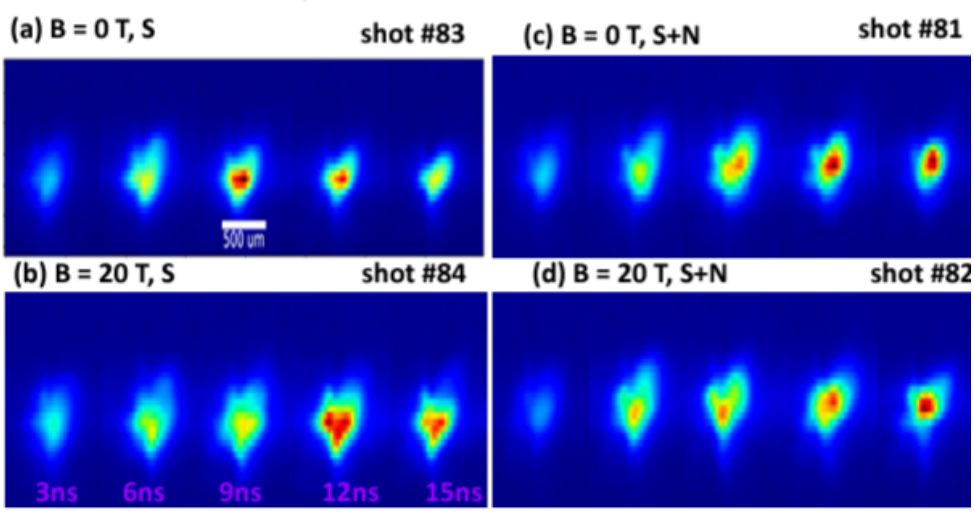

Figure S6 – Reconstructed images from the HISAC diagnostic using the (a) south beam without B-field (b) south beam with B-field (20 T) (c) south and north beam without B-field (d) south and north beam with B-field (20 T).

overall duration of the experiment. Similarly, when both South and North beams (S+N) are applied, better transmission is observed in the first ns with an external magnetic field (B=20 T).

Yet, this improved transmission in the first ns does not exhibit a consistent trend for the overall duration of the experiment. The findings suggest that the presence of an external magnetic field (B=20 T) enhances light transmission in the initial nanoseconds for both the single beam and combined south and north beam scenarios. However, this effect does not persist as a consistent trend throughout the entire duration of the experiment.

6.2 Thomson scattering-Temperature measurement

Thomson scattering [179] is a widely used diagnostic technique for measuring the electron temperature in plasmas. It relies on the elastic scattering of an incident electromagnetic wave by free electrons. When a laser beam with known wavelength and intensity interacts with a plasma, the scattered radiation carries information about the electron velocity distribution. The spectral broadening of the scattered light is directly related to the thermal motion of the electrons, which follows a Maxwellian distribution in thermal equilibrium. The width of the scattered spectrum, $\Delta\lambda$, can be used to determine the electron temperature T_e through the relation:

$$\Delta\lambda \propto \lambda\sqrt{\frac{k_B T_e}{m_e c^2}}, \tag{6.1}$$

where λ is the laser wavelength, k_B is the Boltzmann constant, m_e is the electron mass, and c is the speed of light. By analyzing the scattered spectrum, one can extract the temperature and density of the electrons in the plasma. An example of obtained results is shown if Fig. S9.a and .b for respectively $n_e = 0.001 n_c$ with B-field and two beams and $n_e = 0.0015 n_c$ without B-field with one beam. It appears like the electron temperature is respectively $T_e = 50 \pm 16$ eV and $T_e = 90 \pm 30$ eV. Thanks to this one can estimate that during this experiment, $k\lambda_D = 0.17 \pm 0.11$

(a)

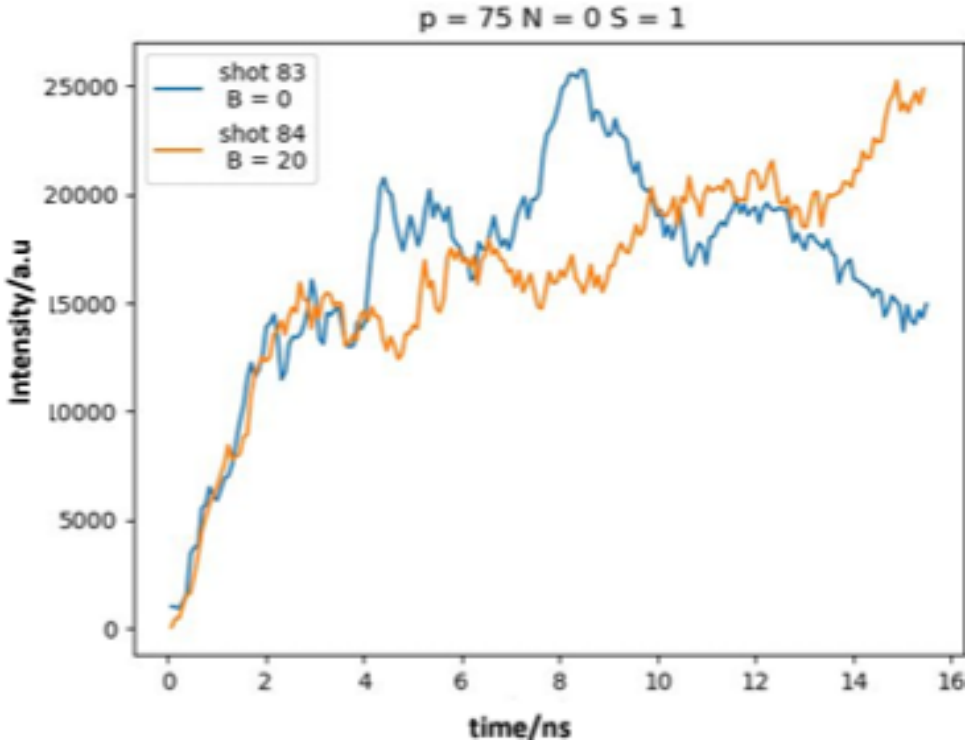

(b)

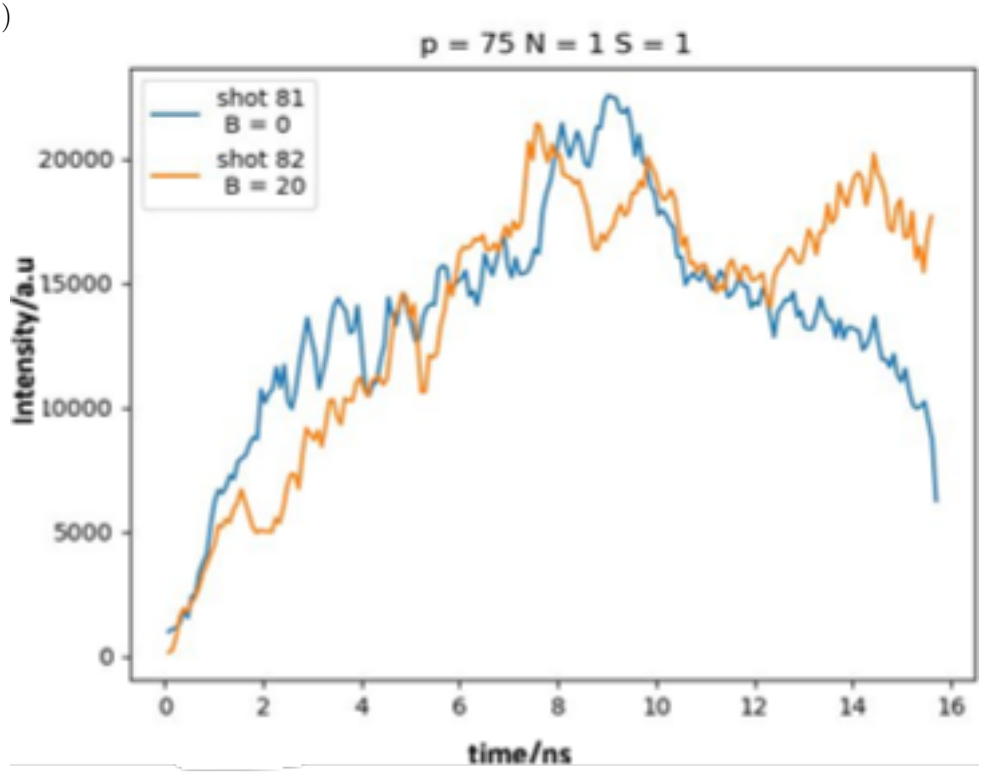

Figure S7 – Intensity get from the HISAC diagnostic using the south and the north beam without B-field (blue line) or with B-field (yellow line) in the case with only south beam (a) or with south and north (b)

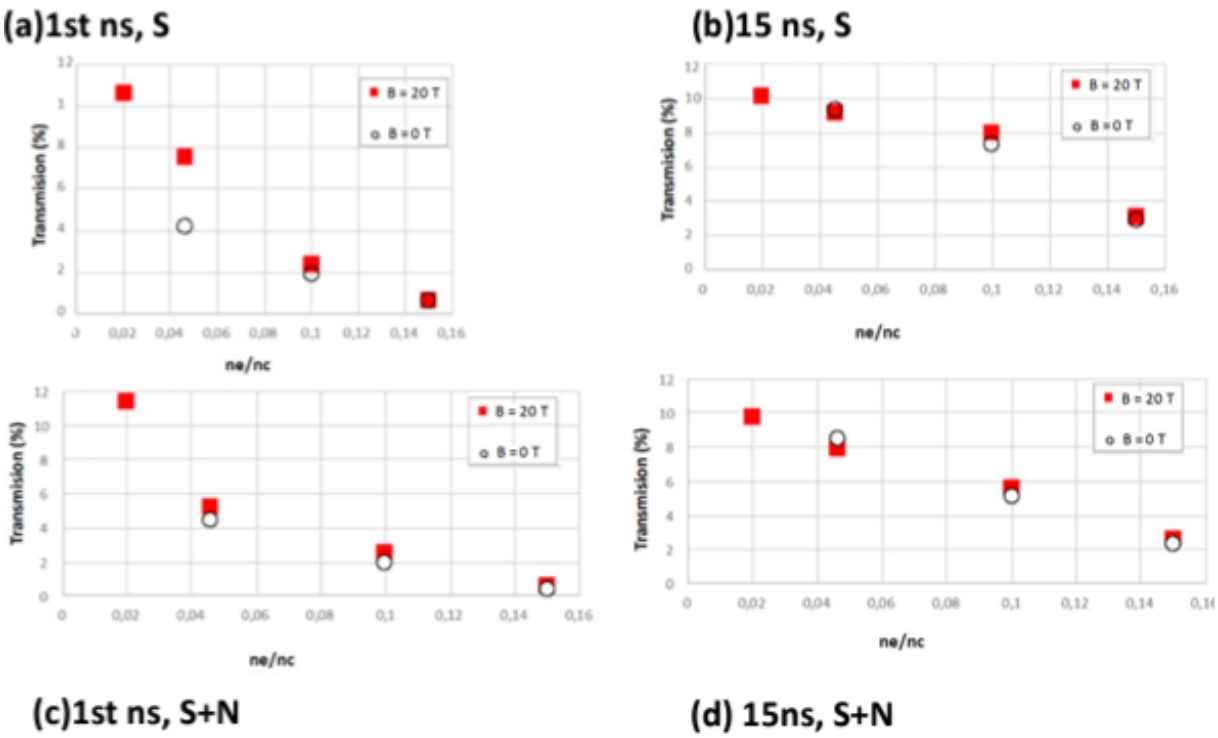

Figure S8 – Light transmission as function of as function of varying electron density n_e/n_c at 1 ns (a) and 15 ns (b) using the south beam, and at 1 ns (c) and 15 ns (d) using south and north beam; with a B-field (red square) or without B-field (white dot).

at low density and 0.34 ± 0.22 at high density. This correspond to χ =1.03 to 1.1.

6.3 Diode trends

Fig.S10 shows trends in diode signals for forward and backward Stimulated Raman Scattering (SRS) as well as backward Stimulated Brillouin Scattering (SBS) over a broad range of electron densities normalized to the critical density (n_e/n_c). Both forward and backward SRS trends are illustrated in the figure respectively in Fig.S10(a) and S10(b), as well as backward SBS (see Fig.S10(c). The observations indicate that with both north and south beams active, adding an external magnetic field reduces the instabilities in SRS and SBS. Conversely, when only the south beam is present, the magnetic field leads to an increase in these instabilities.

The results presented on Fig.S11 suggest that Laser-Plasma Interaction (LPI) is reduced when multiple beams are active, with this reduction becoming even more pronounced under the influence of an external magnetic field. These diode signal observations for SRS and SBS indicate that the interaction between laser beams and plasma weakens significantly with multiple beam input, and this weakening is amplified by magnetization. The analytical model in Sec. 5.3.3 predicts similar behavior, showing strong agreement between our theoretical predictions and experimental outcomes. Experiment align with the predictions from the analytical model presented in Sec. 5.3.1 for SBS when $\chi_B < \chi_{noB}$ and in Sec. 5.3.2 for SRS, as summarized in Fig. S4. At low densities, backward SRS is intensified under the magnetic field, consistent with our predictions that attribute this effect to strong Landau damping at lower densities.

(a)

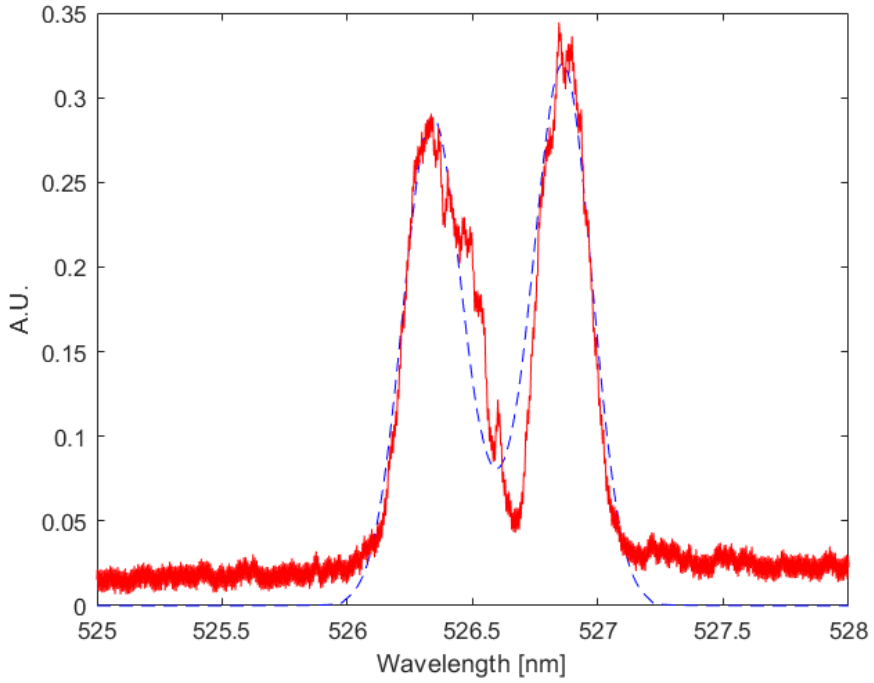

(b)

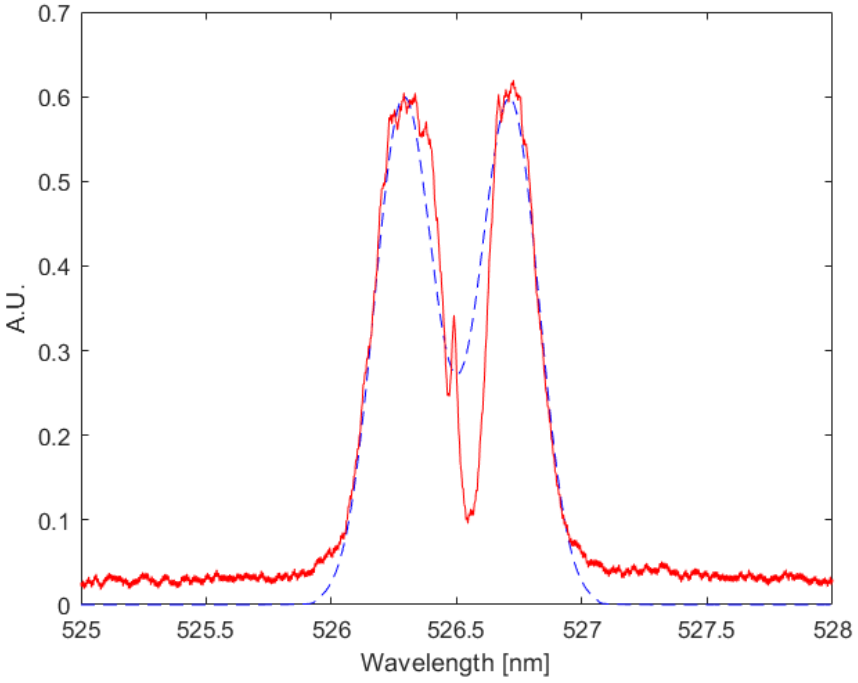

Figure S9 – Examples of TS measurement (red curve) and the fit get thanks to the LLNL code `https://github.com/LLNL/Thomson-Scattering-Cross-Section-Calculator`, for a $n_e = 0.1n_c$ with B-field and two beams (a) and $n_e = 0.15n_c$ without B-field with one beam (b)

(a)

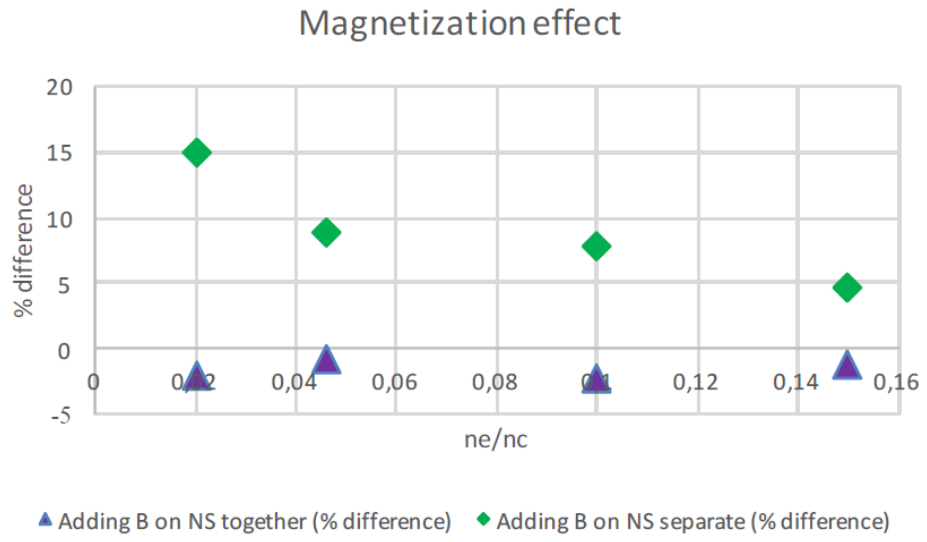

(b)

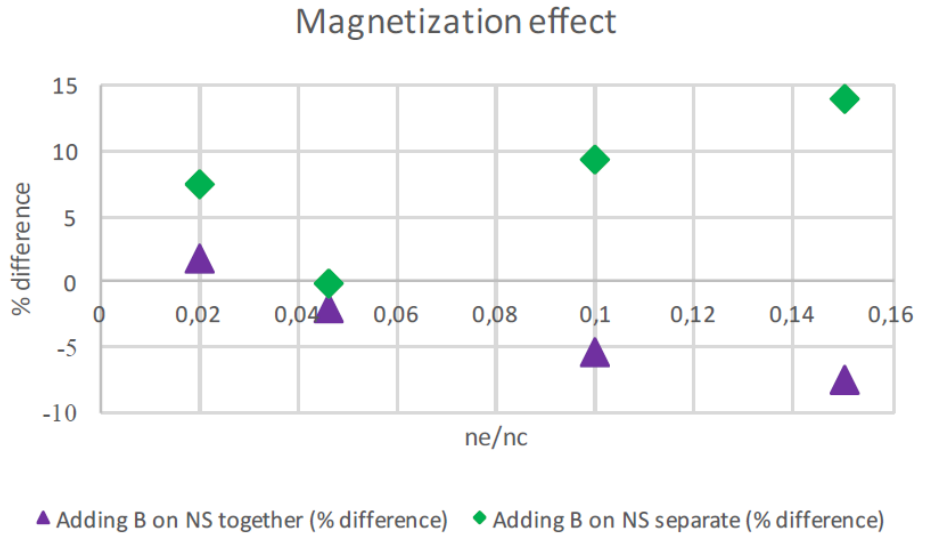

(c)

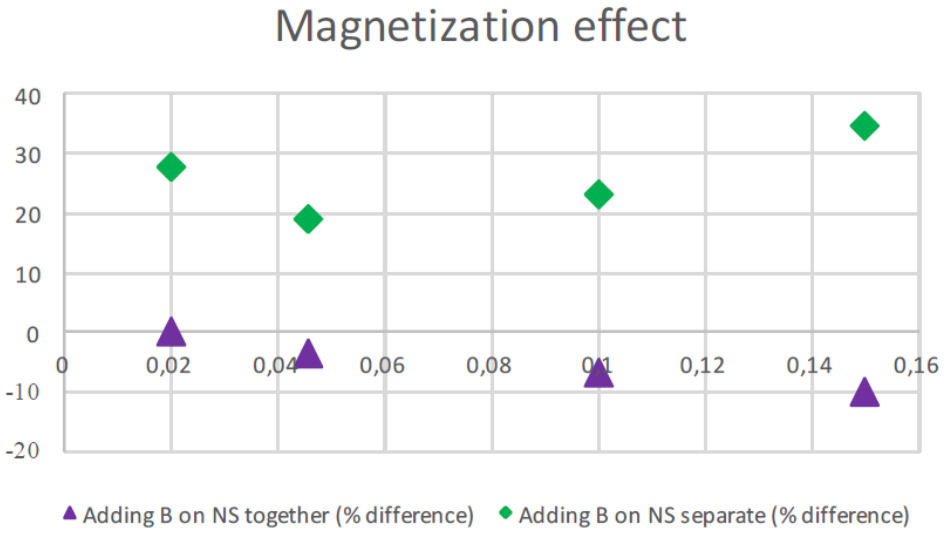

Figure S10 – Effect of the magnetic field on the forward SRS (a), backward SRS (b), backward SBS (c) as function of varying electron density n_e/n_c using a magnetic field and south and north beam normalized with the case with south and north beam without magnetic field (purple triangle) or only south beam normalized with the case with only south beam without magnetic field (green diamond).

(a)

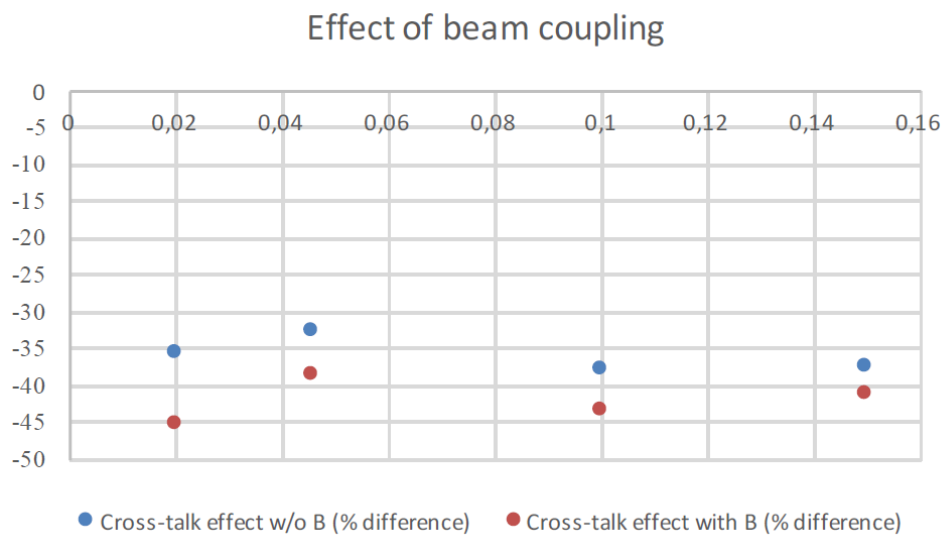

(b)

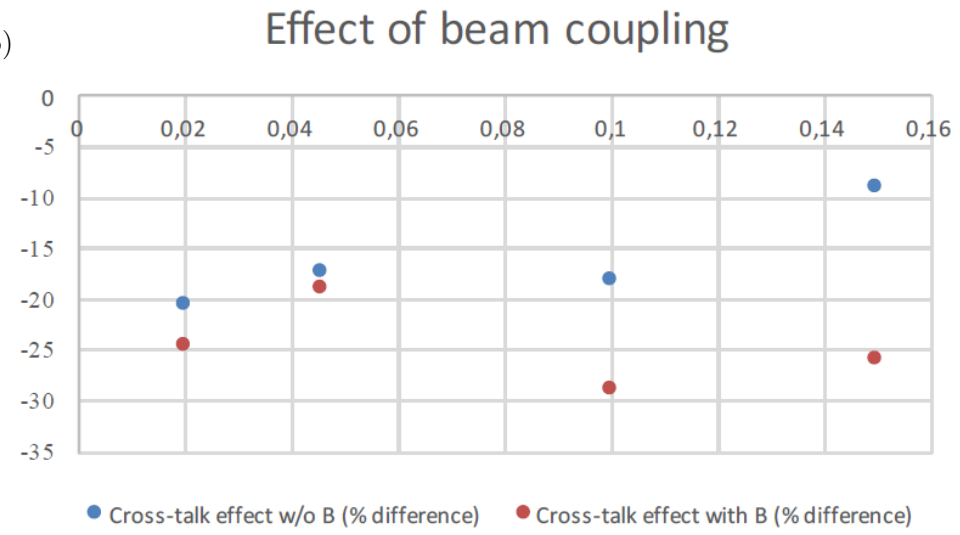

(c)

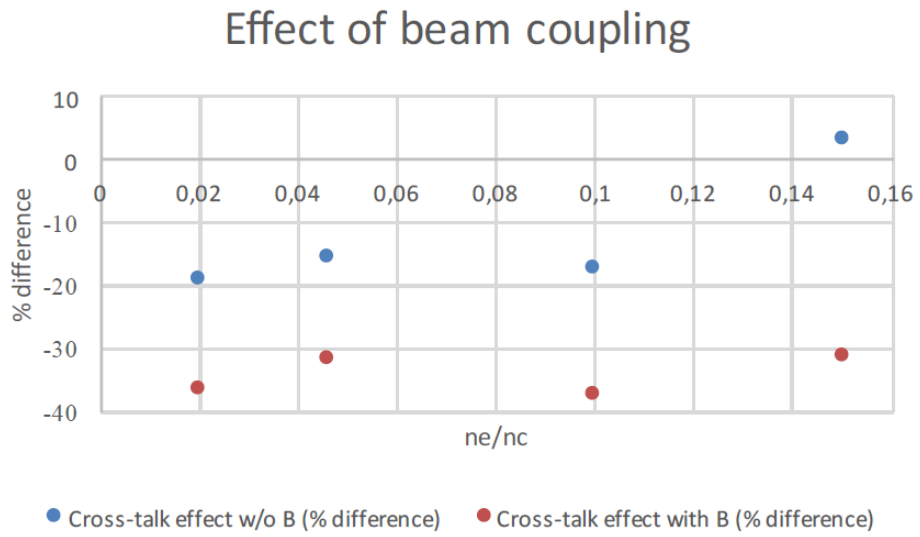

Figure S11 – Effect of the beam coupling on the forward SRS (a), backward SRS (b), backward SBS (c) as function of varying electron density n_e/n_c using south and north beam without B-field (blue dot) or with B-field (red dot), normalized with the case with only one laser without magnetic field.

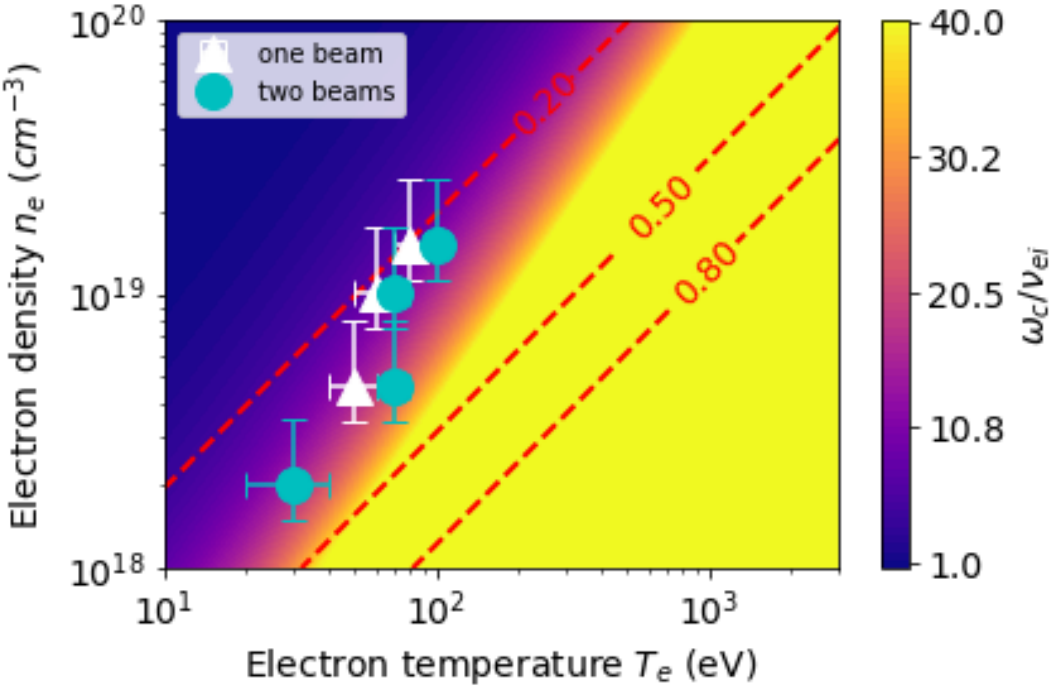

Figure S12 – Map of the hall parameter as a function of electron density and temperature. The red doted line is the contour line of the $k\lambda_D$ factor. This map proves the non-collisional aspect of our plasma and shows the limit of our model (high density and low temperature).

The model predicts that adding a magnetic field influences SBS by altering the ion-to-electron fluctuation density ratios (χ), while its impact on SRS is strongly linked to plasma density through Landau damping effects. The experimental results confirm this predicted behavior: in the absence of an external magnetic field, the presence of two laser beams reduces the growth of SRS and SBS compared to a single-beam configuration.

Overall, the presence of both an external magnetic field and two laser beams leads to a reduction in SRS and SBS compared to the two-beam case without a magnetic field. Conversely, in the single-beam case, the presence of an external magnetic field results in an increase in SRS and SBS compared to the configuration without a magnetic field. These findings are in excellent agreement with previous simulations [10] and with our analytical model previously presented.

7 Discussion of the model limits

Figure S12 shows the map of the Hall parameter, which, when greater than 1, characterizes the plasma as collisionless, thereby defining the domain of validity of our model (non-collisional model). It shows a Hall parameter during our experiment higher than 10. Thus, it confirms the validity of our model for our experimental parameters.

Figure S13 illustrates the expected Faraday rotation angle θ as a function of the electron density n_e for a linearly polarized probe laser with wavelength $\lambda = 1.053\,\mu$m propagating through a plasma of length $L = 3\,$mm under a longitudinal magnetic field of $B = 20\,$T. The angle increases linearly with n_e in this density regime, as predicted by the standard expression for the Faraday

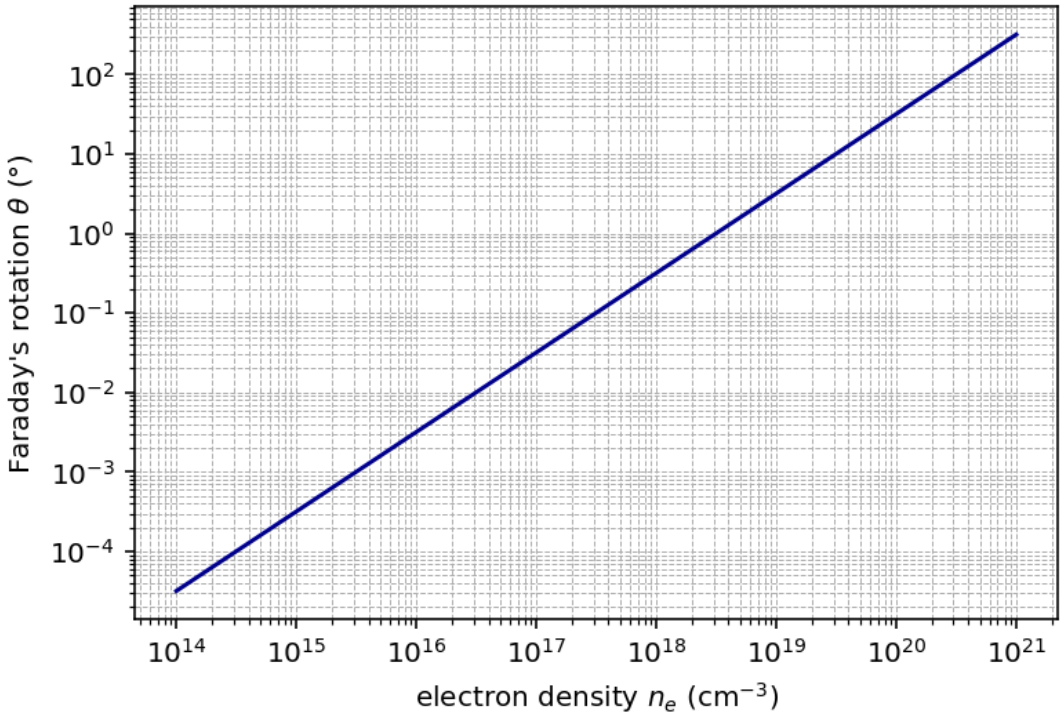

Figure S13 – Faraday rotation angle θ (in degrees) as a function of electron density n_e for a probe laser of wavelength $\lambda = 1.053\,\mu$m propagating through a plasma of length $L = 3\,$mm under a longitudinal magnetic field $B = 20\,$T.

effect in magnetized plasmas,

$$\theta = \frac{e^3\lambda^2}{8\pi^2\varepsilon_0 m_e^2 c^3} n_e B \cdot L \tag{7.1}$$

.

For typical experimental conditions with electron densities ranging from 10^{18} to $2\times10^{19}\,\mathrm{cm}^{-3}$, the rotation remains below 5°, which justifies the assumption that the probe beam remains approximately linearly polarized. For upper value of electron density than $\sim 10^{20}\,\mathrm{cm}^{-3}$, the Faraday's rotation is not anymore negligible.

8 Conclusion

This extensive study investigates the effects of external magnetization on cross-talk (CT) and laser-plasma instabilities, yielding significant insights. Using a robust experimental platform alongside well-established diagnostics, we assessed plasma conditions, the evolution of laser intensity profiles, and the dynamics of light transmission through the plasma.

Our findings reveal a marked influence of an external magnetic field on CT behavior. Notably, diode signals for stimulated Raman scattering (SRS) and stimulated Brillouin scattering (SBS) show clear attenuation when multiple beams are used simultaneously, an effect that is further amplified by the presence of the external magnetic field.

Furthermore, our theoretical model, which treats SRS and SBS processes separately, aligns well with the experimental data. It predicts that the introduction of a magnetic field affects SBS

by altering the ratios of ion to electron density fluctuation, while its impact on SRS is closely related to plasma density and temperature through Landau damping effects. The experimental results confirm these predictions showing that SBS decreases under magnetic fields when both beams are present but increases with a single beam; conversely, SRS is intensified with one beam and shows increased intensity at lower densities with two beams, linked to the Landau damping, while decreasing at higher densities.

Future research will focus on calculating the dispersion relation and conducting Particle-In-Cell (PIC) or hydrodynamic simulations. These efforts will enhance our understanding of how magnetic fields influence magneto-hydrodynamic behaviors.

In upcoming experiments, we plan to investigate the effects of varying the difference of frequency between the two laser beams to test the limits and hypotheses of our model. We will also explore variations in the external magnetic field's amplitude and direction (both parallel and perpendicular to the laser beam) to determine their impacts on laser-plasma interactions and cross-beam energy transfer. This comprehensive approach will refine our model and improve its predictive capability for future inertial confinement fusion (ICF) experiments.